A Terahertz Holography Imaging System for Concealed Weapon Detection Application

A thesis submitted to the University of London in partial fulfilment of the requirements for the degree of Doctor of Philosophy

By

Min Zhou

Supervisors: Prof. Xiaodong Chen and Dr. Yasir Alfadhl

School of Electronic and Engineering and Computer Science

Queen Mary, University of London

October 2017

Statement of originality

I, Min Zhou, confirm that the research included within this thesis is my own work or that where it has been carried out in collaboration with, or supported by others, that this is duly acknowledged below and my contribution indicated. Previously published material is also acknowledged below.

I attest that I have exercised reasonable care to ensure that the work is original, and does not to the best of my knowledge break any UK law, infringe any third party's copyright or other Intellectual Property Right, or contain any confidential material.

I accept that the College has the right to use plagiarism detection software to check the electronic version of the thesis.

I confirm that this thesis has not been previously submitted for the award of a degree by this or any other university.

The copyright of this thesis rests with the author and no quotation from it or information derived from it may be published without the prior written consent of the author.

Signature: Min Zhou

Date: 31/10/2017

To My Family

Acknowledgements

I would like to thank my supervisors, Professor Xiaodong Chen and Dr. Yasir Alfadhl for their guidance over the years.

I would like to thank all my colleagues in the antenna group, particularly Dr. Xiang Li, Dr. Cheng Yang, Dr. Yang Zeng, Dr. Guangwei Jiang, Dr. Lei Li, Liang Yang, Qianyun Zhang, Shaoqing Hu, Chao Shu, Qiao Cheng, Dr. Jing Tian, Muhammad Rafaqat Ali Qureshi and Hai Wang, who gave me such a great enlightenment in my work.

My thanks also go to Dr. Massimo Candotti, Dr. Max Munoz Torrico, Dennis Ife, Dr. Ben Milson and Ho Huen, who devoted their time in helping me out in experiments.

I would like to thank Ms. Chunyan Wei for her care and company.

Last but not least, a sincere thanks to my family. Their support was my ultimate motivation and I really appreciate their unconditional love and care for me.

Abstract

Many research groups have conducted the investigation into terahertz technology for various applications over the last decade. THz imaging for security screening has been one of the most important applications because of its superior performance of high resolution and not health hazardous. Due to increasing security requirements, it is desirable to devise a high-speed imaging system with high image quality for concealed weapon detection. Therefore, this thesis presents my research into a low-cost and fast THz imaging system for security application.

This research has made a number of contributes to THz imaging, such as proposing the beam scanning imaging approach to reduce the scanning time; developing the simulation method of the scanned imaging system; investigating new reconstruction algorithms; studying the optimal spatial sampling criterion; and verifying the beam scanning scheme in experiment. Firstly, the beam scanning scheme is proposed and evaluated in both simulation and experiment, compared to the widely applied raster scanning scheme. A better mechanic rotation structure is developed to reduce the scanning time consumed and realise a more compact system. Then, a rotary Dragonian multi-reflector antenna subsystem, comprising two rotated reflectors is designed to form a similar synthetic aperture being realised in the raster scanned scheme. Thirdly, the simulation of the THz scanning imaging system is achieved by employing Physical Optics algorithm. The transposed convolution and partial inverse convolution reconstruction algorithms are investigated to speed up the image re-construction. Finally, two THz imaging systems based on the raster and beam scanning schemes are assessed and compared in the experiments. The back-propagation, transposed convolution and partial inverse convolution algorithms are applied in these experiments to reconstruct the images. The proposed beam scanning scheme can be further explored together with antenna arrays to provide a compact, fast and low-cost THz imaging system in the future.

Table of contents

List of figures 1

List of tables 15

Abbreviations 17

Chapter 1. Introduction 19

1.1 Background of THz detection 20

1.2 Review of the state-of-the-art development 24

1.2.1 Research work in universities, laboratories and institutes 24

1.2.2 Current commercial products 42

1.3 Challenges and motivations.. 47

1.4 Objectives 49

1.5 Organisation of the thesis 50

1.6 References 51

Chapter 2. Terahertz imaging theory and proposed beam scanning scheme 57

2.1 Introduction of holography theory 57

2.1.1 Optical holography 57

2.1.2 Microwave holography 59

2.2 Proposed beam scanning scheme 62

2.3 Proposed beam scanning THz holography imaging system 63

2.4 Summary 73

2.5 References 73

Chapter 3. Design of Dragonian dual-reflector scanning sub-system 75

3.1 Review of reflector antennas 75
3.2 Dragonian antenna sub-system design 79
3.2.1 Study of path length error 83
3.2.2 Parameter sweep investigation 89
3.2.3 Optimisation and results 95
3.3 Simulation results analysis 98
3.3.1 Comparison between Dragonian antenna and single ellipsoidal antenna 98
3.3.2 Rotation analysis of the Dragonian antenna 100
3.3.3 Scanning beam performance in the scanning area 113
3.4 Summary 116
3.5 References 117
Chapter 4. Simulation of THz scanning schemes and assessment of two novel algorithms 119
4.1 Brief introduction to PO algorithm 119
4.2 Validation of PO algorithm in Matlab 121
4.2.1 Geometry of the single off-axis reflector antenna 121
4.2.2 Simulations of the single offset reflector antenna 122
4.3 Simulations of different scanning schemes 126
4.3.1 Simulation settings in Matlab 126
4.3.2 Study of the raster scanning scheme and the reconstruction algorithm 126
4.3.3 Comparison of the raster scanning scheme and the beam scanning

scheme..129

4.4 Transposed convolution algorithm, partial inverse convolution algorithm and imaging result comparison..135

4.4.1 Transposed convolution (TC) algorithm 135

4.4.2 Partial inverse convolution (PIC) algorithm 146

4.5 Summary 153

4.6 References 154

Chapter 5. Experimental evaluation of THz imaging systems 156

5.1 Introduction 156

5.2 Experimental configuration of the raster scanning system and imaging result analysis..156

5.2.1 Holography transformations in the experimental system.........159

5.2.2 Spatial sampling interval 160

5.2.3 Line spread function (LSF) 163

5.2.4 Calibration of the imaging system...166

5.2.5 Imaging results and analyses...167

5.2.6 Image SNR and NE**Δ**R..176

5.2.7 Study on transceiver antenna positioning/alignment...............181

5.2.8 Evaluation of TC and PIC algorithms 183

5.3 Experimental configuration of the beam scanning system and imaging result analysis..190

5.4 Summary 201

5.5 References 202

Chapter 6. Summary and future works 204

6.1 Summary 204

6.2 Key contributions 206

6.3 Future work 208

List of publications 209

Appendix I: Parameters calculation in Dragonian antenna design 211

Appendix II: Physical optics derivation 213

Appendix III: Ideal gaussian feed 217

List of figures

Figure 1-1 Stand-off Imaging System for Personnel Screening [17]..................22

Figure 1-2 0.6 ~ 1.2 THz FPA camera (a) Photograph of the camera and the FPA in it (b) THz image of a steel screw placed inside an envelope [27]. 25

Figure 1-3 140 THz FMCW ISAR imaging system (a) Photograph of 140 GHz radar imaging scenes (b) Corner reflector made 'CAEP' (top) and the imaging results (bottom) with the 140 GHz ISAR [29]..26

Figure 1-4 675GHz FMCW radar system (a) Photograph of the system (b) Image captures of an mannequin with concealed PVC pipes with focus and LO settings chosen by the focusing algorithm for targets at 14 meters, 25 meters, and 30 meters [32]. 27

Figure 1-5 Setup of the 645-GHz transceiver and the active 300-GHz system. Both consist of three parts: The quasi-optical part, the source/detector units and the data acquisition unit. Inset: Image of the SynViewHead 300. The different transceivers can be interchanged easily [33]. 28

Figure 1-6 Data processing using triangulation: First, the angle pairs are converted to Cartesian coordinates (upper), then the points are connected to form triangles (middle), and finally the triangle area is filled by interpolating between its edges (lower) [33]..29

Figure 1-7 Profile of the baseline CEGRS antenna and main geometrical parameters (upper), frontal view of the target plane and beam trajectory (lower left) and prototype photograph and labels for the different parts of the electronics and antenna subsystems (lower right) [17]...............................30

Figure 1-8 Target scenario, where a simulated explosive is hidden under a mannequin’s T-shirt and the reconstructed image based on the most powerful detection [17]. 31

Figure 1-9 Structure and the scanning principle of the 350 GHz standoff imaging system: Photograph of the complete prototype standoff imaging system (upper), top view layout of the quasi-optical focusing system for the standoff imaging system (lower left) and scan pattern for the high-speed conical scanner design (lower right) [34]. 32

Figure 1-10 Standoff imaging results for a man with a concealed mock explosive device including the optical image (left), and several angular projections (right three images) [34]. 33

Figure 1-11 Schematic illustration of the proposed system and the inner structure of the beam-scanning antenna [35]. 34

Figure 1-12 Scanning manner of the proposed scanning system [35]. 34

Figure 1-13 Imaging results of the spot-beam imager [35]. 35

Figure 1-14 Terahertz imaging scheme based on the combination of fan-beam scanning and aperture synthesized techniques [36]. 36

Figure 1-15 Optical image (upper left), 0.2-THz single-frequency image (upper right), and wideband (0.195–0.205 THz) 3-D images of a mannequin wearing a T-shirt and concealing a plastic cap gun with the front view, the 35° left-side view, and the 35° right-side view, respectively (lower) [36]...............36

Figure 1-16 The TeraSCREEN system consisted of a passive subsystem and an active subsystem [37]..37

Figure 1-17 Principle of the active subsystem [37]. 38

Figure 1-18 Prototype photograph of TeraSCREEN [38]...................................38

Figure 1-19 Photograph of the double lens optical system and the cryosat vacuum chamber [39]. 39

Figure 1-20 Photograph of the 2500-pixel KID bolometer array prototype [39].39

Figure 1-21 CAD model of CONSORTIS 340 GHz radar [40]...........................40

Figure 1-22 Photographs of the short range and the long range systems. [42]....41

Figure 1-23 Normalized radiation patterns of the short range and the long range systems [42]. 41

Figure 1-24 3-D near-field microwave holography system (a) Setup of the system (b) Dielectric targets (c) Reconstructed images for the targets. [43]...........42

Figure 1-25 ThruVision T5000 security system. [44]..43

Figure 1-26 ThruVis TS4-C security system [45]..43

Figure 1-27 TeraSnap B01 [47]. 44

Figure 1-28 The imaging system developed by SafeView Company used for airport security [46]...45

Figure 1-29 SubTera B1080. [48]..45

Figure 1-30 Photograph of QPASS system (without cover) and a cluster unit [49]. 46

Figure 1-31 The detector array corridor concept proposed by Rohde Schwarz [50]. 46

Figure 2-1 Recording a hologram in optical holography. 58

Figure 2-2 Reconstructing the image from the hologram in optical holography. 58

Figure 2-3 Recording a hologram in microwave holography. 60

Figure 2-4 Reconstructing the image from the hologram in microwave holography. 61

Figure 2-5 Holographic imaging system configuration. 61

Figure 2-6 Configurations of two different scanning schemes 64

Figure 2-7 Framework of the proposed beam scanning THz holography imaging system. 65

Figure 2-8 Schematic of the proposed beam scanning scheme in the imaging system (a) Transverse scanning (b) Longitudinal scanning. 66

Figure 2-9 Structure of the beam scanning part of the proposed beam scanning THz holography imaging system (red solid arrows show the transmitting beam and green dashed arrows show the receiving beam). 67

Figure 2-10 Scanning trajectory of the proposed system....................................67

Figure 2-11 Crank-rocker structure...68

Figure 2-12 Dual-gear driven structure for the main reflector rotation. 69

Figure 2-13 Calculated (a) Scanning path and (b) Scanning points with the crank-rocker structure and the dual-gear driven structure in Matlab. 70

Figure 2-14 The rotated main reflector model with dual-gear and the servo motor in Solidworks. 71

Figure 2-15 The rotated flat mirror model with crank rocker and the servo motor in Solidworks. 71

Figure 2-16 The scanning sub-system model in Solidworks. Some structures in lower figure have been hidden for better observation (red solid arrows show the transmitting beam and green dashed arrows show the receiving beam). 72

Figure 3-1 Configurations of reflector antennas (a) Paraboloidal reflector antenna (b) Ellipsoidal reflector antenna. 76

Figure 3-2 Configurations of off-axis reflector antennas (a) Off-axis paraboloidal reflector antenna (b) Off-axis ellipsoidal reflector antenna. 77

Figure 3-3 Configurations of dual-reflector antennas (a) Newton reflector antenna (b) Cassegrain reflector antenna (c) Gregorian reflector antenna (d) Dragonian reflector antenna. 79

Figure 3-4 Configuration of Dragonian antenna with the ellipsoidal main reflector. 80

Figure 3-5 The geometry of the Dragonian system and parameters. 81

Figure 3-6 The schematic of the rotating Dragonian antenna. 82

Figure 3-7 The designed Dragonian antenna simulated in Matlab. 84

Figure 3-8 The ray path of the designed Dragonian antenna. 85

Figure 3-9 The ray path of the designed Dragonian antenna when the collimated beam is rotated 3°. 86

Figure 3-10 The ray path error of the designed Dragonian antenna when the collimated beam is rotated 3° 87

Figure 3-11 The ray path of the designed Dragonian antenna when the collimated beam is rotated -3°. 87

Figure 3-12 The ray path error of the designed Dragonian antenna when the collimated beam is rotated -3°. 88

Figure 3-13 E field distributions of co-polarization and cross-polarization when the feed is moved in the local x-axis from -0.03 m to 0.03 m. 89

Figure 3-14 E field distributions of co-polarization and cross-polarization when the feed is moved in the local y-axis from -0.03 m to 0.03 m. 91

Figure 3-15 E field distributions of co-polarization and cross-polarization when the main reflector position (*h*) varies ranging from 1.13 m to 1.33 m......... 92

Figure 3-16 E field distributions of co-polarization and cross-polarization when the sub reflector half vertex distance (*a*) varies from 0.29 m to 0.39 m. 93

Figure 3-17 E field distributions of co-polarization and cross-polarization when the sub reflector half foci distance (*c*) varies from 0.69 m to 0.79 m. 95

Figure 3-18 The model of the designed Dragonian antenna in GRASP [9]. 97

Figure 3-19 Simulated near field of the main reflector at 3 m [9]. 97

Figure 3-20 Schematics of different scanning antennas (a) the single ellipsoidal reflector scanning antenna (b) the Dragonian scanning antenna. 98

Figure 3-21 Simulation results of single ellipsoidal antenna with different scanning angle. 99

Figure 3-22 Simulation results of Dragonian antenna with different scanning angle. 100

Figure 3-23 Scanning sub-system including the feed, the sub reflector, the main reflector and the flat mirror with the global coordinate and local coordinates of different components. 101

Figure 3-24 E field distributions of co-polarization and cross-polarization at beam spot centre positions when the main reflector is rotated around the local y-axis: (a) 1°, (b) -1°, (c) 2°, (d) -2°, (e) 3°, (f) -3°, (g) 4° and (h) -4°. 103

Figure 3-25 E field distributions of co-polarization and cross-polarization at beam spot centre positions when the flat mirror is rotated around the local x-axis: (a) 1°, (b) -1°, (c) 2°, (d) -2°, (e) 3°, (f) -3°, (g) 4°, (h) -4°, (i) 5°, (j) -5°, (k) 6°, (l) -6°, (m) 7°, (n) -7°, (o) 8° and (p) -8°. 107

Figure 3-26 E field distributions of co-polarization and cross-polarization at beam spot centre positions when the main reflector is rotated around the local x-axis: (a) 1°, (b) -1°, (c) 2°, (d) -2°, (e) 3°, (f) -3°, (g) 4°, (h) -4°, (i) 5°

and (j) -5°. 110

Figure 3-27 E field distributions of co-polarization and cross-polarization at beam spot centre positions when the flat mirror is rotated around the local y-axis: (a) 1°, (b) -1°, (c) 2°, (d) -2°, (e) 3°, (f) -3°, (g) 4° and (h) -4°........112

Figure 3-28 E field beam cuts for situations the flat mirror is rotated from -4 degrees to 4 degrees with the step of 1 degree..113

Figure 3-29 E field beam grids for situations the flat mirror is rotated from -4 degrees to 4 degrees with the step of 1 degree. (The legend indicates the normalised values in dB) 114

Figure 3-30 E field beam cuts for situations the main reflector is rotated from -5 degrees to 5 degrees with the step of 1 degree..114

Figure 3-31 E field beam grids for situations the main reflector is rotated from -5 degrees to 5 degrees with the step of 1 degree. (The legend indicates the normalised values in dB) 115

Figure 3-32 E field beam grids for the centre point and corner points. (The legend indicates the normalized values in dB) 116

Figure 4-1 Induced electric current on the illuminated scatterer. 120

Figure 4-2 The scattered electromagnetic field from the scatter........................120

Figure 4-3 Configuration of the single offset reflector antenna. 121

Figure 4-4 Comparison of far field patterns obtained by Matlab PO and GRASP 9 (a) $\phi = 0^\circ$ (b) $\phi = 90^\circ$. 124

Figure 4-5 Comparison of near field patterns obtained by Matlab PO and GRASP 9 (a) $\phi = 0^\circ$ (b) $\phi = 90^\circ$. 125

Figure 4-6 The simulated model built in Matlab. 126

Figure 4-7 Amplitude of the received signal at the aperture plane and the reconstructed image of the rectangular plate (The legend indicates the normalised values in dB). 127

Figure 4-8 Amplitude of the received signal at the aperture plane and the reconstructed image of the rectangular plate with a T-shaped slot (The legend indicates the normalized values in dB). The sampling number is 41 * 41.128

Figure 4-9 Amplitude of the received signal at the aperture plane and the reconstructed image of the rectangular plate with a T-shaped slot (The legend indicates the normalized values in dB). The sampling number is 81 * 81.129

Figure 4-10 Comparison between the amplitude of the received signal at the aperture plane, the reconstructed image of the rectangular plate with a T-shaped slot and the target (The legend indicates the normalised values in dB). The sampling number is 81 * 81. The dark lines give the profile of the imaged target. 129

Figure 4-11 Configuration of the raster scanning [11].....................................130

Figure 4-12 Configuration of the beam scanning [11].....................................130

Figure 4-13 The target used in the raster scanning scheme simulation [11]......131

Figure 4-14 Simulated E-field amplitude(a) and phase(b) distribution based on signals received by raster scanning on the aperture plane. (The legend indicates the normalised values in dB and degrees) [12]..........................132

Figure 4-15 The reconstructed image of the reflector in raster scanning. (The legend indicates the normalized values in dB) [12].................................133

Figure 4-16 The target used in the beam scanning scheme simulation 133

Figure 4-17 Simulated E-field amplitude(a) and phase(b) distribution based on signals received by beam scanning on the equivalent aperture plane. (The legend indicates the normalised values in dB and degrees) [12]...............134

Figure 4-18 The reconstructed image of the reflector in beam scanning. (The legend indicates the normalised values in dB) [12] 135

Figure 4-19 Scanning transceivers and beam spot in the scanning area. 138

Figure 4-20 Zero padding from the scattering factor values to the convolution kernel. 138

Figure 4-21 Visualization of the received signal from the convolution perspective. 139

Figure 4-22 The relationship between the data on different plane 141

Figure 4-23 The amplitude distribution for the convolution result (left) and the unit impulse function (right) (The legend indicates the normalised values in dB). 141

Figure 4-24 Amplitude of the received signal at the aperture plane (a) and the reconstructed image of the rectangular plate using BP holography algorithm (b) (The legend indicates the normalised values in dB). 142

Figure 4-25 Amplitude of the received signal at the aperture plane (a) and the reconstructed image of the rectangular plate using inverse convolution algorithm (b) (The legend indicates the normalised values in dB). 143

Figure 4-26 Amplitude of the received signal at the aperture plane (a) and the reconstructed image of the rectangular plate using inverse convolution algorithm with a broken convolution kernel (b) (The legend indicates the normalised values in dB). 143

Figure 4-27 Simulated E-field (a) amplitude and (b) phase distribution based on signals received by the raster scanned antenna (The legend indicates the normalised values in dB and degrees) [5]. 145

Figure 4-28 Reconstructed images by applying (a) backpropagation algorithm; (b) proposed transposed convolution algorithm for the simulation evaluation

(The legend indicates the normalised values in dB) [5]. 145

Figure 4-29 The conversion of the unprocessed matrix to a column vector......147

Figure 4-30 The zero padding: from the small-sized Ckmat to the large-sized Ckmat'..148

Figure 4-31 Calculated partial inverse kernels with different size: (a) 21-element amplitude, (b) 21-element phase, (c) 15-element amplitude, (d) 15-element phase, (e) 11-element amplitude, (f) 11-element phase, (g) 9-element amplitude and (h) 9-element phase (The legend indicates the normalised values in dB and degrees). 150

Figure 4-32 Reconstructed images with different PIC kernels: (a) 21-element, (b) 15-element, (c) 11-element and (d) 9-element (The legend indicates the normalised values in dB). 151

Figure 4-33 Reconstructed images with different normalized PIC kernels: (a) 21-element, (b) 15-element, (c) 11-element and (d) 9-element (The legend indicates the normalised values in dB). 152

Figure 4-34 The zero padding for elements near area edges: from the small-sized Ckmat to the large-sized Ckmat'. 153

Figure 5-1 Raster scanning system configuration..157

Figure 5-2 Schematic of terahertz imaging system...158

Figure 5-3 Photographs of the experimental environment (a) the NSI 2000 scanner and the target and (b) the PNA-X and horn antennas. 159

Figure 5-4 The schematic for sampling interval calculation. The maximum phase shift between two sampling points is approximatively $2k_0\Delta L$. 163

Figure 5-5 Photograph of the knife-edge target...164

Figure 5-6 The schematic of parameters of the knife edge...............................165

Figure 5-7 Experimental LSF results (horizontal-dotted line, vertical-dashed line) compared to the theoretical PSF (solid line). 165

Figure 5-8 Photograph of the rectangular metal target used in the raster scanning experiment 166

Figure 5-9 Uncalibrated (a) amplitude and (b) phase images constructed by signals received at the aperture plane. (The legend indicates the normalised values in dB and degrees) 166

Figure 5-10 Calibrated (a) amplitude and (b) phase images constructed by signals received at the aperture plane. (The legend indicates the normalised values in dB and degrees) 167

Figure 5-11 The image of the rectangular target recorded at the aperture plane. (The legend indicates the normalised values in dB) 168

Figure 5-12 The reconstructed image of the rectangular target. (The legend indicates the normalised values in dB) 168

Figure 5-13 The image of the rectangular target with resolution enhanced. (The legend indicates the normalised values in dB) 169

Figure 5-14 The image of the rectangular target at the aperture plane with 201 sampling points in each dimension. (The legend indicates the normalised values in dB) 170

Figure 5-15 The image of the rectangular target on the original data with 201 sampling points in each dimension. (The legend indicates the normalized values in dB) 170

Figure 5-16 Photograph of the gun-shaped metal target. 171

Figure 5-17 The image of the gun-shaped target at the aperture plane. (The legend indicates the normalised values in dB) 172

Figure 5-18 The image of the gun-shaped target on the original data. (The legend indicates the normalised values in dB) 172

Figure 5-19 The image of the gun-shaped target with resolution enhanced. (The legend indicates the normalised values in dB)...173

Figure 5-20 Photograph of the gun-shaped target with partially metal foil wrapped. 174

Figure 5-21 The image of the gun-shaped target partially metal foil wrapped at the aperture plane. (The legend indicates the normalised values in dB) 174

Figure 5-22 The image of the gun-shaped target partially metal foil wrapped on the original data. (The legend indicates the normalised values in dB)......175

Figure 5-23 The image of the gun-shaped target partially metal foil wrapped with resolution enhanced. (The legend indicates the normalised values in dB) 175

Figure 5-24 Images of the rectangular target with different sampling points (a) 201×201 (b) 101×101 (c) 81×81 (d) 61×61 (e) 51×51 (f) 41×41 (g) 31×31 (h) 21×21. (The legend indicates the normalised values in dB) 177

Figure 5-25 SNRI versus sampling points and the sampling interval (The theoretical sampling interval being 2.87λ while the practical sampling interval being 5.74λ)...179

Figure 5-26 Images of the rectangular target with different sizes of the aperture (mm^2) (a) 250×250 (b) 400×400 (c) 500×500. 180

Figure 5-27 $\mathrm{SNR_I}$ and $\mathrm{NE\Delta R}$ vs. distance from the aperture of the rectangular target. 181

Figure 5-28 $\mathrm{SNR_I}$ and $\mathrm{NE\Delta R}$ vs. distance from the aperture of the gun-shaped target. 181

Figure 5-29 Different transceiver antenna alignments [6]. 182

Figure 5-30 Experimental E-field (a) amplitude and (b) phase distribution based on signals received by the raster scanned antenna (The legend indicates the normalised values in dB and degrees). 184

Figure 5-31 Reconstructed images by applying (a) backpropagation algorithm; (b) proposed transposed algorithm for the experimental evaluation (The legend indicates the normalised values in dB). 184

Figure 5-32 The reference row in the reconstructed image for more comparison (The legend indicates the normalised values in dB). 185

Figure 5-33 Comparison between the reconstructed single row result for BP and TC algorithms. 185

Figure 5-34 Comparison between BP and TC algorithms under different sampling point situations and the efficiency increase of TC algorithm. 186

Figure 5-35 Reconstructed images with different sampling points using normalized PIC kernels: (a) 21 by 21, (b) 31 by 31, (c) 41 by 41, (d) 51 by 51, (e) 61 by 61, (f) 81 by 81, (g) 101 by 101 (The legend indicates the normalised values in dB). 187

Figure 5-36 Comparison between BP, TC and PIC algorithms under different sampling point situations (only reconstruction time included). 189

Figure 5-37 Beam scanning system configuration...191

Figure 5-38 The conversion structure from the raster scanning to angular scanning: (a) The central part of the target plane is covered, (b) The edge part of the target plane is covered. 192

Figure 5-39 Solidworks model of the planar to angular scanner conversion structure..193

Figure 5-40 Schematic of the experimental beam scanned imaging system. 194

Figure 5-41 Photographs of the experimental environment (a) the front side (b) the back side..195

Figure 5-42 Photograph of the rectangular metal target used in the beam scanning experiment..196

Figure 5-43 (a) amplitude and (b) phase images constructed by signals received and the area size has been transferred from 0.3 m to 0.6 m. (The legend indicates the normalised values in dB and degrees) 197

Figure 5-44 The detection distance change in the beam scanning experimental system. 198

Figure 5-45 Reconstructed images of the rectangular target with different sampling points: (a) 201×201 (b) 101×101 (c) 81×81 (d) 61×61 (e) 41×41. (The legend indicates the normalised values in dB).................201

Figure 6-1 The thesis structure of the THz holography imaging system. 206

List of tables

Table 1-1 Terahertz detectors developed in recent years [6]................................23

Table 1-2 Summary of existed imaging systems reported by groups all over the world and the objective of this work..47

Table 3-1 Primary parameters of Dragonian antenna. 83

Table 3-2 Other calculated parameters of Dragonian antenna.............................84

Table 3-3 Maximum co-polarisation and cross-polarisation values where the feed is moved in the local x-axis ranging from -0.03 m to 0.03 m......................90

Table 3-4 Maximum co-polarisation and cross-polarisation values when the feed is moved in the local y-axis ranging from -0.03 m to 0.03 m......................91

Table 3-5 Maximum co-polarisation and cross-polarisation values when the main reflector position (*h*) varies ranging from 1.13 m to 1.33 m........................92

Table 3-6 Maximum co-polarisation and cross-polarisation values when the sub reflector half vertex distance (*a*) varies from 0.29 m to 0.39 m. 94

Table 3-7 Maximum co-polarisation and cross-polarisation values when the sub reflector half foci distance (*c*) varies from 0.69 m to 0.79 m. 95

Table 3-8 Optimised parameters of Dragonian antenna. 96

Table 3-9 Rotation angles and beam spot centre positions of the main reflector in scheme 1 (scanning in x dimension)..102

Table 3-10 Rotation angles and beam spot centre positions of the flat mirror in scheme 1 (scanning in y dimension)..104

Table 3-11 Rotation angles and beam spot centre positions of the main reflector in scheme 2 (scanning in y dimension)...108

Table 3-12 Rotation angles and beam spot centre positions of the flat mirror in scheme 2 (scanning in x dimension)...110

Table 3-13 Rotation angles of the flat mirror and the main reflector corresponded to points shown in Figure 3-32. 116

Table 4-1 Comparisons between these two scanning schemes [12]. 135

Table 4-2 Filtering coefficients for different sampling points in an area of 0.4 m by 0.4 m. 146

Table 4-3 Required PIC kernel size for different sampling points. 153

Table 5-1 SNRI and NEΔR of images in Figure 5-24....................................178

Table 5-2 SNRI and NEΔR of images in Figure 5-26....................................180

Table 5-3 SNRI and NEΔR of the rectangular target in different horns settings [6]..182

Table 5-4 Reconstruction time comparison for different sampling points in an area of 0.4 m by 0.4 m. 188

Table 5-5 Reconstruction similarity between BP, TC and PIC for different sampling points in an area of 0.4 m by 0.4 m (BP results are taken as the reference). 189

Table 5-6 The relation of the step set on the planar scanner and the real scanned step in the target area for the experimental beam scanning system. 199

Table 5-7 The number of sampling points for two experimental systems for the same scanning interval. 199

Abbreviations

BP	Back Propagation
CEGRS	Confocal Elliptical Gregorian Reflector System
CMOS	Complementary Metal Oxide Semiconductor
CW	Continuous Wave
CWD	Concealed Weapon Detection
DBF	Digital Beam Forming
DFT	Discrete Fourier Transformation
EM	Electro Magnetic
ESF	Edge Spread Function
FET	Field-Effect Transistor
FFT	Fast Fourier Transformation
FMCW	Frequency Modulated Continuous Wave
FOV	Field of View
FT	Fourier Transformation
FPA	Focal Plane Arrays
GB	Gaussian Beam
GFET	Graphene Field Effect Transistor
GO	Geometrical Optics
GTD	Geometrical Theory of Diffraction
HBD	Heterostructure Backward Diode
HEMT	High-Electron-Mobility Transistor
HPBW	Half Power Beam Width
IF	Intermediate Frequency
ISAR	Inverse Synthetic Aperture Radar
KID	Kinetic Inductance Detector
LO	Local Oscillator
LSF	Line Spread Function
MMIC	Monolithic Microwave Integrated Circuit
MMW	Millimetre Wave
NEDT	Noise Equivalent Differential Temperature
NEP	Noise Equivalent Power
NEΔR	Noise Equivalent Reflectivity Difference
NW	Nanowire
PIC	Partial Inverse Convolution
PLE	Path Length Error
PNA	Performance Network Analyzer
PO	Physical Optics
PSF	Point Spread Function

PTD$_1$	Physical Theory of Diffraction
PTD$_2$	Pulsed Time Domain
PWS	Plane Wave Spectrum
QCL	Quantum Cascade Lasers
RF	Radio Frequency
SBD	Schottky Barrier Diode
SNR	Signal Noise Ratio
SNR	Signal Noise Ratio of the Image
TC	Transposed Convolution
TPBW	Threshold Power Beam Width
T/R	Transmitter/Receiver

Chapter 1. Introduction

There is an increased interest in terahertz (THz) applications today. Generally speaking, the THz band is commonly accepted as the EM spectrum ranging from 0.1 THz to10 THz. THz wave can penetrate most materials and provide unique spectral information with high spatial resolution. So terahertz is widely used for imaging and spectroscopic analysis of materials and substances. Potential applications span across various scientific disciplines and cover areas such as radio astronomy [1], biological research [2], security screening [3], radar [4], chemical and explosive detection.

THz imaging systems have been employed for security screening in public places lately. They can be broadly divided into two families: passive and active schemes. From the principle of passive imager perspective, small differences in temperatures from the radiating object need to be detected and discriminated against the sky background. Passive imaging techniques have been proved very successful at microwave and millimetre-wave frequencies. By scaling in frequencies to terahertz range, some passive imagers were developed. However, the much warmer background sky at the terahertz frequency band due to high atmospheric absorption limits its wide application. But at the same time, passive imagers can't provide enough scene contrast at THz frequencies. However, in an active imager, the target is illuminated by a terahertz beam. Then the reflected/scattered signal is collected to build an image. In this case, the active imager will provide high quality images with high resolution and good contrast against the background [5].

For active THz imaging, various methods have been explored, including pulsed time-domain (PTD) and continuous wave (CW) technologies. Time-domain systems operating in a wider bandwidth have the advantage of depth ranging and the spectroscopy information of different materials, but suffer from long image acquisition time and short imaging distance owing to the typically weak illumination power. As a comparison, CW systems operating in a narrower bandwidth can offer relatively high power and long range imaging. In the frequency range above 1 THz, Quantum Cascade Lasers (QCLs) have shown excellent performance but require cooling and pulsed mode operation for terahertz. For the frequency located at around 1 THz and below, CW sources derived from microwave electronics including Gunn oscillators, backward wave oscillators and diode-multiplied sources can be deployed while the detection can be realised with down-conversion mixers. To collect the scattered signals from the targets, various detector system including single detector scanned systems, arrays and focal plane arrays (FPAs) have also been employed. High power, low cost and compact sources that do not require cryogenic cooling and low cost, sensitive and uncooled detectors are two main requirements for active THz imaging systems [6].

1.1 Background of THz detection

All radiation detection systems in THz spectral range can be divided into two main categories: incoherent (direct) detection and coherent detection.

The direct detectors have been under development for many years. Different kind of cooled semiconductor detectors (hot electro InSb, Si, Ge bolometers, extrinsic Si and Ge) [7-9] with the response time of $\tau \approx 10^{-6} \sim 10^{-8}\ s$, the Noise Equivalent Power of $NEP \approx 10^{-13} \sim 5 \times 10^{-17}\ \mathrm{W/Hz^{1/2}}$ (NEP can remain constant for one system in different situations) and operating at $\mathrm{T} \sim 4\ \mathrm{K}$ are developed. Even very low NEP only limited by cosmic background radiation fluctuations can be realised by some bolometers cooled to $T \approx 100 \sim 300$ mK. However, the required cryogenic devices deployed in cooled detectors are the obstacles to achieve small size and low cost. The development of room temperature detectors is the trend of future researches. With relatively long response time ($\tau \approx 10^{-2} \sim 10^{-3}$ s) and modest sensitivity, many new uncooled detectors have been put into applications. Among them, there are Golay cells [10, 11], pyroelectric detectors [12], different kind of thermal direct detection detectors (bolometers and microbolometer) [13, 14], which use antennas to couple power to a small thermally absorbing region. Typically, the NEP value for uncooled detectors typically varies from 10^{-10} to $10^{-9}\ \mathrm{W/Hz^{1/2}}$.

Compared with other uncooled detectors, Schottky Barrier Diode (SBD) and Field-Effect Transistor (FET) ones are relatively sensitive, have a much wider dynamic range and can be assembled into arrays by integration technologies. With room temperature operation and high measurement rates, SBD and FET detectors and their arrays have been employed in THz wave detection in emerging THz camera systems. SBD detectors have good responsivity (about hundreds of V/W) and modest NEP (about $10^{-10}\ \mathrm{W/Hz^{1/2}}$). The NEP was limited by bias circuits in SBD detection systems. Then, zero-bias Schottky diodes were proposed to tackle this problem to achieve a NEP at level of $10^{-12}\ \mathrm{W/Hz^{1/2}}$. Another kind of detectors, FET detectors, have a much better responsivity (even more than 10 kV/W). Since the result of a photo-response appears in the form of a dc voltage between the source and drain while the bias is added to the gate, FET detectors have much lower noise. They can also be directly tunable by changing the gate voltage. A more recent approach exploits FET focal-plane arrays (FPAs) either as III-V high-electron-mobility transistors (HEMTs) or Si-based complementary metal oxide semiconductor (CMOS) transistors. This approach was also recently extended with graphene field-effect transistors (GFET) [15] and InAs nanowires (NWs) [16] operating at room temperature.

For coherent detection systems, heterodyne receivers are commonly consisted of monolithic microwave integrated circuits (MMICs). In heterodyne detectors, signals working at THz frequencies are down-converted to an intermediate frequency (IF) for processing, where both of the amplitude and phase information of the incoming radiation are preserved. In general, heterodyne detection offers a higher spectral resolution with both amplitude and phase information than direct detection. Compared to the direct detection, fluctuations in W_{LO} rather than background noise determine the dominant noise in heterodyne detection, thus providing discrimination against background fluctuation, etc. So in heterodyne systems, the local oscillator (LO) acts as a critical component. IF conversion provides the gain, so the output signal may be stronger than the thermal and generation-recombination noise. If the conversion gain is set proportional to W_{LO}/W_S , signals with much weaker radiation power compared to direct detection can be detected. With much better performance in sensitivity and resolution than direct detection, heterodyne detection is the most promising candidate for stand-off detection (illustrated in Figure 1-1). Table 1-1 gives a summary of THz detectors developed in recent years [6].

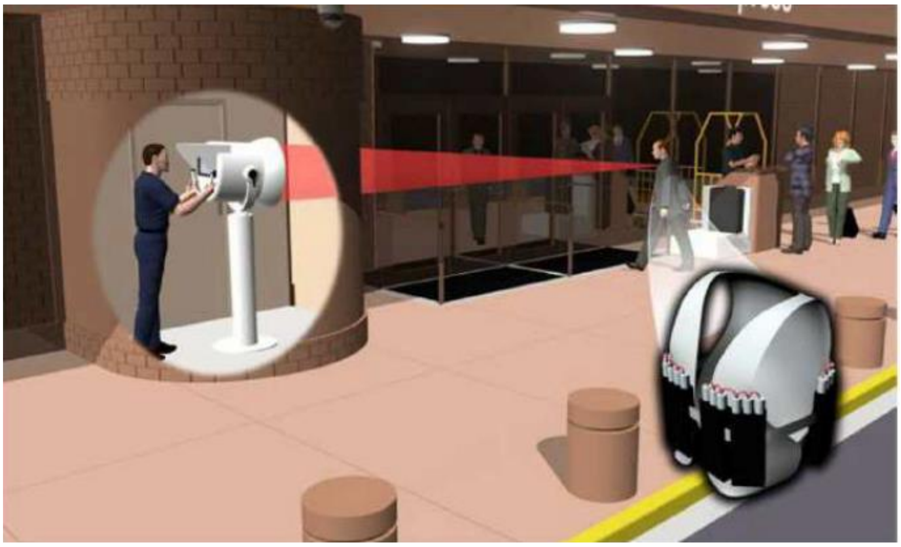

Figure 1-1 Stand-off Imaging System for Personnel Screening [17].

The active imager will provide high-quality images with high resolution and good contrast against the background. With the development of semiconductor technology, new MMIC devices along with more advanced processing technologies will lead to innovative terahertz imaging systems.

Table 1-1 Terahertz detectors developed in recent years [6].

Detector	Freq. (THz)	R_v (VW^{-1})	NEP	Frame rate/ response time	FPA size	Year	Commercial	Ref.
Schottky barrier diode (SBD)	0.11-0.17 0.9-1.4 1.1-1.7	2000 100 100	13.2 113.7 113.7	42 ns 25ns 25ns	Single detector	2007	VDI	-
	0.86 0.28	273 336	42 290 pW	~1us	Single detector 4*4	2013	-	[18]
Photo conductive folded dipole antenna FET FPA	0.1-4.0	-	-	-	Single	2011 1985	EKSPLA	-
	0.6-1.0 0.7-1.1	800 (1.027 |THz) 115×10^3 (0.856 THz)	66 (1.027 THz) 12 nW (0.856 THz)	- 25 Hz	Single 32 × 32	2011 2012	STM	-
VOx microbolometer	2.5 2.5	72×10^3 ($2\mu A$) 5620 (100 nA)	37 (15 Hz mod.) 3.6 μW	68 ms 194 ms	Single 5 × 5	2013 2015	-	[19] [20]
Bolometer	4.25 2.54	-	24.7 pW 76.4 pW	50 Hz	384 × 288	2013	INO	-
Golay cells	0.2-20	10×10^3 (12.5 Hz mod.)	10×10^3	25 ms	Single	2009	Microtech	-
Microbolometer	1.0-7.0	-	<100 pW (4 THz)	30 Hz	320 × 240	2014	NEC	-
LiTaO3 Pyroelectric	0.1-300	-	96 nW (50 Hz mod.)	50 Hz	320 × 320	2014	Ophir Photonics	-
Pyroelectric	0.3, 1.0, 3.010	18.3×10^3 (10 Hz mod.)	440	10 Hz	Single	2009	QMC	-
Hot electron bolometer	0.89	0.095	7.4×10^3	200 Hz	Single	2007	-	[21]
SixGey:H microbolometer	0.934	170	200	1 ms	Single	2010	-	[22]
α -Si microbolometer	2.4	14×10^6 5.9×10^6	30 pW 68pW	-	320 × 240	2011	CEA-Leti	[23]-
Nb5N6 microbolometer	0.1	100.5	398	1 KHz	Single	2008	-	[24]
VOx microbolometer	2.8	200×10^3	35 pW	30 Hz	160 × 120	2008	Infrared Systems	
Antenna QW cavity	2.0-4.0	12.6 × 10 (2.5 THz)	32 pW (2.5 THz)	25 Hz	320 × 240	2014	CEA-Leti	[25]
VOx microbolometer	3.1	-	280 pW	16 ms	640 × 480	2008	NEC	-
Folded dipole antenna FET	0.65	1.1×10^3 (0.15 V bias)	50	-	Single	2010	STM	-
	0.2-4.3	528 (1.4 THz)	28 (1.4 THz)	-	Single	2012	-	[26]

1.2 Review of the state-of-the-art development

This section gives a review on the recent development of THz imaging systems for security screening in academia and industry, respectively.

1.2.1 Research work in universities, laboratories and institutes

Ohio State University

For the direct detection, the broadband (0.6~ 1.2 THz) focal plane array (FPA) THz imaging camera developed by researchers in the Ohio State University (See Figure 1-2) is a typical example in recent years [27]. They designed the first broadband real-time HBD (heterostructure backward diode)-based FPA consisted of broadband planar slot antennas, integrated sensor devices and the quasi-optical system for THz imaging applications. The prototype FPA realised a compact (8 mm*6.4 mm area with 31*31 pixels) planar device. This camera has a five frames-per-second image acquisition speed and a sub-millimetre resolution with a pixel optical responsivity of 600 V/W at 0.7 THz [27].

China Academy of Engineering Physics

Many works have also been published in heterodyne detection [28-43]. Inverse Synthetic Aperture Radar (ISAR) technology has been introduced in terahertz imaging applications [28]. A 140 THz frequency-modulated continuous-wave (FMCW) radar technique with a 5 GHz bandwidth, 3 cm range resolution ISAR imaging system by China Academy of Engineering Physics has been reported (Figure 1-3) [29]. The 2-D (range and cross-range) imaging resolution is 3 cm * 3 cm with a real time image frame rate of 5 Hz [28].

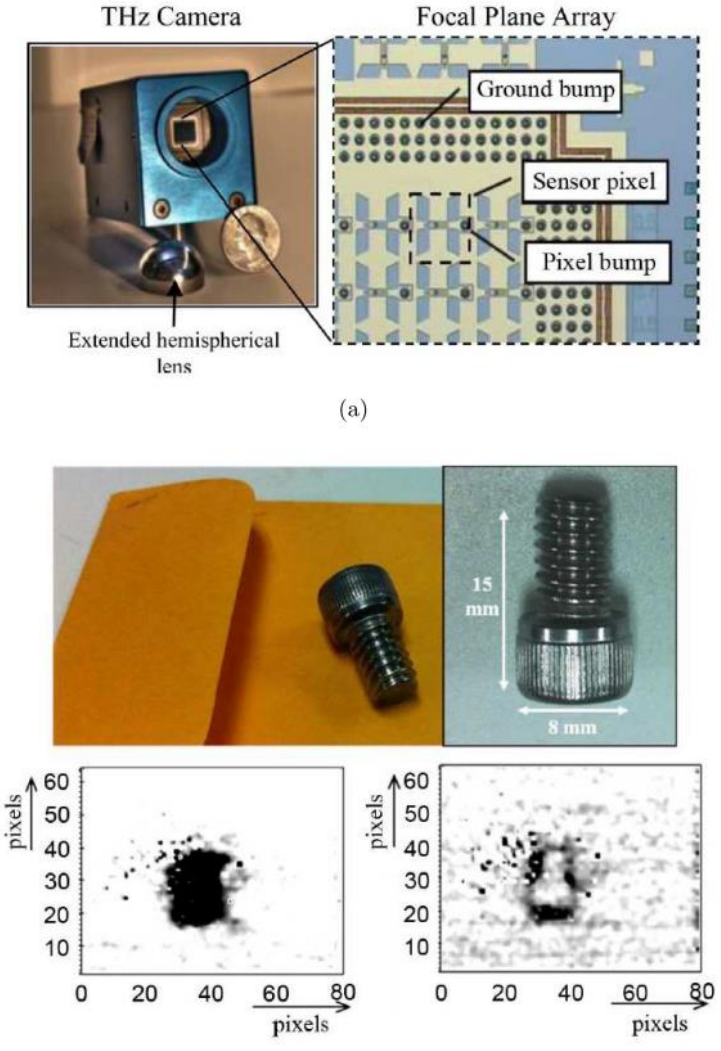
THz Camera
Focal Plane Array
Ground bump
Sensor pixel
Pixel bump
Extended hemispherical lens
(a)
15 mm
8 mm
pixels
60
50
40
30
20
10
0
20
40
60
80
pixels
(b)

Figure 1-2 0.6 ~ 1.2 THz FPA camera (a) Photograph of the camera and the FPA in it (b) THz image of a steel screw placed inside an envelope [27].

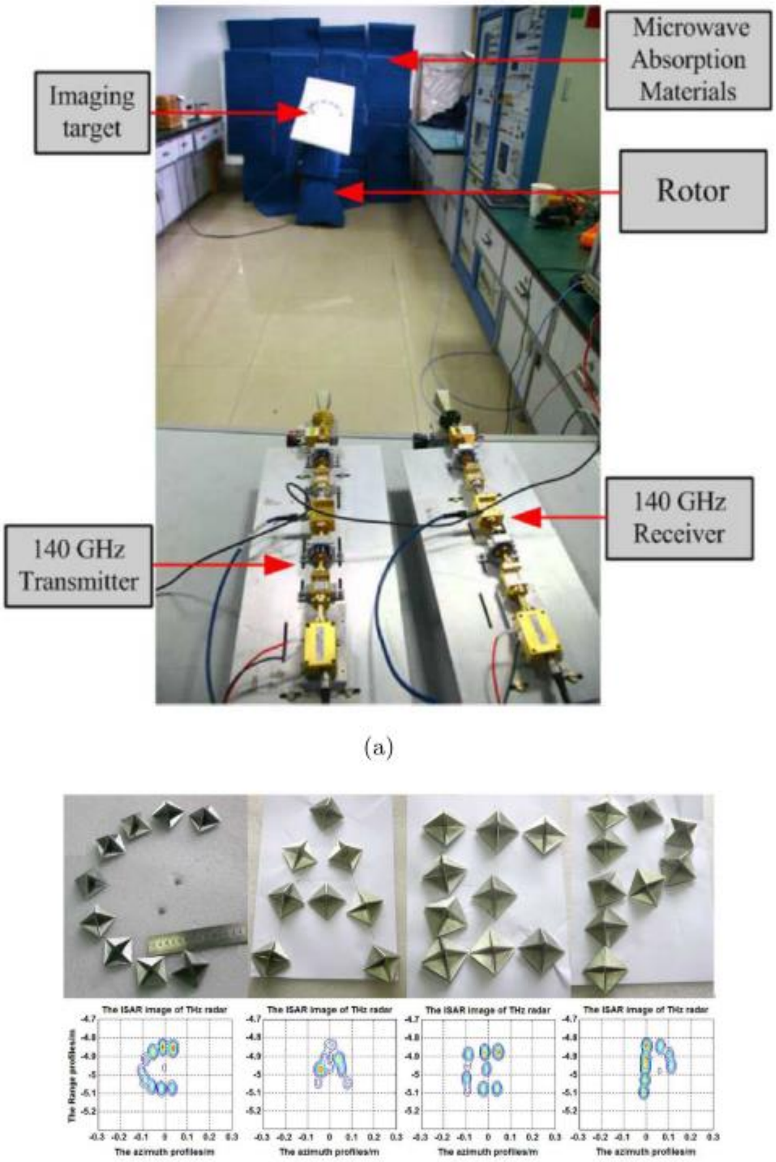
Imaging target
Microwave Absorption Materials
Rotor
140 GHz Receiver
140 GHz Transmitter
The ISAR image of THz radar
The Range profiles/m
The azimuth profiles/m

(a)

(b)

Figure 1-3 140 THz FMCW ISAR imaging system (a) Photograph of 140 GHz radar imaging scenes (b) Corner reflector made 'CAEP' (top) and the imaging results (bottom) with the 140 GHz ISAR [29].

Jet Propulsion Laboratory

Researches in Jet Propulsion Laboratory (JPL) have developed several frequency modulated continuous wave (FMCW) radars used for THz imaging [30, 31]. A 675 GHz FMCW radar working at room temperature designed by JPL has sub-centimetre range resolution by utilising a 30 GHz bandwidth with target distances from 14 to 34 meters

(Figure 1-4) [32].

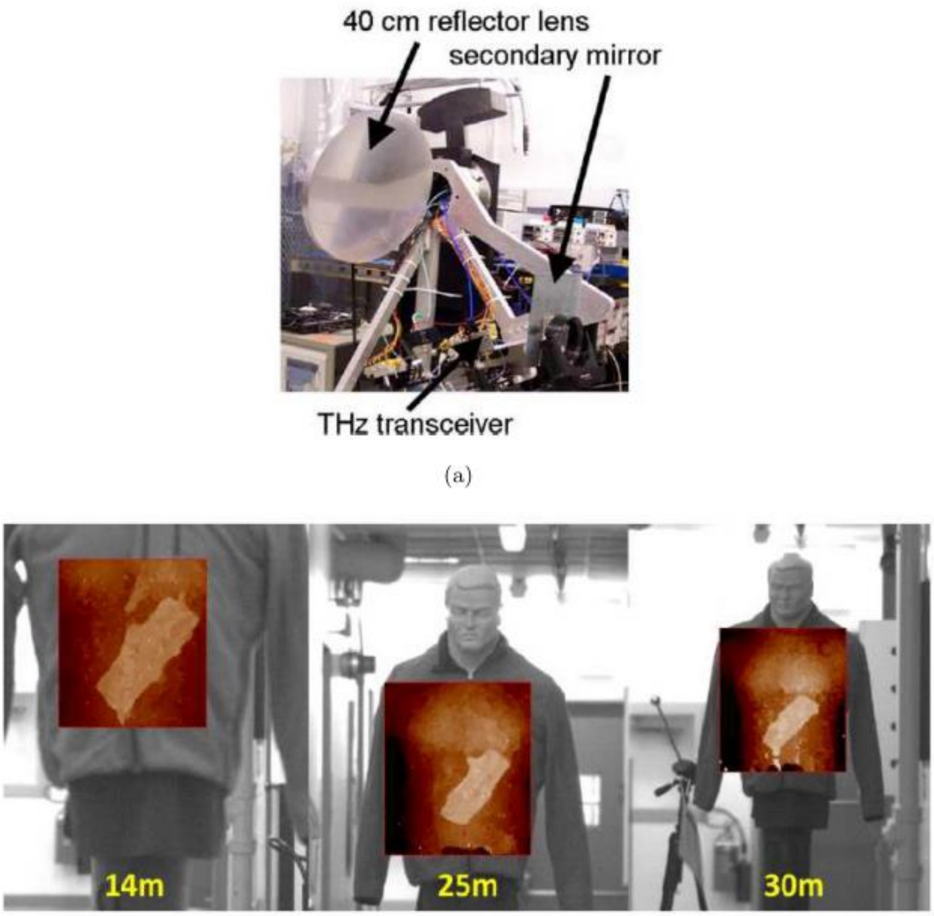

(a)

(b)

Figure 1-4 675GHz FMCW radar system (a) Photograph of the system (b) Image captures of an mannequin with concealed PVC pipes with focus and LO settings chosen by the focusing algorithm for targets at 14 meters, 25 meters, and 30 meters [32].

Johann Wolfgang Goethe-University (C. A. Weg's group)

C. A. Weg's group in Johann Wolfgang Goethe University reported two active imaging systems, operating at room temperature, fully electronic THz cameras working at 300 GHz and 645 GHz in Ref. [33]. Images with more than 55000 pixels can be acquired in 9 seconds. The typical imaging distance of this system is about 75-150 cm, and the image size is in the order of hundreds of square centimetre suitable for the standoff detection of concealed weapons. The setup of the 645-GHz transceiver and the active 300-GHz system can be found in Figure 1-5. The quasi-optical part consists of two hyperbolically shaped lens L1 and L2, one beam splitter (BS), one rotating flat reflector M3, one spherical reflector M2 and one elliptical reflector M1 in the 645 GHz system while for the 300 GHz system, only L1, M1, M2 and M3 remain with the employment of the SynViewHead 300. By combining the fast spin and the slow rotation of the slightly tilted flat reflector M3 in two dimensions, the scanning path can cover a long rectangular area with many sampling points on circles which are demonstrated in Figure 1-6. In the data processing, the triangulation and the interpolation have been applied to acquire consistent results [33].

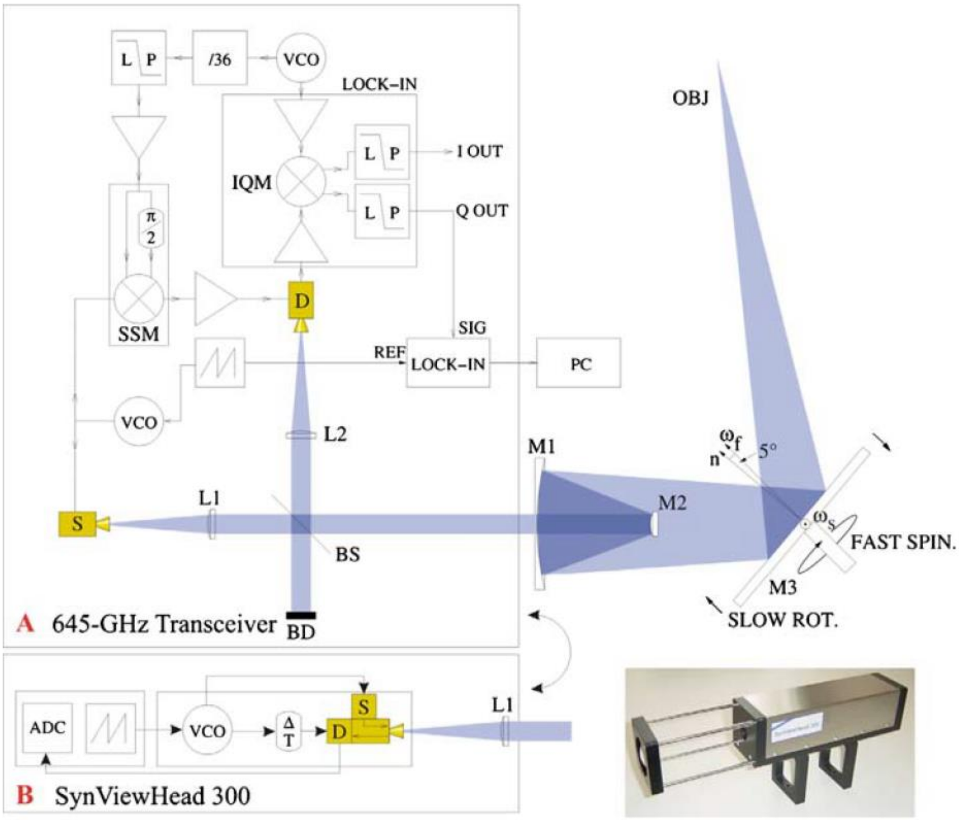
L P
/36
VCO
LOCK-IN
IQM
L P
I OUT
L P
Q OUT
π/2
SSM
D
SIG
REF
LOCK-IN
PC
VCO
L2
L1
S
BS
M1
M2
OBJ
ω_f
n
5°
ω_s
FAST SPIN.
M3
SLOW ROT.
A 645-GHz Transceiver
BD
ADC
VCO
ΔT
S
D
L1
B SynViewHead 300

Figure 1-5 Setup of the 645-GHz transceiver and the active 300-GHz system. Both consist of three parts: The quasi-optical part, the source/detector units and the data acquisition unit. Inset: Image of the SynViewHead 300. The different transceivers can be interchanged easily [33].

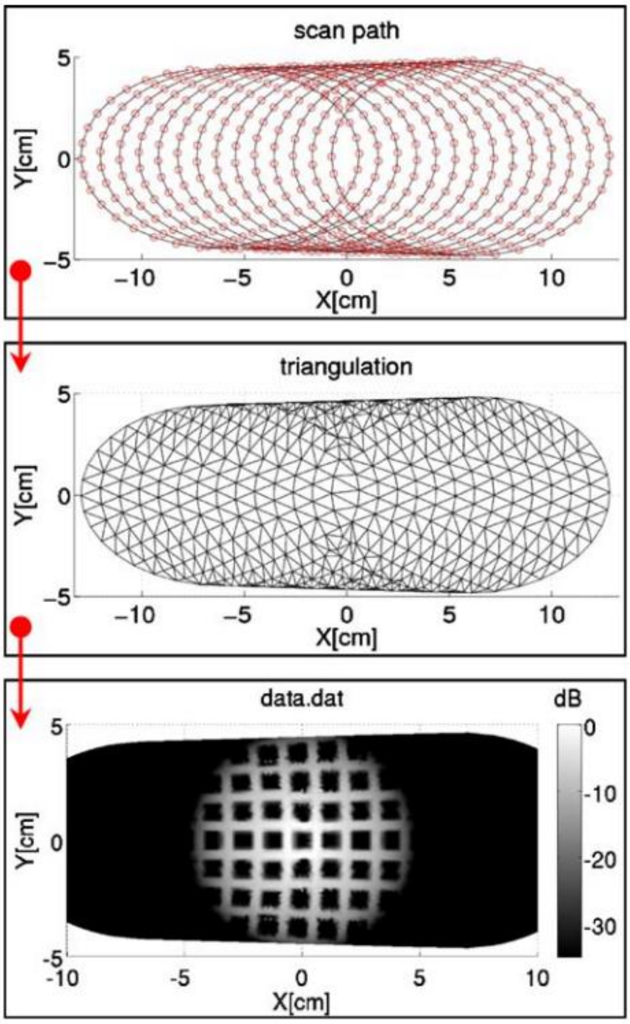

Figure 1-6 Data processing using triangulation: First, the angle pairs are converted to Cartesian coordinates (upper), then the points are connected to form triangles (middle), and finally the triangle area is filled by interpolating between its edges (lower) [33].

University of Vigo (A. Garcia-Pino's group)

In the 300 GHz imaging system developed by C. A. Weg's group in University of Vigo, the Cassegrain antenna is used to acquire images at 8 m over a large (80 cm×50 cm) field of view (FoV) as demonstrated in Figure 1-7 [17]. The increased FoV is obtained by the use of an antenna system composed by a bifocal elliptical Gregorian reflector with an extended sub-reflector to allow for fast scanning of a beam spot. The scanning is realised by the combination of the rotation and vertical tilting of a flat small secondary mirror. The beam trajectory shown in Figure 1-7 is similar to the scanning system in Figure 1-6. Figure 1-7 also gives the prototype photograph and labels for the different parts of the electronics and antenna subsystems. The whole scanning process can be finished in 1 second, and the target scenario, where a simulated explosive is hidden under a mannequin's T-shirt and the reconstructed image based on most powerful detection is illustrated in Figure 1-8 [17].

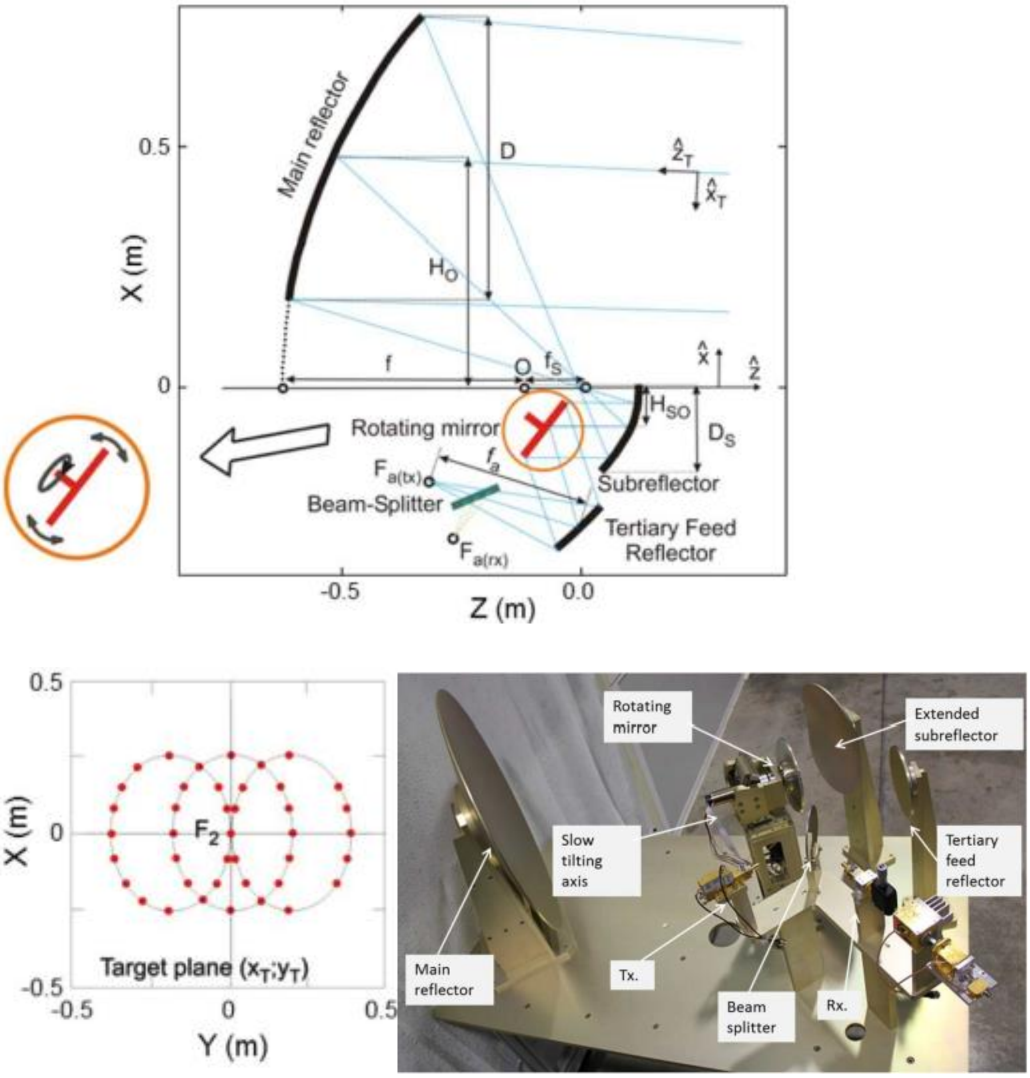
Main reflector
0.5
0
X (m)
D
$\hat{z}_T$
$\hat{x}_T$
H_O
f
O
f_S
$\hat{x}$
$\hat{z}$
H_{SO}
D_S
Rotating mirror
f_a
$F_{a(tx)}$
Beam-Splitter
$F_{a(rx)}$
Subreflector
Tertiary Feed Reflector
-0.5
0.0
Z (m)
0.5
0
-0.5
X (m)
F_2
Target plane $(x_T;y_T)$
-0.5
0
0.5
Y (m)
Rotating mirror
Extended subreflector
Slow tilting axis
Tertiary feed reflector
Main reflector
Tx.
Beam splitter
Rx.

Figure 1-7 Profile of the baseline CEGRS antenna and main geometrical parameters (upper), frontal view of the target plane and beam trajectory (lower left) and prototype photograph and labels for the different parts of the electronics and antenna subsystems (lower right) [17].

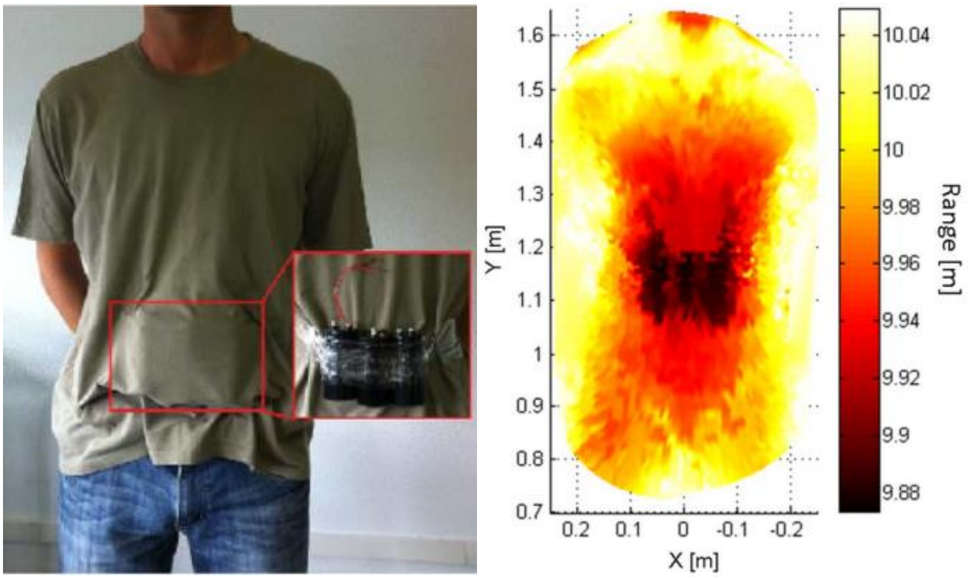

Figure 1-8 Target scenario, where a simulated explosive is hidden under a mannequin’s T-shirt and the reconstructed image based on the most powerful detection [17].

Pacific Northwest National Laboratory (D. M. Sheen’s group)

In Pacific Northwest National Laboratory (PNNL), D. M. Sheen proposed the first active millimetre wave standoff personal screening system with the application of microwave holography [34]. A simple quasi-optical structure was built with an elliptical reflector and a tilted mirror which can be rotated in two dimensions to realise the beam rotation. Figure 1-9 gives the photograph of the complete prototype standoff imaging system, the layout of the quasi-optical system and the scanning path. The scanning has been divided into two routines: one is the rotation of the flat mirror to scan the beam spot on the target plane in a circular trajectory, and the other is the variation of the tilted angle of the mirror to move the scanning circle in one direction as shown in the lower right figure of Figure 1-9 [34].

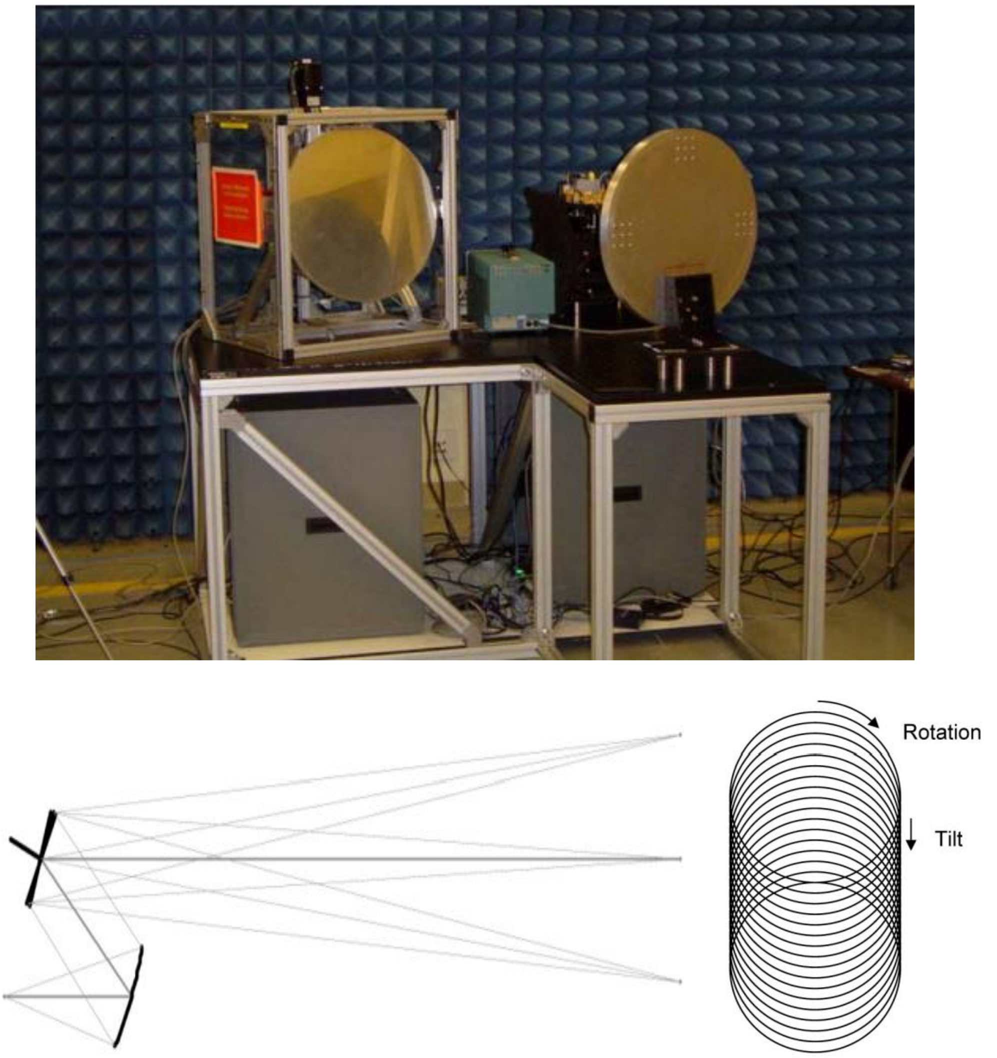

Figure 1-9 Structure and the scanning principle of the 350 GHz standoff imaging system: Photograph of the complete prototype standoff imaging system (upper), top view layout of the quasi-optical focusing system for the standoff imaging system (lower left) and scan pattern for the high-speed conical scanner design (lower right) [34].

Left figure in Figure 1-10 shows a man with a concealed mock explosive wearing a T-shirt and denim jeans. Three different angular projections of the 3-D image data are shown in the right figures to illustrate the 3-D range-resolved nature of the image data.

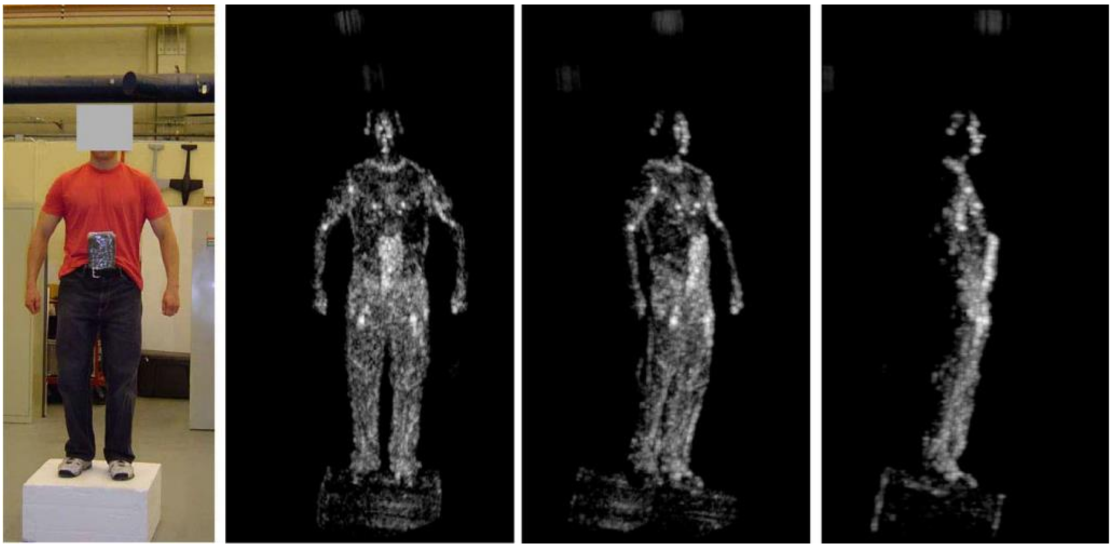

Figure 1-10 Standoff imaging results for a man with a concealed mock explosive device including the optical image (left), and several angular projections (right three images) [34].

Institute of Electronics, Chinese Academy of Sciences (G. Fang's group)

Two 0.2 THz single-frequency terahertz holographic imaging systems have been reported by Beijing Research Institute of Telemetry and Chinese Academy of Science which can be seen in Figure 1-11 and Figure 1-14 [35, 36].

1. Spot-beam imaging system.

The proposed design employs special pillbox-like quasi-optics that can generate a spot beam with nearly translational scanning pattern to ensure the image uniformity as shown in the right figure in Figure 1-11. The fixed primary reflector can focus the output beam at a short distance of about 0.07 m away from the aperture. By rotating the sub-reflector, the illumination angle of the beam can be changed to achieve spots along the horizontal direction. At the same time, the antenna box can be moved in the vertical dimension with rotated lead screw. Synthesis of these two motions can build the scanning manner shown in Figure 1-12. The final designed antenna has a size of 1100 mm* 780mm* 60 mm, with 10-mm separation between parallel plates and an aperture length of 600 mm. With the sub-reflector rotating 28.2 degrees anticlockwise, the spot-beam scans over 50 cm in the y-direction [35].

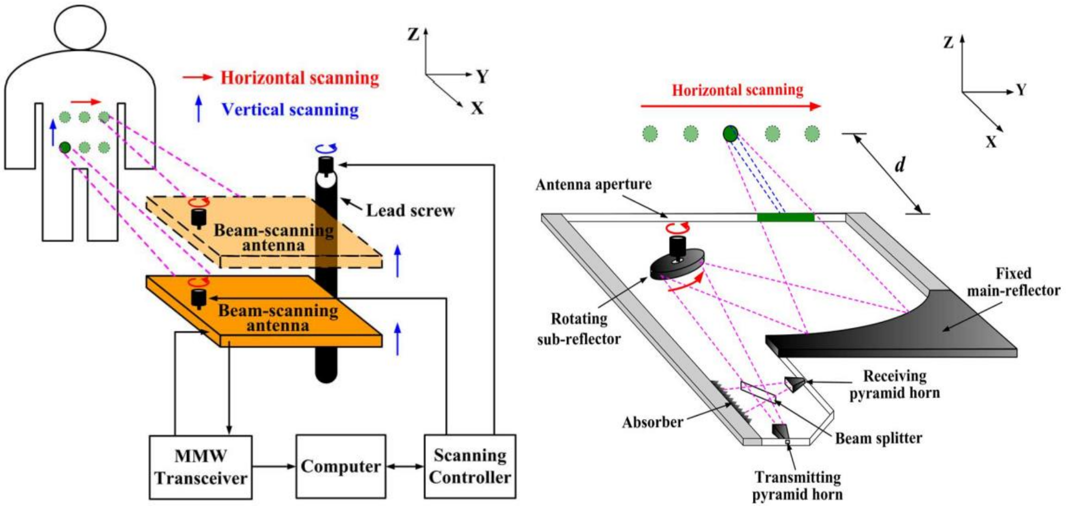
Horizontal scanning
Vertical scanning
Z
Y
X
Lead screw
Beam-scanning antenna
Beam-scanning antenna
MMW Transceiver
Computer
Scanning Controller
Horizontal scanning
Z
Y
X
d
Antenna aperture
Fixed main-reflector
Rotating sub-reflector
Receiving pyramid horn
Absorber
Beam splitter
Transmitting pyramid horn

Figure 1-11 Schematic illustration of the proposed system and the inner structure of the beam-scanning antenna [35].

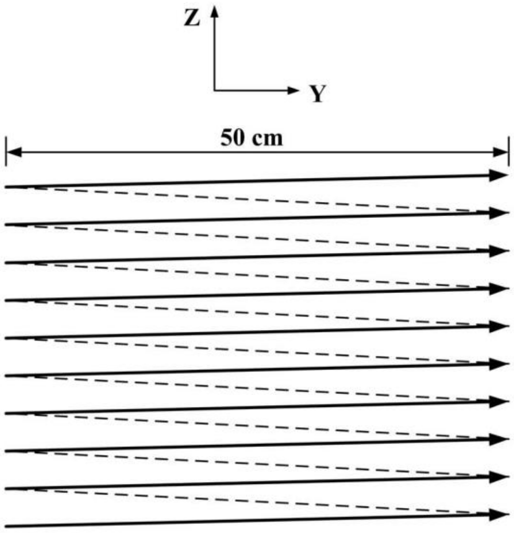

Figure 1-12 Scanning manner of the proposed scanning system [35].

Figure 1-13 is the image and the photograph of a mannequin wearing a white T-shirt, with a hidden plastic cap gun and a metal knife [35].

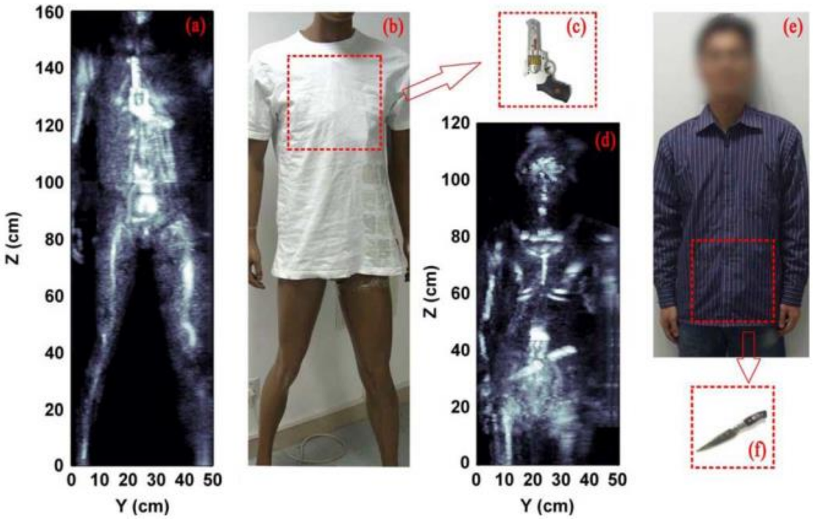

Figure 1-13 Imaging results of the spot-beam imager [35].

2. Fan-beam imaging system

The employed fan-beam scanning scheme is demonstrated in Figure 1-14. By rotating the sub-reflector, the illumination angle of the beam can be changed to achieve spots along the horizontal direction. At the same time, the antenna box can be moved in the vertical dimension with rotated lead screw. The difference between the spot-beam scanning mentioned above and the fan-beam scanning here lies in that the detection distance here (0.35-0.55 m) is larger than the previous one. The beam spot in will be extended to an elliptically shaped area in which the major axis is located in the x-direction. The aperture synthesised algorithm has been applied in the x-direction to off-axis the broad side of the fan-beam and improve the resolution of results. The scanning path acts in the same way with the previous spot-beam way as shown in Figure 1-12. Figure 1-15 gives the comparison between the optical image, single frequency image and 3-D images in three different viewed angles of a mannequin wearing a T-shirt and a concealed plastic cap gun [36].

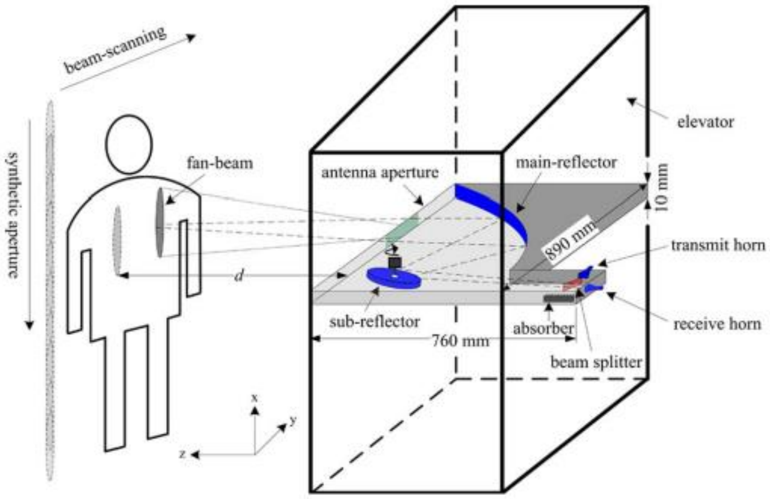
beam-scanning
synthetic aperture
fan-beam
antenna aperture
main-reflector
elevator
10 mm
890 mm
transmit horn
d
sub-reflector
760 mm
absorber
beam splitter
receive horn
x
y
z

Figure 1-14 Terahertz imaging scheme based on the combination of fan-beam scanning and aperture synthesized techniques [36].

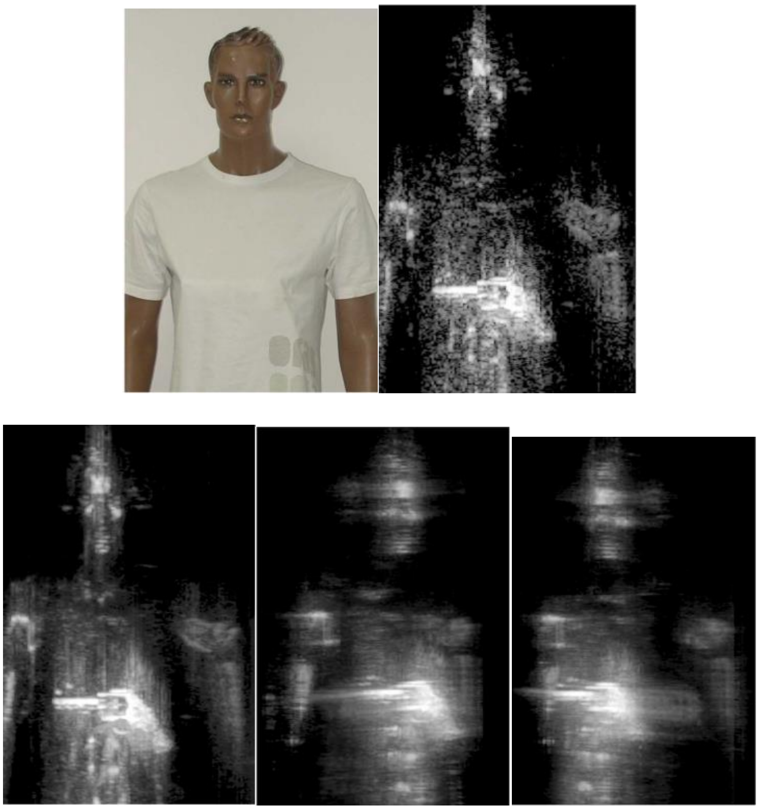

Figure 1-15 Optical image (upper left), 0.2-THz single-frequency image (upper right), and wideband (0.195–0.205 THz) 3-D images of a mannequin wearing a T-shirt and concealing a plastic cap gun with the front view, the 35° left-side view, and the 35° right-side view, respectively (lower) [36].

TeraSCREEN

Financially supported by the European Union under the Seventh Framework Programme (FP7), the collaborative project TeraSCREEN aims to realise the automatic detection and classification of the concealed threats for security screening. The objective is the multi-frequency multi-mode Terahertz screening for border checks.

The TeraSCREEN system can be divided into two parts as shown in Figure 1-16 [37]. A passive subsystem works at 94/220/360 GHz to demonstrate differences between materials, thus giving out a preliminary image. Besides, an active subsystem operating at 360 GHz illuminates the target area and collects the reflected/scattered signals to reconstruct the 3D image. In the active subsystem, combining the MIMO approach and the rotary reflector as illustrated in Figure 1-17, the scanning can be completed efficiently. The integration of these two subsystems contributes to the high frame rate and optional imaging modes, raising the reliability of the system. Prototype photograph is illustrated in Figure 1-18 [38].

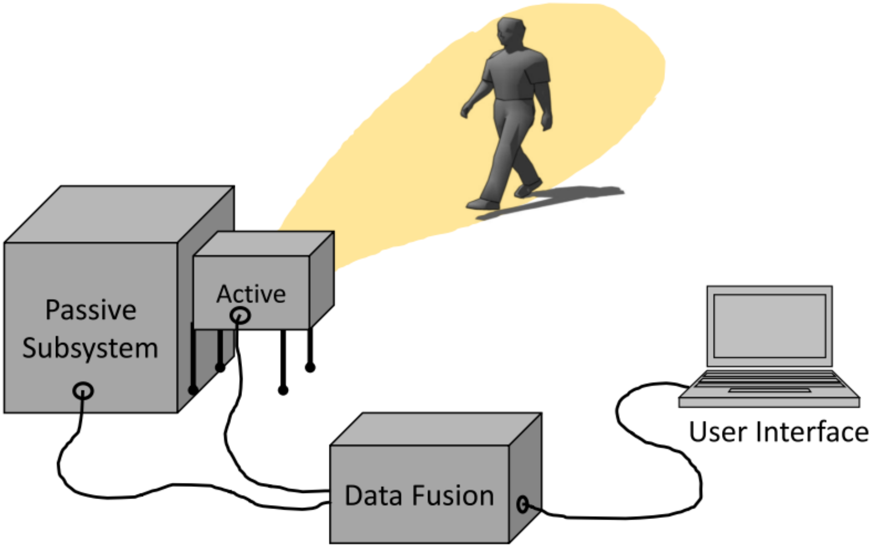

Figure 1-16 The TeraSCREEN system consisted of a passive subsystem and an active subsystem [37].

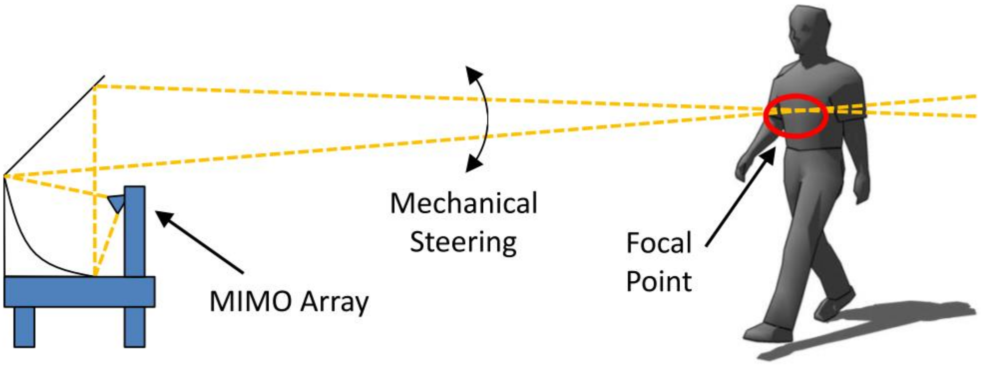

Figure 1-17 Principle of the active subsystem [37].

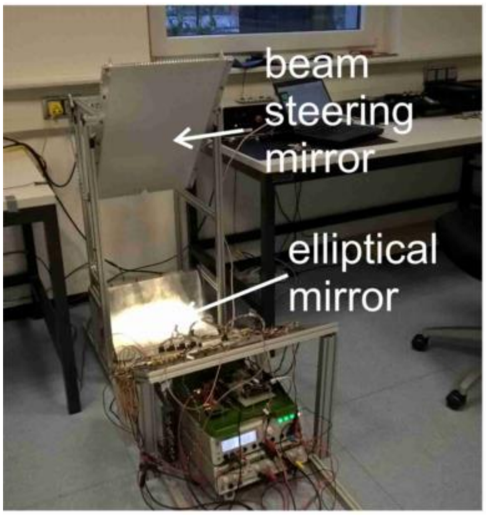

Figure 1-18 Prototype photograph of TeraSCREEN [38].

CONSORTIS (Concealed Object Stand-Off Real-Time Imaging for Security)

This work is another collaborative project funded by the European Union under the Seventh Framework Programme. The kinetic inductance detector (KID) technology is employed in the CONSORTIS system where 65644 pixels working at 500 GHz with the NEDT (Noise Equivalent Differential Temperature) of 0.4 K and 16416 pixels working at 250 GHz with the NEDT of 0.3 K are integrated into a focal plane array (FPA). An additional optical system was designed to enable the standoff imaging at the range of 5 metres (Figure 1-19). The KID bolometer array prototype consisted of 2500 elements (as shown in Figure 1-20) was proved to cover a limited field of view of about 55 cm in the cross range dimension by researchers from VTT Technical Research

Centre of Finland Ltd. [39]. Meanwhile, University of St Andrews, Wasa Millimetre Wave AB and Technical University of Delft reported the CONSORTIS 340 GHz radar which is consisted of 16 homodyne FMCW transceivers based on the Pathfinder architecture (the CAD model can be found in Figure 1-21) [40].

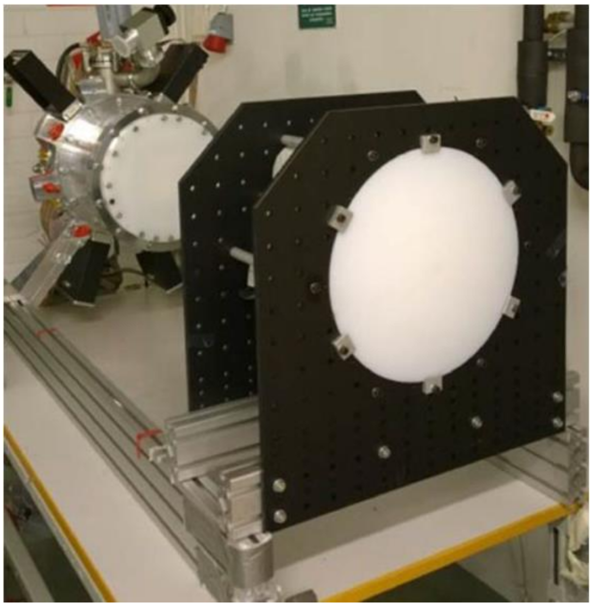

Figure 1-19 Photograph of the double lens optical system and the cryosat vacuum chamber [39].

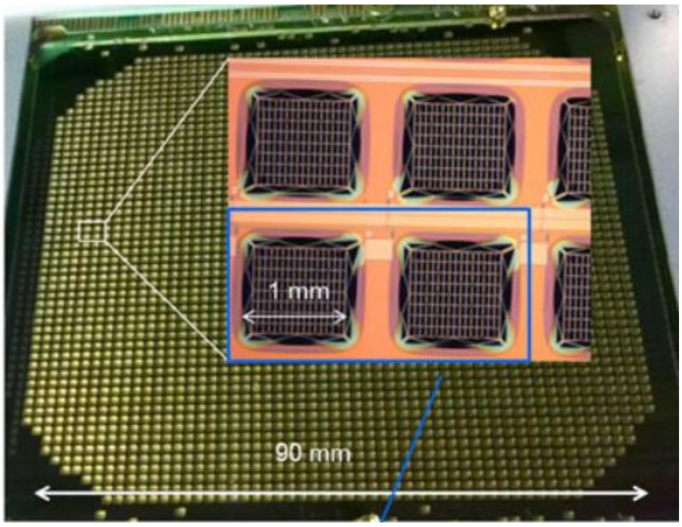

Figure 1-20 Photograph of the 2500-pixel KID bolometer array prototype [39].

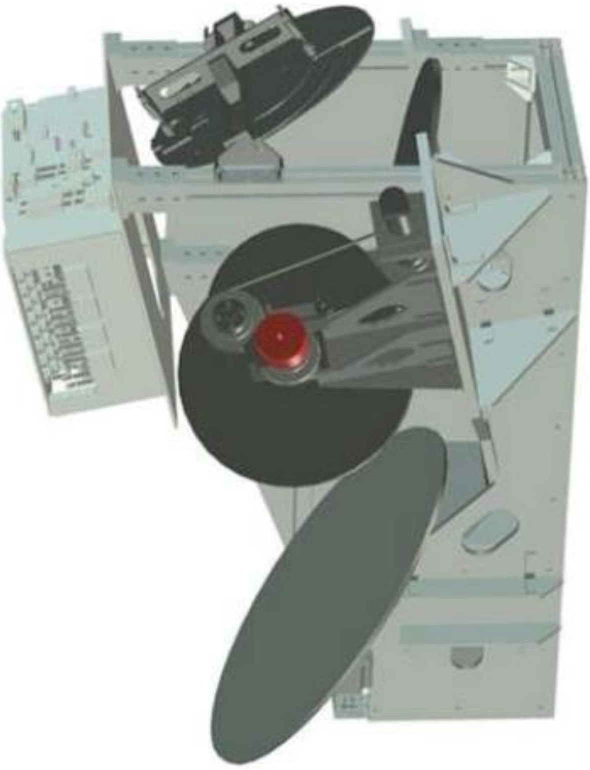

Figure 1-21 CAD model of CONSORTIS 340 GHz radar [40].

TIPPSI (THz Imaging Phenomenology Platforms for Stand-off IED Detection)

Besides participating in the CONSORTIS project, Dr Nuria Llombart of Delft University also leads another collaborative team working on a mechanically scanning imager project named TIPPSI, which is funded by the European Defence Agency (EDA). Cooperating with A. Garcia-Pino's group of University of Vigo, TIPPSI group developed a fast screening system combining the sparse 8-element transceivers focal plane array operating at 220 GHz and quasi-optical reflector subsystem. Compared to the work of A. Garcia-Pino's group, the TIPPSI system offers two options of screening standoff distances, short and long range, in single system (photographs are demonstrated in Figure 1-22). The effective FOV (Field of View) varies following the selection of the detection range of the imager. For the short range application, the field of view can reach about 1.2 m 1.2 m. For the long range detection scenario, an area of 70 cm 80cm can be covered and the resolution is less than 1.2 cm over the entire FOV (as shown in Figure 1-23) [41, 42].

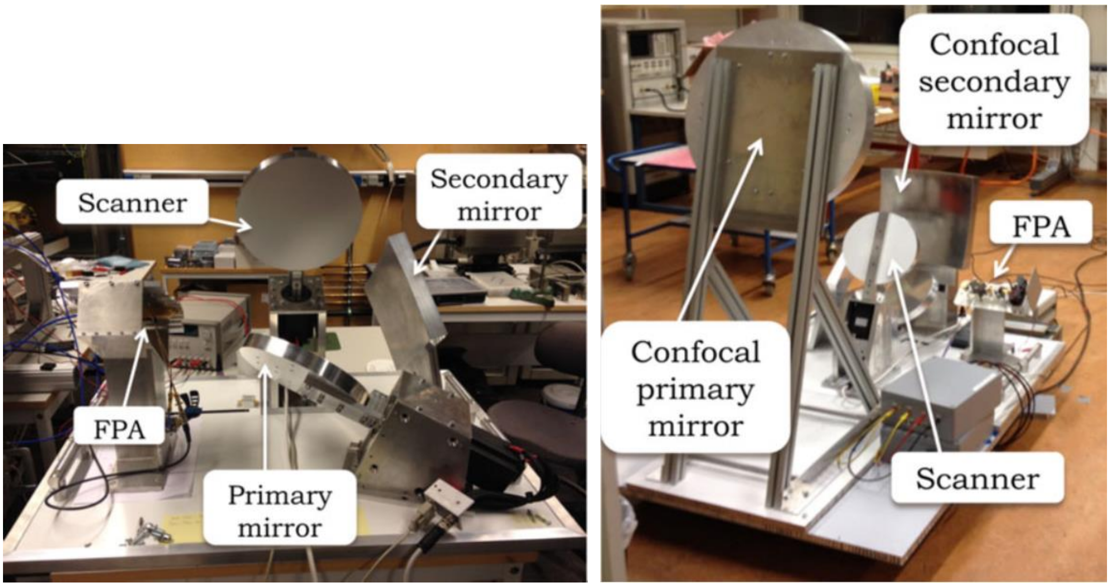
Scanner
Secondary mirror
FPA
Primary mirror
Confocal secondary mirror
FPA
Confocal primary mirror
Scanner

Figure 1-22 Photographs of the short range and the long range systems. [42]

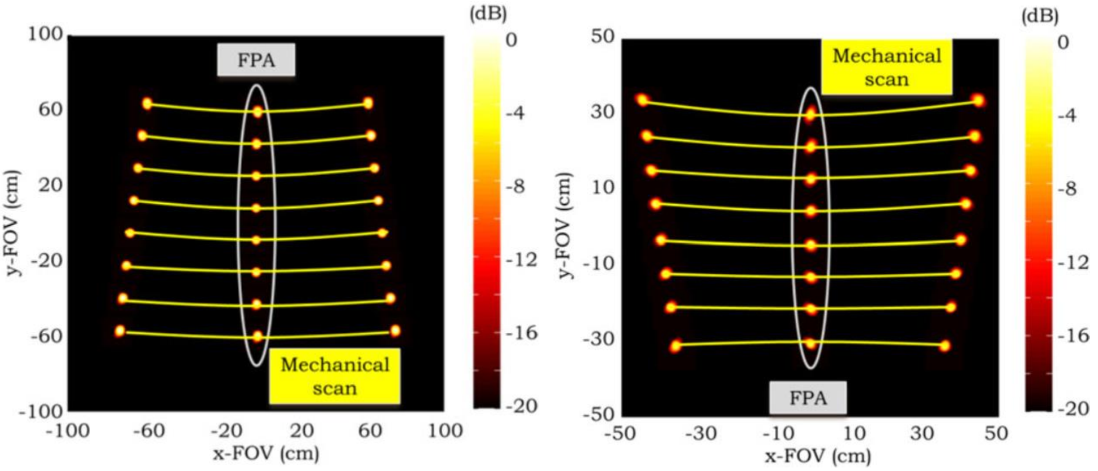

Figure 1-23 Normalized radiation patterns of the short range and the long range systems [42].

McMaster University

Microwave/millimetre holography techniques have been conducted at McMaster University. A three-dimensional near-field microwave holography using reflected and transmitted signals have been studied as shown in Figure 1-24 [43]. Sparse array technique is also applied in the imaging to reduce the number of antennas in the imaging array [44].

1.2.2 Current commercial products

ThruVis, UK

In the aspect of commercial product development, the passive Terahertz perspective imaging device T5000 developed by ThruVision Company, UK has also been successfully equipped in several civil airports and London's financial centre for the safety of passengers and baggage detection as shown in Figure 1-25. The technical principle comes from the British astronomer and Rutherford Appleton Laboratory at Oxford, and the passive terahertz imaging technology is used to reveal concealed weapons in both stationary and mobile subjects at a detection distance of up to 25 meters. The latest product is ThruVis TS4-C [45] shown in Figure 1-26. TS4-C working at 0.25 THz screens stationary individuals at a distance of around 3.5 m.

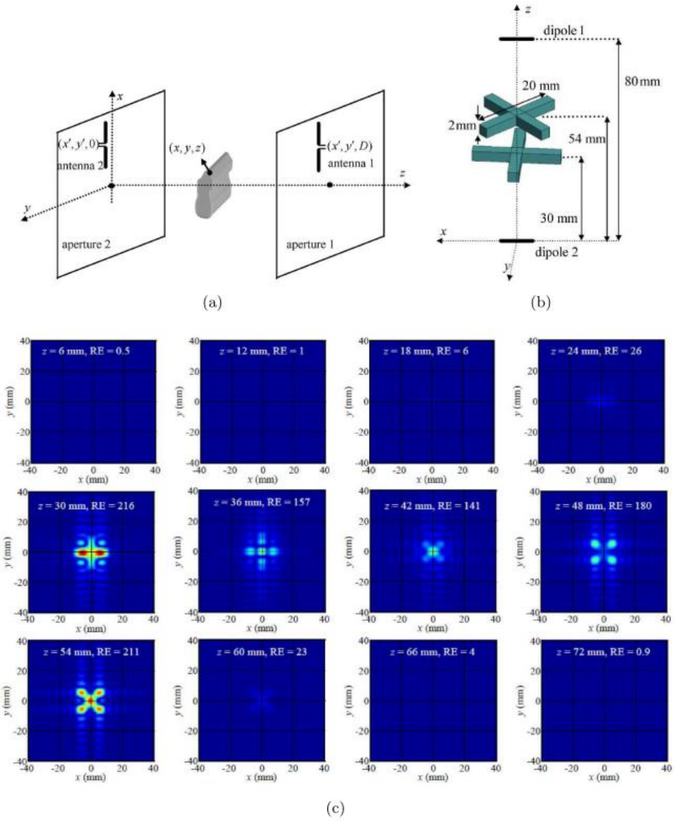
(x', y', 0)
antenna 2
(x, y, z)
(x', y', D)
antenna 1
aperture 2
aperture 1
x
y
z
(a)
dipole 1
20 mm
80 mm
2 mm
54 mm
30 mm
dipole 2
(b)
z = 6 mm, RE = 0.5
z = 12 mm, RE = 1
z = 18 mm, RE = 6
z = 24 mm, RE = 26
z = 30 mm, RE = 216
z = 36 mm, RE = 157
z = 42 mm, RE = 141
z = 48 mm, RE = 180
z = 54 mm, RE = 211
z = 60 mm, RE = 23
z = 66 mm, RE = 4
z = 72 mm, RE = 0.9
y (mm)
x (mm)
(c)

Figure 1-24 3-D near-field microwave holography system (a) Setup of the system (b) Dielectric targets (c) Reconstructed images for the targets. [43]

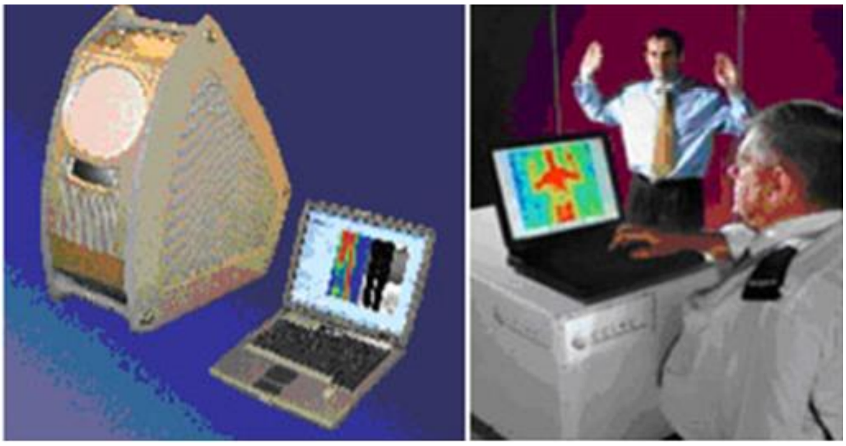

Figure 1-25 ThruVision T5000 security system. [44]

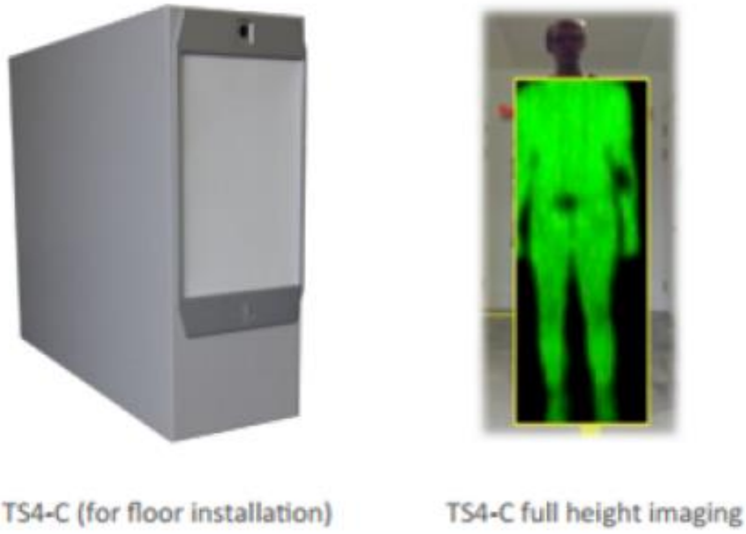

TS4-C (for floor installation)

TS4-C full height imaging

Figure 1-26 ThruVis TS4-C security system [45].

SafeView, USA

The SafeView Company in the USA has developed a three-dimensional active human security imaging system working in the frequency band ranges from 30 GHz to 300 GHz. It takes 10 seconds to complete whole human body scanning, which has been used in some European countries [46] as shown in Figure 1-28. The millimetre wave (MMW) technology in L3's advanced personnel screening systems uses millimetre waves to reveal objects that may be concealed. A broad variety of materials including both metallic and non-metallic threats can be detected [46].

TeraSnap, China

The first terahertz body scanner developed in East China Research Institute of Electronic Engineering, China was demonstrated in IFSEC (International Fire and Security Exhibition and Conference) International 2014, in London, the UK on 17th-19th, June 2014. The THz human security device TeraSnap (as shown in Figure 1-27) was designed on the principle of compressed sensing and passive THz imaging technology. The 2-D surface intensity of human body can be obtained according to the strength contrast among different materials when the THz source is illuminated [47].

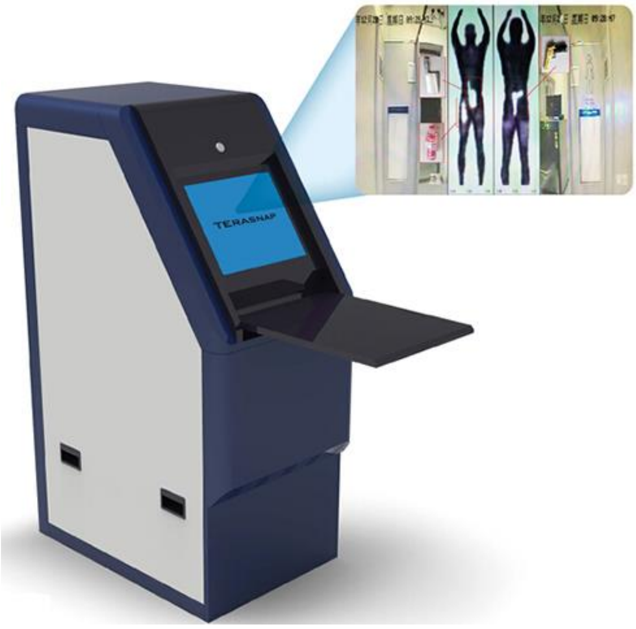

Figure 1-27 TeraSnap B01 [47].

SubTera, UK

Figure 1-29 shows SubTera B1080 [48] developed by SubTeraNDT. SubTera detection system can complete the inspection in a non-invasive way underneath paints, insulation, fireproofing and other protective coatings in a passive mode. SubTera B1080 is operating at a single frequency or an optical range to suit coatings found in the oil and gas industries. SubTera B1080 employs a similar technique applied in ThruVis TS4-C, and can achieve comparable images [48].

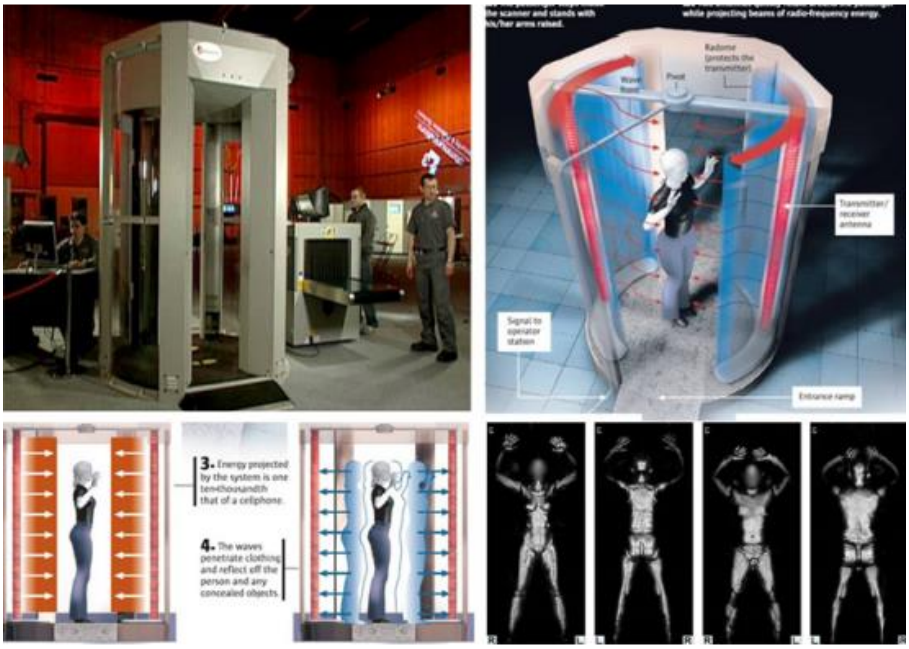
the scanner and stands with
his/her arms raised.
while projecting beams of radio-frequency energy.
Radome
(protects the
transmitter)
Pivot
Transmitter/
receiver
antenna
Signal to
operator
station
Entrance ramp
3. Energy projected
by the system is one
ten-thousandth
that of a cellphone.
4. The waves
penetrate clothing
and reflect off the
person and any
concealed objects.
R
L
L
R
R
L
L
R

Figure 1-28 The imaging system developed by SafeView Company used for airport security [46].

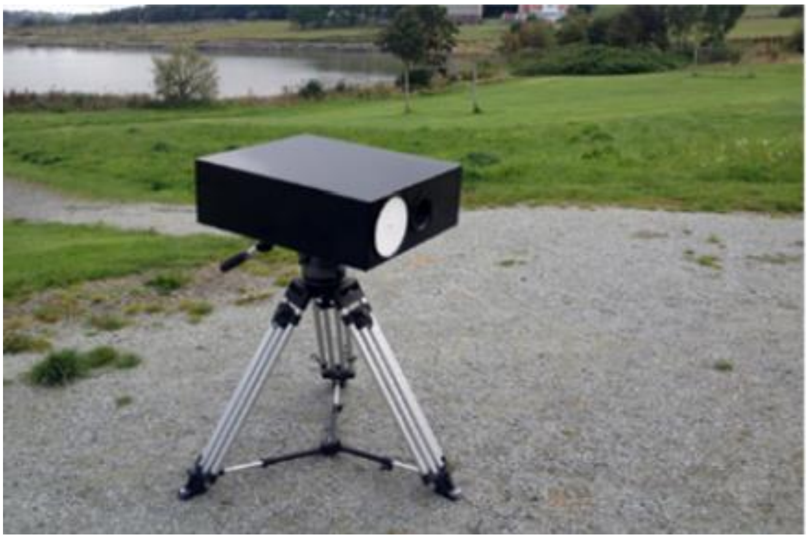

Figure 1-29 SubTera B1080. [48]

Rohde & Schwarz, Germany

In 2012, Dr S. S. Ahmed and his colleagues in Rohde & Schwarz reported their Quick Personnel Safe Screening system (QPASS) as shown in Figure 1-30. The QPASS was developed from multi-static digital-beamforming (DBF) technology to provide close-range personnel screening at airports and critical infrastructure buildings. The imaging array operates from 70 to 80 GHz with frequency-stepped continuous-wave technique. Two arrays of the square aperture are stacked vertically, where each includes 1536 Tx channels and 1536 Rx channels, making a total of 6144 RF channels. The large array aperture ensures proper illumination of the human body [49].

Furthermore, Figure 1-31 illustrates the detector array corridor concept proposed by Rohde & Schwarz based on the QPASS system introduced above [50].

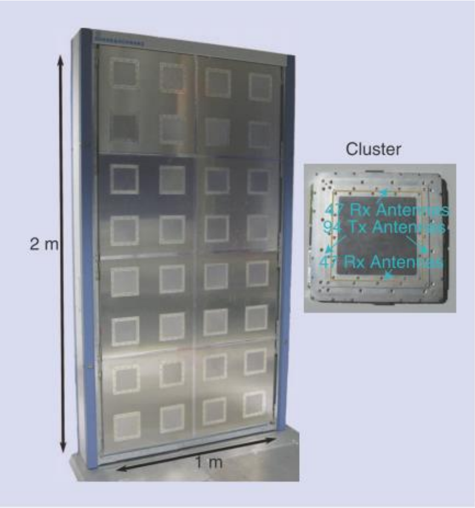

Figure 1-30 Photograph of QPASS system (without cover) and a cluster unit [49].

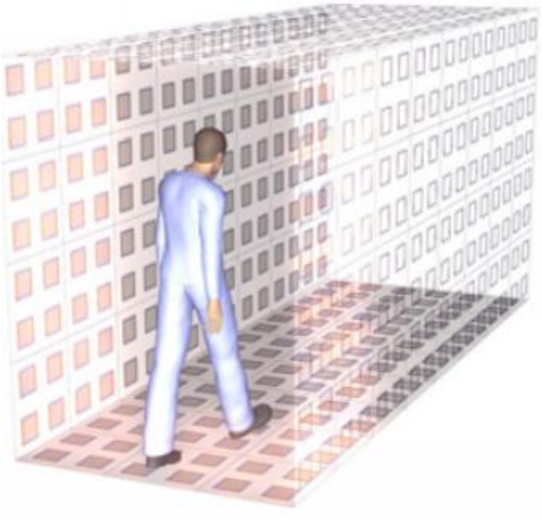

Figure 1-31 The detector array corridor concept proposed by Rohde Schwarz [50].

1.3 Challenges and motivations

A summary of THz imaging systems reviewed in Sections 1.2.1 and 1.2.2 is given in Table 1-2, where only lists active, heterodyne, single detector scanned systems as references to this research work. The passive imaging systems are not included as they suffer poor resolution in general. Right two columns indicate whether the image of the listed system was reconstructed with holography algorithm and in which dimension the algorithm was applied (transversal and longitudinal). The 'Amp based' column with 'T/L' means the holography technique has not been applied in the imaging system. The 'Amp & Phase' column with 'T/L' means the holography technique has been employed in this imaging system. The row with 'T' in the 'amp based' column and 'L' in the 'Amp & Phase' indicates that the holography technique is only applied in one dimension (the longitudinal dimension).

Table 1-2 Summary of existed imaging systems reported by groups all over the world and the objective of this work.

	Freq (GHz)	Scanning Time (s)	Distance (m)	Resolution (mm)	Field of View (m * m)	Amp based	Amp. &Phase	Note
C.A.Weg	600 & 300	9	0.75-1.5	15	0.2*0.3	T&L		Rotation
D.Sheen	350	10	6	1	0.6*0.6		T&L	Rotation
JPL	676.5	1	25	10	0.4*0.4	T&L		Rotation
Fang 1	200	5	0.07	-	0.5*0.9	T&L		Raster+Rotation
Fang 2	200	5	0.35-0.55	4	0.53*0.9	T	L	Raster+Rotation
A.Garcia	300	1	8	20	0.5*0.8	T&L		Rotation
TeraSCREEN	94/220/360	0.125	2.5-5	6.8	0.5*1.2	T&L		Rotation+Array +Passive
CONSORTIS	340	~1	1.5	<10	1*1	T&L		Rotation+Array
TIPPSI	220	-	3.5/4.4	10	0.7*0.8	T&L		Rotation+Array
This work	220	2	3	5	0.8*0.8		T&L	Rotation

Some notes are also listed in the right column of the table. Different techniques are applied in different groups, so these systems can’t be compared directly. The employment of detector array and passive detectors can reduce the scanning time dramatically. At the same time, raster scanned system can cover a larger area though the system will be less compact. The application of holographic imaging technique will also introduce higher resolution while retaining less sampling points.

As reviewed earlier, there are considerable advancements in THz imaging technology in terms of resolution and imaging time over the last decade. However, there still exist several further development needs.

1. The need for a fast scanning system.

Compared to the shortest image acquisition time listed in the TeraSCREEN, the imaging time of other systems can’t meet the real-time screening goal for the objects in motion. Even so, we need to note the passive subsystem where large detector array is included in the TeraSCREEN system contributes to the high-speed imaging. As to the active part, the acquisition time is still limited by the mechanical movement.

Raster scanning is currently considered as one of the most popular scanning approach used in THz holography imagers. Target images can be constructed by using the amplitude/phase information received directly on the receiver aperture. However, the long scanning time and large scanner size limit a wide deployment of raster scanning imagers. On the other hand, the fast angular beam scanning method has been widely used in the passive THz imagers and proved effective [51].

Meanwhile, the inadequate mechanical movement leads to the overlapped scanning trajectory. Lots of unnecessary sampling points and scanning time is wasted during the data collection process. This project aims to develop an angular beam scanning system, instead of a raster scanning one, in the THz imaging system to reduce the imaging time.

2. The need for an image algorithm for large-scaled objects.

To construct a high-resolution image, most existing systems have adopted the narrow illuminating beam method, thus resulting in a large number of sampling points on the large-scaled target. If the target is under sampled, the image resolution image will not be assured. To address this dilemma, this project is to develop an improved holographic THz imager, in which the amplitude/phase information can be combined to produce high-quality images of targets with the efficient algorithms.

1.4 Objectives

This project aims to develop a fast Terahertz holographic imaging system for CWD (Concealed Weapon Detection) applications. The objectives of this thesis are outlined as below:

1. To validate the scanning imaging system in the simulation. Two scanning schemes are discussed and compared. The beam scanning scheme will be deployed to reduce the imaging time.
2. To design and develop a multi-reflector full-scanning sub-system which can maintain the beam consistency during the scanning procedure and ensure the compactness of the sub-system.
3. To develop new image reconstruction algorithms which are less time consuming compared to the conventional back-propagation algorithm while maintaining the comparable image quality. The algorithms will be evaluated in simulations and experiments. Detailed comparison results will be listed as a reference to the algorithm applied in the imaging system.
4. To set up and investigate an experimental prototype of the terahertz holography imaging system. The holography algorithm needs to be tested on the assembled imaging system, and the reconstructed images will be analysed.

1.5 Organisation of the thesis

The rest of the thesis is organised as follows:

Chapter 2 gives a detailed introduction to the holography theory firstly. Optical holography and microwave holography are presented and compared. The equations of the image reconstruction are derived. Then, two different scanning schemes: the raster scanning scheme and the beam scanning scheme are compared. A new scanning mechanic structure is demonstrated. Required parameters of the scanning schematic are calculated. The new THz imaging system is proposed on the beam scanning scheme.

Chapter 3 presents the design of Dragonian dual-reflector scanning sub-system. First, constructions and characteristics of various reflector antennas are reviewed. A Dragonian reflector antenna is introduced in our proposed beam scanning scheme. Detailed design procedure and parameters are presented. Simulation in GRASP 9 is used to demonstrate the scanning performance of both the single ellipsoidal reflector antenna and the designed Dragonian reflector antenna. Two different scanning structures are simulated and compared. The performance of the scanning beam at various points on the target plane is studied.

Chapter 4 describes the theory of Physical Optics and the application in the simulation of two scanning schemes. PO algorithm is briefly presented at first. Then the PO algorithm in Matlab is validated with a single off-axis reflector antenna compared simulated results from GRASP 9. The transposed convolution algorithm and the inverse convolution algorithm are compared and discussed with the holography algorithm in reconstructed images. In the final part, different scanning schemes are studied using the proposed simulation method.

Chapter 5 mainly focuses on the experimental evaluation of the THz holography imaging systems based on the raster scanning scheme and the beam scanning scheme, respectively. Experiments are conducted on simplified 2D holography systems. Spatial sampling interval and Line Spread Function of the deployed system are analysed.

Reconstructed images are investigated finally.

Chapter 6 concludes the research work demonstrated in this report. Achievements are highlighted and planned work to implement and improve the THz holographic imaging system is also proposed.

1.6 References

[1] P. De Maagt, P. H. Bolivar, and C. Mann. Terahertz Science, Engineering and Systemsfrom Space to Earth Applications. New York: Weily, 2005.

[2] A. G. Markelz. Terahertz dielectric sensitivity to biomolecular structure and function, IEEE Journal of Selected Topics in Quantum Electronics, vol. 14, no. 1, pp. 180–190, 2008.

[3] D. L. Woolard, J. O. Jensen, and R. J. Hwu. Terahertz science and technology for military and security applications. world scientific, vol. 46, 2007.

[4] H. Essen, A. Wahlen, R. Sommer, et al. High-bandwidth 220 GHz experimental radar, Electronics Letters, vol. 43, no. 20, pp. 1114–1116, 2007.

[5] G. Chattopadhyay, K. B. Cooper, R. Dengler, N. Llombart, and P. H. Siegel. Imaging at a stand-off distance with terahertz FMCW radar, General Assembly and Scientific Symposium, IEEE 2011 XXXth URSI, 2011.

[6] S. S. Dhillon, et al. The 2017 terahertz science and technology roadmap. Journal of Physics D: Applied Physics, vol. 50, no. 4, pp. 043001, 2017.

[7] P. H. Siegel. Terahertz technology, IEEE Transactions on Microwave Theory and Techniques, vol. 50, no. 3, pp. 910–928, 2002.

[8] F. Sizov and A. Rogalski, THz detectors. Progress in Quantum Electronics, vol. 34, no. 5, pp. 278–347, 2010.

[9] H.-W. Hbers, S. Pavlov, K. Holldack, U. Schade, and G. Wstefeld. Long wavelength

response of unstressed and stressed Ge: Ga detectors, Astronomical Telescopes and Instrumentation. International Society for Optics and Photonics, Conference Proceedings, pp. 627505, 2006.

[10] S. Hargreaves and R. A. Lewis. Terahertz imaging: materials and methods, Journal of materials science: Materials in electronics, vol. 18, no. 1, pp. 299–303, 2007.

[11] N. Karpowicz, H. Zhong, J. Xu, et al. Non-destructive sub-THz CW imaging, Integrated Optoelectronic Devices 2005. International Society for Optics and Photonics, Conference Proceedings, pp. 132–142, 2005.

[12] A. Dobroiu, M. Yamashita, Y. N. Ohshima, et al. Terahertz imaging system based on a backward-wave oscillator, Applied optics, vol. 43, no. 30, pp. 5637–5646, 2004.

[13] A. W. Lee, Q. Qin, S. Kumar, et al. Real-time terahertz imaging over a standoff distance (25 meters), Applied Physics Letters, vol. 89, no. 14, pp. 141 125, 2006.

[14] A. W. Lee, B. S. Williams, S. Kumar, et al. Real-time imaging using a 4.3-THz quantum cascade laser and a 320 times 240 microbolometer focal-plane array, IEEE Photonics Technology Letters , vol. 18, no. 13, pp. 1415–1417, 2006.

[15] L. Vicarelli, M. Vitiello, D. Coquillat, et al. Graphene field-effect transistors as room-temperature terahertz detectors, Nature materials, vol. 11, no. 10, pp. 865–871, 2012.

[16] M. S. Vitiello, D. Coquillat, L. Viti, et al. Room-temperature terahertz detectors based on semiconductor nanowire field-effect transistors, Nano letters, vol. 12, no. 1, pp. 96–101, 2011.

[17] A. Garcia-Pino, B. Gonzalez, O. Rubinos, et al. Bifocal reflector antenna for a standoff radar imaging system with enhanced field of view. IEEE Transactions on Antennas and Propagation vol. 62, no. 10, pp. 4997-5006, 2014.

[18] R. Han, Y. Zhang, Y. Kim, et al. Active terahertz imaging using Schottky diodes in CMOS: Array and 860-GHz pixel. IEEE Journal of Solid-State Circuits, vol. 48, no. 10,

pp. 2296-2308, 2013.

[19] J. Grant, I. Escorcia - Carranza, C. Li, et al. A monolithic resonant terahertz sensor element comprising a metamaterial absorber and micro - bolometer, Laser & Photonics Reviews, vol. 7, no. 6, pp. 1043-1048, 2013.

[20] I. E. Carranza, J. Grant, J. Gough, et al. Metamaterial-based terahertz imaging. IEEE Transactions on Terahertz Science and Technology, vol. 5, no. 6, pp. 892-901, 2015.

[21] V. Dobrovolsky, and F. Sizov. A room temperature, or moderately cooled, fast THz semiconductor hot electron bolometer, Semiconductor science and technology, vol. 22, no. 2, pp. 103, 2006.

[22] A. Kosarev, S. Rumyantsev, M. Moreno, et al. SixGey: H-based micro-bolometers studied in the terahertz frequency range. Solid-State Electronics, vol. 54, no. 4, pp. 417-419, 2010.

[23] Simoens, François, J. Lalanne-Dera, J. Meilhan, et al. Active imaging with THz fully-customized uncooled amorphous-silicon microbolometer focal plane arrays. 2011 IEEE 36th International Conference on Infrared, Millimeter and Terahertz Waves (IRMMW-THz), 2011.

[24] X. H. Lu, L. Kang, J. Chen, et al. A terahertz detector operating at room temperature. Photonics and Optoelectronics Meetings. International Society for Optics and Photonics, 2008.

[25] S. François, J. Meilhan, and J. -A. Nicolas. Terahertz real-time imaging uncooled arrays based on antenna-coupled bolometers or FET developed at CEA-Leti. Journal of Infrared, Millimeter, and Terahertz Waves, vol. 36, no. 10, pp. 961-985, 2015.

[26] S. Boppel, A. Lisauskas, D. Seliuta, et al. CMOS integrated antenna-coupled field-effect-transistors for the detection of 0.2 to 4.3 THz. 2012 IEEE 12th Topical Meeting on Silicon Monolithic Integrated Circuits in RF Systems, SiRF 2012-Digest of Papers.

[27] G. C. Trichopoulos, H. L. Mosbacker, D. Burdette, and K. Sertel. A broadband focal plane array camera for real-time THz imaging applications, IEEE Transactions on Antennas and Propagation, vol. 61, no. 4, pp. 1733–1740, 2013.

[28] D. Jinshan, M. Kahl, O. Loffeld, and P. H. Bolivar. THz 3-D image formation using SAR techniques: Simulation, processing and experimental results, IEEE Transactions on Terahertz Science and Technology, vol. 3, no. 5, pp. 606–616, 2013.

[29] C. Binbin, J. Ge, W. Cheng, Y. Chen, et al. Real-time imaging with a 140 GHz inverse synthetic aperture radar, IEEE Transactions on Terahertz Science and Technology, vol. 3, no. 5, pp. 594–605, 2013.

[30] K. B. Cooper, R. J. Dengler, G. Chattopadhyay, et al. A high-resolution imaging radar at 580 GHz, IEEE Microwave and Wireless Components Letters, vol. 18, no. 1, pp. 64–66, 2008.

[31] K. B. Cooper, R. J. Dengler, N. Llombart, et al. Penetrating 3-D imaging at 4- and 25-m range using a submillimeter-wave radar, IEEE Transactions on Microwave Theory and Techniques, vol. 56, no. 12, pp. 2771–2778, 2008.

[32] A. Tang, K. B. Cooper, R. J. Dengler, N. Llombart, and P. H. Siegel. Automatic focusing for a 675 GHz imaging radar with target standoff distances from 14 to 34 meters, in Microwave Symposium Digest (IMS), 2013 IEEE MTT-S International Conference Proceedings, pp. 1–3.

[33] C. A. Weg, W. von Spiegel, R. Henneberger, et al. Fast active THz cameras with ranging capabilities. Journal of Infrared, Millimeter, and Terahertz Waves, vol. 30, no. 12, pp. 1281-1296, 2009.

[34] D. Sheen, D. McMakin, and T. Hall. Near-field three-dimensional radar imaging techniques and applications, Applied Optics, vol. 49, no. 19, pp. E83–E93, 2010.

[35] X. Gao, C. Li, S. Gu, et al. Study of a new millimeter-wave imaging scheme suitable for fast personal screening. IEEE Antennas and Wireless Propagation Letters,

vol. 11, pp. 787-790, 2012.

[36] S. Gu, C. Li, X. Gao, et al. Terahertz aperture synthesized imaging with fan-beam scanning for personnel screening, IEEE Transactions on Microwave Theory and Techniques, vol. 60, no. 12, pp. 3877–3885, 2012.

[37] N. E. Alexander, B. Alderman, F. Allona, et al. TeraSCREEN: multi-frequency multi-mode Terahertz screening for border checks. Passive and Active Millimeter-Wave Imaging XVII. Vol. 9078. 2014.

[38] R. Herschel, S. Nowok, R. Zimmermann, et al. MIMO based 3D imaging system at 360 GHz. Passive and Active Millimeter-Wave Imaging XIX. Vol. 9830. 2016.

[39] A. Timofeev, J. Luomahaara, L. Grönberg, et al. Optical and Electrical Characterization of a Large Kinetic Inductance Bolometer Focal Plane Array. IEEE Transactions on Terahertz Science and Technology, vol. 7, no. 2, pp. 218-224, 2017.

[40] D. A. Robertson, D. G. MacFarlane, S. L. Cassidy, et al. Submillimetre wave 3D imaging radar for security applications, 5-4, 2016.

[41] E. Gandini, J. Svedin, T. Bryllert, et al. On the development of a quasi-optical system for short and long range standoff imagers, 2015 IEEE 40th International Conference on Infrared, Millimetre and Terahertz waves (IRMMW-THz), 2015.

[42] E. Gandini, J. Svedin, T. Bryllert, et al. Optomechanical System Design for Dual-Mode Stand-Off Submillimetre Wavelength Imagers. IEEE Transactions on Terahertz Science and Technology, 2017.

[43] R. K. Amineh, M. Ravan, A. Khalatpour, and N. K. Nikolova. Three-dimensional near-field microwave holography using reflected and transmitted signals, IEEE Transactions on Antennas and Propagation, vol. 59, no. 12, pp. 4777–4789, 2011.

[44] D. M. Sheen and T. E. Hall. Reconstruction techniques for sparse multistatic linear array microwave imaging, International Society for Optics and Photonics, SPIE Defense+ Security, Conference Proceedings, pp. 90 780I, 2014.

[45] ThruVis, ThruVis TS4-C datasheet, https://www.digitalbarriers.com/storage/app/media//Downloads/Solutions/ThruVis/DB-ThruVision TS4C-FinalE.pdf/, 2014.

[46] Safeview, Safeview L-3, http://www.sds.l-3com.com/, 2016.

[47] www.cetcthz.com.

[48] SubTera, SubTera NDT B1080, http://subterandt.com/products/, 2016.

[49] S. S. Ahmed, A. Schiessl, F. Gumbmann, et al. Advanced microwave imaging. IEEE microwave magazine, vol. 13, no. 6, pp. 26-43, 2012.

[50] S. S. Ahmed. Advanced fully-electronic personnel security screening technology, 2015 IEEE 9th European Conference on Antennas and Propagation (EuCAP), 2015.

[51] M. Zhou, Y. Alfadhl, and X. Chen. Study on a THz beam-scanning system with offset Dragonian dual-reflector antenna, 9th UK-Europe-China Workshop on Millimetre Waves and Terahertz Technologies (UCMMT 2016), 2016.

Chapter 2. Terahertz imaging theory and proposed beam scanning scheme

In chapter 1, a detailed review of the THz imaging technologies was presented. Some state-of-art THz imaging systems are demonstrated and compared in different aspects, indicating two further developing requirements: faster imaging speed and better reconstructed images. To meet these requirements, we propose to introduce the microwave holographic technique and the beam scanning approach in our proposed THz imaging system.

This chapter provides an introduction to the holographic imaging. The differences between the optical holography and the microwave holography are discussed in details. Two different scanning schemes will be presented and compared. The schematic of the THz imaging system is proposed based on the beam scanning scheme.

2.1 Introduction of holography theory

2.1.1 Optical holography

In optical holography, both light amplitude and phase information need to be recorded to reconstruct the image. A reference light wave is introduced along with the scattered illumination wave from the object on the recording media. This coherent illumination results in the interference pattern on the photographic plate. The source wave is normally divided into two parts: one acting as the illumination wave for the object, the other being reflected to the plate by some optical mirrors sequentially.

The intensity at any point in this pattern depends on the phase as well as the amplitude of the original object wave. Accordingly, the processed photographic plate, which is called a hologram (or whole record), contains both phase and amplitude information of the object wave. However, this information is in a coded form, and the hologram itself bears no resemblance to the object. Figure 2-1 shows the hologram recording schematic [1].

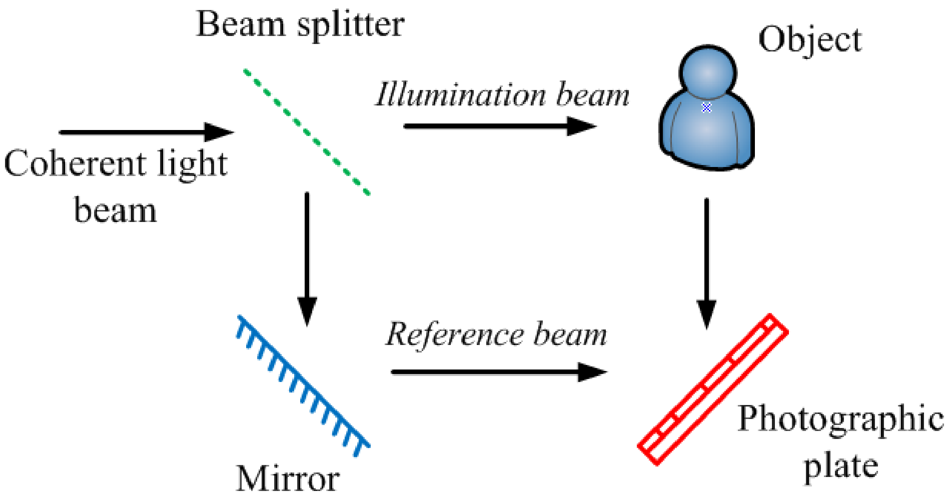
Beam splitter
Object
Illumination beam
Coherent light beam
Reference beam
Mirror
Photographic plate

Figure 2-1 Recording a hologram in optical holography.

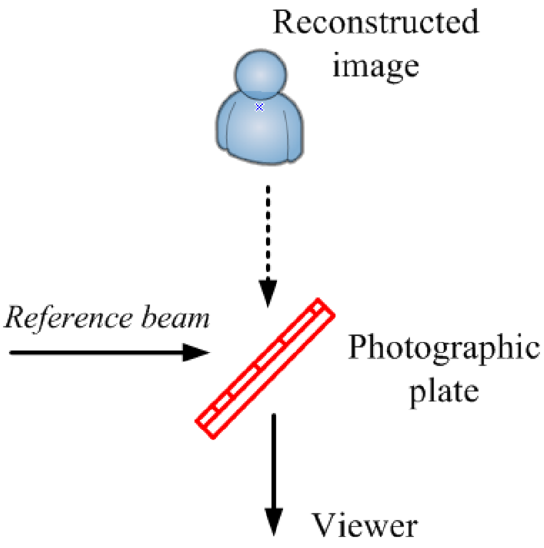
Reconstructed image
Reference beam
Photographic plate
Viewer

Figure 2-2 Reconstructing the image from the hologram in optical holography.

The hologram, after processing, is illuminated with the same reference wave from the laser. Light diffracted by the hologram appears to illuminate from the original object. To an observer, the reconstructed wave is indistinguishable from the original object wave; the observer sees a three-dimensional image that exhibits all the normal effects of perspective and depth of focus that the object would exhibit if it were still there [10]. The image reconstruction is illustrated in Figure 2-2. What needs to be noted is that each small area on the hologram records the information of the whole object so the image can be reconstructed even with a fragment of the hologram.

2.1.2 Microwave holography

Similarly, microwave holographic imaging is based on the interference of two beams of electromagnetic waves in microwave band. In some early experiments, continuous detectors including liquid crystal films and Polaroid films are employed to record interfered waves. These films are illuminated and heated by waves. The colour changes following the temperature increment due to the illumination. Return waves from target interfere with the reference beam and amplitudes, and phases across films are recorded. Different strength levels of the illumination wave strength can result in different colour ripples on films. Although liquid crystal films and Polaroid films are proved feasible in experimental microwave holography, the detection threshold is relatively high to be about $10\ \mathrm{mW/cm^2}$. The low sensitivity of liquid crystal films and Polaroid films limits wide applications of microwave holography.

With the development of the microwave measurement technology, the amplitude and phase can be recorded electrically respectively in devices, such as PNA (Performance Network Analyzer) and saved in computers. The antenna array is one option for the fast data acquisition, but the disadvantage is apparently the high cost. Another option is the mechanic scanning using a single antenna, but the shortcoming is the long scanning time consumption because of the scanning delay. Considering the cost issue, the mechanical scanning is still preferred for practical applications.

Figure 2-3 demonstrates one example of the typical hologram recording schematic (raster scanning mono-static antenna). Two transceiver antennas can be moved in XOY plane where they are pointed to the direction of *zf* axis. Coherent back-scattered signals are acquired on the surface in a similar way to the conventional holography. A virtual data matrix can be formed with the scattered signals on the aperture plane. This data matrix here acts as the role of the hologram.

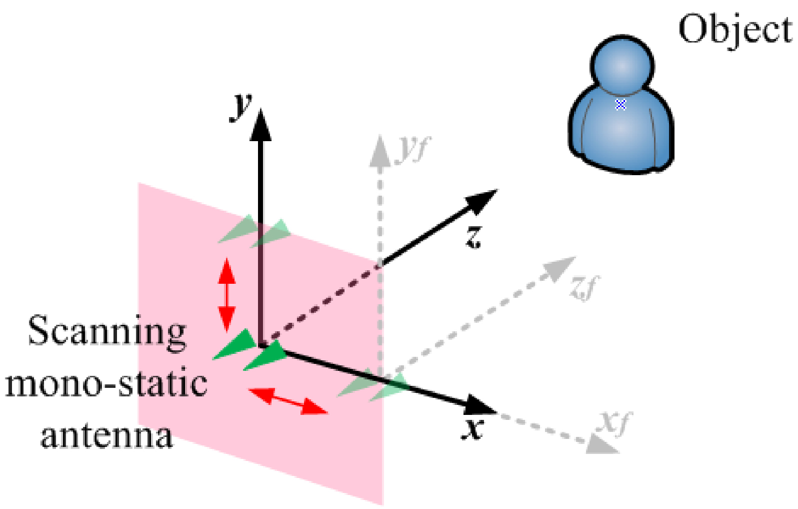

Figure 2-3 Recording a hologram in microwave holography.

Then a holographic processing algorithm is used to reconstruct the target image. Take the conventional Back Propagation (BP) as an example. The reconstruction of the target is based on a sequence of Fourier Transformation, multiplication and Inverse Fourier Transformation. The image reconstruction is completed in the computer digitally as shown in Figure 2-4.

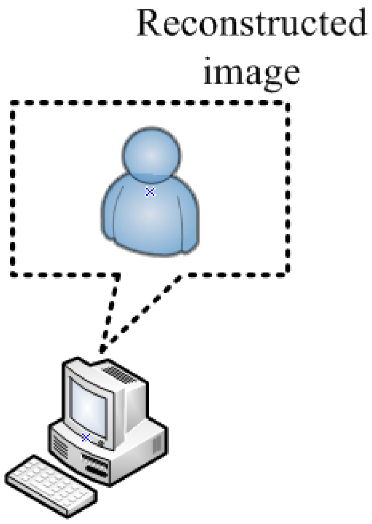
Reconstructed image

Figure 2-4 Reconstructing the image from the hologram in microwave holography.

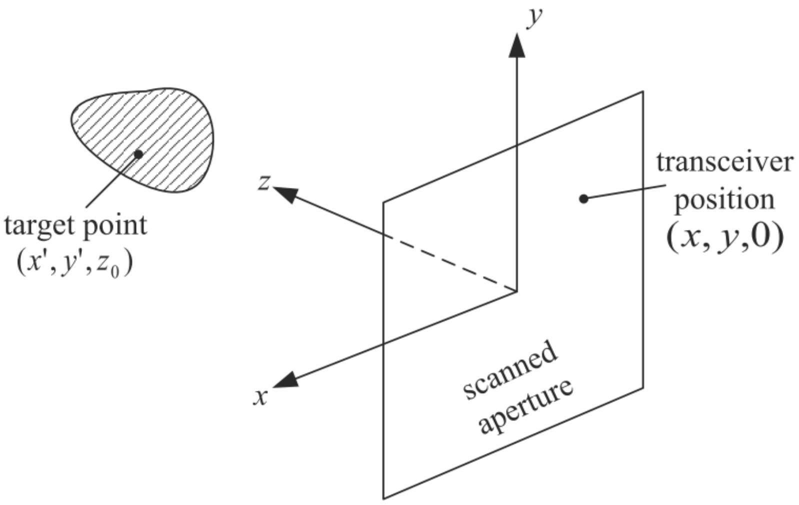
y
z
x
target point
(x', y', z_0)
transceiver position
$(x, y, 0)$
scanned aperture

Figure 2-5 Holographic imaging system configuration.

The main principle of the reconstruction is the wave transformation in the space-frequency domain (k-domain). The illuminating and scattered waves are regarded as the accumulation of plane waves with different propagation directions. Applying the Fourier Transformation, waves are transformed into k-domain. Each kx-ky-kz pair corresponds to one plane wave with the specific propagation orientation where the propagation vector is determined by values of k_x, k_y and k_z. In the back propagation process, all the decomposed plane waves are backpropagated in the $(0,0,k_z)$ direction with a distance z_0 by multiplying an exponent part. Finally, these backpropagated plane waves are accumulated to reconstructed waves with an Inverse Fourier Transformation. Here the configuration shown in Figure 2-5 is under consideration. The source is assumed to be at position $(x, y, 0)$, and a general point on the target is assumed to be at position (x', y', z_0). The target is assumed to be characterized by a reflectivity function $f(x', y', z')$, which is simply the ratio of reflected field to incident field [2-4]. The reconstruction algorithm is summarized by

$$f(x, y) = FT_{2D}^{-1}\left[FT_{2D}[s(x, y)]e^{-j\sqrt{4k^2-k_x^2-k_y^2}z_0}\right] \quad (2\text{-}1)$$

where k_x and k_y are the Fourier transform variables corresponding to x and y, respectively. FT_{2D} indicates 2-D Fourier transformation. It has to be noted again that, in the microwave holography, both of the amplitude and phase information are included in the signal collection and reconstruction. Details of the derivation can be found in Ref. [2]. Fundamental relationships in discrete situation are illustrated in Ref. [5].

2.2 Proposed beam scanning scheme

As introduced in the previous chapter, a wide range of imaging systems have been developed in millimetre wave band and THz band. However, some common features have limited their development, such as the raster scanning method and the amplitude only imaging. Raster scanning approach is simple to be achieved in both design and fabrication, but needs long scanning time [4]. Large scanning area for the transmitter and receiver is needed to image a target. When it comes to the amplitude based imaging, the image quality cannot meet the requirement of high resolution (mm-scale) detection in security applications. By utilising both amplitude and phase information of the scattered signal in the holographic imaging, a much better image can be realised. Therefore, microwave holographic imaging can be scaled up into the terahertz band. At the same time, this project aims to adopt the angular beam scanning, instead of a raster scanning, in the THz holographic imaging system in order to reduce the imaging time.

The difference between the raster scanning scheme and the proposed scanning scheme can be shown in Figure 2-6. Field of View (FoV) of transceivers limits the detected target size because the signal scattered outside of FoV would fall below the detection threshold. When the centre of transceivers is oriented to a point on the target plane, the covered area can be approximately presented as the small spot around this point illustrated in Figure 2-6 (a). For the raster scanning scheme, FoV of transceivers can cover the target area by moving in x-direction and y-direction. At each sampling point, transceivers will record the scattered signal as the information of the detected area showed as the solid part in Figure 2-6 (a). After the scanning of the whole target area, signals received are put into a virtual matrix correspondingly to build the image of the target. In our proposed beam scanning scheme, the target area has also been covered by FoV of transceivers and transceivers are pointed to sampling points to record scattered signals. But instead of moving transceivers, antennas are rotated to realise the similar function of the raster scanning as shown as the solid part in Figure 2-6 (b). To remain the stability of transceivers, some optical components can be added to complete the beam rotation rather than the rotation of transceivers.

2.3 Proposed beam scanning THz holography imaging system

The framework of the proposed beam scanning THz holography imaging system is shown in Figure 2.7. The system mainly consists of the scanning module, the controlling module and the processing module. Schematic of the scanning part can be found in Figure 2-8. The transverse scanning will be realized by rotating the main reflector, while the longitudinal scanning is realized by rotating the whole scanning module. Figure 2-9 shows the detailed structure of the beam scanning part. Three reflectors can be adopted in this scheme to reduce the size. The main reflector and the flat mirror can be rotated to achieve the beam steering.

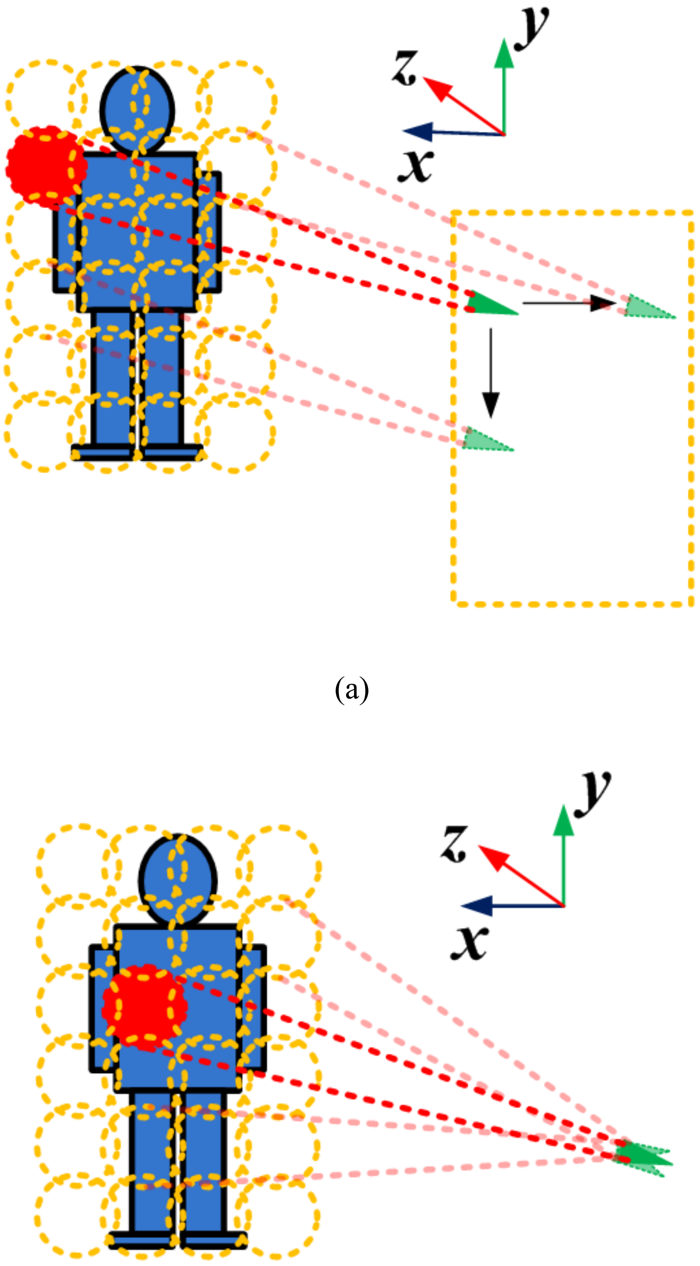

(a)

(b)

Figure 2-6 Configurations of two different scanning schemes

(a) Raster scanning scheme (b) Proposed beam scanning scheme.

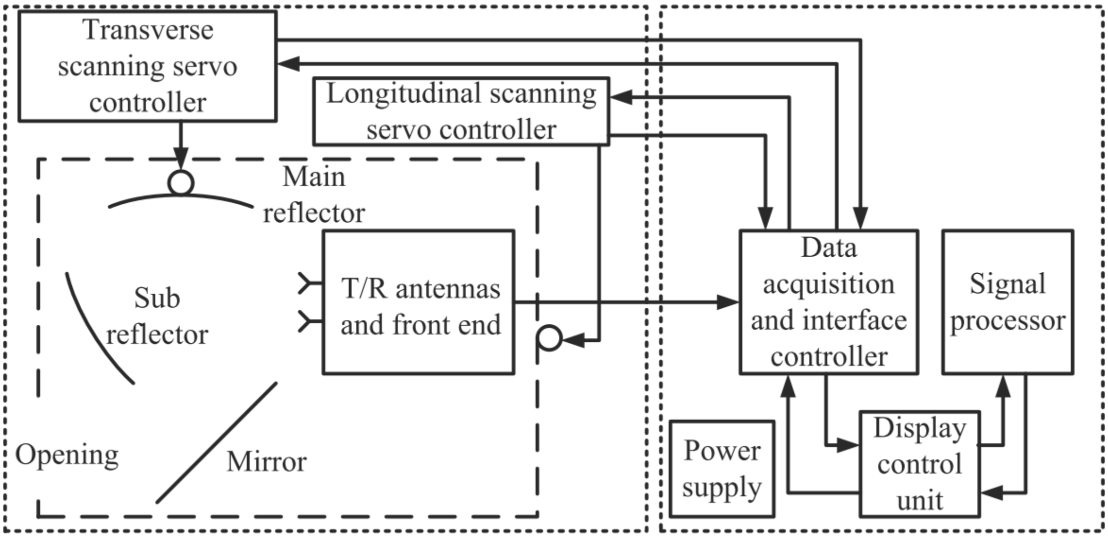
Transverse scanning servo controller
Longitudinal scanning servo controller
Main reflector
Sub reflector
T/R antennas and front end
Opening
Mirror
Data acquisition and interface controller
Signal processor
Power supply
Display control unit

Figure 2-7 Framework of the proposed beam scanning THz holography imaging system.

The scanning trajectory is illustrated in Figure 2-10. This zigzag path can be realised by combining the transverse scanning and the longitudinal scanning. For the transverse scanning, the beam spot will be moved from one side to the other side and then it will be turned to the reverse scanning direction. When it comes to the longitudinal scanning, the beam spot will be moved in one direction for single frame imaging while for the multi frame imaging, the beam spot will be conducted in a back and forth motion. Let us assume that the whole scanning time for single frame is T_{total} the side length of the scanning area is L and the number of sampling points is $N \times N$, then the longitudinal scanning speed will be L/T_{total} and the transverse scanning speed is $L/T_{total}/N$. In the selection of motors for the scanning and the structure design, the rotation speed of the transverse scanning has to be quite fast.

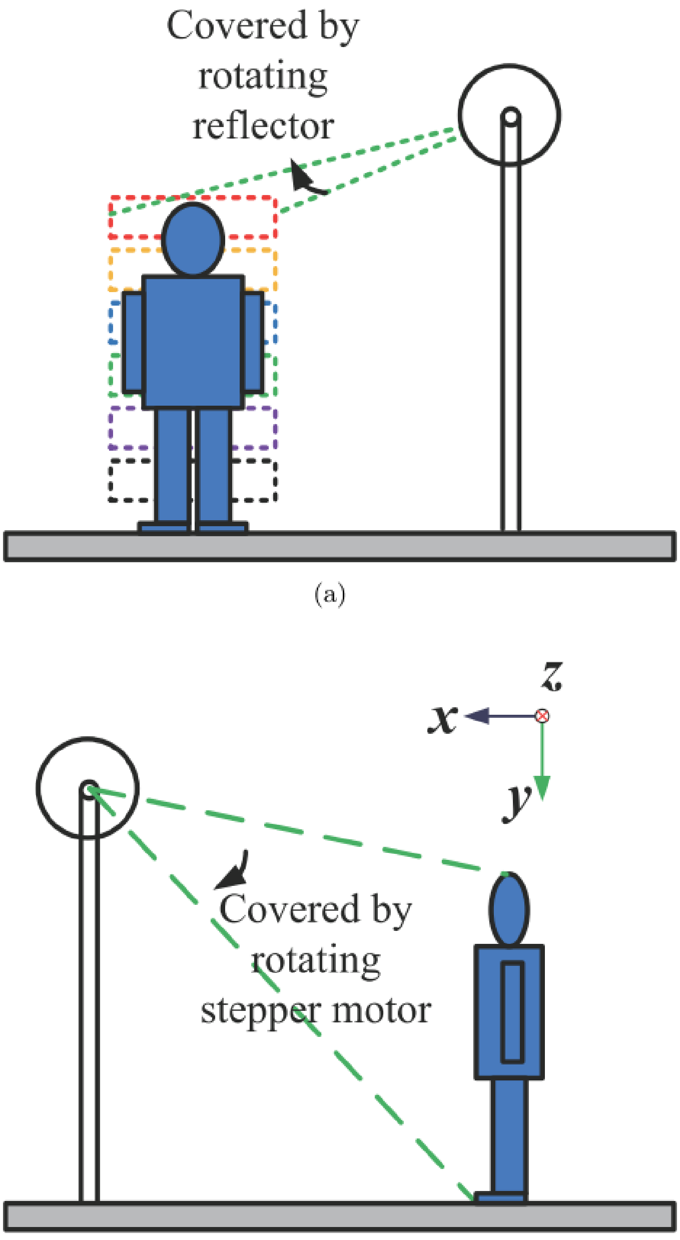
Covered by rotating reflector
z
x
y
Covered by rotating stepper motor

(a)

(b)

Figure 2-8 Schematic of the proposed beam scanning scheme in the imaging system (a) Transverse scanning (b) Longitudinal scanning.

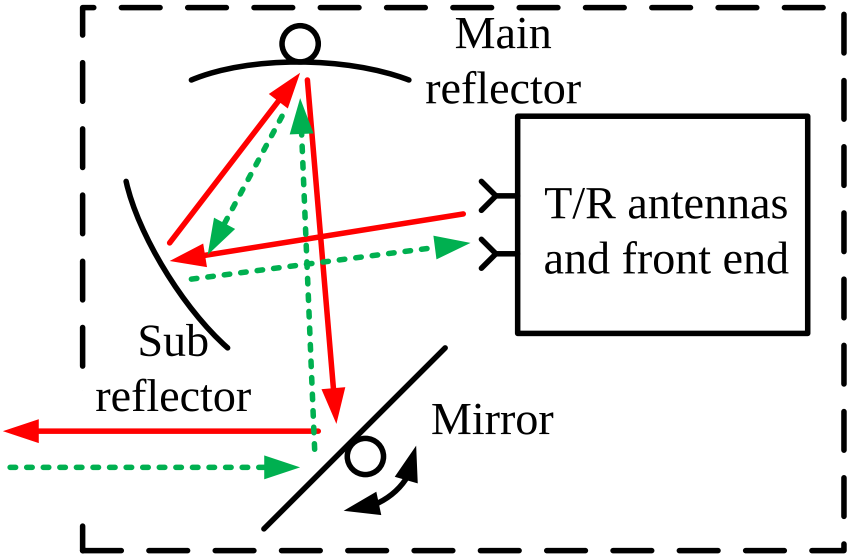
Main
reflector
T/R antennas
and front end
Sub
reflector
Mirror

Figure 2-9 Structure of the beam scanning part of the proposed beam scanning THz holography imaging system (red solid arrows show the transmitting beam and green dashed arrows show the receiving beam).

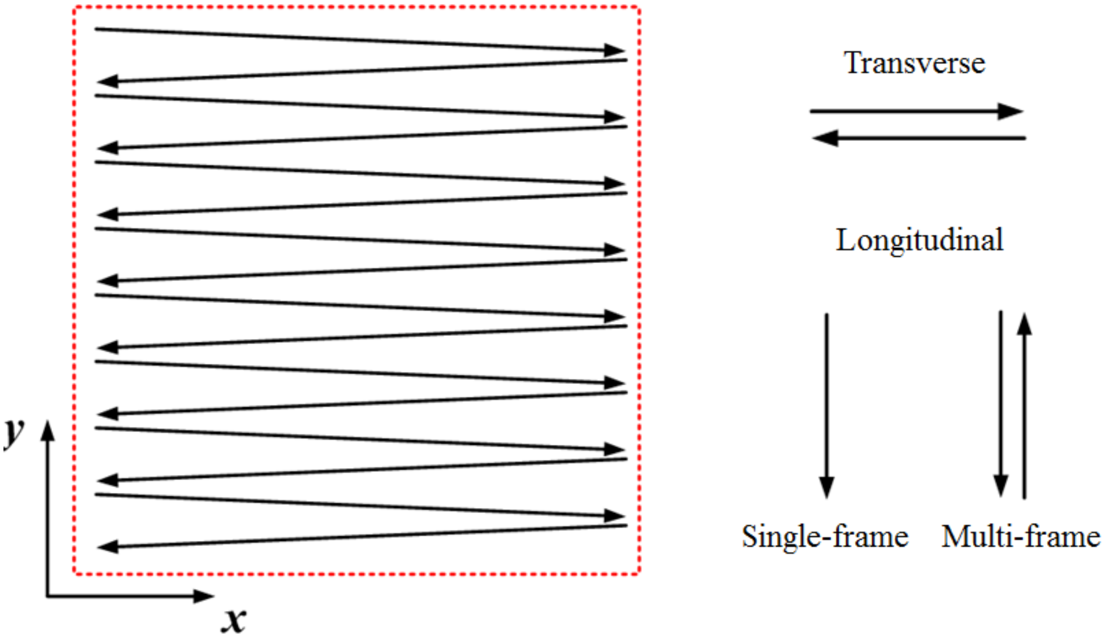
Transverse
Longitudinal
Single-frame
Multi-frame
y
x

Figure 2-10 Scanning trajectory of the proposed system.

Consider the goal set in Chapter 1, the imaging system needs to complete the scanning on the area of 0.8 m*0.8 m in 2 seconds. Here 80*80 points are sampled in the scanning area. To cover the scanning area, the main reflector will be rotated in the angle range of -4.33 degrees to 4.33 degrees and the flat mirror is rotated in the angle range of -3.8 degrees and 3.8 degrees (these angle values can be found in Chapter 3 below). Then rotation speeds will be 1.443 rpm (round per minute)/ 0.02405 rps (round per second) for the main reflector and 101.333 rpm/1.689 rps for the flat mirror, respectively. The rotation steps for the main reflector and the flat mirror are 0.108 degrees and 0.095 degrees.

It has to be noted that these parameters are calculated on the mechanical structure that the main reflector and the flat mirror are driven directly by the motor spindles. From calculated results above, the flat mirror motor will rotate at a relatively high speed compared with the main reflector motor and many back and forth motions will be repeated frequently. In order to ensure the stability, maintain the efficiency and prolong the service life, the high-speed motor will drive the flat mirror via the crank-rocker structure as shown in Figure 2-11. The motor spindle is fixed at the point A and the rotation axis of the flat mirror is fixed at the point D. When the motor at point A rotates continuously in the path of the black dashed circle shown in Figure 2-11, the flat mirror located at point D can be rotated in the angle range shown as the red dashed area. Lengths of poles, a, b, c and d - the distance between point A and D are set as 11.13 mm, 440.57 mm, 185 mm and 400 mm, respectively. The rotation speed of the flat mirror motor will be changed to 2400 rpm/40rps.

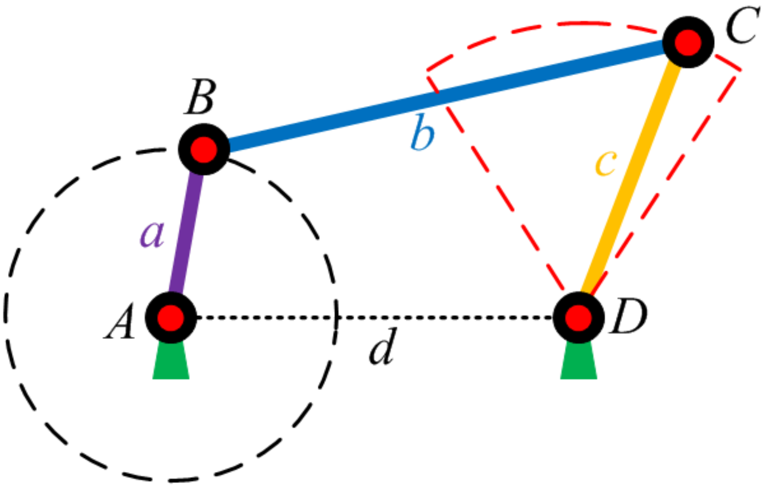

Figure 2-11 Crank-rocker structure.

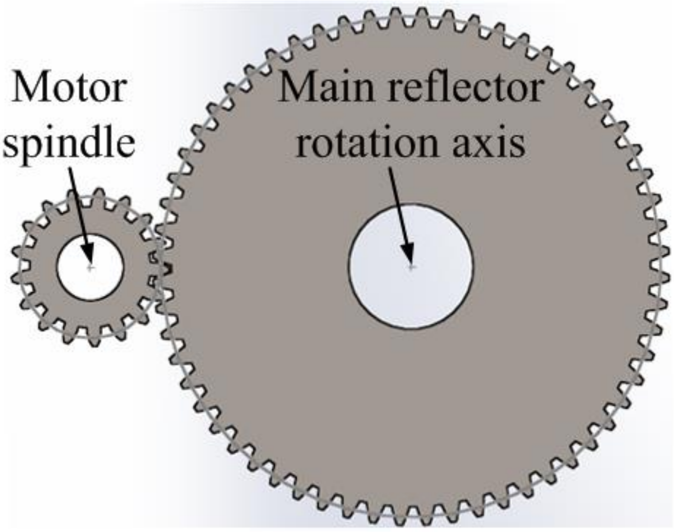

Figure 2-12 Dual-gear driven structure for the main reflector rotation.

The rotation of the main reflector is driven by a dual-gear driven structure (demonstrated as Figure 2-12) instead of being driven by the motor spindle to avoid the heavy main reflector affecting the normal operating condition of the motor. The small gear will be driven by the motor while the large gear will drive the main reflector rotation axis. The gear module is selected to be 2 for both of gears. Numbers of gear teeth for the active gear (small) and the slave gear (large) are set to be 17 and 60, respectively. The rotation speed of the main reflector motor will be changed to 5 rpm/0.083 rps.

The scanning path and the required scanning points with parameters calculated above can be simulated in Matlab as illustrated in Figure 2-13. But the final scanning points will be determined by switches. Analysed in Figure 2-13 (b), the maximum space between points is about 0.0168 m. Compared with the scanning path of imaging systems developed by other groups reviewed in Chapter 1, advantages of the scanning path in this proposed scanning sub-system include more uniform points, easier controlling and more efficient scanning.

The required power of the main reflector motor and the flat mirror motor are 0.076 W and 1.666 W. The torque of the main reflector motor and the flat mirror motor are 0.431Nm and 6.63 Nm.

Figure 2-16 gives the scanning sub-system model drawn in Solidworks.

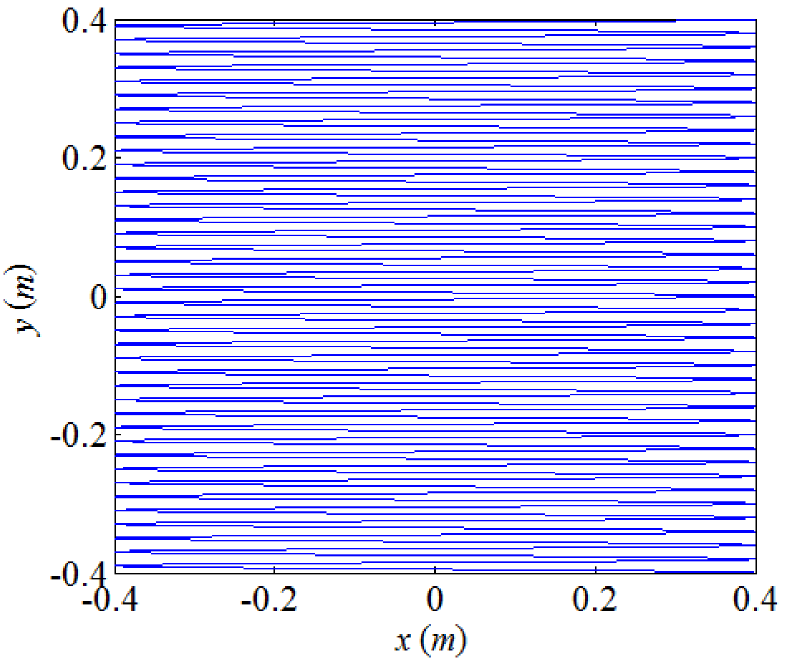

(a)

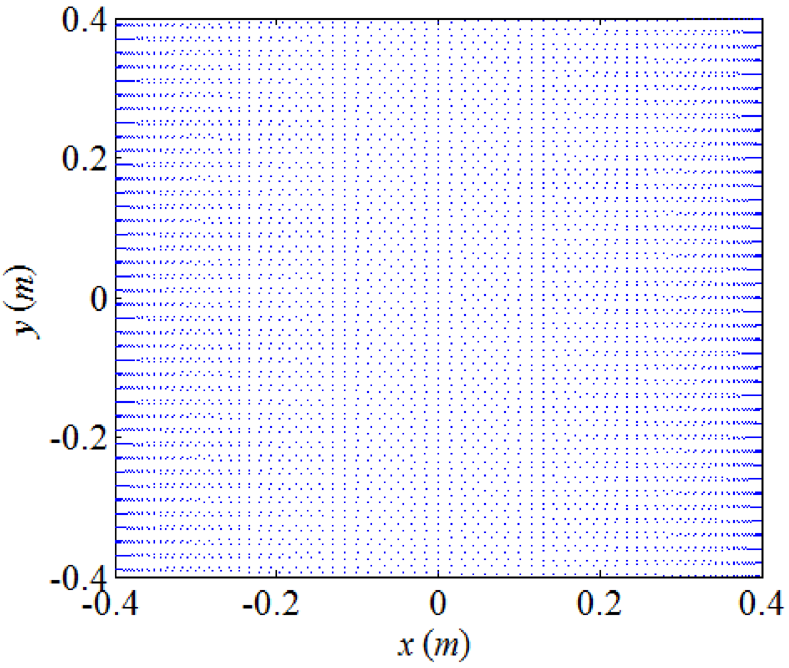

(b)

Figure 2-13 Calculated (a) Scanning path and (b) Scanning points with the crank-rocker structure and the dual-gear driven structure in Matlab.

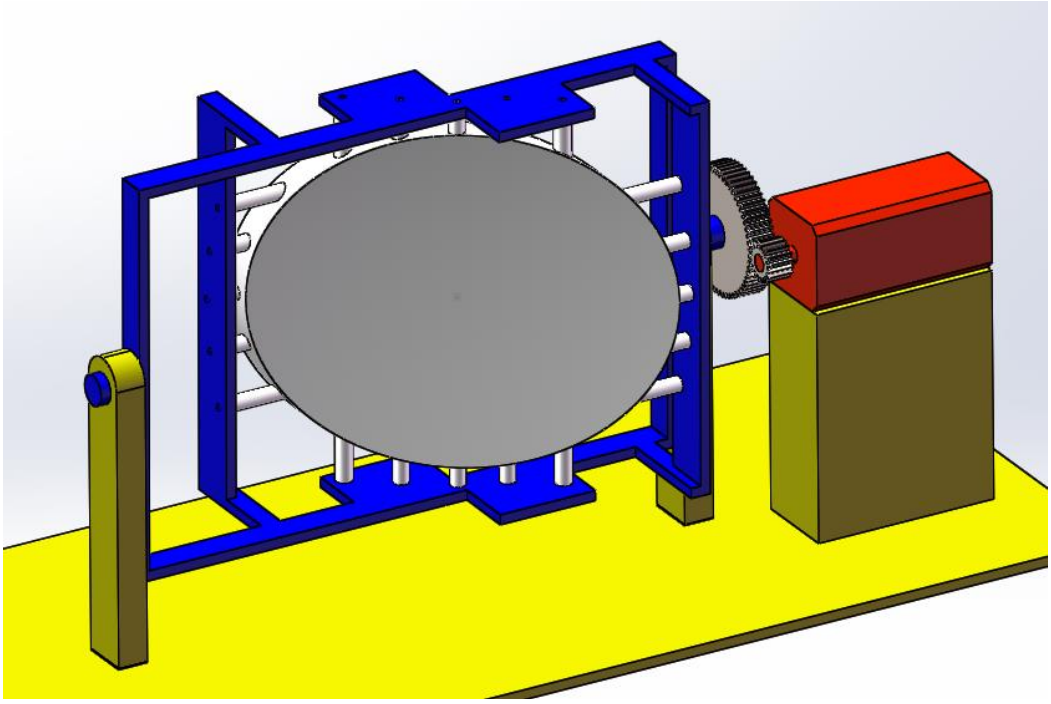

Figure 2-14 The rotated main reflector model with dual-gear and the servo motor in Solidworks.

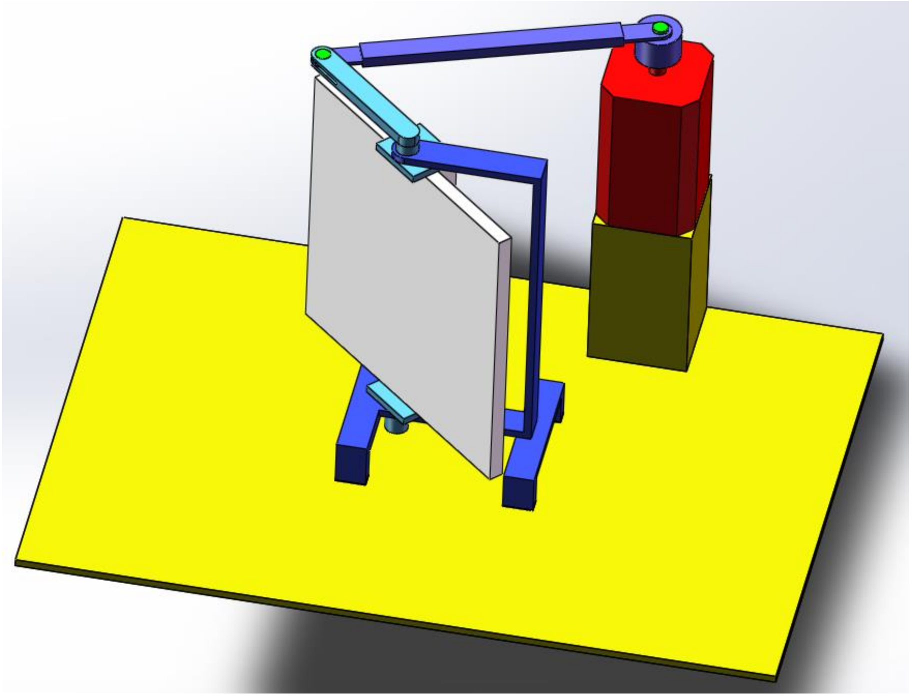

Figure 2-15 The rotated flat mirror model with crank rocker and the servo motor in Solidworks.

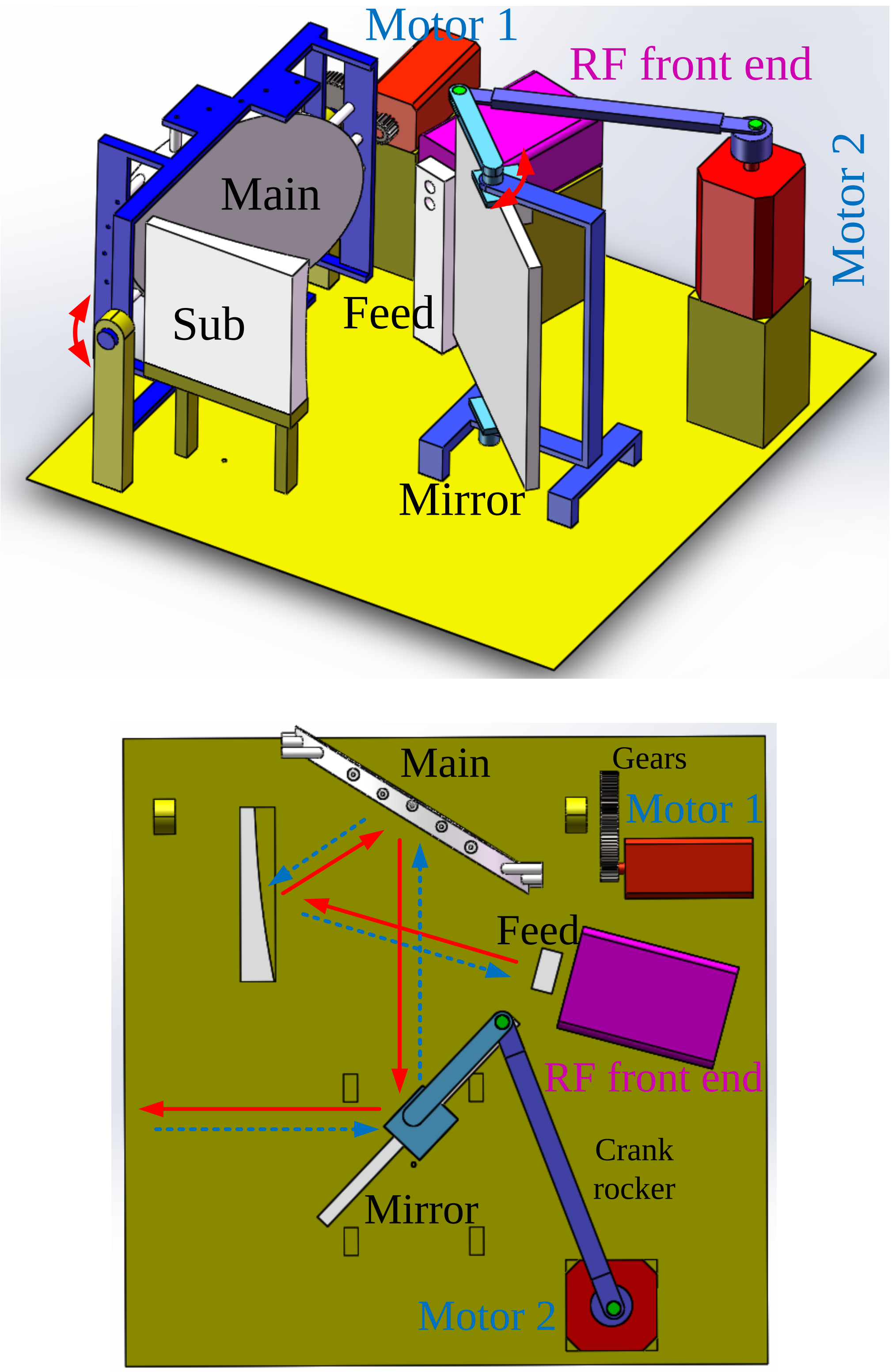
Motor 1
RF front end
Motor 2
Main
Sub
Feed
Mirror
Main
Gears
Motor 1
Feed
RF front end
Crank
rocker
Mirror
Motor 2

Figure 2-16 The scanning sub-system model in Solidworks. Some structures in lower figure have been hidden for better observation (red solid arrows show the transmitting beam and green dashed arrows show the receiving beam).

2.4 Summary

This chapter has introduced the theory of holography imaging. Based on the optical holography, the microwave holography follows the similar principle and becomes more convenient to be implemented by employing new measurement technology. To resolve the dilemma between the time consumption and the system complexity, we have proposed a new scanning scheme for the THz holography system. Mechanical components are designed carefully to meet the scanning trajectory and assembling requirements. The investigation into the proposed imaging system will be presented in the following chapters.

2.5 References

[1] P. Hariharan. Optical Holography: Principles, techniques and applications. Cambridge University Press, 1996.

[2] D. M. Sheen, D. L. McMakin, and T. E. Hall. Three-dimensional millimetre-wave imaging for concealed weapon detection, IEEE Transactions on Microwave Theory and Techniques, vol. 49, no. 9, pp. 1581–1592, 2001.

[3] E. B. Joy and D. Paris. Spatial sampling and filtering in near-field measurements, IEEE Transactions on Antennas and Propagation, vol. 20, no. 3, pp. 253–261, 1972.

[4] J. J. H. Wang. An examination of the theory and practices of planar near-field measurement, IEEE Transactions on Antennas and Propagation, vol. 36, no. 6, pp. 746-753, 1988.

[5] E. B. Joy, D. Paris. Spatial sampling and filtering in near-field measurements, IEEE Transactions on Antennas and Propagation, vol. 20, no. 3, pp. 253-261, 1972.

[6] S. Gu, C. Li, X. Gao, Z. Sun, and G. Fang. Terahertz aperture synthesized imaging with fan-beam scanning for personnel screening, IEEE transactions on Microwave Theory and Techniques, vol. 60, no. 12, pp. 3877–3885, 2012.

[7] D. M. Sheen, D. McMakin, and T. Hall. Near-field three-dimensional radar imaging techniques and applications, Applied Optics, vol. 49, no. 19, pp. E83–E93, 2010.

[8] D. M. Sheen and T. E. Hall. Reconstruction techniques for sparse multistatic linear array microwave imaging, SPIE Defense+ Security. International Society for Optics and Photonics, Conference Proceedings, pp. 90 780I, 2014.

[9] C. Granet. Designing classical dragonian offset dual-reflector antennas from combinations of prescribed geometric parameters, IEEE Antennas and Propagation Magazine, vol. 43, no. 6, pp. 100–107, 2001.

[10] S. Chang and A. Prata. The design of classical offset dragonian reflector antennas with circular apertures, IEEE Transactions on Antennas and Propagation, vol. 52, no. 1, pp. 12–19, 2004.

[11] N. Llombart, K. B. Cooper, R. J. Dengler, T. Bryllert, and P. H. Siegel. Confocal ellipsoidal reflector system for a mechanically scanned active terahertz imager, IEEE Transactions on Antennas and Propagation, vol. 58, no. 6, pp. 1834–1841, 2010.

.

Chapter 3. Design of Dragonian dual-reflector scanning sub-system

In order to develop a proposed terahertz holography imaging system working at 220 GHz for CWD application based on the holography algorithm introduced in Chapter 2, a beam scanning sub-system needs to be studied and developed. In this chapter, some typical multi-reflector systems are introduced at first. Then the Dragonian dual-reflector configuration is selected as the scanning sub-system. Parameters of the designed Dragonian dual-reflector sub-system are calculated and optimised using Granet's principles.

3.1 Review of reflector antennas

Reflector antennas have been widely applied in radars, remote sensing, radio astronomy, satellite communications, tracking and microwave communications. Reflector antennas have many advantages, such as high gain (normally larger than 30-40 dB), low cross-polarization, etc. The simplest reflector antenna consists of one reflector (normally it is paraboloidal) and a feed antenna (for better performance, horn antennas are used). The feed antenna is placed at the focal point of the shape of the reflector (as shown in Figure 3-1 and Figure 3-2). The output beam of the reflector can be controlled by selecting different kinds of shape of the reflector. For the typical paraboloidal reflector antenna, the phase of the output beam will be consistent on the transverse plane (Figure 3-2 (a)). While for the ellipsoidal reflector, the output beam of the reflector will be focused at another focal point of the ellipsoid (Figure 3-2 (b)). In order to remove the blocking effect of feeds located in front of reflectors, off-axis configurations can be adopted (Figure 3-2).

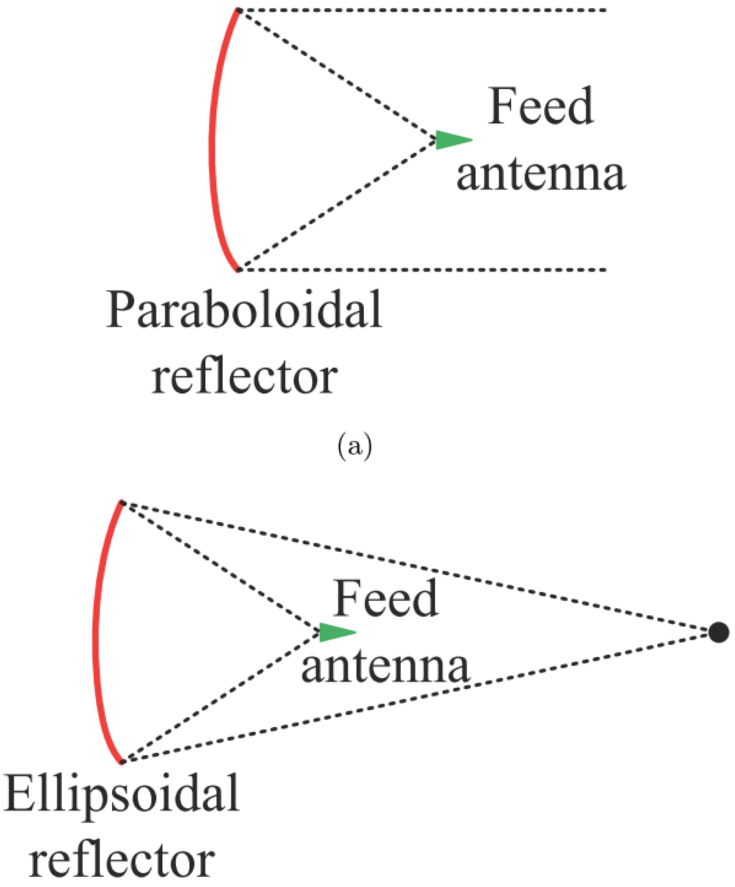
Feed
antenna
Paraboloidal
reflector
Feed
antenna
Ellipsoidal
reflector

(a)

(b)

Figure 3-1 Configurations of reflector antennas (a) Paraboloidal reflector antenna (b) Ellipsoidal reflector antenna.

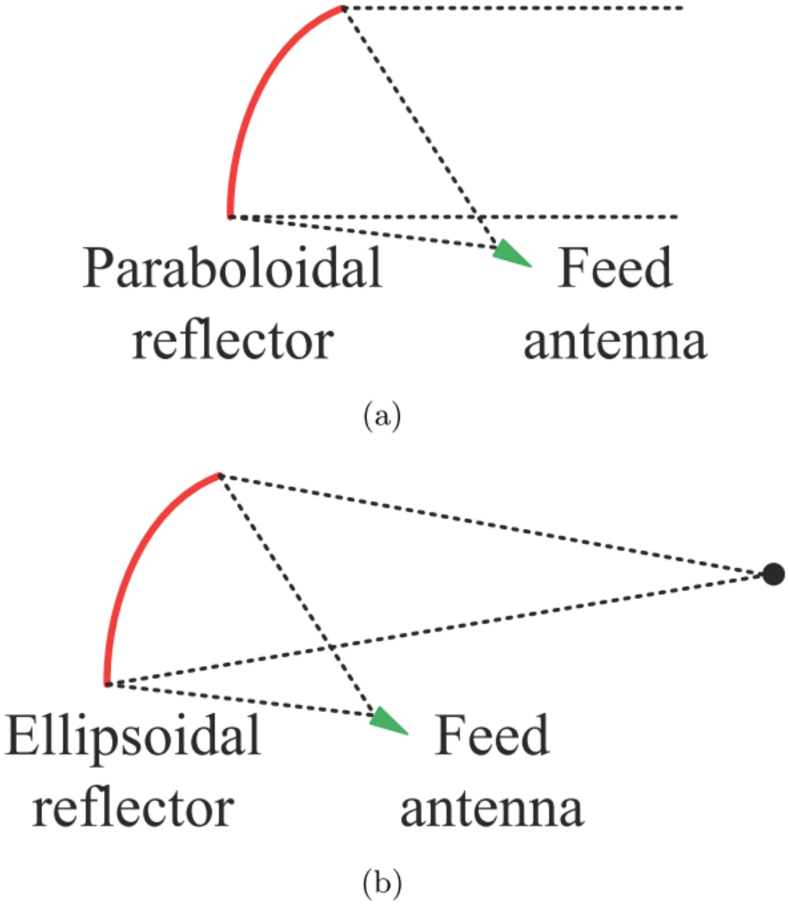

Figure 3-2 Configurations of off-axis reflector antennas (a) Off-axis paraboloidal reflector antenna (b) Off-axis ellipsoidal reflector antenna.

Compared with the single reflector antenna, the dual-reflector or multi-reflector antenna can achieve comparatively compact size with larger Focal Length to Diameter (F/D) ratio. There are several common dual-reflector systems: Newton system, Cassegrain system, Gregorian system and Dragonian system, etc. Newton system consists of one paraboloidal main reflector and one flat mirror (which is shown in Figure 3-3 (a)). Cassegrain system consists of one paraboloidal main reflector and one hyperboloidal secondary reflector as shown in Figure 3-3 (b). Gregorian system consists of one paraboloidal main reflector and one ellipsoidal secondary reflector as shown in Figure 3-3 (c). Dragonian system consists of one paraboloidal main reflector and one hyperboloidal secondary reflector as shown in Figure 3-3 (d). The difference between off-axis Cassegrain system and Dragonian system lies in the hyperboloidal secondary reflector. The secondary reflector in the Cassegrain system is convex while the one in the Dragonian system is concave. Feed antennas in these different systems are located at different focal points of the hyperboloid [1, 2].

Among dual-reflector antenna systems, Dragonian is the system that allows the largest field of view (FoV) due to its small magnification. This characteristic means Dragonian system can scan a wider area when the main reflector is rotated. Or the scan loss of the Dragonian system can be lower than other systems scanning in the same area.

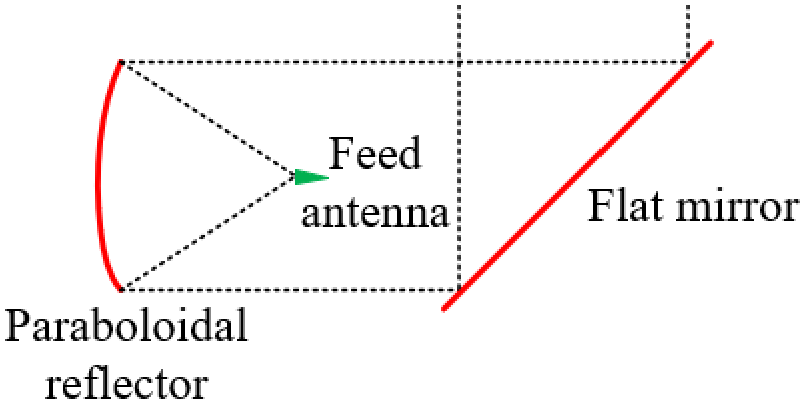
Feed
antenna
Flat mirror
Paraboloidal
reflector

(a)

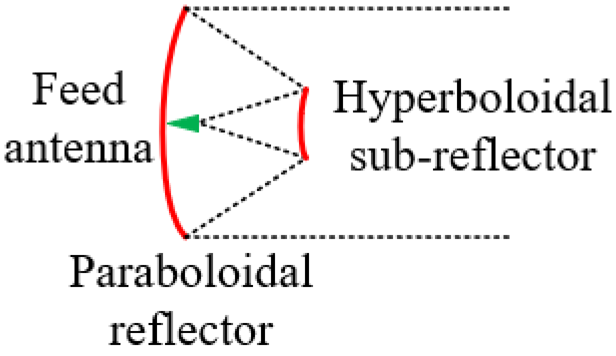
Feed
antenna
Hyperboloidal
sub-reflector
Paraboloidal
reflector

(b)

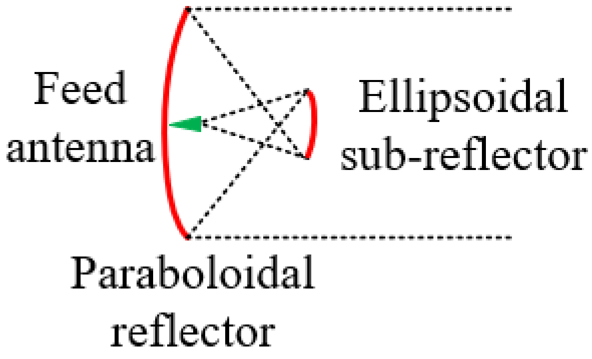
Feed
antenna
Ellipsoidal
sub-reflector
Paraboloidal
reflector

(c)

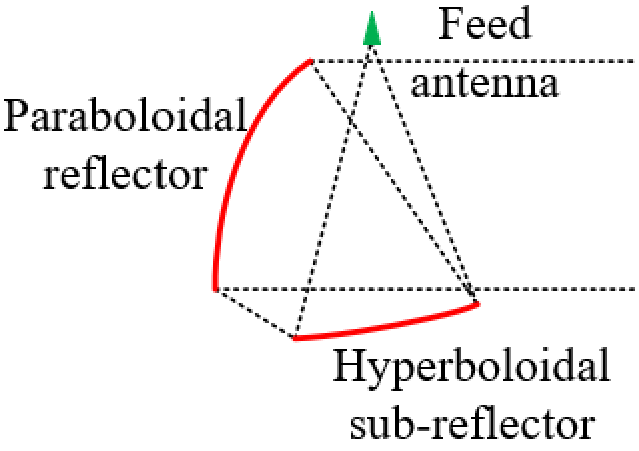
Feed
antenna
Paraboloidal
reflector
Hyperboloidal
sub-reflector

(d)

Figure 3-3 Configurations of dual-reflector antennas (a) Newton reflector antenna (b) Cassegrain reflector antenna (c) Gregorian reflector antenna (d) Dragonian reflector antenna.

3.2 Dragonian antenna sub-system design

The Dragonian antenna sub-system consists of three parts: the feed, the main reflector and the secondary reflector. The main reflector is a paraboloid while the secondary reflector is a hyperboloid. The feed is located at one focus of the concave hyperboloidal secondary reflector. The paraboloidal main reflector shares the other focus of the hyperboloidal secondary reflector. When the feed illuminates the hyperboloidal secondary reflector at the focus, the output ray of the secondary reflector can be regarded as illuminated from the shared focus. In view of Geometrical Physics (GO), the output field will approximately be the quasi plane wave [3].

In the design here, the main paraboloidal reflector is replaced by an ellipsoidal reflector to realise a secondary focus point on the target plane as shown in Figure 3-4. d is the distance between the centre point of the main reflector. When rotating the main reflector, the beam spot will move on the target plane which contributes to the field of view (FoV) of the scanning system. The enlarged lower figure shows more details of the designed Dragonian antenna here.

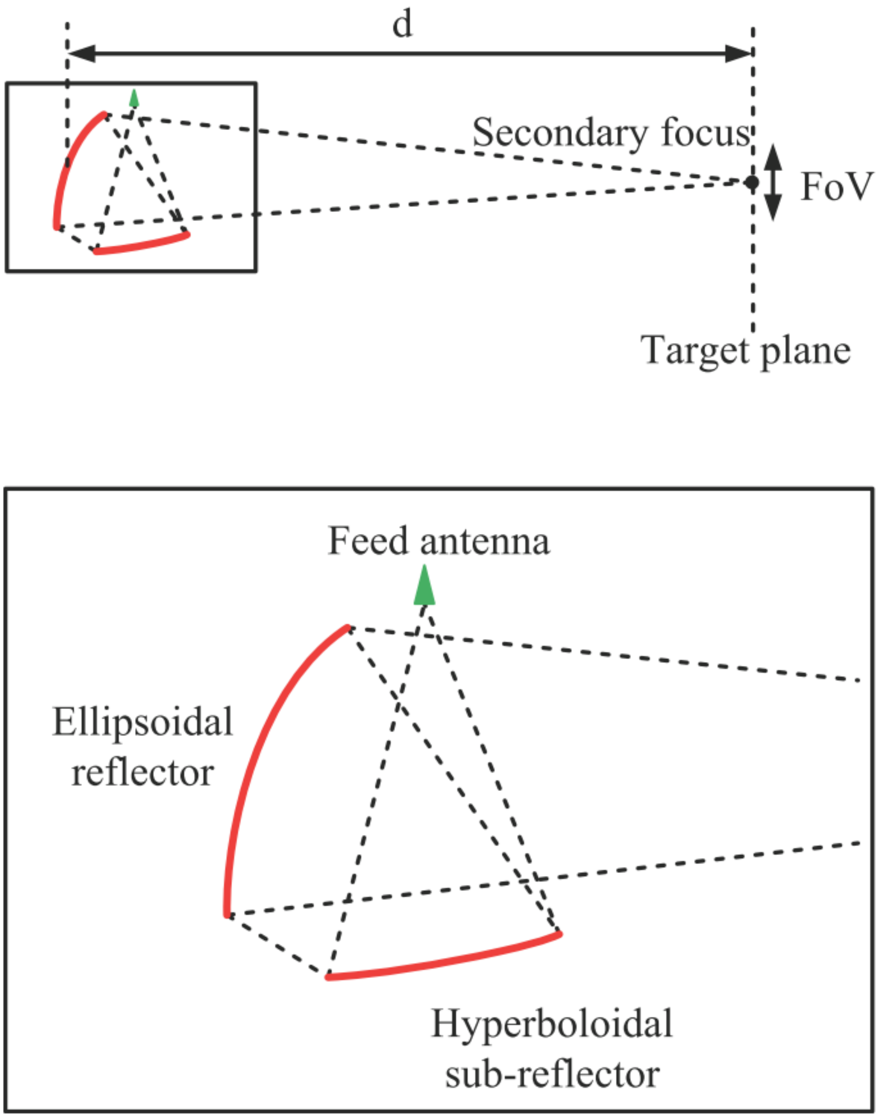
d
Secondary focus
FoV
Target plane
Feed antenna
Ellipsoidal reflector
Hyperboloidal sub-reflector

Figure 3-4 Configuration of Dragonian antenna with the ellipsoidal main

reflector.

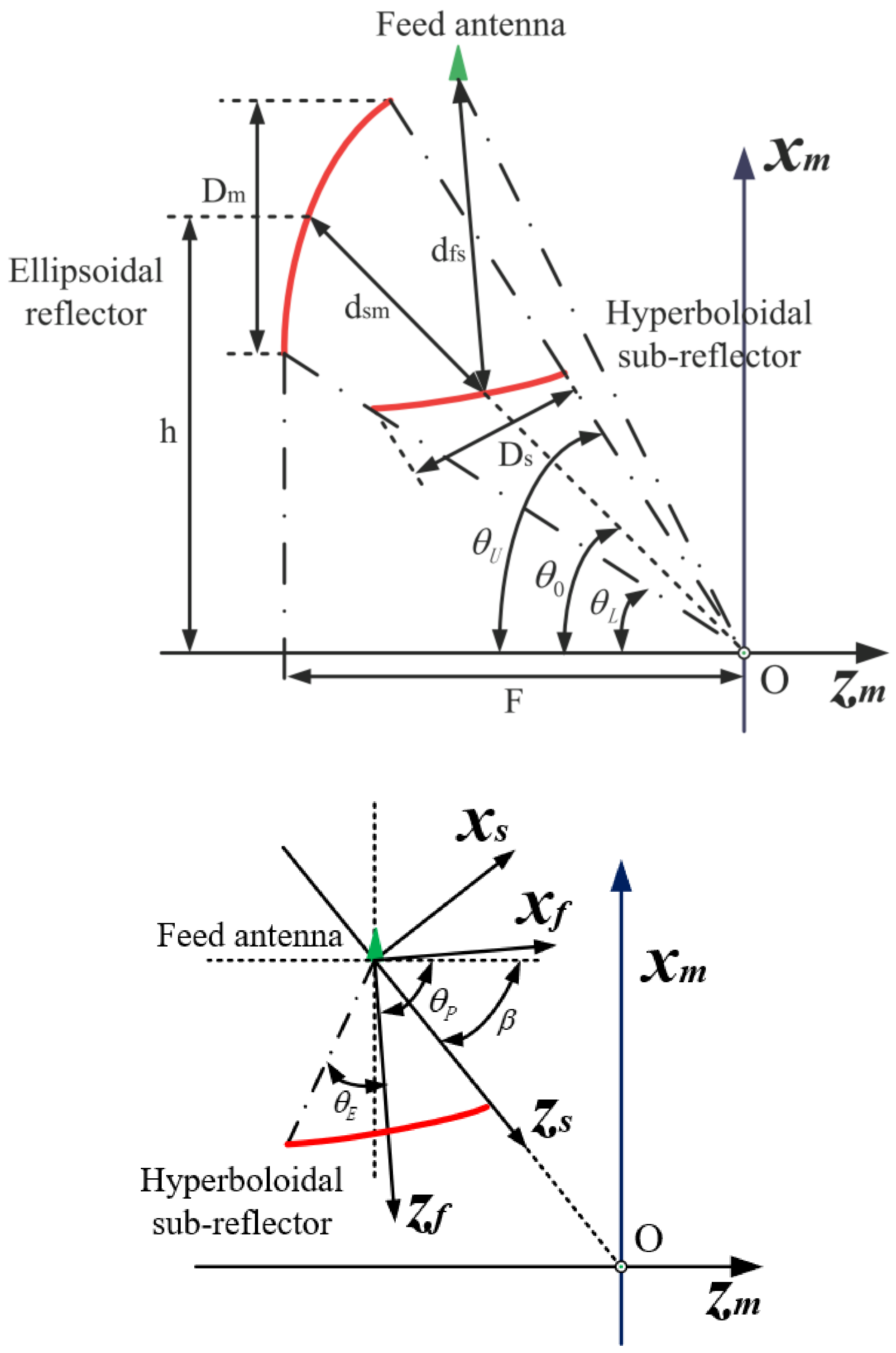
Feed antenna
Dm
Ellipsoidal reflector
dfs
dsm
Hyperboloidal sub-reflector
h
Ds
x_m
θ_U
θ_0
θ_L
O
z_m
F
x_s
x_f
Feed antenna
θ_P
β
θ_E
z_s
x_m
Hyperboloidal sub-reflector
z_f
O
z_m

Figure 3-5 The geometry of the Dragonian system and parameters.

The configuration of Dragonian system is demonstrated in Figure 3-5. D_m is the diameter of the main reflector when projected on the x-y plane. F_m is the focal length of the main reflector. h is the off-axis distance of the main reflector. θ_0 is the off-axis angle of the main reflector. θ_U is the off-axis angle of the top of the main reflector. θ_L is the off-axis angle of the bottom of the main reflector. F is the focal length of the main reflector. β is the tilt angle between the secondary reflector coordinate system z_s axis and the main reflector coordinate system z_m axis. a and b are surface parameters of the hyperboloid. θ_P is the tilt angle between the main reflector coordinate system z_m axis and the feed coordinate system z_f axis. θ_E is the angle between the feed coordinate system z_f axis and the edge of the secondary reflector. d_{sm} is the distance between the centre point of the main reflector and the secondary reflector. d_{fs} is the distance between the centre point of the secondary reflector and the feed [4, 5].

In the design of Dragonian system here, D_m, F, θ_E, d_{sm} and θ_P are selected as initial parameters. Other parameters can be calculated from these initial parameters [4, 5].

Figure 3-6 shows the schematic of the rotating Dragonian antenna. When the main reflector is rotated around the centre, the direction of the output beam will be pointed to different points on the target plane. By collecting different scattered signals from the scatter with corresponding different rotating angle value, a virtual data matrix covering the target area can be formed.

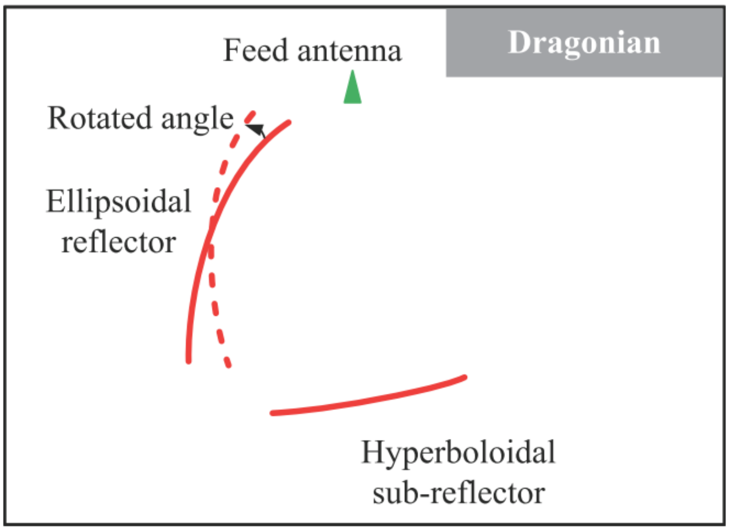

Figure 3-6 The schematic of the rotating Dragonian antenna.

After the trade off between the size of the designed antenna, the output beam width and the blockage problem of the feed on the main reflector aperture, initial parameters of the designed Dragonian antenna are confirmed as shown in Table 3-1. Following calculation procedure of other parameters, additional parameters of the Dragonian antenna can be adjusted as demonstrated in Table 3-2. Appendix I gives calculation relationships of these parameters.

3.2.1 Study of path length error

To investigate the propagation path of the proposed Dragonian antenna design, the ray path from the feed to a reference plane which is perpendicular to the output ray of a paraboloidal main reflector can be drawn in Matlab as shown in Figure 3-7. The paraboloidal main reflector and the hyperboloidal secondary reflector share the same focus at the origin of the main reflector coordinate. The secondary focus of the hyperboloidal reflector is located at the feed point shown as the other dark spot above the multi-reflector structure. The reference plane (shown as the red line in this figure) is set as parallel to the z_m axis. The output ray of the paraboloidal main reflector is perpendicular to the reference plane due to the characteristic of the paraboloid.

Table 3-1 Primary parameters of Dragonian antenna.

Parameter	***Value***
D_m	$0.333m$
F	$0.999m$
θ_E	18°
d_{sm}	$0.25m$
θ_P	-105°

Table 3-2 Other calculated parameters of Dragonian antenna.

Parameter	***Value***	***Parameter***	***Value***
β	-74°	θ_U	-70°
α	-30°	θ_L	-56°
e	2.11	d_{fs}	0.43m
θ_0	-63°	a	0.34m
h	1.23m	f	0.74m

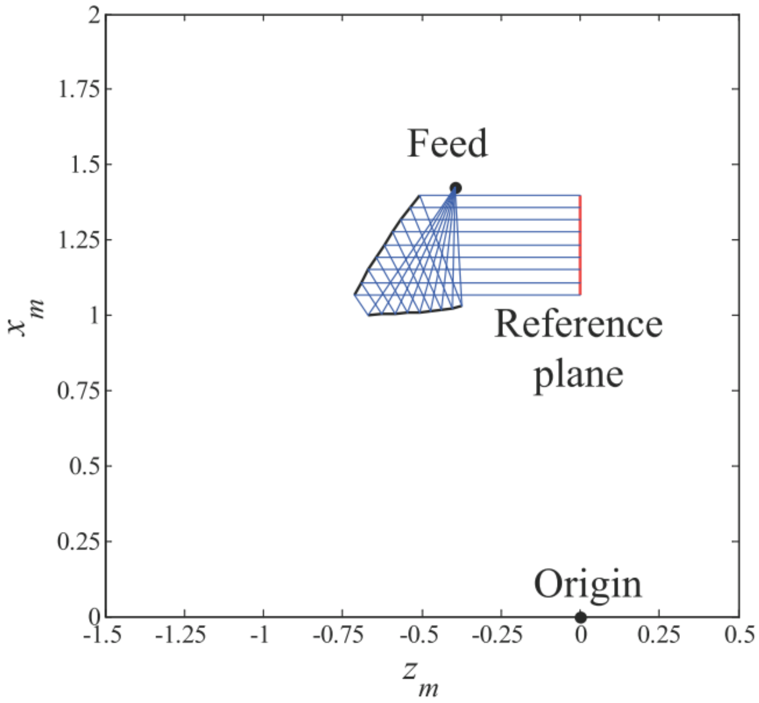

Figure 3-7 The designed Dragonian antenna simulated in Matlab.

Figure 3-8 shows the enlarged configuration of the designed Dragonian antenna. It can be observed that locations of the feed and reflectors have been optimized to realize a very compact size. The path length error (PLE) of the situation in Figure 3-8 has also been studied in Matlab. The beam is illuminated from the reference plane along the z_m axis of the main reflector coordinate. Points on the main aperture along x_m

axis are set as the x-axis and the path length error (ΔL) of nine sampling points on the aperture are compared with the central ray. The PLE value is always 0 along the aperture plane when the main reflector is illuminated exactly parallel to the axis of the paraboloid. The directed rays will finally be focused at the feed points. Observed results agree with the optical characteristics of the paraboloidal reflector and the hyperboloidal reflector.

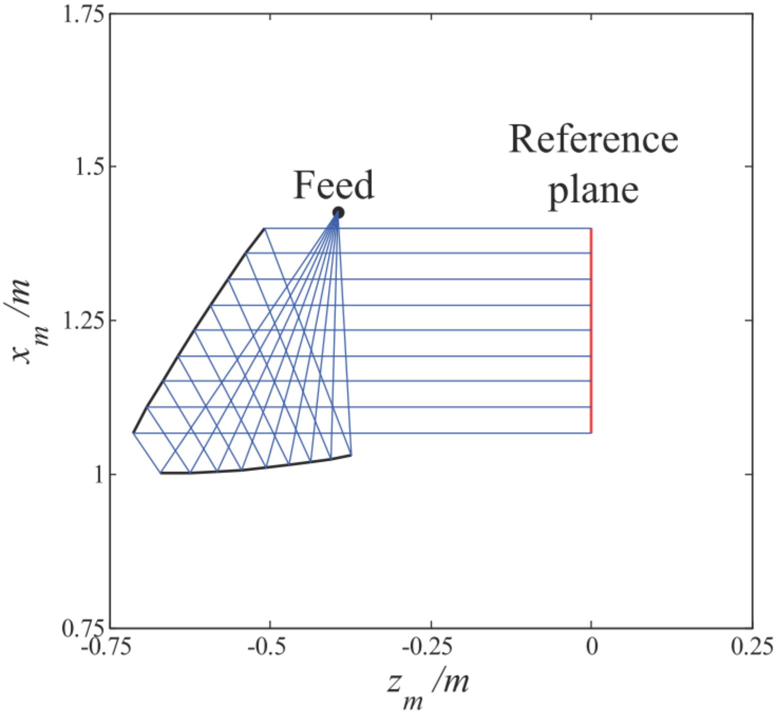

Figure 3-8 The ray path of the designed Dragonian antenna.

Figure 3-9 shows the enlarged configuration of the designed Dragonian antenna when the reference plane has been rotated 3° from the z_m axis. Locations of the feed and reflectors are same as the situation of the above one. The rays are also illuminated from the reference plane and perpendicular to the reference plane. The path length error (PLE) of the situation in Figure 3-9 has also been studied in Matlab [6, 7]. Figure 3-10 demonstrates the path length error information when rays are illuminated from the reference plane along the z_m axis of the main reflector coordinate. In this figure, points on the main aperture along $\mathrm{x_m}$ axis are also set as the x-axis and the path length error (ΔL) of nine sampling points on the aperture are given here compared with the central ray. From the path length error figure, it can be seen that the value varies along the aperture plane because the main reflector is not illuminated parallel to the axis of the paraboloid. This situation does not agree with the optical characteristics of the paraboloidal reflector and the hyperboloidal reflector. So another point of intersection can be observed in Figure 3-9 at the left side of the feed point which is also one focus of the hyperboloidal reflector. Errors margins associated with the path length could vary in the range from -0.16 m to 0.48 m.

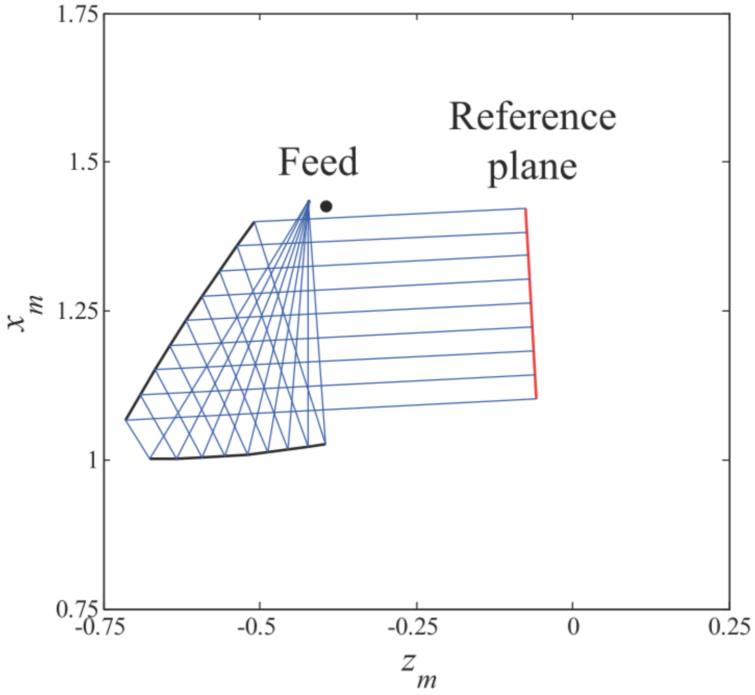

Figure 3-9 The ray path of the designed Dragonian antenna when the collimated beam is rotated 3°.

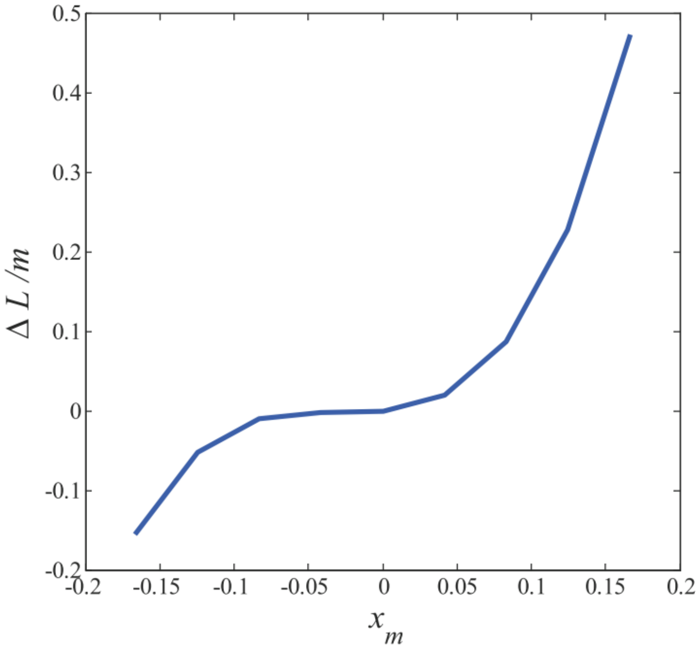

Figure 3-10 The ray path error of the designed Dragonian antenna when the collimated beam is rotated 3°.

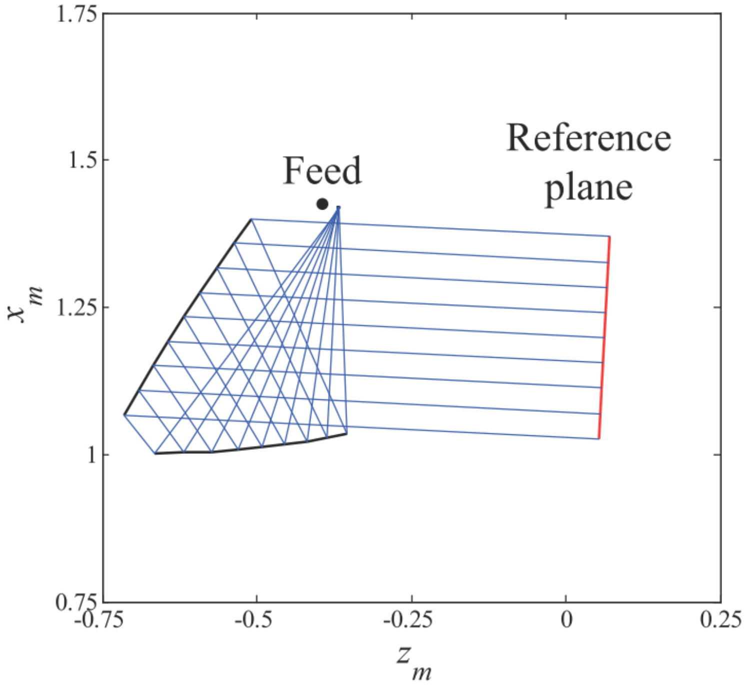
1.75
1.5
1.25
1
0.75
x m
Feed
Reference plane
-0.75
-0.5
-0.25
0
0.25
z m

Figure 3-11 The ray path of the designed Dragonian antenna when the collimated beam is rotated −3°.

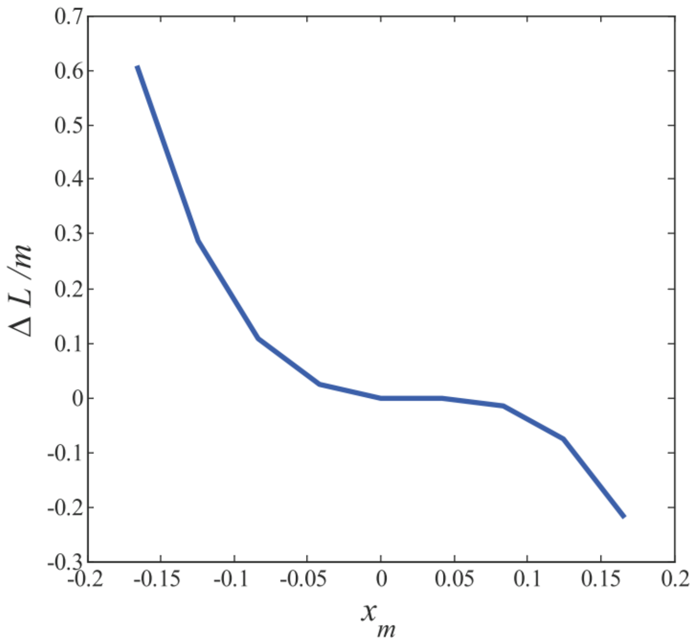

Figure 3-12 The ray path error of the designed Dragonian antenna when the collimated beam is rotated $-3°$.

Figure 3-11 shows the enlarged configuration of the designed Dragonian antenna when the reference plane has been rotated $-3°$ from the z_m axis. Locations of the feed and reflectors are same as the situation of the above one. The rays are also illuminated from the reference plane and perpendicular to the reference plane. And the path length error (PLE) of the situation in Figure 3-11 has also been studied in Matlab. Figure 3-12 demonstrates the path length error information when rays are illuminated from the reference plane along the z_m axis of the main reflector coordinate. In this figure, the points on the main aperture along x_m axis are also set as the x-axis and the path length error (ΔL) of nine sampling points on the aperture are given here compared with the central ray. From the path length error figure, it can be seen that the value varies along the aperture plane because the main reflector is not illuminated parallel to the axis of the paraboloid. This situation does not agree to the optical characteristics of the paraboloidal reflector and the hyperboloidal reflector. So another point of intersection can be observed in Figure 3-11 at the right side of the feed point which is also one focus of the hyperboloidal reflector. Path length error values vary in the range from -0.2 m to 0.6 m.

3.2.2 Parameter sweep investigation

1. Feed

The feed position can be moved in both of local x and y axes. Figure 3-13 shows the E field distributions of co-polarization and cross-polarization when the feed is moved in the local x-axis from -0.03 m to 0.03 m in the step of 0.01 m. Maximum co-polarisation and cross-polarisation values where the feed is moved in the local x-axis ranging from -0.03 m to 0.03 m are summarised in Table 3-3. When the feed is moved 0.03 m away from the centre, the beam can be observed about a 0.22 m off-axis distance from the centre. Maximum co-polarisation E field values are listed with less than 4 dB variation for different feed positions. Side lobes appear for large moving values. Cross-polarization E field values are also given in this table with more than 20 dB difference compared with peaks of co-polarisation E field values. There is less variation for the cross-polarisation.

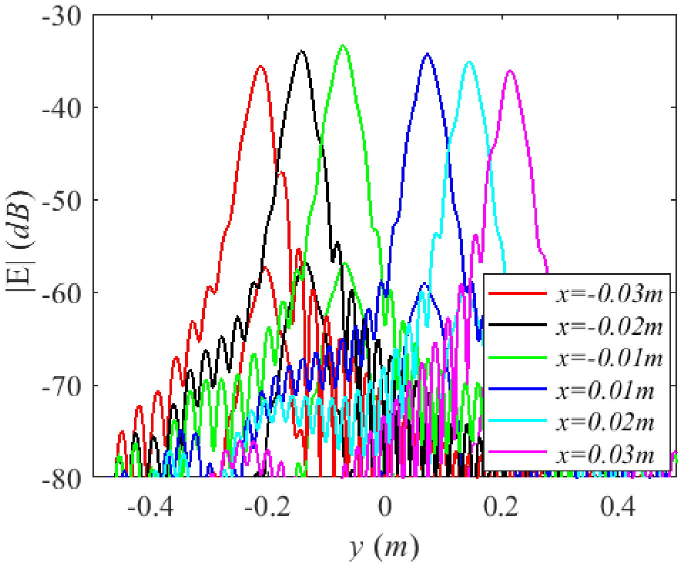

Figure 3-13 E field distributions of co-polarization and cross-polarization when the feed is moved in the local x-axis from -0.03 m to 0.03 m.

Table 3-3 Maximum co-polarisation and cross-polarisation values where the feed is moved in the local x-axis ranging from -0.03 m to 0.03 m.

x (m)	***Max Co (dB)***	***Max Cx (dB)***
-0.03	*-35.62*	*-57.39*
-0.02	*-34.02*	*-56.74*
-0.01	*-33.45*	*-56.91*
0.01	*-34.36*	*-59.12*
0.02	*-35.15*	*-59.74*
0.03	*-36.11*	*-59.86*

Figure 3-14 shows the E field distributions of co-polarization and cross-polarization when the feed is moved in the local y-axis from -0.03 m to 0.03 m in the step of 0.01 m. Maximum co-polarisation and cross-polarisation values where the feed is moved in the local x-axis ranging from -0.03 m to 0.03 m are summarised in Table 3-4. When the feed is moved 0.03 m away from the centre, the beam can be observed about a 0.2 m off-axis distance from the centre. Maximum co-polarisation E field values are listed with less than 3 dB variation for different feed positions. Side lobes appear for large moving values. Cross-polarization E field values are also given in this table with more than 20 dB difference compared with peaks of co-polarisation E field values. There is less variation for the cross-polarisation.

From above results of different feed positions, we can conclude that the movement of feed in x-axis will affect the system performance slightly more.

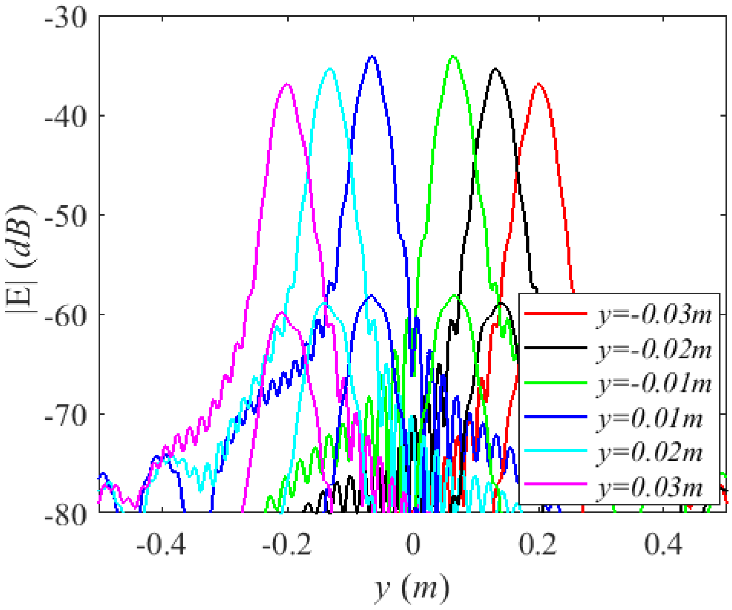

Figure 3-14 E field distributions of co-polarization and cross-polarization when the feed is moved in the local y-axis from -0.03 m to 0.03 m.

Table 3-4 Maximum co-polarisation and cross-polarisation values when the feed is moved in the local y-axis ranging from -0.03 m to 0.03 m.

y (m)	***Max Co (dB)***	***Max Cx (dB)***
-0.03	*-36.95*	*-59.88*
-0.02	*-35.33*	*-58.94*
-0.01	*-34.12*	*-58.16*
0.01	*-34.12*	*-58.16*
0.02	*-35.33*	*-58.94*
0.03	*-36.95*	*-59.88*

2. Main reflector

Figure 3-15 shows the E field distributions of co-polarization and cross-polarization when the main reflector position (h) varies ranging from 1.13 m to 1.33 m.

Maximum co-polarisation and cross-polarisation values where the main reflector position (h) varies ranging from 1.13 m to 1.33 m are summarised in Table 3-5. When the main reflector is moved 0.1 m away from the centre, no obvious off-axis movement of the beam can be observed. Maximum co-polarisation E field values are listed with less than 1 dB variation for different main reflector positions. Side lobes appear for large moving values. Cross-polarization E field values are also given in this table with more than 24 dB difference compared with peaks of co-polarisation E field values. From results listed, we can draw a conclusion that the position of the main reflector won't affect the antenna performance much.

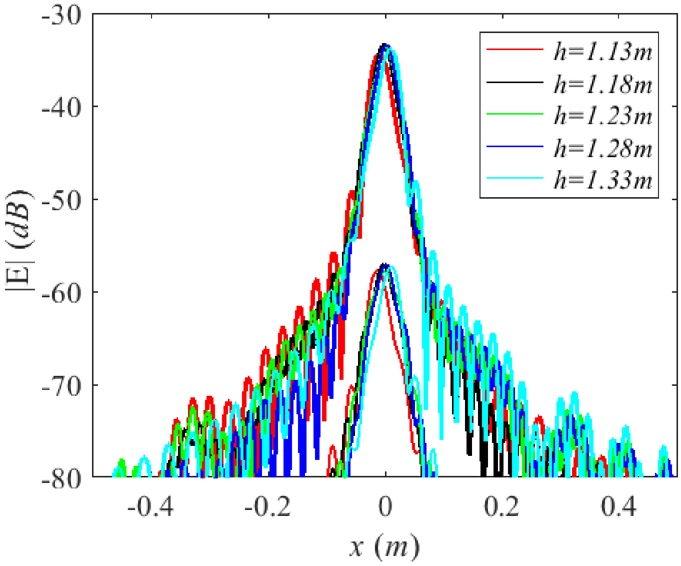

Figure 3-15 E field distributions of co-polarization and cross-polarization when the main reflector position (h) varies ranging from 1.13 m to 1.33 m.

Table 3-5 Maximum co-polarisation and cross-polarisation values when the main reflector position (h) varies ranging from 1.13 m to 1.33 m.

h (m)	***Max Co (dB)***	***Max Cx (dB)***
1.13	*-34.33*	*-57.73*
1.18	*-33.40*	*-57.09*
1.23	*-33.67*	*-57.87*

1.28	*-33.43*	*-57.11*
1.33	*-33.87*	*-57.28*

3. Sub reflector

Figure 3-16 shows the E field distributions of co-polarization and cross-polarization when the sub reflector half vertex distance (*a*) varies from 0.29 m to 0.39 m. Maximum co-polarisation and cross-polarisation values where the sub reflector half vertex distance (*a*) varies from 0.29 m to 0.39 m are summarised in Table 3-6. When the sub reflector is moved 0.05 m away from the centre, no obvious off-axis movement of the beam can be observed. Maximum co-polarisation E field values are listed with less than 2 dB variation for different sub reflector positions. Side lobes appear for large moving values. Cross-polarization E field values are also given in this table with more than 24 dB difference compared with peaks of co-polarisation E field values.

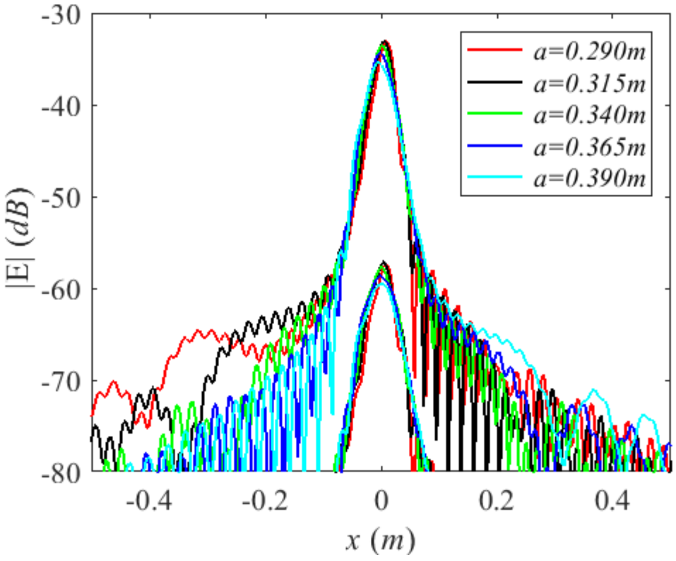

Figure 3-16 E field distributions of co-polarization and cross-polarization when the sub reflector half vertex distance (*a*) varies from 0.29 m to 0.39 m.

Table 3-6 Maximum co-polarisation and cross-polarisation values when the sub reflector half vertex distance (*a*) varies from 0.29 m to 0.39 m.

a (m)	***Max Co (dB)***	***Max Cx (dB)***
0.290	*-33.10*	*-57.34*
0.315	*-33.06*	*-57.16*
0.340	*-33.53*	*-57.71*
0.365	*-34.37*	*-58.68*
0.390	*-35.45*	*-59.55*

Figure 3-17 shows the E field distributions of co-polarization and cross-polarization when the sub reflector half foci distance (*c*) varies from 0.69 m to 0.79 m. Maximum co-polarisation and cross-polarisation values where the sub reflector half foci distance (*c*) varies from 0.69 m to 0.79 m are summarised in Table 3-7. When the sub reflector is moved 0.05 m away from the centre, the beam can be observed about a 0.08 m off-axis distance from the centre. Maximum co-polarisation E field values are listed with more than 4 dB variation for different sub reflector positions. Cross-polarization E field values are also given in this table with more than 22 dB difference compared with peaks of co-polarisation E field values.

From above results of different sub reflector parameters, we can conclude that the half foci distance (*c*) can affect the system performance more than the half vertex distance (*a*).

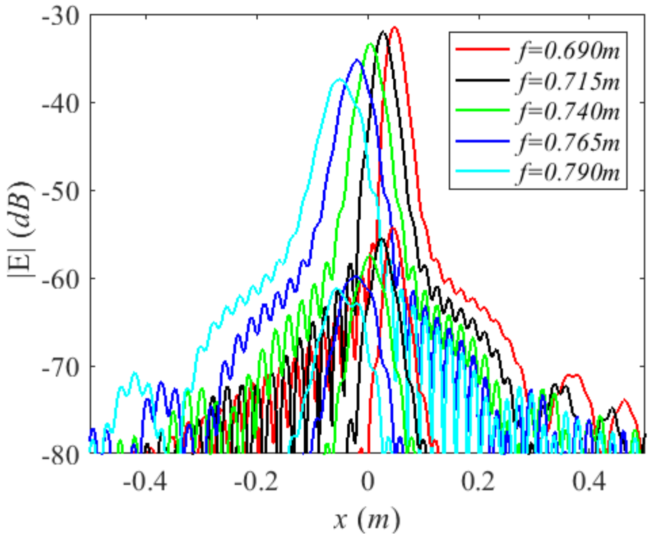

Figure 3-17 E field distributions of co-polarization and cross-polarization when the sub reflector half foci distance (c) varies from 0.69 m to 0.79 m.

Table 3-7 Maximum co-polarisation and cross-polarisation values when the sub reflector half foci distance (c) varies from 0.69 m to 0.79 m.

***f* (m)**	***Max Co (dB)***	***Max Cx (dB)***
0.690	*-31.47*	*-54.27*
0.715	*-32.05*	*-55.50*
0.740	*-33.35*	*-57.44*
0.765	*-35.28*	*-59.83*
0.790	*-37.45*	*-61.19*

3.2.3 Optimisation and results

From discussions above, the optimisation should be more focused on the position of the feed (mainly in x-axis) and the half foci distance of the sub reflector. The radiation pattern of the designed Dragonian antenna is simulated in GRASP. Optimised parameters of Dragonian antenna are listed in Table 3-8.

Table 3-8 Optimised parameters of Dragonian antenna.

Parameter	***Value***	***Parameter***	***Value***	***Parameter***	***Value***
D_m	$0.333m$	β	-74.53°	θ_U	-70.05°
F	$0.999m$	α	-30.47°	θ_L	-56.22°
θ_E	18°	e	2.1151	d_{fs}	0.4304m
d_{sm}	$0.25m$	θ_0	-63.39°	a	0.3498m
θ_P	-105°	h	1.2338m	f	0.7398m

The system feed for this geometry was chosen to an ideal Gaussian beam with gain loss of 6 dB at the half angle of $12°$. In the previous discussions, the main reflector is set as a paraboloidal reflector which provides focusing in the far field. In the simulation here, the paraboloidal reflector is replaced to an ellipsoidal reflector to realize another focus at a near field distance. The model built in GRASP is shown in Figure 3-18. The ellipsoidal main reflector used here is designed to have a secondary focus at a 3 m distance away from the central point of the main reflector [9].

The simulated near field distribution of the main reflector at 3 m can be seen in Figure 3-19 [9].

Actually, when replacing the secondary reflector shape to a bifocal structure or deform the secondary reflector surface, less beam distortion and better results can be realized. However, the fields shown in Figure 3-19 are more than adequate for required scanning objective. GRASP simulation results indicate that even larger scan angles are possible with minimal distortion.

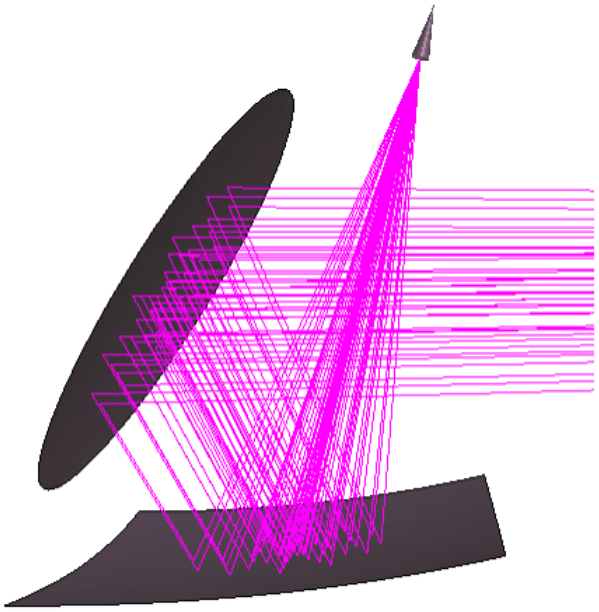

Figure 3-18 The model of the designed Dragonian antenna in GRASP [9].

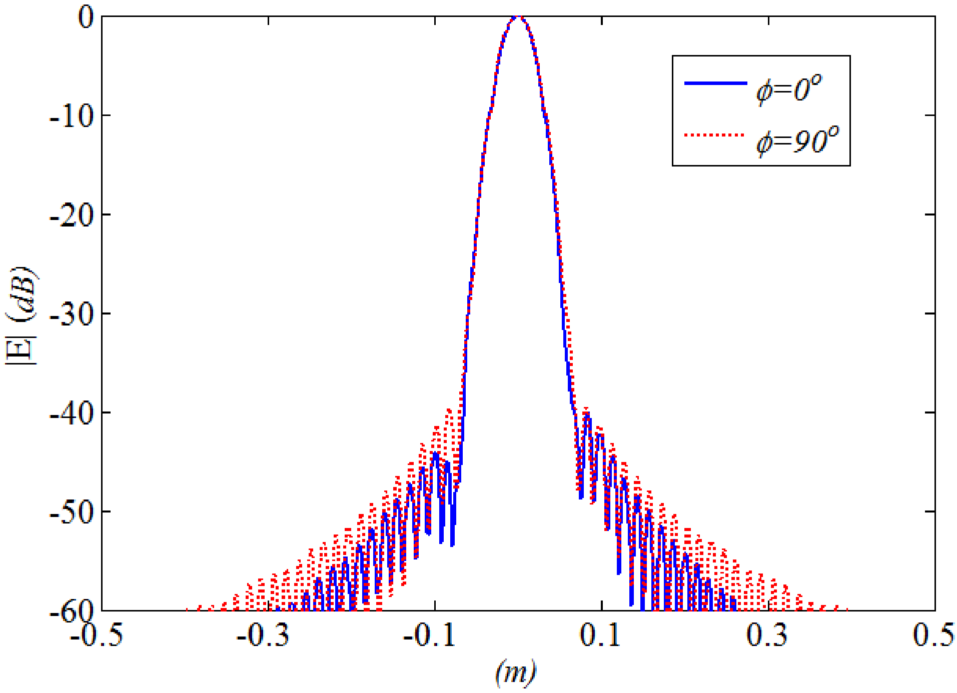

Figure 3-19 Simulated near field of the main reflector at 3 m [9].

3.3 Simulation results analysis

3.3.1 Comparison between Dragonian antenna and single ellipsoidal antenna

Here comparisons between the single ellipsoidal reflector scanning antenna and the Dragonian scanning antenna are presented. Figure 3-20 shows the schematics of rotated angle of the single ellipsoidal reflector scanning antenna and the Dragonian scanning antenna. The ellipsoidal reflectors adopted in both of these antennas are the same. Same feeds are used and locations of different parts of antennas are designed to realize that feeds are located at the focuses. In both antennas, the ellipsoidal reflectors are rotated at 3°, 0° and −3°.

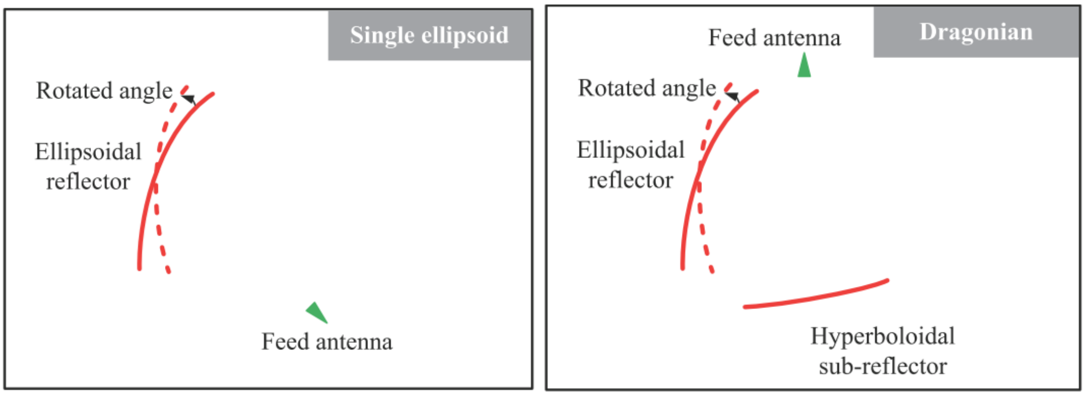
Single ellipsoid
Rotated angle
Ellipsoidal reflector
Feed antenna
Dragonian
Feed antenna
Rotated angle
Ellipsoidal reflector
Hyperboloidal sub-reflector

(a) (b)

Figure 3-20 Schematics of different scanning antennas (a) the single ellipsoidal reflector scanning antenna (b) the Dragonian scanning antenna.

Figure 3-21 presents the simulated results of the single ellipsoidal reflector scanning antenna. When the main reflector has been rotated 3° and −3°, the beam will be off-axis 0.38 m from the centre of the y-axis. But the peak values of these off-axis beams will deteriorate by 2-3 dB. The side lobes will increase largely for these off-axis situations. The consistent of main beams is poor for scanning. Therefore, the single ellipsoidal reflector antenna is simple and easy to be designed and fabricated but this structure is not adequate for the scanning approach here. The single ellipsoidal reflector antenna is more suitable for static antennas.

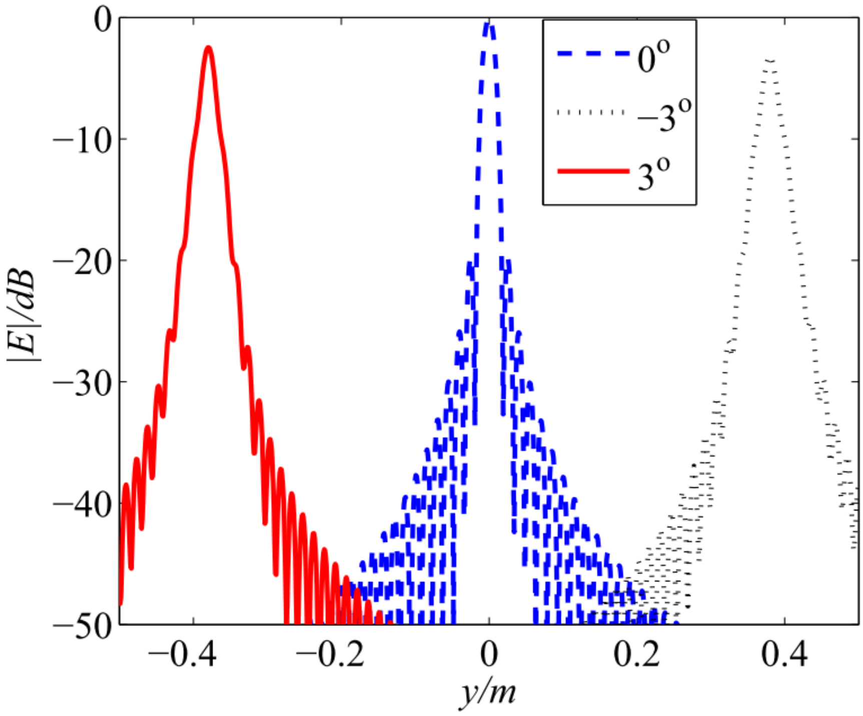

Figure 3-21 Simulation results of single ellipsoidal antenna with different scanning angle.

Figure 3-22 presents the simulated results of the Dragonian scanning antenna. Compared with results of the single ellipsoidal reflector antenna, much better performance can be observed for the Dragonian antenna. When the main reflector has been rotated 3° and −3°, the beam will also be off-axis 0.38 m from the centre of the y-axis as the same as the single ellipsoidal antenna. But the peak values of these off-axis beams will only vary less than 0.5 dB. The side lobes remain similar levels for these off-axis situations. The consistent of main beams is almost the same during the scanning. Therefore, the Dragonian antenna is adequate for the scanning approach in our imaging scanning design here though its structure is relatively complicated compared to the single ellipsoidal reflector antenna.

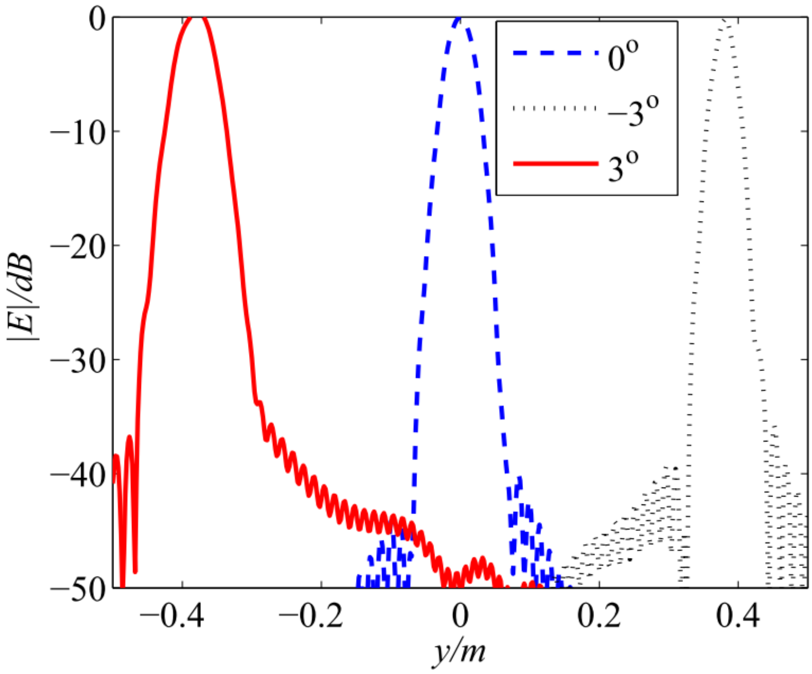

Figure 3-22 Simulation results of Dragonian antenna with different scanning angle.

3.3.2 Rotation analysis of the Dragonian antenna

The scanning in two dimensions can be divided into the rotation of the main reflector and the rotation of the flat mirror. The flat mirror is added after the main reflector to simplify the rotation mechanical structure in this scanning sub-system. Here two different rotation schemes are compared to weigh out the better scanning scheme.

Scheme 1: the main reflector in x-direction and the flat mirror in y- direction

In this scheme, the main reflector will be rotated around yma-axis in the local coordinate of the main reflector to scan along x-direction while the flat mirror is rotated around xmi-axis in the local coordinate of the flat mirror to scan along y-direction as shown in Figure 3-23.

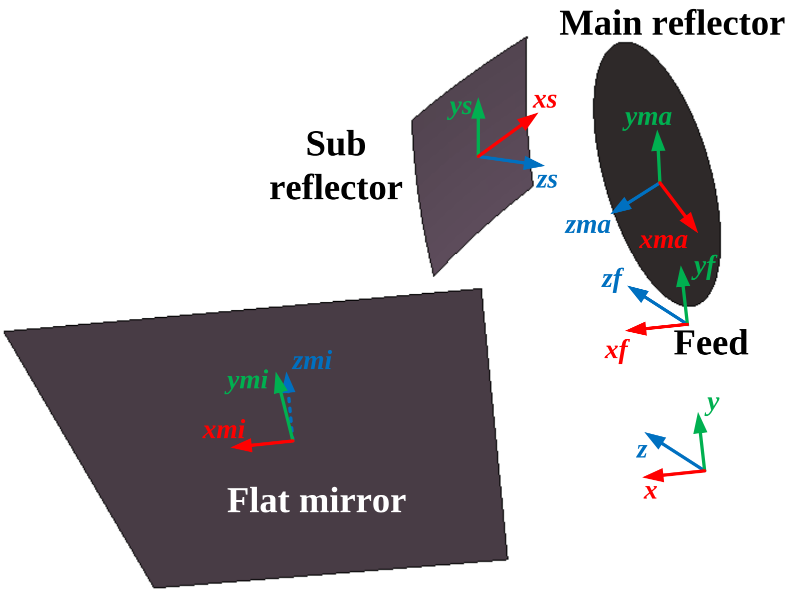

Figure 3-23 Scanning sub-system including the feed, the sub reflector, the main reflector and the flat mirror with the global coordinate and local coordinates of different components.

i) Rotation of the main reflector:

Rotation angles and corresponding beam spot centre positions at the plane z=3 m are summarized in Table 3-9. When the main reflector is rotated with 4 degrees, the beam spot centre point is located at 0.508 m away from the centre of the scanning area which is larger than the goal of 0.4 m. Maximum co-polarization E field values are listed with less than 1 dB variation for different rotation angles. Normalized cross-polarization E field values are also given in this table with more than 37.93 dB difference compared with peaks of co-polarization E field values. Figure 3-24 shows the E field distribution of co-polarization and cross-polarization at beam spot centre positions when the main reflector is rotated around the local y-axis from -4 degrees to 4 degrees in the step of 1 degree. The cross-polarization E field at 0° is much smaller (less than -100 dB) than others so it is not demonstrated in these figures. The beamwidth becomes different for the co-polarization E field distribution at 0 degree and 90 degrees when the rotation angle varies from 1 degree to 4 degrees. The beam contour is changed to an ellipse rather than a circle at the point far away from the centre of the target plane.

Table 3-9 Rotation angles and beam spot centre positions of the main reflector in scheme 1 (scanning in x dimension).

Rotation angle (degree)	**Position (m)**	**Max Co* (dB)**	**Max Cx** (N***) (dB)**	**Rotation angle (degree)**	**Position (m)**	**Max Co* (dB)**	**Max Cx** (N***) (dB)**
1	(-0.126, 0)	-20.65	-41.79	-1	(0.126, 0)	-20.60	-40.27
2	(-0.253, 0)	-20.43	-42.36	-2	(0.253, 0)	-20.58	-39.35
3	(-0.380, 0)	-20.39	-40.74	-3	(0.380, 0)	-20.54	-39.11
4	(-0.508, 0)	-19.63	-37.93	-4	(0.508, 0)	-20.48	-39.00

* Co is in short of co-polarization, ** Cx is in short of cross-polarization and *** N means that the cross-polarization value here is normalized by the max co-polarization value.

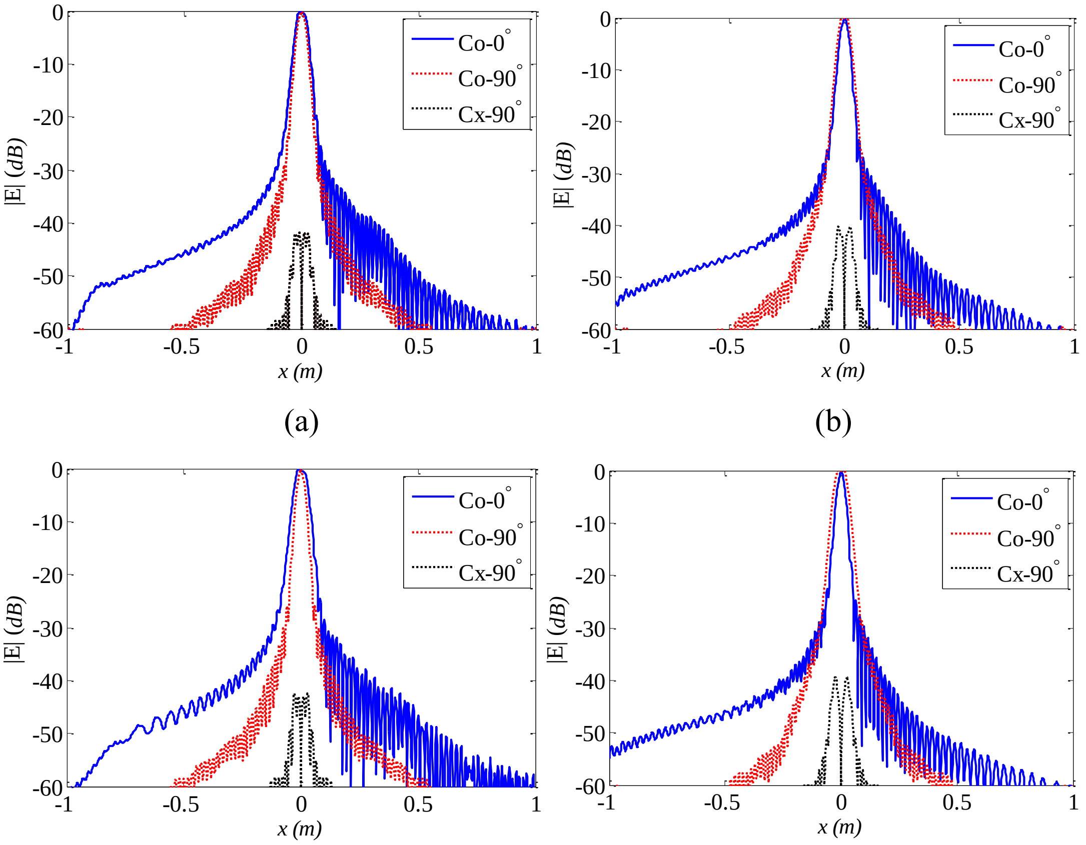

(a) (b)

(c) (d)

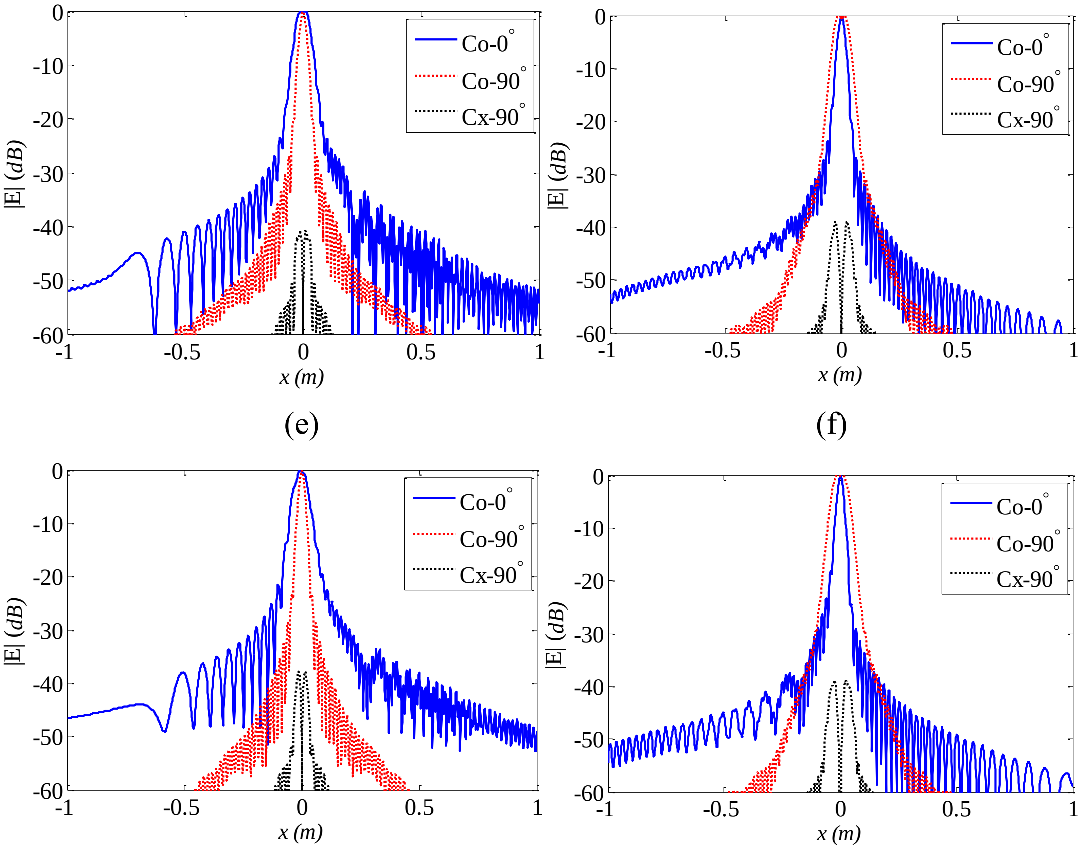

(e) (f)

(g) (h)

Figure 3-24 E field distributions of co-polarization and cross-polarization at beam spot centre positions when the main reflector is rotated around the local y-axis: (a) 1°, (b) -1°, (c) 2°, (d) -2°, (e) 3°, (f) -3°, (g) 4° and (h) -4°.

ii) Rotation of the flat mirror:

Rotation angles and corresponding beam spot centre positions at the plane z=3 m are summarized in Table 3-10. When the flat mirror is rotated with 8 degrees, the beam spot centre point is located at 0.417 m away from the centre of the scanning area which is larger than the goal of 0.4 m. Maximum co-polarization E field values are listed with less than 0.6 dB variation for different rotation angles. Normalized cross-polarization E field values are also given in this table with more than 16.68 dB difference compared with peaks of co-polarization E field values. Results here can be observed symmetric on the rotation direction. It has to be noted that the cross-polarization E field values vary from -32.22 dB to -16.68 dB when the rotation angle increases. Figure 3-25 shows the E field distribution of co-polarization and cross-polarization at beam spot centre positions when the flat mirror is rotated around the local x-axis from -8 degrees to 8 degrees in the step of 1 degree. The cross-polarization E field at 0° can also be observed and it is comparable with the co-polarization one in these figures. The beamwidth at 0 degree and 90 degrees are illustrated consistently when the rotation angle varies from 1 degree to 8 degrees.

Table 3-10 Rotation angles and beam spot centre positions of the flat mirror in scheme 1 (scanning in y dimension).

Rotation angle (degree)	**Position (m)**	**Max Co* (dB)**	**Max Cx** (N***) (dB)**	**Rotation angle (degree)**	**Position (m)**	**Max Co* (dB)**	**Max Cx** (N***) (dB)**
1	(-0.001, -0.052)	-20.64	-32.22	-1	(-0.001, 0.052)	-20.64	-32.22
2	(-0.004, -0.104)	-20.66	-27.75	-2	(-0.004, 0.104)	-20.66	-27.75
3	(-0.008, -0.157)	-20.71	-24.79	-3	(-0.008, 0.157)	-20.71	-24.79
4	(-0.015, -0.209)	-20.78	-22.55	-4	(-0.015, 0.209)	-20.78	-22.55
5	(-0.023, -0.261)	-20.87	-21.76	-5	(-0.023, 0.261)	-20.87	-21.76
6	(-0.033, -0.314)	-20.97	-19.56	-6	(-0.033, 0.314)	-20.97	-19.56
7	(-0.045, -0.366)	-21.09	-17.97	-7	(-0.045, 0.366)	-21.09	-17.97
8	(-0.058, -0.417)	-21.22	-16.86	-8	(-0.058, 0.417)	-21.22	-16.86

* Co is in short of co-polarization, ** Cx is in short of cross-polarization and *** N means that the cross-polarization value here is normalized by the max co-polarization value.

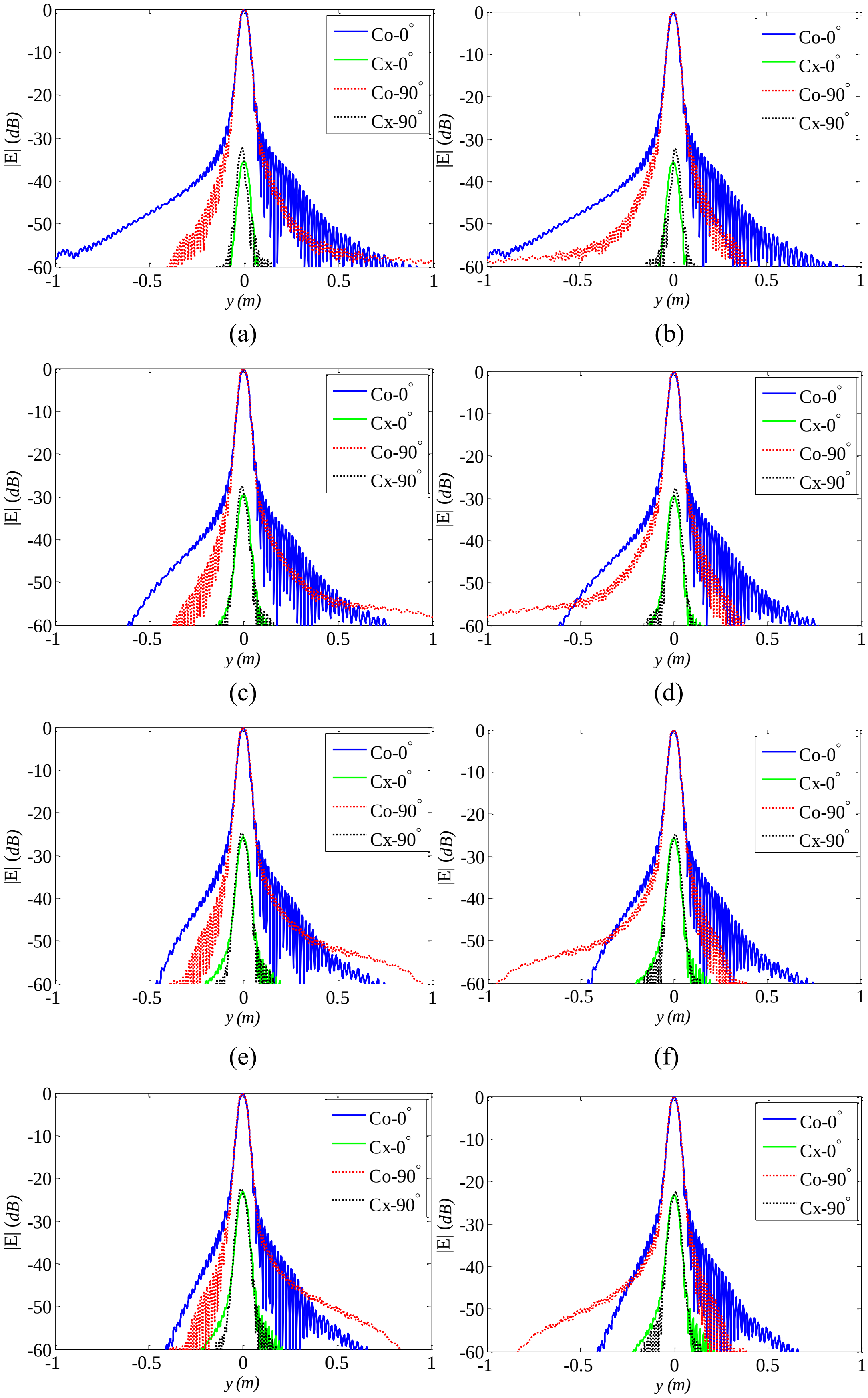

(a) (b)

(c) (d)

(e) (f)

(g) (h)

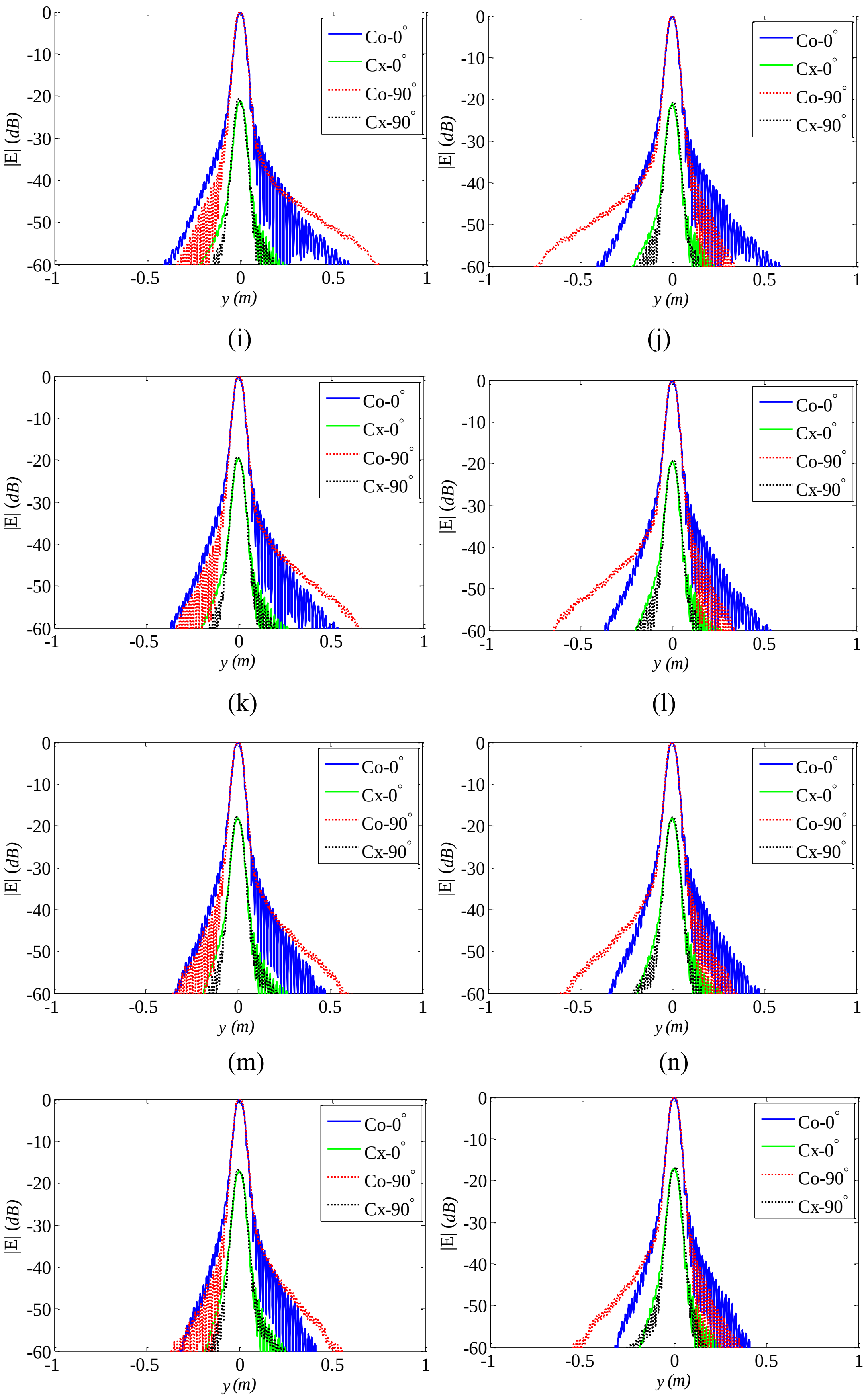

(i) (j)

(k) (l)

(m) (n)

(o) (p)

Figure 3-25 E field distributions of co-polarization and cross-polarization at beam spot centre positions when the flat mirror is rotated around the local x-axis: (a) 1°, (b) -1°, (c) 2°, (d) -2°, (e) 3°, (f) -3°, (g) 4°, (h) -4°, (i) 5°, (j) -5°, (k) 6°, (l) -6°, (m) 7°, (n) -7°, (o) 8° and (p) -8°.

Scheme 2: the main reflector in y direction and the flat mirror in x direction

In this scheme, the main reflector will be rotated around xma-axis in the local coordinate of the main reflector to scan along y direction while the flat mirror is rotated around ymi-axis in the local coordinate of the flat mirror to scan along x direction as shown in Figure 3-23.

i) Rotation of the main reflector:

Rotation angles and corresponding beam spot centre positions at the plane z=3 m are summarized in Table 3-11. When the main reflector is rotated with 5 degrees, the beam spot centre point is located at 0.460 m away from the centre of the scanning area which is larger than the goal of 0.4 m. Maximum co-polarization E field values are listed with less than 0.1 dB variation for different rotation angles. Normalized cross-polarization E field values are also given in this table with more than 19.69 dB difference compared with peaks of co-polarization E field values. Results here can be observed symmetric on the rotation direction. It has to be noted that the cross-polarization E field values vary from -31.84 dB to -19.69 dB when the rotation angle increases. Figure 3-26 shows the E field distribution of co-polarization and cross-polarization at beam spot centre positions when the main reflector is rotated around the local x-axis from -5 degrees to 5 degrees in the step of 1 degree. The cross-polarization E field at 0° can also be observed and it is comparable with the co-polarization one in these figures. The beamwidth at 0 degree and 90 degrees are illustrated consistently when the rotation angle varies from 1 degree to 5 degrees.

Table 3-11 Rotation angles and beam spot centre positions of the main reflector in scheme 2 (scanning in y dimension).

Rotation angle (degree)	**Position (m)**	**Max Co* (dB)**	**Max Cx** (N***) (dB)**	**Rotation angle (degree)**	**Position (m)**	**Max Co* (dB)**	**Max Cx** (N***) (dB)**
1	(0, 0.092)	-20.63	-31.84	-1	(0, -0.092)	-20.63	-31.84
2	(-0.001, 0.182)	-20.65	-26.93	-2	(-0.001, -0.182)	-20.65	-26.93
3	(-0.002, 0.275)	-20.66	-23.76	-3	(-0.002, -0.275)	-20.66	-23.76
4	(-0.004, 0.367)	-20.68	-21.46	-4	(-0.004, -0.367)	-20.68	-21.46
5	(-0.006, 0.460)	-20.70	-19.69	-5	(-0.006, -0.460)	-20.70	-19.69

* Co is in short of co-polarization, ** Cx is in short of cross-polarization and *** N means that the cross-polarization value here is normalized by the max co-polarization value.

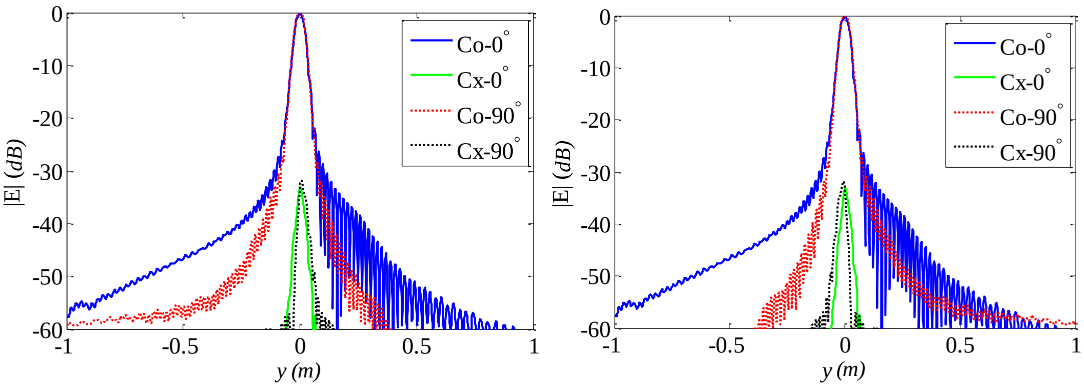

(a)

(b)

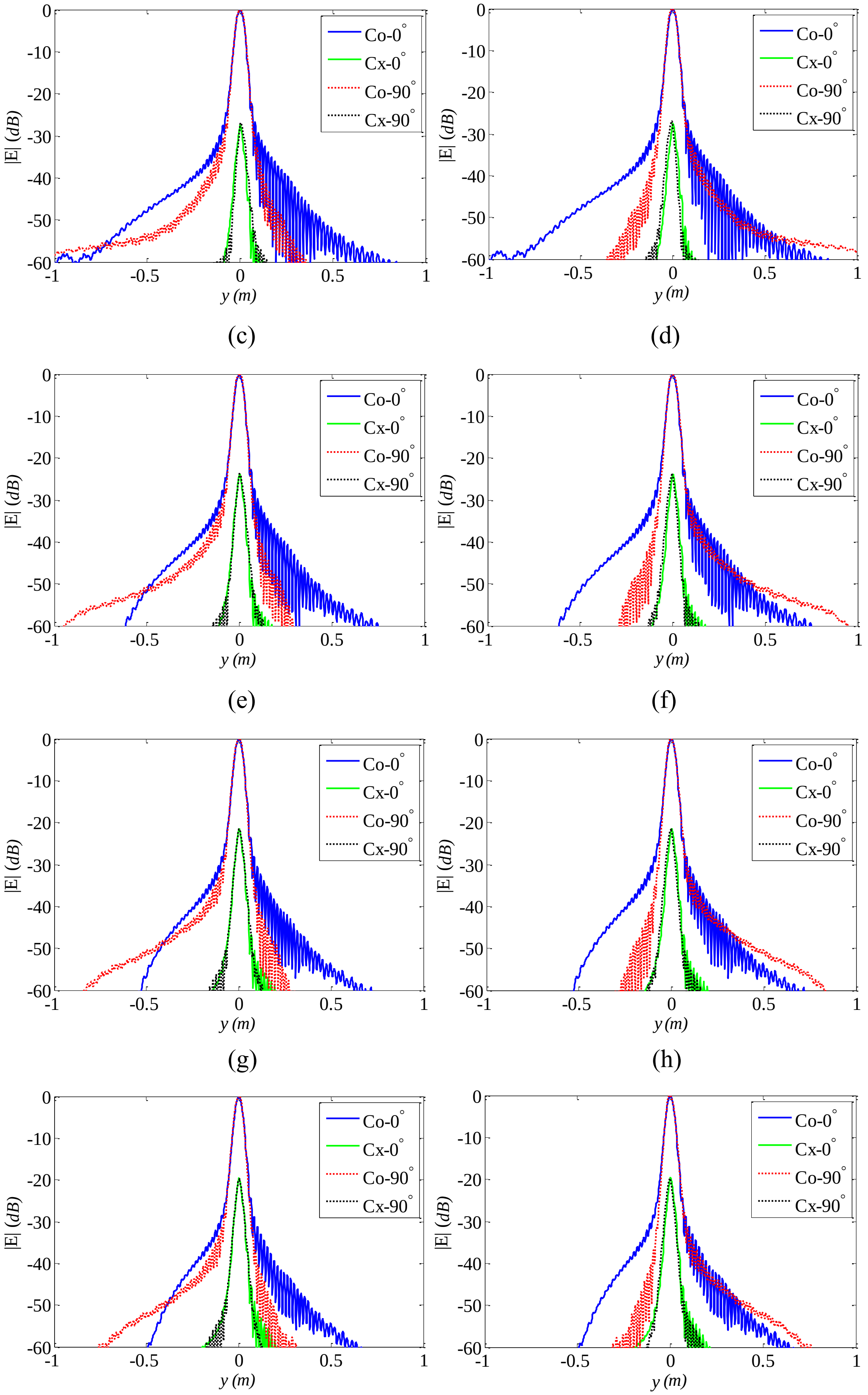

(c) (d)

(e) (f)

(g) (h)

(i) (j)

Figure 3-26 E field distributions of co-polarization and cross-polarization at beam spot centre positions when the main reflector is rotated around the local x-axis: (a) 1°, (b) -1°, (c) 2°, (d) -2°, (e) 3°, (f) -3°, (g) 4°, (h) -4°, (i) 5° and (j) -5°.

ii) Rotation of the flat mirror:

Rotation angles and corresponding beam spot centre positions at the plane z=3 m are summarized in Table 3-12. When the flat mirror is rotated with 4 degrees, the beam spot centre point is located at 0.421 m away from the centre of the scanning area which is larger than the goal of 0.4 m. Maximum co-polarization E field values are listed with less than 0.4 dB variation for different rotation angles. Normalized cross-polarization E field values are also given in this table with more than 39.41 dB difference compared with peaks of co-polarization E field values. It has to be noted that the cross-polarization E field values vary from -43.15 dB to -39.41 dB when the rotation angle increases. Figure 3-27 shows the E field distribution of co-polarization and cross-polarization at beam spot centre positions when the flat mirror is rotated around the local y-axis from -4 degrees to 4 degrees in the step of 1 degree. The cross-polarization E field at 0° is much smaller (less than -100 dB) than others so it is not demonstrated in these figures. The beamwidth at 0 degree and 90 degrees are illustrated consistently when the rotation angle varies from 1 degree to 4 degrees.

Table 3-12 Rotation angles and beam spot centre positions of the flat mirror in scheme 2 (scanning in x dimension).

Rotation angle (degree)	**Position (m)**	**Max Co* (dB)**	**Max Cx** (N***) (dB)**	**Rotation angle (degree)**	**Position (m)**	**Max Co* (dB)**	**Max Cx** (N***) (dB)**
1	(0.105, 0)	-20.66	-40.65	-1	(-0.105, 0)	-20.66	-41.96
2	(0.210, 0)	-20.74	-40.10	-2	(-0.210, 0)	-20.74	-42.47

3	(0.315, 0)	-20.88	-39.88	-3	(-0.315, 0)	-20.87	-42.95
4	(0.421, 0)	-21.06	-39.41	-4	(-0.421, 0)	-21.05	-43.15

* Co is in short of co-polarization, ** Cx is in short of cross-polarization and *** N means that the cross-polarization value here is normalized by the max co-polarization value.

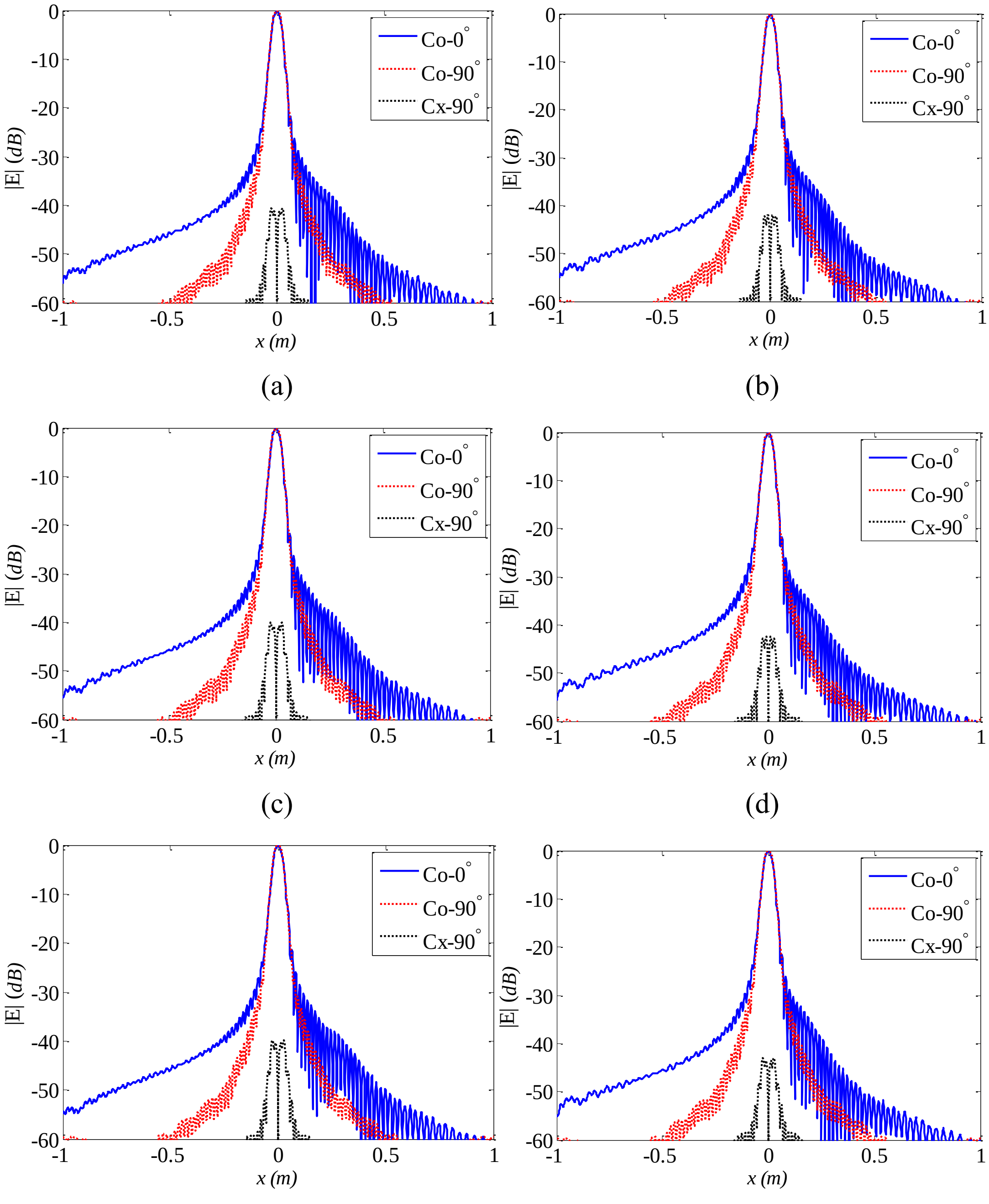

(a) (b)

(c) (d)

(e) (f)

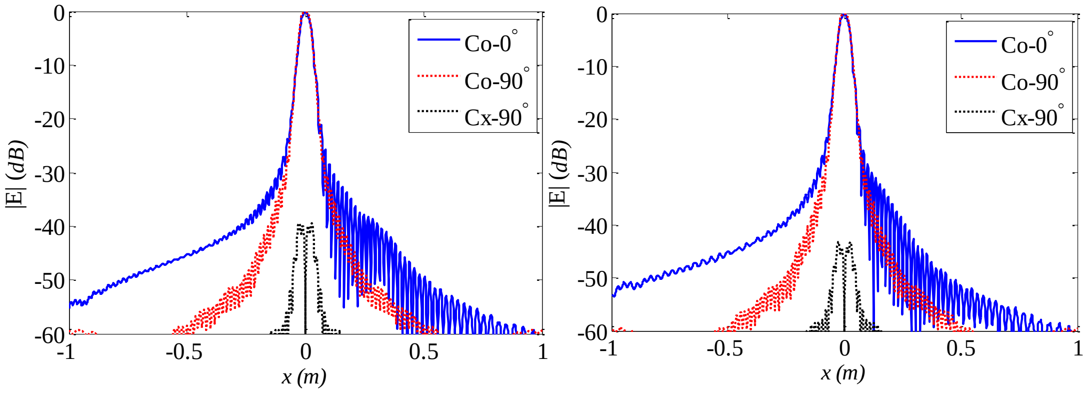

(g) (h)

Figure 3-27 E field distributions of co-polarization and cross-polarization at beam spot centre positions when the flat mirror is rotated around the local y-axis: (a) 1°, (b) -1°, (c) 2°, (d) -2°, (e) 3°, (f) -3°, (g) 4° and (h) -4°.

Discussions:

From results demonstrated above, scheme 2 shows a much better performance than scheme 1.

1. In scheme 2, the main reflector and the flat mirror are not rotated much as in the scheme 1 especially for the y dimension scanning on the same covered area. Fewer structure modifications mean less degradation of the beam performance.

2. The variation of the scanning beam in scheme 2 is less than the one in scheme 1.

3. The cross-polarisation performance in scheme 2 is better than scheme 1. The cross-pol value can be controlled under -20 dB.

4. The beamwidth on 0 degree and 90 degrees plane can be remained the same in scheme 2 while there is a noticeable difference for the large rotation angle situation in scheme 1.

So scheme 2 will be deployed as the scanning scheme in our scanning sub-system.

3.3.3 Scanning beam performance in the scanning area

As discussed above, scheme 2, i.e. the main reflector rotating in y direction and the flat mirror in x direction is chosen in the scanning sub-system.

When the flat mirror is rotated from -4 degrees to 4 degrees, the beam location off-axis distance will vary from -0.421 m to 0.421 m. E field beam cuts and grids for situations the flat mirror is rotated from -4 degrees to 4 degrees with the step of 1 degree are demonstrated in Figure 3.24 and Figure 3-29, respectively.

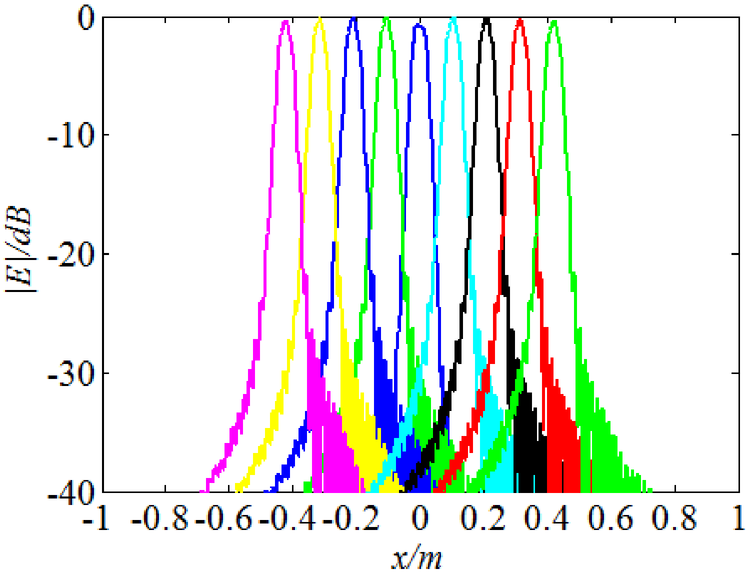

Figure 3-28 E field beam cuts for situations the flat mirror is rotated from -4 degrees to 4 degrees with the step of 1 degree.

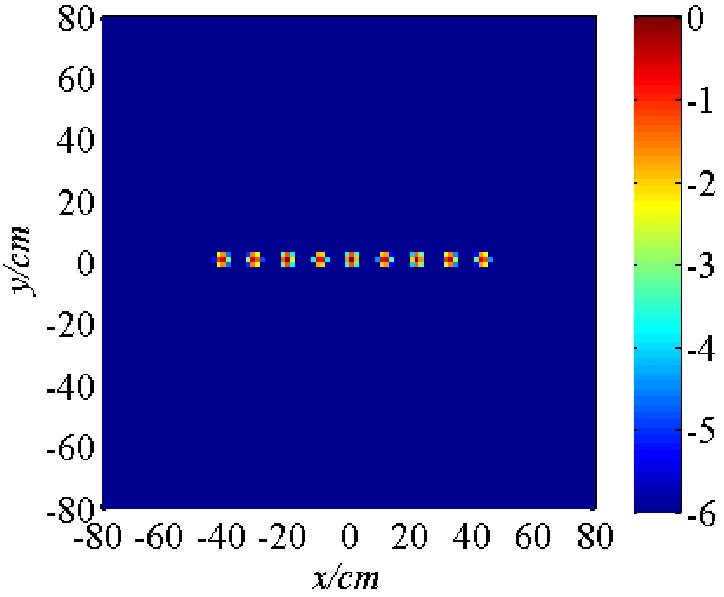

Figure 3-29 E field beam grids for situations the flat mirror is rotated from -4 degrees to 4 degrees with the step of 1 degree. (The legend indicates the normalised values in dB)

When the main reflector is rotated from -5 degrees to 5 degrees, the beam location off-axis distance will vary from -0.46 m to 0.46 m. E field beam cuts and grids for situations the main reflector is rotated from -5 degrees to 5 degrees with the step of 1 degree are demonstrated in Figure 3-30 and Figure 3-31, respectively.

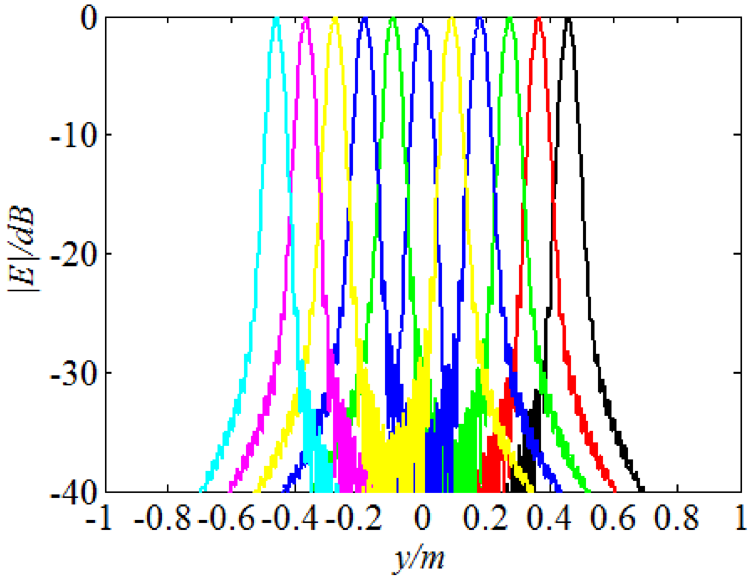

Figure 3-30 E field beam cuts for situations the main reflector is rotated

from -5 degrees to 5 degrees with the step of 1 degree.

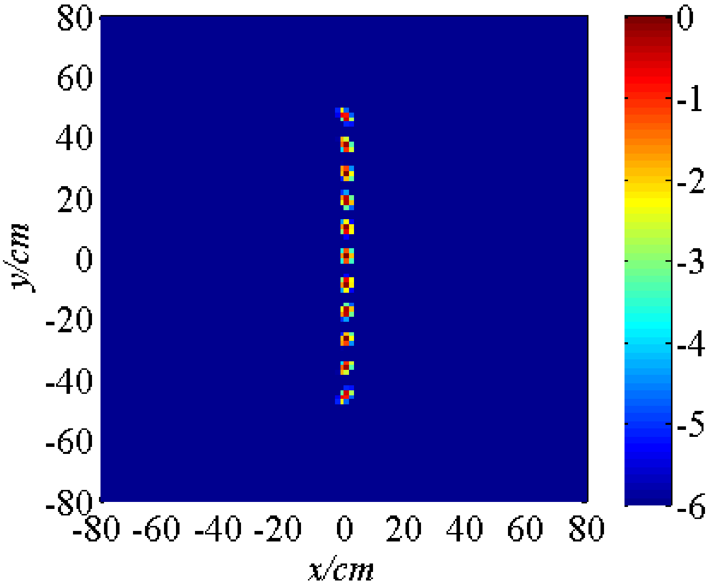

Figure 3-31 E field beam grids for situations the main reflector is rotated from -5 degrees to 5 degrees with the step of 1 degree. (The legend indicates the normalised values in dB)

When the main reflector and the flat mirror are rotated angles demonstrated in Table 3-13, the beam spot can cover different points located at the centre and corners illustrated in Figure 3-32. Compared with rotation angle values of the flat mirror, the rotation angle values of the flat mirror are not symmetric. The reason is the beam deviation which can be characterised by beam deviation factor (BDF).

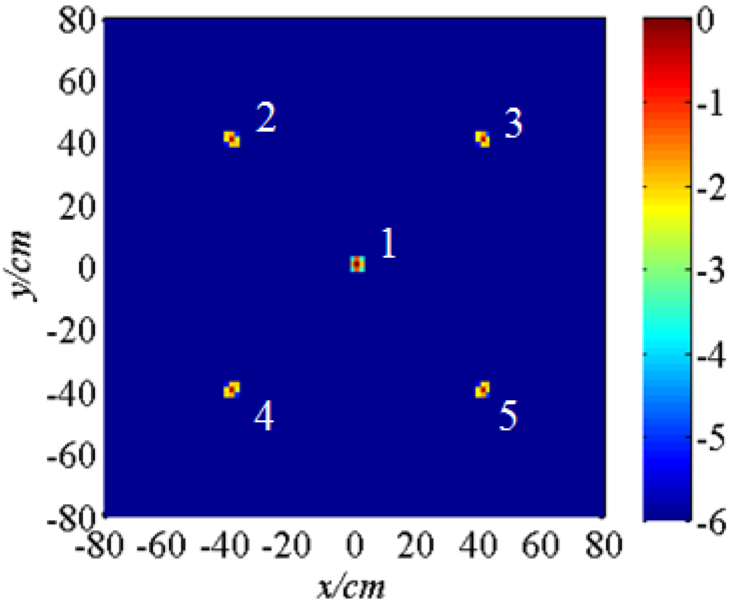

Figure 3-32 E field beam grids for the centre point and corner points. (The legend indicates the normalized values in dB)

Table 3-13 Rotation angles of the flat mirror and the main reflector corresponded to points shown in Figure 3-32.

Point	**Plate (degrees)**	**Main (degrees)**
1	0	0
2	-3.76	4.33
3	3.84	4.33
4	-3.76	-4.33
5	3.84	-4.33

3.4 Summary

This chapter introduced and compared different kinds of reflector antennas at first. In order to keep a consistent performance of the scanning beam, a Dragonian reflector antenna was introduced in our proposed beam scanning scheme. Near field comparison shows that the designed Dragonian reflector antenna can have a better beam performance than the single ellipsoidal dual reflector antenna. More analyses were conducted to investigate two rotation schemes. The scanning sub-system was proved to remain the beam consistent in the whole scanning area with the loss variation less than 1 dB.

3.5 References

[1] W. L. Stutzman and G. A. Thiele, Antenna theory and design. John Wiley & Sons, 2012.

[2] H. Lehpamer, Microwave transmission networks: planning, design, and deployment. McGraw-Hill New York, 2010.

[3] S. Chang and A. Prata, The geometrical theory of aberrations of classical offset dual-reflector antennas, IEEE Antennas and Propagation Society International Symposium, 2001, vol. 1, 2001, pp. 530–533.

[4] C. Granet, Designing classical dragonian offset dual-reflector antennas from combinations of prescribed geometric parameters, IEEE Antennas and Propagation Magazine, vol. 43, no. 6, pp. 100–107, 2001.

[5] S. Chang and A. Prata, The design of classical offset dragonian reflector antennas with circular apertures, IEEE Transactions on Antennas and Propagation, vol. 52, no. 1, pp. 12–19, 2004.

[6] N. Llombart, K. B. Cooper, R. J. Dengler, T. Bryllert, and P. H. Siegel, Confocal ellipsoidal reflector system for a mechanically scanned active terahertz imager, IEEE Transactions on Antennas and Propagation, vol. 58, no. 6, pp. 1834–1841, 2010.

[7] E. Gandini, J. Svedin, T. Biyllert, and N. Llombart, On the development of a quasi-optical system for short and long range standoff imagers, 2015 IEEE 40th International Conference on Infrared, Millimeter, and Terahertz waves (IRMMW-THz), pp. 1–1, 2015.

[8] A. Garcia-Pino, B. Gonzalez-Valdes, O. Rubiños, et al. Bifocal reflector antenna for a standoff radar imaging system with enhanced field of view. IEEE Transactions on Antennas and Propagation, vol. 62, no. 10, pp. 4997-5006, 2014.

[9] M. Zhou, Y. Alfadhl and X. Chen, Study on a THz image scanning system with ellipsoidal reflector, 8th UK-China Millimetre Waves and Terahertz Technology Workshop (UCMMT 2015), 2015,

Chapter 4. Simulation of THz scanning schemes and assessment of two novel algorithms

4.1 Brief introduction to PO algorithm

There are several analysis methods for reflector antennas, such as: Physical Optics (PO), Physical Theory of Diffraction (PTD), Geometrical Optics (GO), Geometrical Theory of Diffraction (GTD) and Gaussian Beam (GB), and etc. PO/PTD is the commonly used method for accurately analysing radiation characteristic of reflector antennas. PO method can obtain accurate results of the main lobe and nearby side lobes while PTD can correct the computational results of far field side lobes. Combination of PO and PTD methods has been adopted in commercial simulators to analyse the radiation characteristic of various reflector antennas [1].

Physical Optics offers an approximated result of the radiation field computed through the integration of the induced current on the surface of the illuminated scatter which is normally set as an ideal electric conductor. The accuracy of the result can meet the engineering requirement when the size of the scatter and the radius of curvature is larger than 5λ, where λ is the wavelength of the radiowave.

In the theory of PO, the induced current on the surface of the illuminated scatter $\vec{J}(\vec{r'})$ can be calculated from the incident magnetic field $\vec{H}^i(\vec{r'})$ at the point with the position vector $\vec{r'}$ and the unit surface normal $\hat{n}$ which points outward on the illuminated side of the surface. $\vec{H}^i(\vec{r'})$, $\vec{J}(\vec{r'})$ and $\hat{n}$ are shown in Figure 4-1.

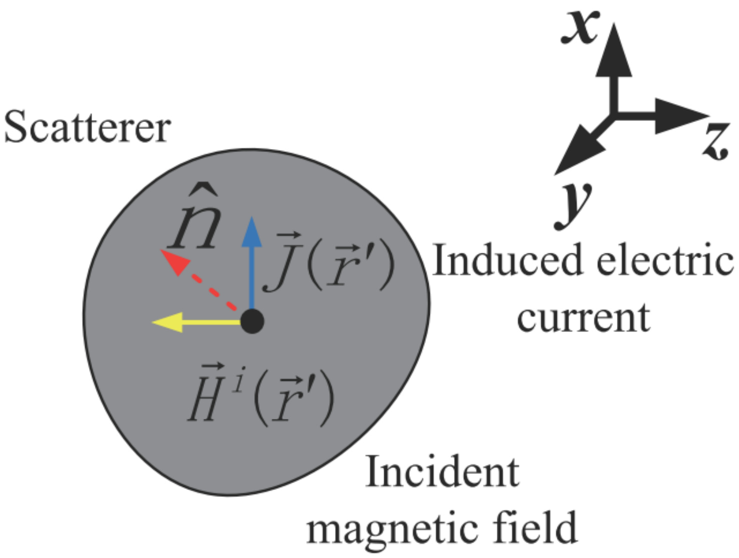
x
z
y
Scatterer
$\hat{n}$
$\vec{J}(\vec{r}')$
Induced electric current
$\vec{H}^i(\vec{r}')$
Incident magnetic field

Figure 4-1 Induced electric current on the illuminated scatterer.

Then the scattered electromagnetic field from the scatterer illustrated in Figure 4-2 can be derived from $\vec{J}(\vec{r'})$. Detailed derivation can be found in Appendix II.

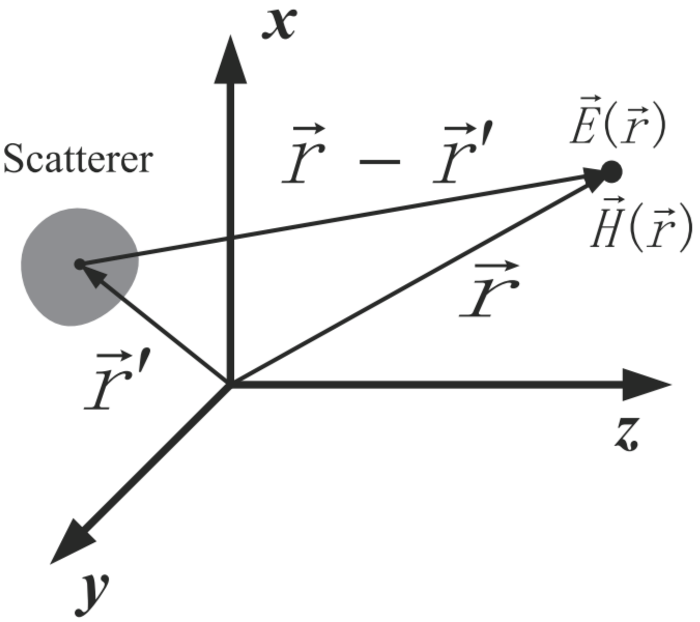
x
Scatterer
$\vec{r} - \vec{r}'$
$\vec{E}(\vec{r})$
$\vec{H}(\vec{r})$
$\vec{r}$
$\vec{r}'$
z
y

Figure 4-2 The scattered electromagnetic field from the scatter.

4.2 Validation of PO algorithm in Matlab

Before the PO algorithm is applied to the simulation of the scanning schemes, a simple example was tested to validate the PO algorithm coded in Matlab. The simulated results will be compared with results obtained by the commercial simulator, GRASP [3].

4.2.1 Geometry of the single off-axis reflector antenna

Here, the near and the far fields of a single off-axis reflector antenna have been calculated and compared with the results obtained from Matlab code and GRASP. The single off-axis paraboloidal reflector antenna is known as one of the most common reflector antennas. Figure 4-3 shows the configuration of the single off-axis reflector antenna.

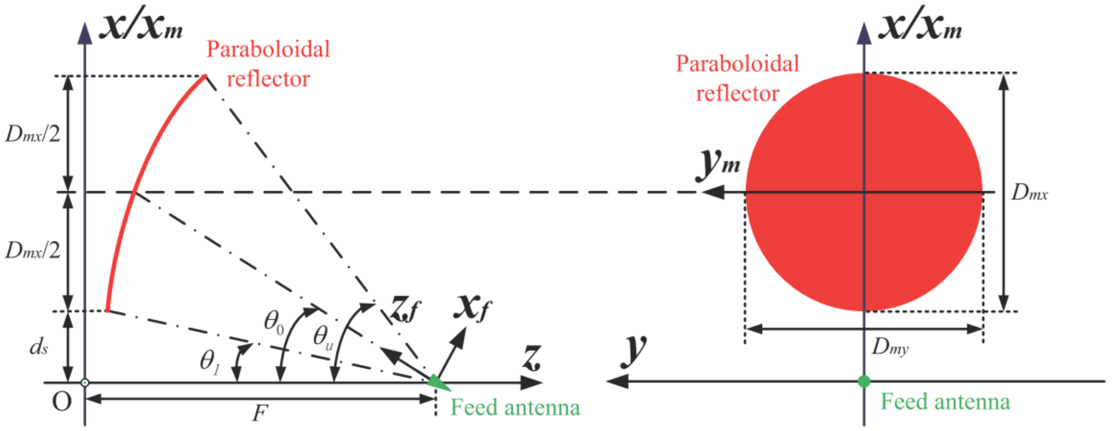

Figure 4-3 Configuration of the single offset reflector antenna.

Its main parameters are: the focus of the reflector F, the projected length along the x-axis of the reflector aperture D_{mx}, the projected length along the y-axis of the reflector aperture D_{my}, the off-axis height along the x-axis of the reflector lower edge d_s, the angle between the line connected with the focus (the position of the feed) and the reflector's lower edge and z-axis θ_l, the angle between the line connected with the focus and the reflector's upper edge and z-axis θ_u and the angle between z-axis and the direction of the feed z_f-axis θ_0. The feed is normally pointed to the centre of the reflector which is corresponded to the centre of the projected curve of the reflector surface on the *xoz* plane.

4.2.2 Simulations of the single offset reflector antenna

In the theoretical computation, the radiation pattern of the ideal feed is normally used to simulate the radiation characteristics of the real feed. A Gaussian feed was chosen as the ideal feed deployed in our model. It can not only be used to approximately simulate the far field radiation pattern, but also give out the near field pattern of the corrugated horn which is crucial for the computation of the reflector located in the near field area of the feed. In recent years, this feed model has been widely applied in many commercial simulators such as, GRASP. The far field of the Gaussian feed has rotational symmetry [3]. The ideal Gaussian feed can be set as described in Appendix III.

The radiation field $\mathbf{E}_t$ consists of three parts:

$$\mathbf{E}_t = \mathbf{E}_{feed} + \mathbf{E}_{PO} + \mathbf{E}_{PTD} \tag{4-1}$$

where $\mathbf{E}_{feed}$ is the radiation field of the feed, $\mathbf{E}_{PO}$ is the radiation field of the induced current on the reflector and $\mathbf{E}_{PTD}$ is the radiation field of the fringe diffraction current. $\mathbf{E}_{PO}$ and $\mathbf{E}_{PTD}$ can be calculated with PO and PTD, respectively. Here only $\mathbf{E}_{PO}$ is considered for simplification. In many related papers, the signal reflection/scatter problem was widely simplified employing the plane wave accumulation theory which has the similar principle with the PO.

As an important specification of the reflector antenna, the directivity can be calculated with:

$$D(\theta,\varphi) = \frac{4\pi r^2|\mathbf{E}_t(\theta,\varphi)|^2}{P_\Sigma} = \frac{4\pi r^2|\mathbf{E}_t(\theta,\varphi)|^2}{\iint|\mathbf{E}_t(\theta,\varphi)|^2 r^2 sin\theta d\theta d\varphi} \tag{4-2}$$

When assuming that the total radiation power of the reflector antenna (P_Σ) is equal to the total radiation power of the feed (P_{total}), Equation above can be transformed to

$$D(\theta,\varphi)=\frac{4\pi r^2|\mathbf{E}_t(\theta,\varphi)|^2}{P_{total}}=\frac{4\pi r^2\left|\mathbf{E}_{feed}(\theta,\varphi)\right|^2}{\iint\left|\mathbf{E}_{feed}(\theta,\varphi)\right|^2 r^2 sin\theta d\theta d\varphi} \tag{4-3}$$

Equation above gives the directivity of the reflector antenna at the point (θ,φ). It is important to note that all descriptions about the polarisation of the radiation field are defined according to the so-called Ludwig's 3rd definition.

To validate the PO code in Matlab, the radiation characteristic of a single off-axis reflector antenna is calculated in this part and compared with the results obtained by GRASP 9. Here we set parameters in Figure 4-3 as following: the projected aperture is an ellipsoid with the length on x-axis D_{mx}=1 m, the length on y-axis D_{my}=1.2 m, the off-axis height d_s=0.1 m, focus length *F*=0.8 m. This antenna works at 12.5 GHz. The feed is a linear x-polarized ideal Gaussian beam feed with the taper of -12 dB at the half angle of $31°$.

Figure 4-4 shows the far field results calculated by PO algorithm in this report and GRASP 9. The normalised pattern results are shown at the $\phi = 0°$ plane and the $\phi = 90°$ plane while θ varies in the range of $-15° \sim 15°$. A good agreement can be observed between the far-field patterns, including the main-lobe, side-lobes.

The validation in the far field is not enough. In our research of the scanned imaging schemes, the near field results are used to build the required images. Figure 4-5 Comparison of near field patterns obtained by Matlab PO and GRASP 9. The normalised pattern results are shown at the $\phi = 0°$ plane and the $\phi = 90°$ plane while the off-axis distance varies in the range of $-2\text{ m} \sim 2\text{ m}$. A good agreement can also be observed between the near field results, including the co-polarisation part and the cross-polarization part.

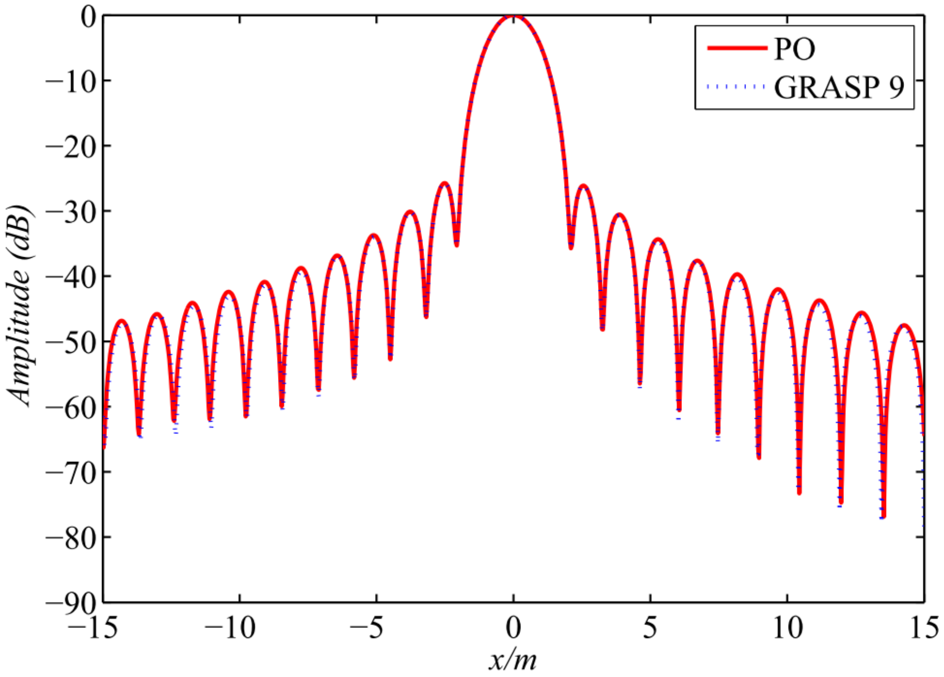

(a)

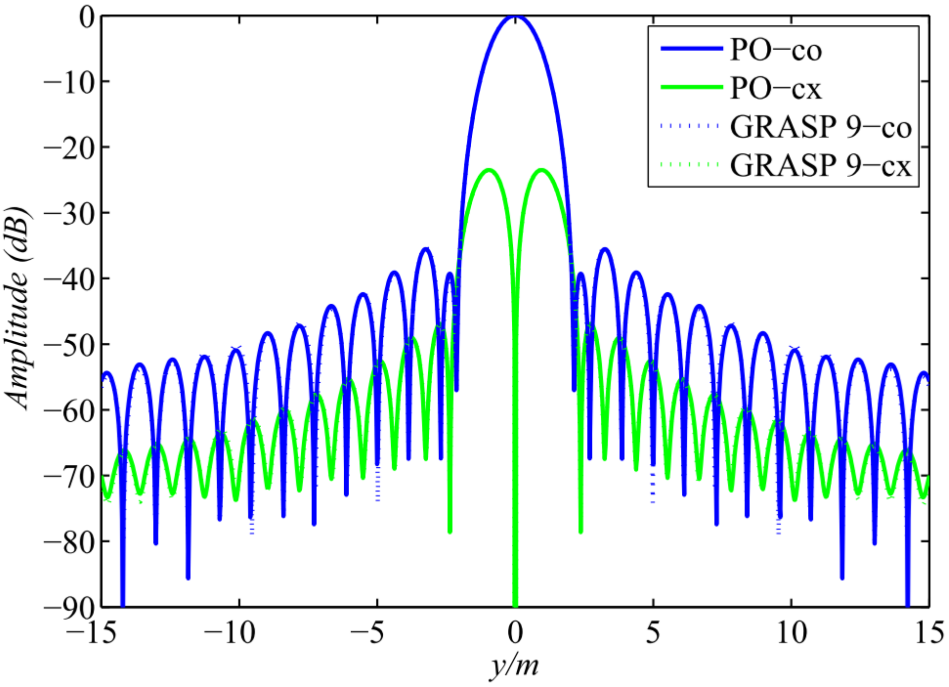

(b)

Figure 4-4 Comparison of far field patterns obtained by Matlab PO and GRASP 9 (a) $\phi = 0°$ (b) $\phi = 90°$.

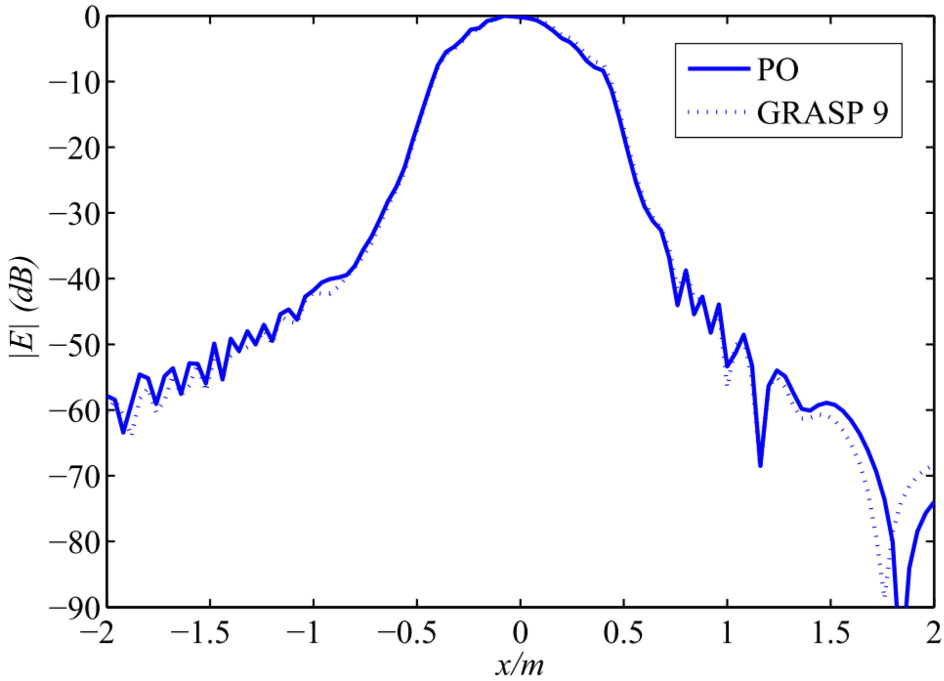

(a)

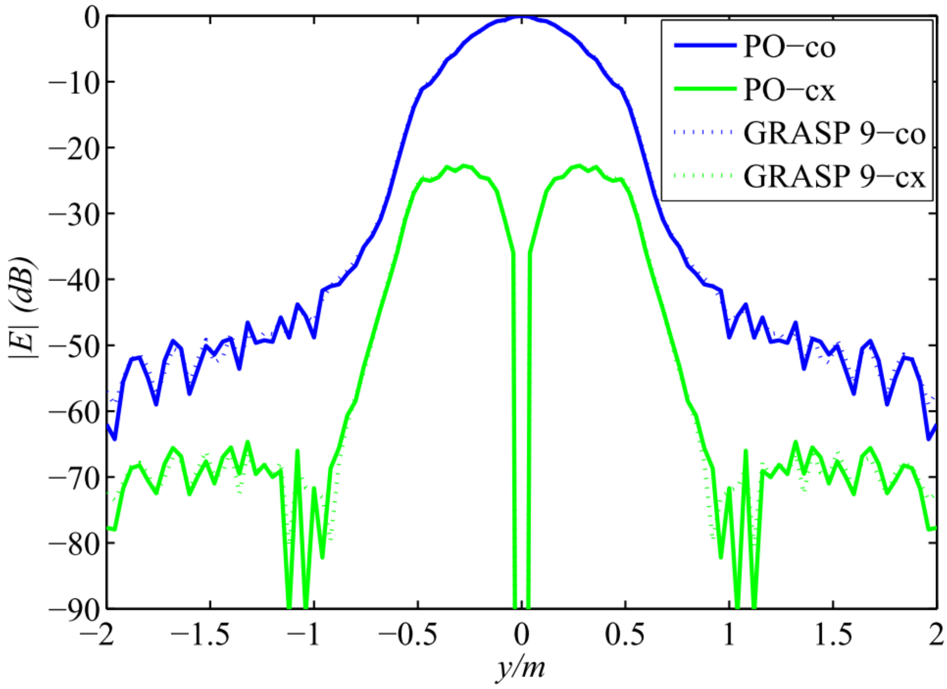

(b)

Figure 4-5 Comparison of near field patterns obtained by Matlab PO and GRASP 9 (a) $\phi = 0°$ (b) $\phi = 90°$.

4.3 Simulations of different scanning schemes

4.3.1 Simulation settings in Matlab

Figure 4-6 shows the simulated model built in Matlab. An ideal Gaussian feed is set as the transmitter antenna. The target can be taken as the scatterer introduced in PO algorithm. The target area will be divided into small areas firstly. The incident current for each small area can be derived from the incident magnetic field of the ideal Gaussian feed. Then E field and H field at the observe point can be calculated by the superposition of the radiation field of the incident current on the target.

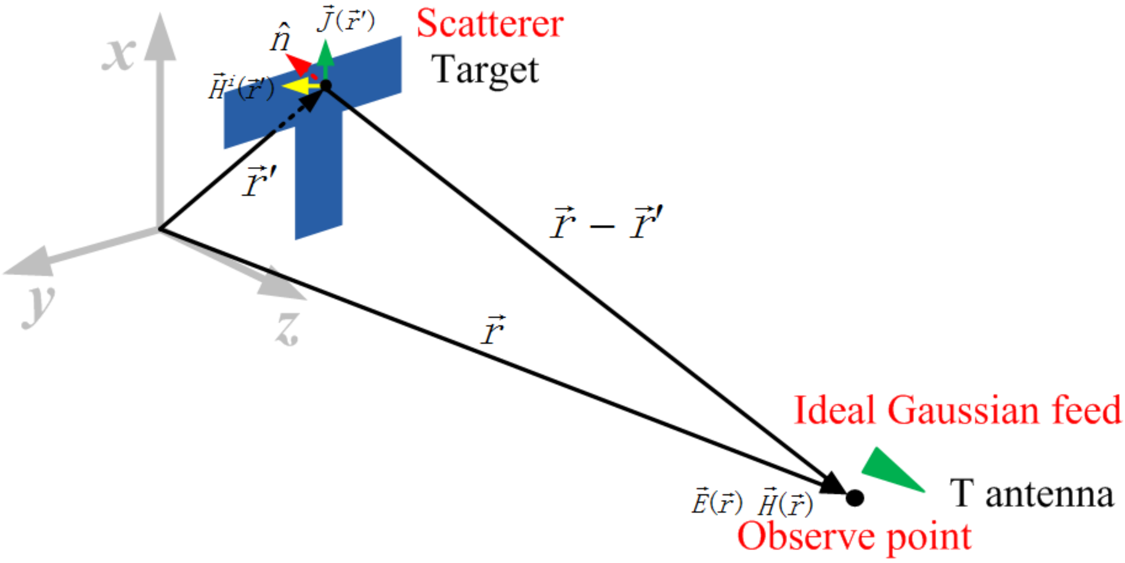
x
$\hat{n}$
$\vec{J}(\vec{r}')$
Scatterer
Target
$\vec{H}^i(\vec{r}')$
$\vec{r}'$
$\vec{r}-\vec{r}'$
y
z
$\vec{r}$
Ideal Gaussian feed
$\vec{E}(\vec{r})$ $\vec{H}(\vec{r})$
T antenna
Observe point

Figure 4-6 The simulated model built in Matlab.

4.3.2 Study of the raster scanning scheme and the reconstruction algorithm

For the raster scanning scheme, the transmitter antenna (the ideal Gaussian feed in the model) and the receiver antenna (the observe point) are raster scanned on the aperture plane. Here they are located at the same point in the scanning process. E field data at the observe point is recorded as the received signal scattered from the target.

Received signals of different locations of transceivers can constitute a virtual data array which can be processed to reconstruct the image.

1. Rectangular plate

First of all, a rectangular metal plate is used as the test target of the PO simulation in Matlab. This plate has the size of 0.1 m * 0.15 m size. The scanning area coverage is 0.4 m* 0.4 m. Figure 4-7 shows the unprocessed image which is built directly from the amplitude of the received signal (left) and the reconstructed image using holography technique (right).

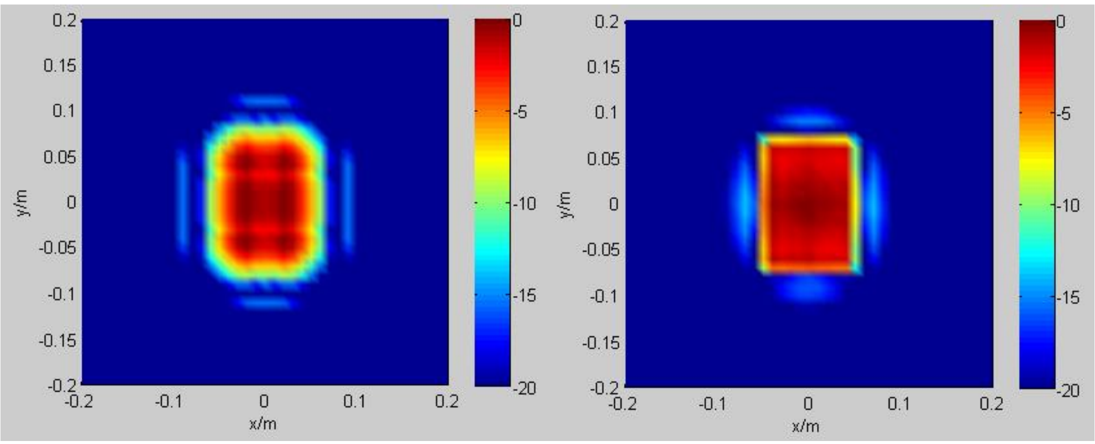

Figure 4-7 Amplitude of the received signal at the aperture plane and the reconstructed image of the rectangular plate (The legend indicates the normalised values in dB).

Edges and corners can be observed clearly in the right figure compared with the original image at the aperture plane in the left figure. The PO simulation of the scanning and imaging in Matlab is proved feasible here and the image reconstruction offers more support to the availability the proposed simulation method.

2. Rectangular plate with a T-shaped slot at the centre

At the second step, a rectangular metal plate with a T-shaped slot at the centre is used as the test target of the PO simulation in Matlab. This plate has the same size as at the first step above. The scanning area coverage is 0.4 m* 0.4 m. Figure 4-8 shows the unprocessed image which is built directly from the amplitude of the received signal (left) and the reconstructed image using holography technique (right). The sampling number on x or y dimension is 41. Compared with the unprocessed image (left), the T shape can be recognised in the reconstructed image (right).

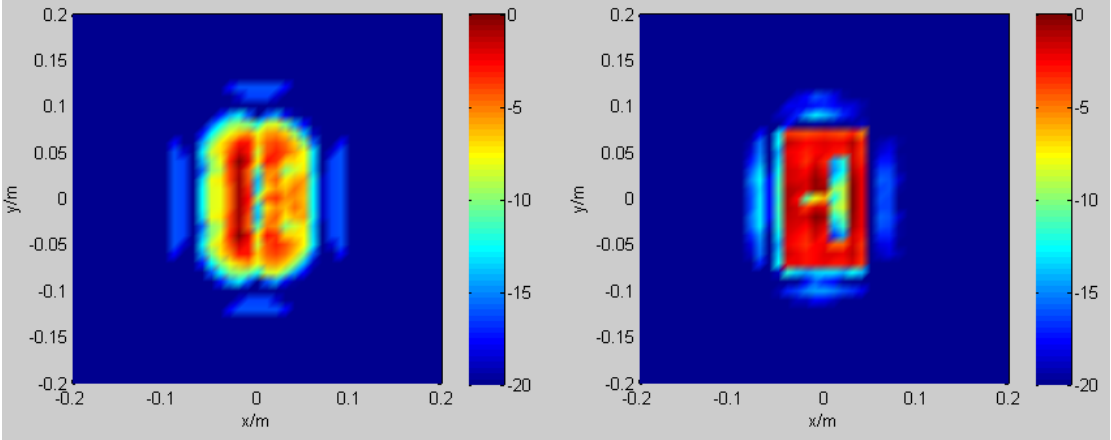

Figure 4-8 Amplitude of the received signal at the aperture plane and the reconstructed image of the rectangular plate with a T-shaped slot (The legend indicates the normalized values in dB). The sampling number is 41 * 41.

Then, the sampling number on x or y axis is improved to 81 to acquire a better image. The unprocessed image (left) and the reconstructed image using holography technique (right) with the sampling points of 81 * 81 are demonstrated in Figure 4-9. The reconstructed image here has the similar shape with the result above but more details can be observed especially the sharp edges of the T-shaped slot. To evaluate images realised, the profile of the target is added in images as dark lines illustrated in Figure 4-10. It can be observed that the reconstructed image fits quite well with the profile lines while the unprocessed image shares much less common points.

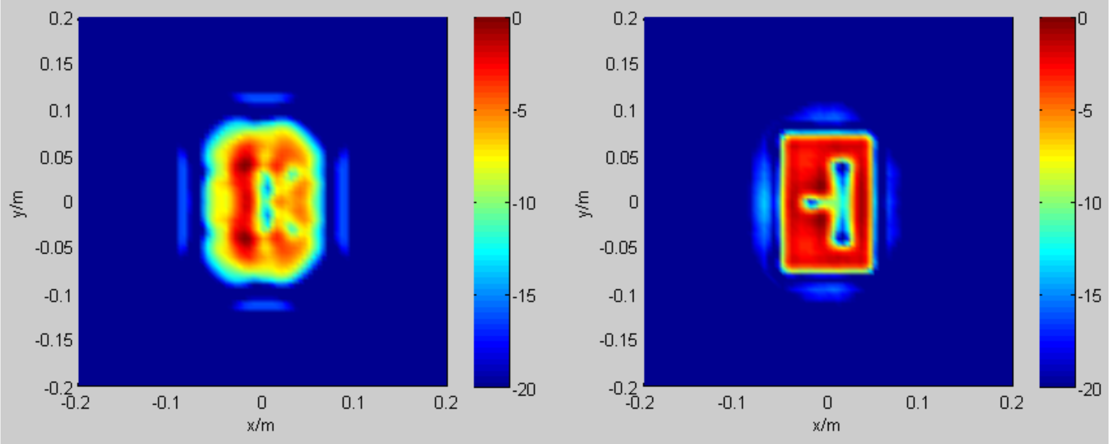

Figure 4-9 Amplitude of the received signal at the aperture plane and the reconstructed image of the rectangular plate with a T-shaped slot (The legend indicates the normalized values in dB). The sampling number is 81 * 81.

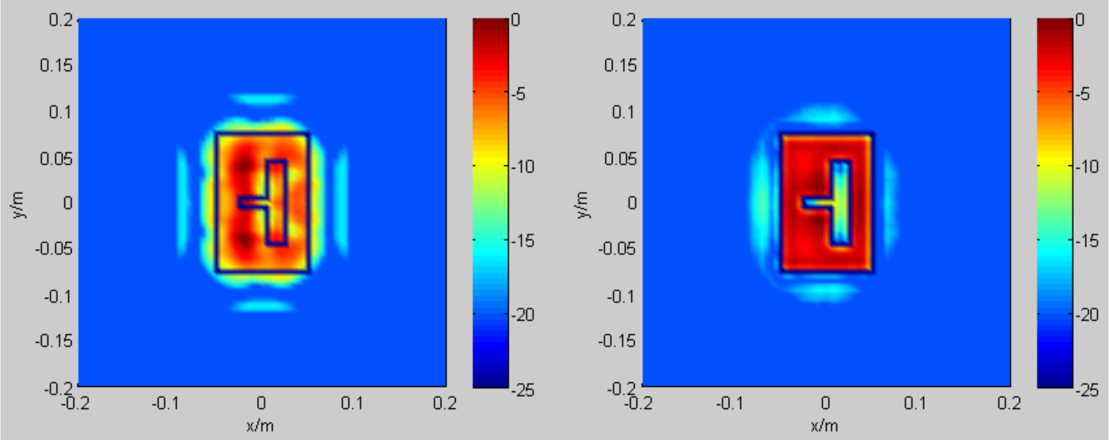

Figure 4-10 Comparison between the amplitude of the received signal at the aperture plane, the reconstructed image of the rectangular plate with a T-shaped slot and the target (The legend indicates the normalised values in dB). The sampling number is 81 * 81. The dark lines give the profile of the imaged target.

4.3.3 Comparison of the raster scanning scheme and the beam scanning scheme

Here we simplify the system to only one rotated antenna which can transmit and receive custom patterns and one target which can reflect/scatter all EM signals. Schematics of two different scanning approaches can be seen in Figure 4-11 and Figure 4-12, respectively. In the raster scanning scheme, as shown in Figure 4-11, Transmitter/Receiver (T/R) antenna is moved on the scanning (aperture) plane. The z_f-axis of the T/R antenna is pointed to different points on the target area. Then in beam scanning scheme (shown in Figure 4-12), T/R antenna is fixed at the origin. For the sake of comparison, the z_f-axis of the T/R antenna is pointed to different points on the target when the whole coordinate rotates [11].

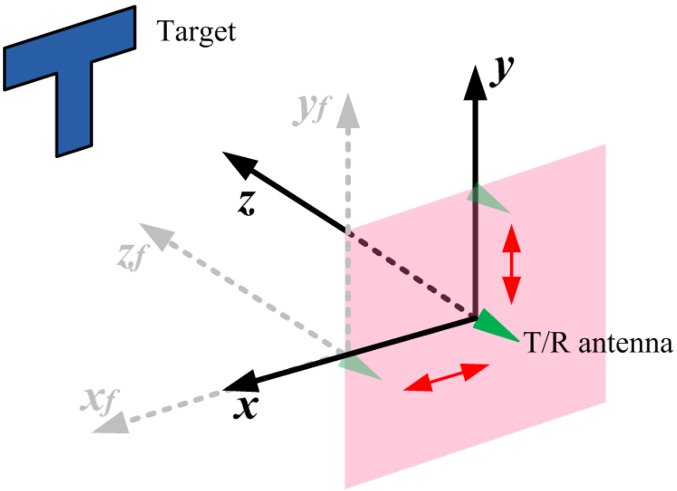

Figure 4-11 Configuration of the raster scanning [11].

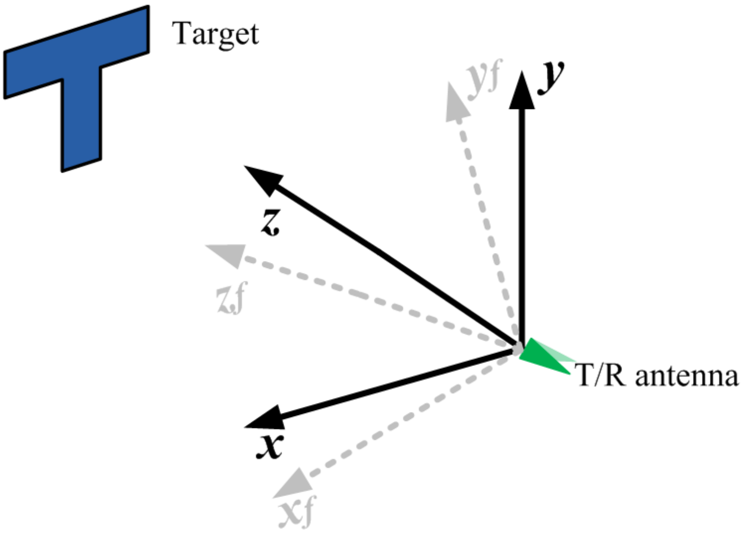

Figure 4-12 Configuration of the beam scanning [11].

Firstly, the PO simulator is applied to model the raster-scanning imager. The scanning beam covers an area of 0.4 m × 0.4 m. The long side along x-axis has the length of 0.14 m and the short side along y-axis has the length of 0.11 m which meet the real shape employed in experiments (the target can be found in Figure 4-13). The reflectivity of the target is set to 1 while the one of the background is 0 to build a high-contrast situation [12].

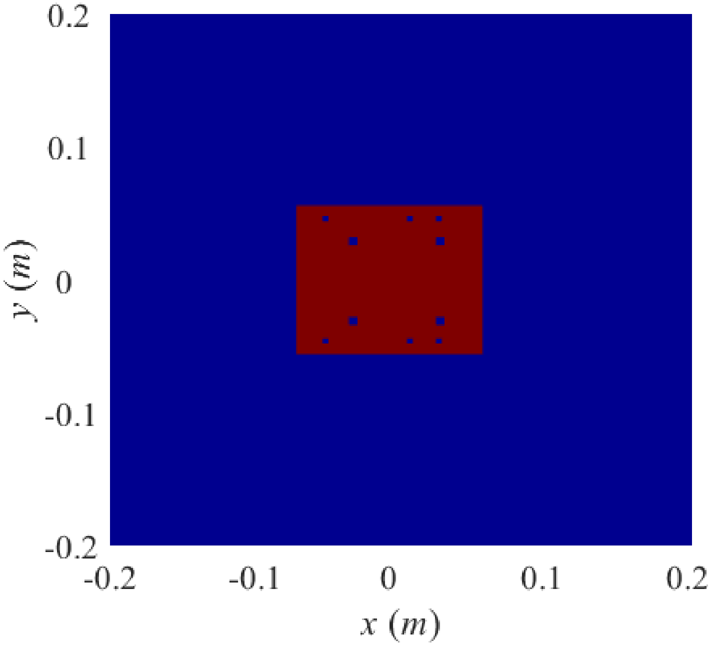

Figure 4-13 The target used in the raster scanning scheme simulation [11].

Figure 4-14 indicates simulated E-field amplitude (upper) and phase (lower) distribution based on signals received by the raster scanned antenna. The target can be observed in the amplitude figure but not clear enough. Figure 4-15 shows the reconstructed image of the reflector based on the microwave holography algorithm. Most details of the target can be found in this reconstructed image [12].

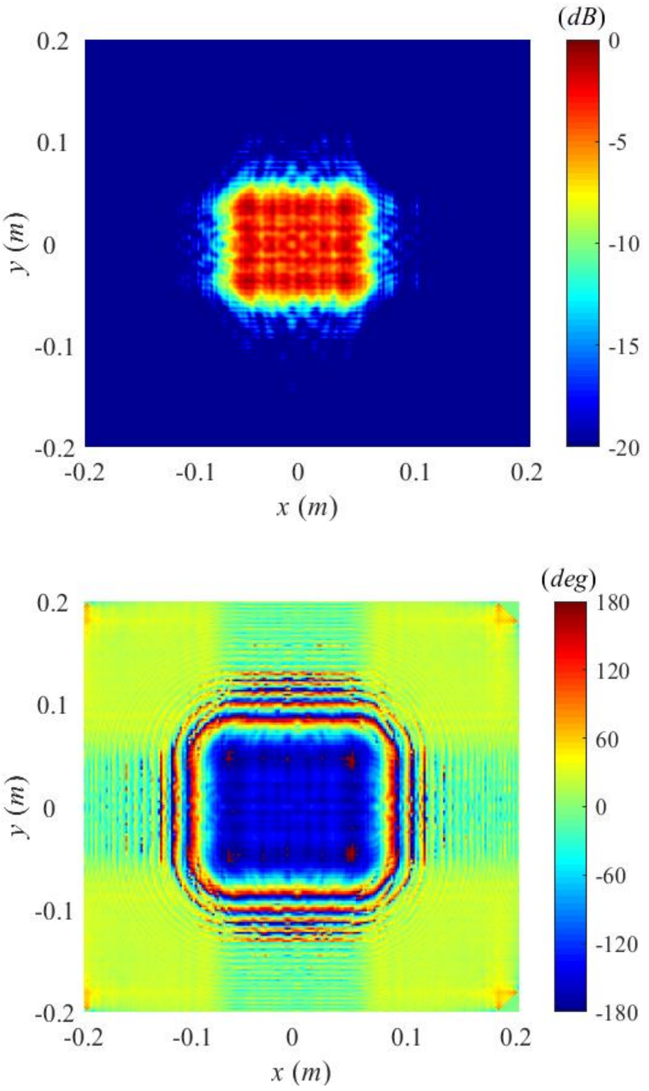

Figure 4-14 Simulated E-field amplitude(a) and phase(b) distribution based on signals received by raster scanning on the aperture plane. (The legend indicates the normalised values in dB and degrees) [12]

After the validation in the raster scanning approach, we extended this simulation method to the proposed beam-scanned imager. The scanning beam covers an area of 0.6 m × 0.6 m. The long side along x-axis has the length of 0.149 m and the short side along y-axis has the length of 0.1595 m which meet the real shape employed in experiments (the target can be found in Figure 4-16). The reflectivity of the target is set to 1 while the one of the background is 0 to build a high-contrast situation. Simulated beam-scanned results of the target in Matlab can be seen in Figure 4-17. Simulated E-field amplitude (upper) and phase (lower) distribution based on signals received on the equivalent aperture plane by the rotated antenna are shown in Figure 4-17. We can observe that there is a target in the area of $0.6\ \mathrm{m} \times 0.6\ \mathrm{m}$. However, the amplitude image here can't meet the demand in practical applications. Microwave/THz holography is then adopted to achieve better results [12].

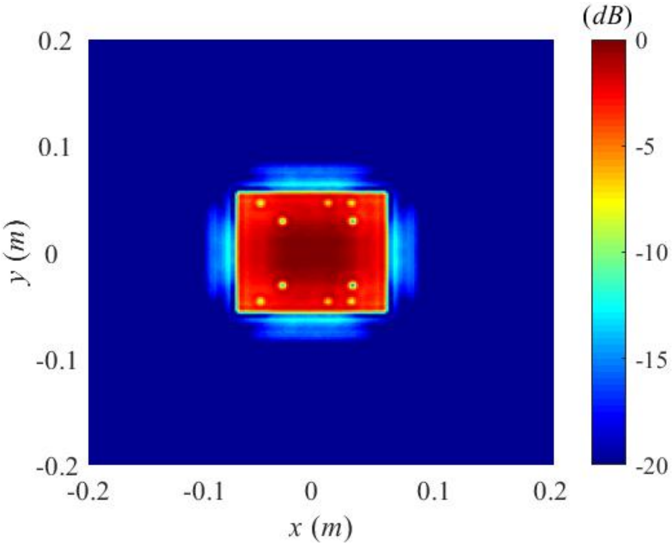

Figure 4-15 The reconstructed image of the reflector in raster scanning.
(The legend indicates the normalized values in dB) [12]

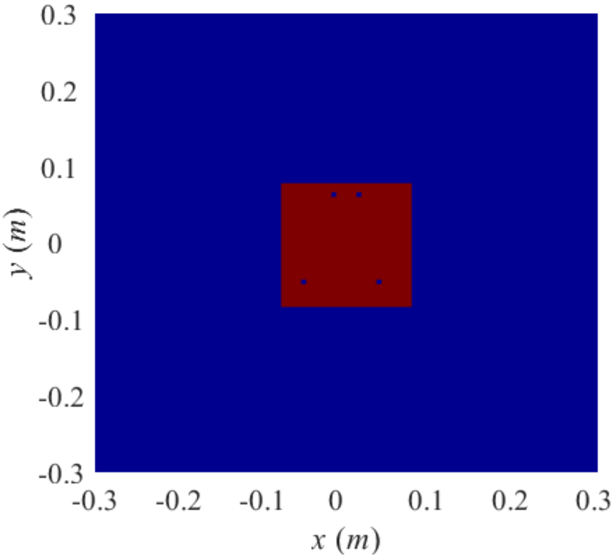

Figure 4-16 The target used in the beam scanning scheme simulation

Figure 4-18 shows the reconstructed image of the reflector based on microwave holography algorithm. The image can be seen obviously improved than results shown in Figure 4-17. The difference between the beam-scanned imager and the raster-scanned imager mainly lies in the compensation of amplitude and phase values at different positions in the *xy*-plane [12]. Comparisons between these two scanning approaches are demonstrated in Table 4-1. Although the time of the angular scanning is shorter than that of raster scanning, the image reconstruction in beam scanning scheme is about a 0.16 s longer time [11].

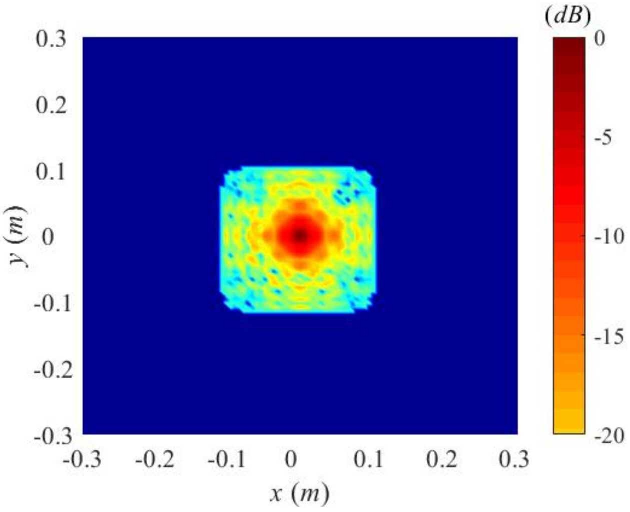

(a)

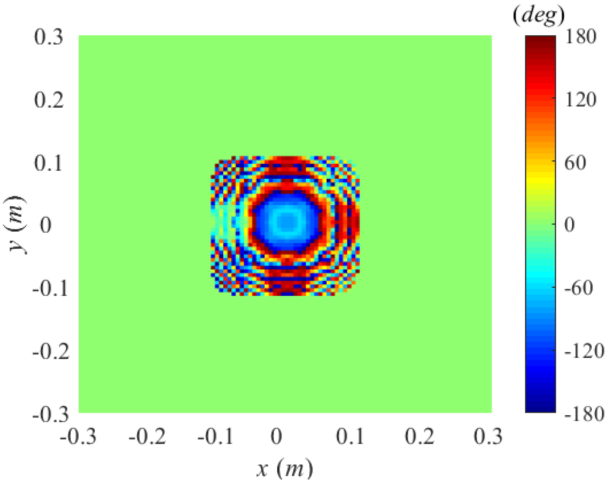

(b)

Figure 4-17 Simulated E-field amplitude(a) and phase(b) distribution based on signals received by beam scanning on the equivalent aperture plane. (The legend indicates the normalised values in dB and degrees) [12]

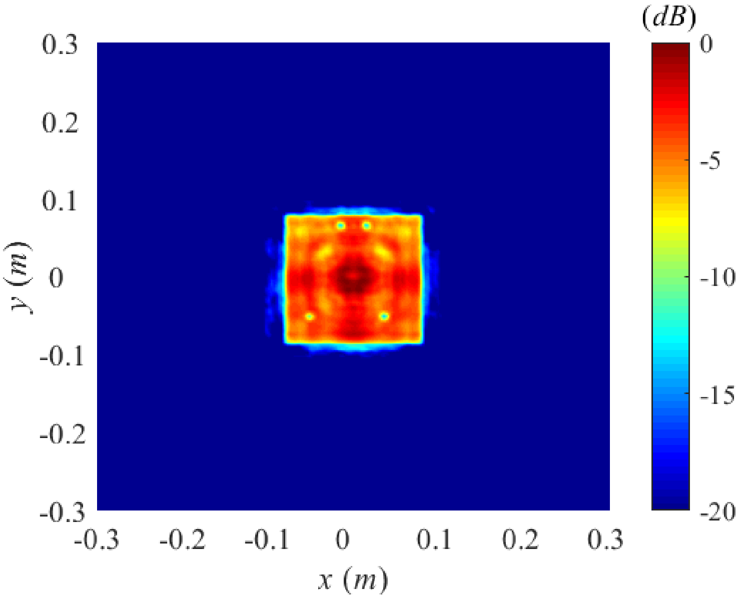

Figure 4-18 The reconstructed image of the reflector in beam scanning. (The legend indicates the normalised values in dB) [12]

Table 4-1 Comparisons between these two scanning schemes [12].

Approach	**Resolution(m)**	**Processing Time(s)**
Raster	0.00195	1.95
Beam	0.00195	2.11

4.4 Transposed convolution algorithm, partial inverse convolution algorithm and imaging result comparison

4.4.1 Transposed convolution (TC) algorithm

In previous studies, reconstructed images are all processed with the Back Propagation (BP) holography algorithm and good performance is realised with this algorithm. Let us go back to the original principle of the BP algorithm. The received signal $s(x, y)$ can be expressed as [13]:

$$\mathrm{s(x,y)} = \iint f(x', y', z') e^{-j2k\sqrt{(x'-x)^2+(y'-y)^2+z_0^2}} dx'dy' \qquad (4\text{-}4)$$

In the BP algorithm, using the plane wave expansion, Equation (4-4) can be converted into an equation which is in the Fourier transformation structure. Then $f(x', y', z')$ can be solved applying the Fourier transformation and the inverse Fourier transformation. One essential point here is the approximation of the plane wave expansion. The other is, in the spatial frequency domain (k-domain), the accumulation element of plane waves is limited in the orientation area $k_x^2 + k_y^2 < k^2$ [13].

If we consider this problem from another perspective, Equation (4-4) can be regarded as the convolution of the target reflectivity $f(x', y', z')$ and an exponential part $e^{-j2k\sqrt{x^2+y^2+z^2}}$. The problem is then simplified to solving the inverse convolution when $\mathrm{s(x,y)}$ and $Ck(x, x', y, y')$ are known, where $Ck(x, x', y, y') = e^{-j2k\sqrt{x^2+y^2+z^2}}$ is noted as the convolution kernel.

The new inverse convolution algorithm is actually inspired from the theory of PO algorithm. In the PO algorithm, the scattered electric field can be expressed as:

$$\mathbf{E}(\mathbf{r}) = -jk\eta \iint_{s'} [g_1\mathbf{J}(\mathbf{r}') - g_2(\mathbf{J}(\mathbf{r}') \cdot \hat{R})\hat{R}] \frac{e^{-jkR}}{4\pi R} ds' \qquad (4\text{-}5)$$

In previous simulations, it can be observed that (regarding the situation that transceivers have linear x-polarization)

$$\begin{cases} J_z = 0 \\ J_x \ll J_y \end{cases} \qquad (4\text{-}6)$$

Consider Equation (4-5) in the discrete situation, E-field can be calculated as the accumulation of the integrand part. The relationship between the detected E-field Ex at each observing point and the induced current can be illustrated as:

$$E_x \approx \sum C\left[g_1 J_x - g_2\left(\mathbf{J}(\mathbf{r}') \cdot \hat{R}\right)\hat{R}_x\right]\frac{e^{-jkR}}{4\pi R} \approx \sum C\left[g_1 J_x - g_2 J_y \hat{R}_y \hat{R}_x\right]\frac{e^{-jkR}}{4\pi R} \quad (4\text{-}7)$$

The induced current at each illuminated point can be calculated as:

$$\mathbf{J}(\mathbf{r}') = 2f(\mathbf{r}')\hat{n} \times \mathbf{H}^i(\mathbf{r}') \tag{4-8}$$

Where $f(\mathbf{r}')$ is the reflectivity of target points, $\hat{n}$ is the normal vector of the target surface, the incident magnetic field $\mathbf{H}^i(\mathbf{r}')$ can be replaced by the radiation of the Gaussian beam with the linear x-polarization:

$$\mathbf{H}_f^i(\theta, \varphi) = e^{kbcos\theta} e^{j\varphi}(1 + cos\theta)(\hat{\theta} sin\varphi + \hat{\varphi} cos\varphi)\frac{e^{-jkR}}{4\pi R} \tag{4-9}$$

Transform Equation (4-9) into the global Cartesian coordinate system and combine Equation (4-8) and (4-9),

$$\mathbf{J}(\mathbf{r}') \approx f(\mathbf{r}')G(\theta_d)W(d_{cp})\frac{d_{cp}}{R}\frac{e^{-jkR}}{4\pi R} \tag{4-10}$$

Where $G(\theta_d)$ is related to the taper angle θ_d which indicates the radiation field of the Gaussian beam. d_{cp} is the distance between illuminated points and the illuminated centre point. Here we also apply the approximation that $\alpha \approx sin\alpha \approx$ $\tan\alpha \approx d_{cp}/R$ under the premise the scale of the illuminated area of the beam is much smaller than the scanning distance. A filtering window $W(d_{cp})$ is added indicating whether the scattered signal of the particular point can be detected which is related to the dynamic range and the position of this point.

Replace J_x and J_y in Equation (4-7) with the corresponding part calculated in Equation (4-10), we can have the relationship equation that

$$E_x = \sum C_1 f(\mathbf{r}')G(\theta_d)W(d_{cp})\frac{d_{cp}}{R}\frac{e^{-j2kR}}{4\pi R^2} \tag{4-11}$$

If we set the received signal as $g(x, y)$, the object reflectivity as $f(x', y')$, then from Equation (4-11), we can have

$$g(x, y) = f(x', y') * h(x, y, x' - x, y' - y) \tag{4-12}$$

Where $h(x, y, x' - x, y' - y)$ is determined by the expression $G(\theta_d)W(d_{cp})\frac{d_{cp}}{R}\frac{e^{-j2kR}}{4\pi R^2}$ in Equation (4-11). The Equation (4-12) reveals that the received field can be the convolution result of the target reflectivity and a beam related convolution kernel, which meets the previous analysis. Figure 4-19 illustrates the scanning transceivers and the corresponding beam spot in the scanning area. Here we placed the assumption that the signal out of the spot is ignored. The illuminated area covered by the beam contains discrete meshes with different reflectivity as shown in Figure 4-20 (a). Corresponding values which can be noted as the scattering factor, determined by the illuminating beam which indicates the scattered signal from these meshes, can be built to the kernel matrix by adding zeros around the beam covered meshes as demonstrated in Figure 4-20 (b). Figure 4-21 visualizes Equation (4-12) as how each point on the aperture plane calculated from the accumulation of illuminated points on the target plane.

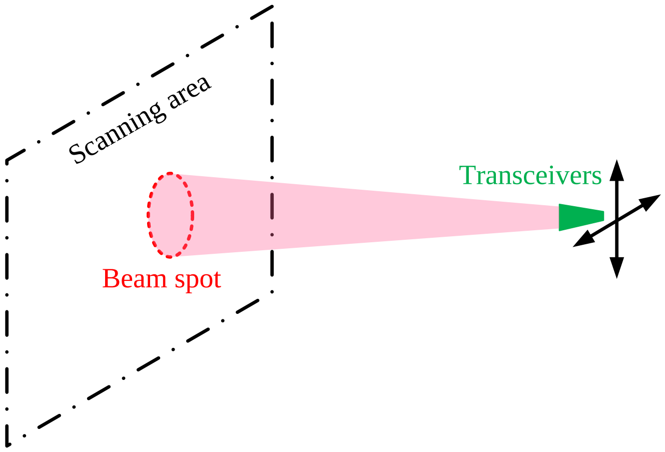

Figure 4-19 Scanning transceivers and beam spot in the scanning area.

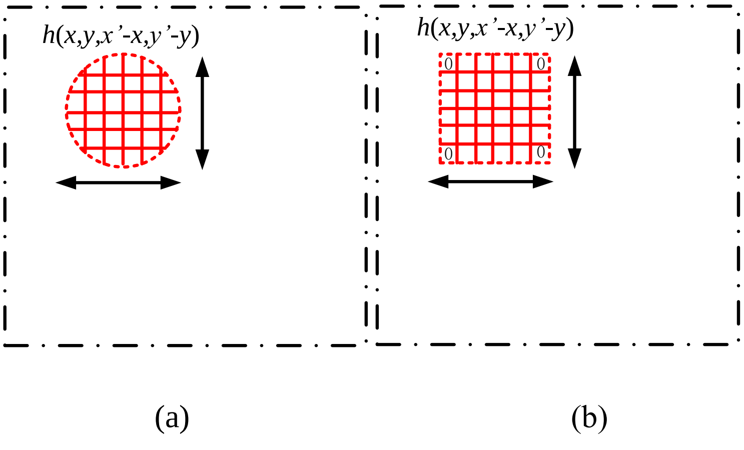

(a) (b)

Figure 4-20 Zero padding from the scattering factor values to the

convolution kernel.

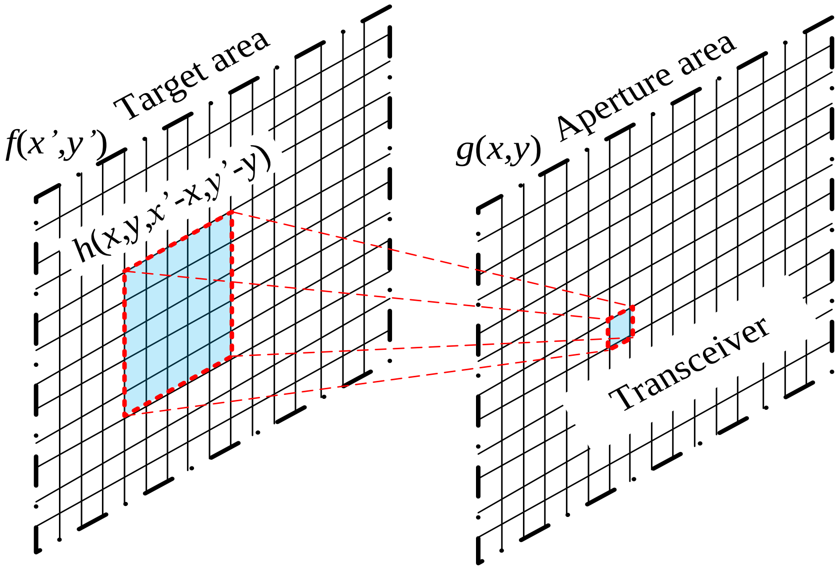

Figure 4-21 Visualization of the received signal from the convolution perspective.

In the raster scanning scheme, $h(x,y,x',y')$ remains the same for each observe point (x,y), which means $g(x,y)$ can be calculated with a direct convolution of $f(x',y')$ and $h(x'-x,y'-y)$ as:

$$g_R(x,y) = f(x',y') * h(x'-x,y'-y) \tag{4-13}$$

So $f(x',y')$ can be reconstructed by employing the convolution theorem to solve the inverse convolution problem. Applying Fourier transform on Equation (4-13), we will have

$$FT_{2D}[g_R(x,y)] = FT_{2D}[f(x',y') * h(x'-x,y'-y)] \tag{4-14}$$

Because

$$FT_{2D}[f(x',y') * h(x'-x,y'-y)] = FT_{2D}[f(x',y')]FT_{2D}[h(x'-x,y'-y)]$$

Equation (4-14) can be converted into

$$FT_{2D}[g_R(x,y)] = FT_{2D}[f(x',y')]FT_{2D}[h(x'-x,y'-y)]$$

$$FT_{2D}[f(x',y')] = FT_{2D}[g_R(x,y)]\{FT_{2D}[h(x'-x,y'-y)]\}^{-1}$$

$$f(x',y') = FT_{2D}^{-1}\{FT_{2D}[g_R(x,y)]\{FT_{2D}[h(x'-x,y'-y)]\}^{-1}\} \quad (4\text{-}15)$$

Compare Equation (4-15) to the BP algorithm:

$$f(x',y') = FT_{2D}^{-1}\{FT_{2D}[s(x,y)]e^{-2j\sqrt{4k_0^2-k_x^2-k_y^2}z_0}\} \quad (4\text{-}16)$$

These two different methods share the same principle in the reconstruction. However, for the inverse convolution problem, we can turn to other solutions. Learning from previous image results, we know that only the relative value is required to demonstrate the target information in the background. Therefore, the accurate amplitude value of the reconstructed image and, furthermore, the inverse convolution kernel are not necessary.

To solve the inverse convolution problem, we introduce the inverse convolution kernel $InvCk(x,x',y,y')$ which satisfies:

$$f(x',y') = s(x,y) * InvCk(x,x',y,y') \quad (4\text{-}17)$$

There are many approaches to calculate $InvCk(x,x',y,y')$, but the time-consuming calculation of the accurate inverse convolution kernel is not desirable for the discrete sampled and beamwidth limited imaging system. One feasible approach is the application of Transposed Convolution (TC) principle from the Deep Learning theory.

For each convolution processing, as shown in Figure 4-22, the result value $s_k(x,y)$ is related to all of original data values is involved in the beamwidth which is noted as $f_k^{i,j}(x',y')$ (*i,j* indicates the point located at different positions in the beam spot). It means that there is a correlation between the result value $s_k(x,y)$ and original data values $f_k^{i,j}(x',y')$. When it moves to the next result value $g_{k+1}(x,y)$, data values of $f_{k+1}^{i,j}(x',y')$ are involved. At the same time, $f_k^{i,j}(x',y')$ and $f_{k+1}^{i,j}(x',y')$ share some common points. We can't calculate $f_k^{i,j}(x',y')$ directly from $s_k(x,y)$, but from the reversal point of view, $f_k^{i,j}(x',y')$ is related to $\{\cdots,s_k^{i-1,j}(x,y),s_k^{i,j}(x,y),s_k^{i+1,j}(x,y),\cdots\}$. To be visualized, $f(x',y')$ in the shared orange part can be obtained from their correlated $s(x,y)$ as demonstrated in Figure 4-22. This is the primary principle of the Transposed Convolution.

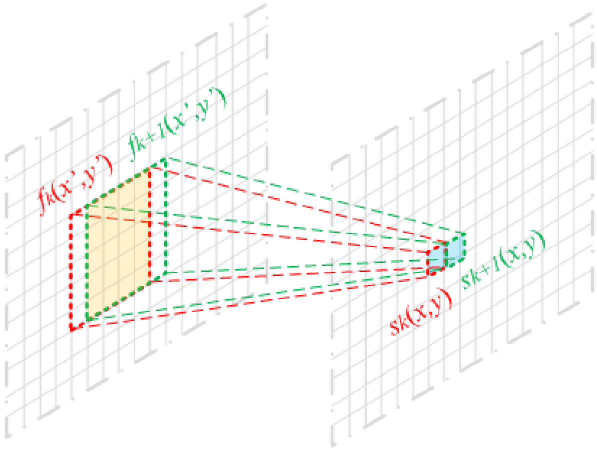

Figure 4-22 The relationship between the data on different plane

One feasible solution of $InvCk(x,x',y,y')$ is $e^{j2k\sqrt{(x-x')^2+(y-y')^2+z_0^2}}$ when the system satisfies Equation (4-4). Figure 4-23 gives amplitude results of $e^{j2k\sqrt{(x-x')^2+(y-y')^2+z_0^2}} * e^{-j2k\sqrt{(x-x')^2+(y-y')^2+z_0^2}}$ and the unit impulse function where the matrix scale is 101 by 101. They share the similar distribution for most points in the matrix.

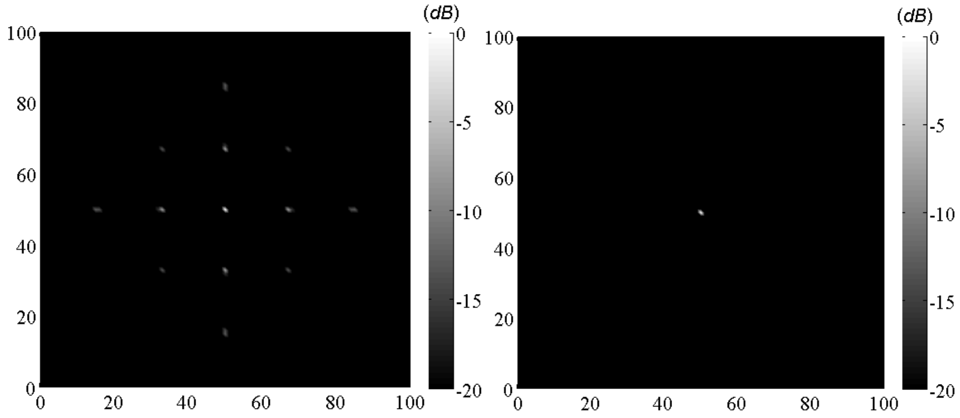

Figure 4-23 The amplitude distribution for the convolution result (left) and

the unit impulse function (right) (The legend indicates the normalised values in dB).

Furthermore, a rectangular metal plate is used as the test target in this part, to primarily evaluate the solution of the TC kernel. This plate has the size of 0.15 m * 0.1 m size. The scanning area coverage is 0.4 m* 0.4 m.

Figure 4-24 shows the unprocessed image which is built directly from the amplitude of the received signal (a) and the reconstructed image using BP holography technique (b). As a comparison, the unprocessed image which is built directly from the amplitude of the received signal (left) and the reconstructed image using the proposed TC algorithm (right) can be found in Figure 4-25. Unprocessed images are exactly the same. At the same time, reconstructed images using the BP algorithm and the TC algorithm have the comparable quality.

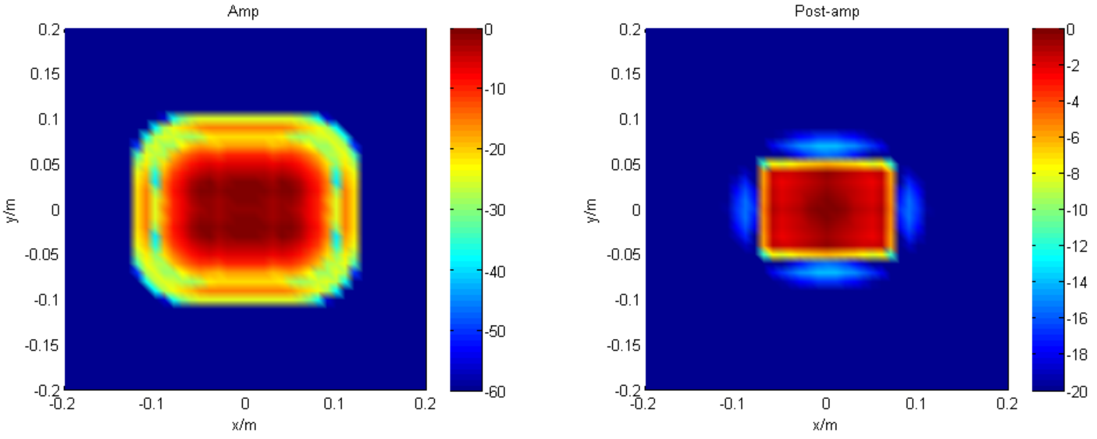

(a) unprocessed (b) processed

Figure 4-24 Amplitude of the received signal at the aperture plane (a) and the reconstructed image of the rectangular plate using BP holography algorithm (b) (The legend indicates the normalised values in dB).

It has to be noted is that the convolution kernel is the critical part of the TC algorithm. Using the target shape and the convolution kernel, we can have the unprocessed image directly. Accordingly, the image can be reconstructed with the unprocessed image and the inverse matrix of the convolution kernel. Normally, we can not measure the convolution kernel directly but it can be calculated because of its uniqueness in each imaging system.

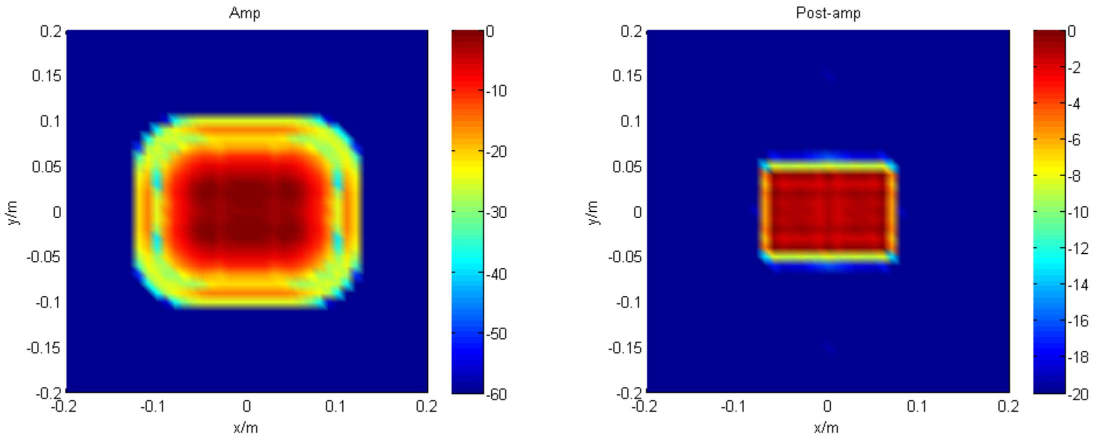

(a) unprocessed (b) processed

Figure 4-25 Amplitude of the received signal at the aperture plane (a) and the reconstructed image of the rectangular plate using inverse convolution algorithm (b) (The legend indicates the normalised values in dB).

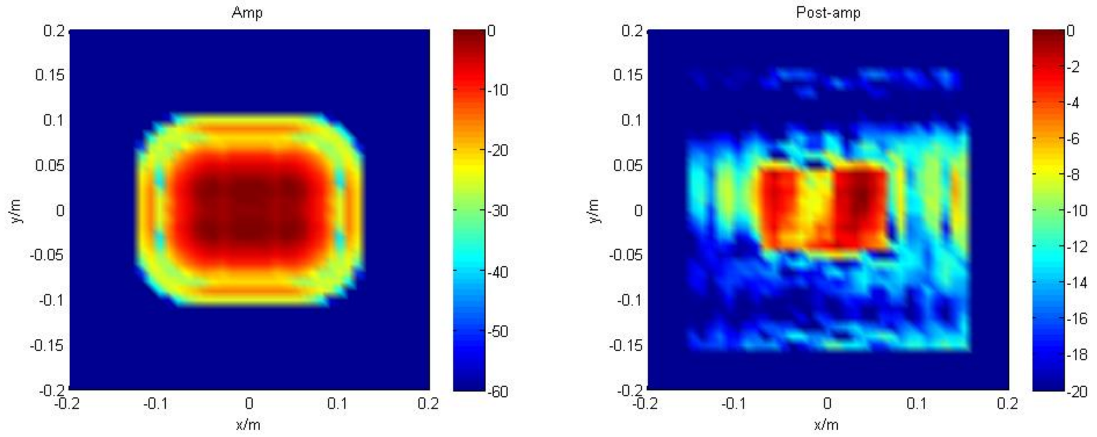

(a) unprocessed (b) processed

Figure 4-26 Amplitude of the received signal at the aperture plane (a) and the reconstructed image of the rectangular plate using inverse convolution algorithm with a broken convolution kernel (b) (The legend indicates the normalised values in dB).

Figure 4-26 gives an idea to acquire the convolution kernel. By setting values at random positions in the convolution kernel matrix used in the TC algorithm above to zero, a broken convolution kernel is applied in the reconstruction. Though it shares the same unprocessed image (left) in this reconstruction, the reconstructed image (right) will be quite different with good results shown above. The unique convolution kernel matrix can be realized with the reconstructed image and the shape of a target acted as the standard. Then this unique convolution kernel can be employed to complete the reconstruction for this imaging system.

What is more, the proposed TC algorithm include the transposed convolution kernel and the additional appropriate filtering window for different system settings to erase the effect of the ghost image. The process can be summarized as a direct convolution of the received signal and the transposed convolution kernel which is window filtered.

Here we build the simulation scenario which consists of a rectangular target which can reflect/scatter all EM signals, an ideal Gaussian beam transmitter and an ideal observe point located at the same place of the transmitter in MATLAB based on PO. In the raster scanned scenario, the transmitter and the detector will be moved in two dimensions simultaneously. Simulated raster-scanned results of the target in MATLAB can be seen in Figure 4-27. E-field amplitude (left) and phase (right) distribution based on signals received indicate that there is a rectangular target in the area of 0.4m*0.4m. However, the amplitude image here can’t meet the demand in practical applications [12]. BP and TC algorithm are applied respectively to reconstruct the original shape of the target [5].

Figure 4-28 shows reconstructed images of the reflector based on BP and TC algorithm where only amplitude distribution results are given. No obvious difference between images reconstructed by applying BP and TC algorithm can be observed, especially in the target area.

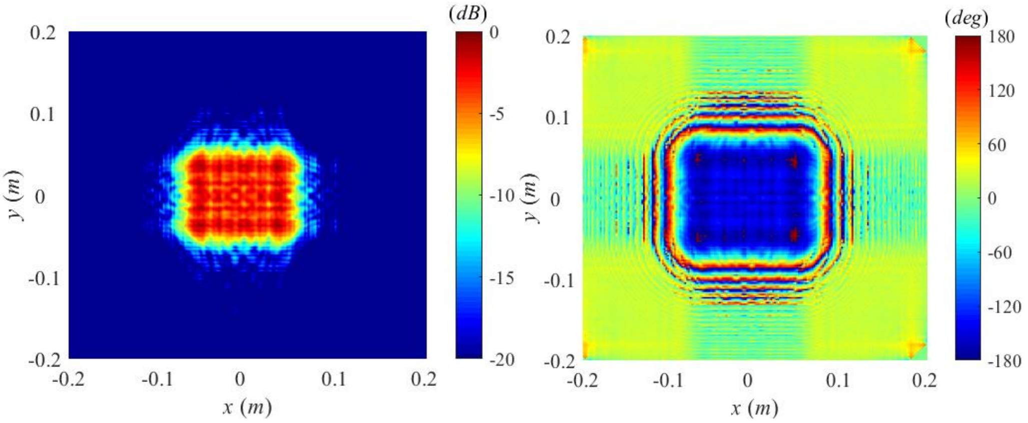

(a) amplitude (b) phase

Figure 4-27 Simulated E-field (a) amplitude and (b) phase distribution based on signals received by the raster scanned antenna (The legend indicates the normalised values in dB and degrees) [5].

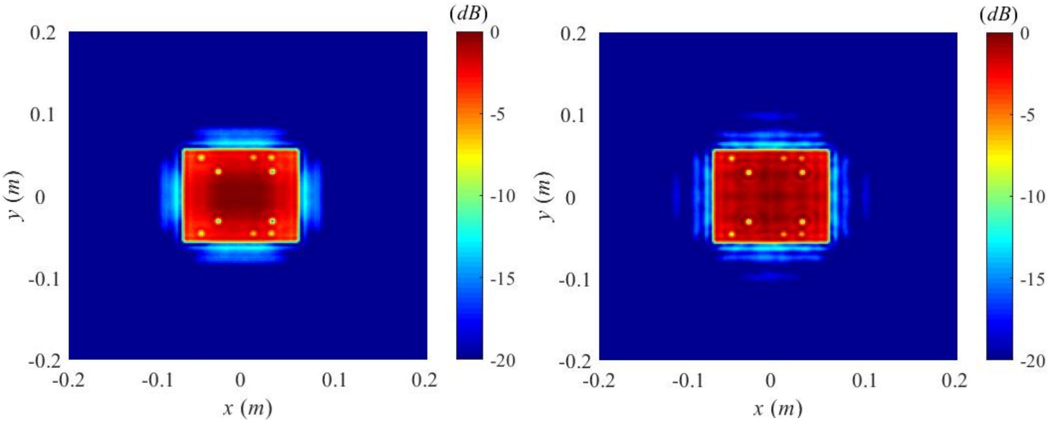

(a) BP (b) TC

Figure 4-28 Reconstructed images by applying (a) backpropagation algorithm; (b) proposed transposed convolution algorithm for the simulation evaluation (The legend indicates the normalised values in dB) [5].

Actually, besides the exponent expression of the proposed TC kernel, a filter on the amplitude of the TC kernel was also applied to avoid the ghost images around the real image. Furthermore, the filter varies for different sampling points. One TC kernel can be defined as:

$$InvCk(x,x',y,y') = e^{-\frac{(x-x')^2+(y-y')^2}{2F_{coef}}} \cdot e^{j2k\sqrt{(x-x')^2+(y-y')^2+z_0^2}} \qquad (4\text{-}18)$$

The generation and suppression of the ghost image can also be found in Ref. [4]. Here some practical referential filtering coefficients are given for different sampling points listed in Table 4-2.

Table 4-2 Filtering coefficients for different sampling points in an area of 0.4 m by 0.4 m.

Points	21	31	41	51	61	81	101
$\boldsymbol{F_{coef}}$ $(\times 10^9)$	1.125	1.125	0.5625	0.3375	0.225	0.12375	0.12375

4.4.2 Partial inverse convolution (PIC) algorithm

Besides the transposed convolution algorithm proposed above which focuses on the relative value of the reconstructed image, a Partial Inverse Convolution (PIC) can give another solution to the inverse convolution.

The scenario of 41 sampling point in each dimension is taken as the evaluation scenario. Firstly, the original target matrix (denoted as f_{mat}) is expanded to a vector f_{vec} as shown in Figure 4-29. At the same time, the convolution kernel matrix Ck_{mat} of each corresponding element in s_{mat} can be extended to a 41×41 matrix Ck'_{mat} by zero padding, and then converted into a column vector Ck'_{vec}. From the relationship:

$$s_{mat}(x,y) = f_{mat}(x',y') * Ck_{mat}(x,y,x',y') \qquad (4\text{-}19)$$

We can have

$$s_{mat}(x,y) = [Ck'_{vec}(x,y)]^{\mathrm{T}} \times f_{vec} \qquad (4\text{-}20)$$

where $s_{mat}(x,y)$ denotes the received signal of the point located at (x,y).

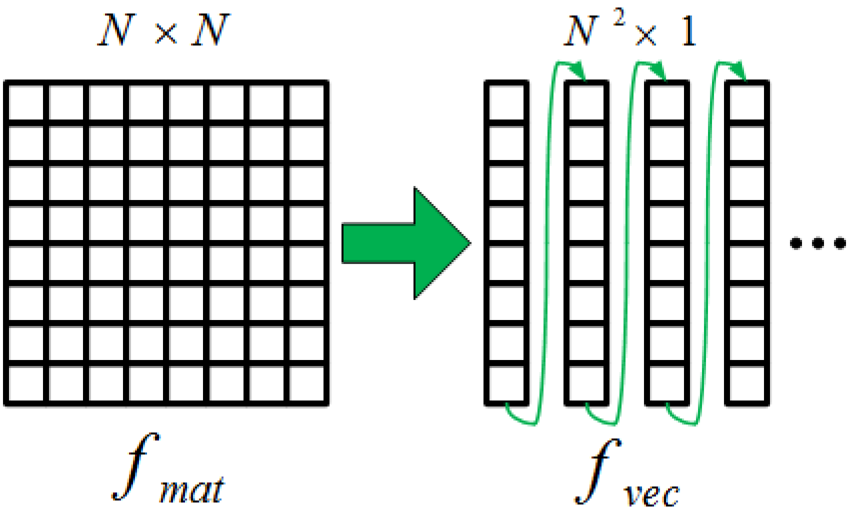

Figure 4-29 The conversion of the unprocessed matrix to a column vector

Actually, in Equation (4-20), the value at the single point is calculated from the multiplication of a 1×41^2 vector and a $41^2 \times 1$ vector. When the convolution kernel Ck_{mat} is fixed, the convolution in Equation (4-19) can realise the same result with Equation (4-20), which meets the normal raster scanning scheme. However, when the convolution kernel Ck_{mat} is variable according to the illuminating/recording point (x, y), Equation (4-19) will be a 'general' convolution which can't be calculated directly. This can be regarded as a 'three-dimensional convolution' problem. So another expression can be introduced to convert this three-dimensional equation to a two-dimensional equation which can be processed in Matlab.

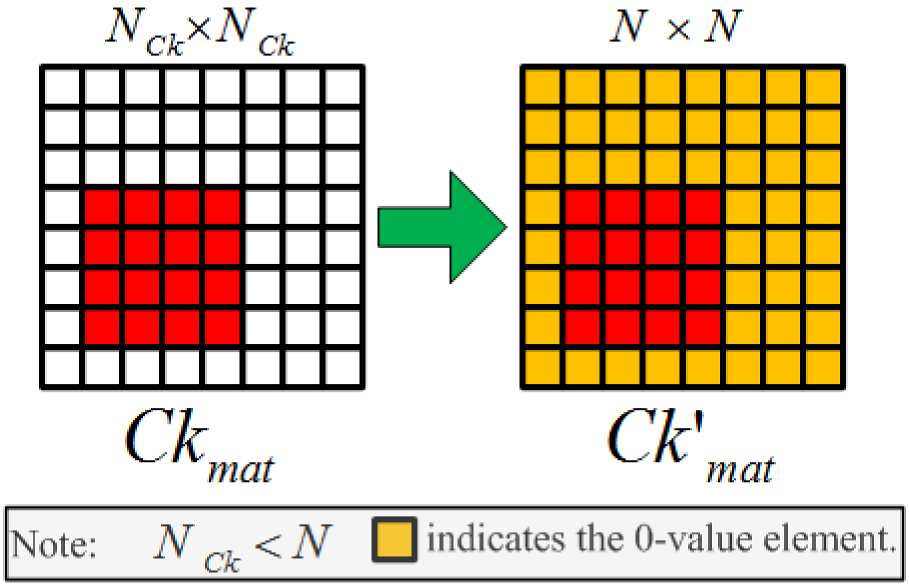

Figure 4-30 The zero padding: from the small-sized Ck_{mat} to the large-sized Ck'_{mat}.

From the previous discussion, we had a column vector Ck'_{vec} at the point of (x, y). Here different column vectors are placed in a row with the same order in f_{vec} to construct a new matrix Ck'_{mat_L} with the size of $41^2 \times 41^2$. Then Equation (4-19) can be expressed as

$$s_{vec} = Ck'_{mat\_L} \times f_{vec} \tag{4-21}$$

where the $41^2 \times 1$ column s_{vec} can be converted from s_{mat} in the same way as Figure 4-29. Normally, we have s_{mat} from the detected signal. To reconstruct the image, following procedures are required:

$$s_{mat} \rightarrow s_{vec}$$

$$f_{vec} = \left(Ck'_{mat_L}\right)^{-1} \times s_{vec}$$

$$f_{vec} \rightarrow f_{mat}$$

Since Ck'_{mat} is a zero-padded matrix which only contains the convolution kernel near the beam centre, $\left(Ck'_{mat_L}\right)^{-1}$ indicates a partial inverse convolution kernel.

Therefore, the reconstruction method here can be noted as Partial Inverse Convolution (PIC) and the core problem becomes the calculation of $\left(Ck'_{mat_L}\right)^{-1}$.

Firstly, the size of the convolution kernel Ck_{mat} needs to be confirmed. The partial inverse convolution kernel is calculated with 21, 15, 11 and 9-element convolution kernel, respectively. Figure 4-31 gives partial inverse convolution kernel results corresponded to the reconstructed point located at the centre.

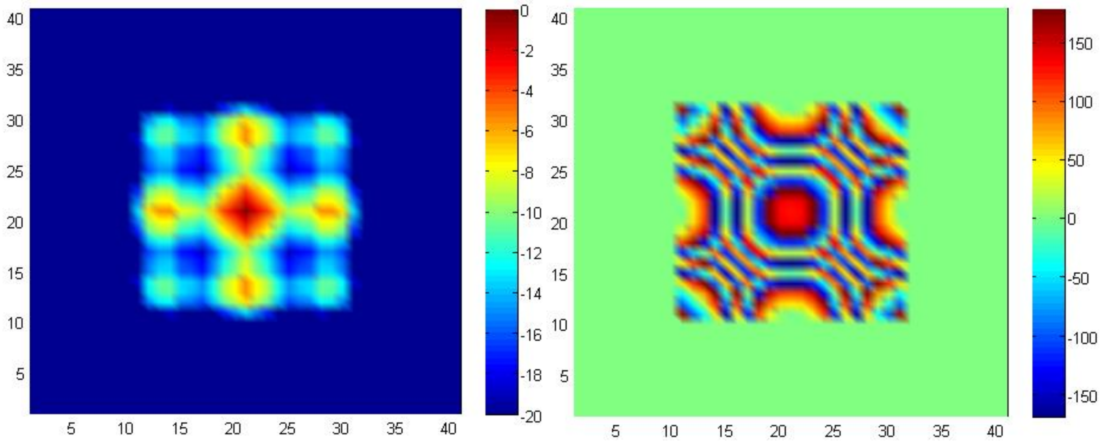

(a) 21-element amplitude

(b) 21-element phase

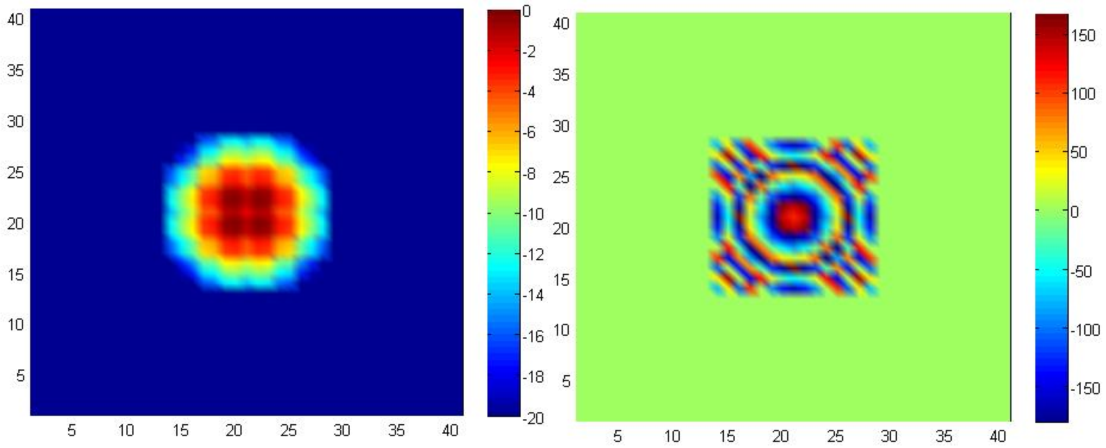

(c) 15-element amplitude

(d) 15-element phase

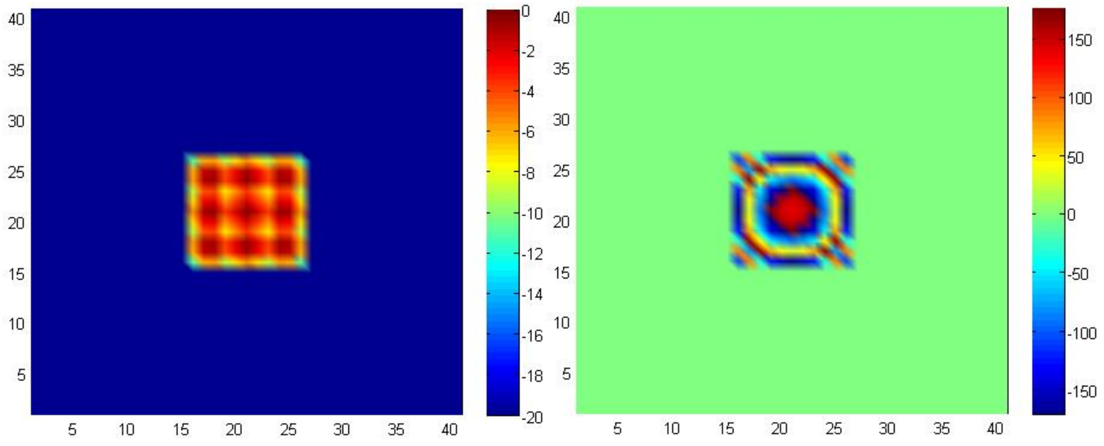

(e) 11-element amplitude (f) 11-element phase

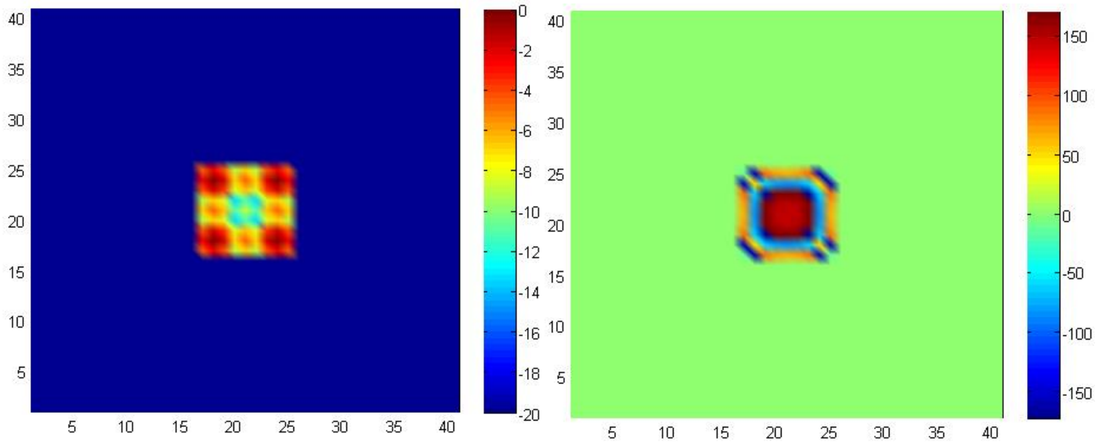

(g) 9-element amplitude (h) 9-element phase

Figure 4-31 Calculated partial inverse kernels with different size: (a) 21-element amplitude, (b) 21-element phase, (c) 15-element amplitude, (d) 15-element phase, (e) 11-element amplitude, (f) 11-element phase, (g) 9-element amplitude and (h) 9-element phase (The legend indicates the normalised values in dB and degrees).

Reconstructed images using these PIC kernels are demonstrated in Figure 4-32. It shows that11-element PIC kernel can reconstruct the best result compared to others. Phase distribution images in Figure 4-31 (b), (d), (f) and (h) share the similar concentric rings shape. However, peripheral parts of phase images for 21 and 15-element kernel doesn't remain the ring shape due to the limited boundary of the original convolution kernel matrix. On the other side, the phase image for 9-element seems too coarse due to the limited element number. So the 11-element PIC kernel is the most proper PIC kernel for the reconstruction. At the same time, it can be observed that the PIC kernel with the most uniform amplitude distribution acts as the best one. What is more, reconstructed images with normalised PIC kernel matrix are illustrated in Figure 4-33.

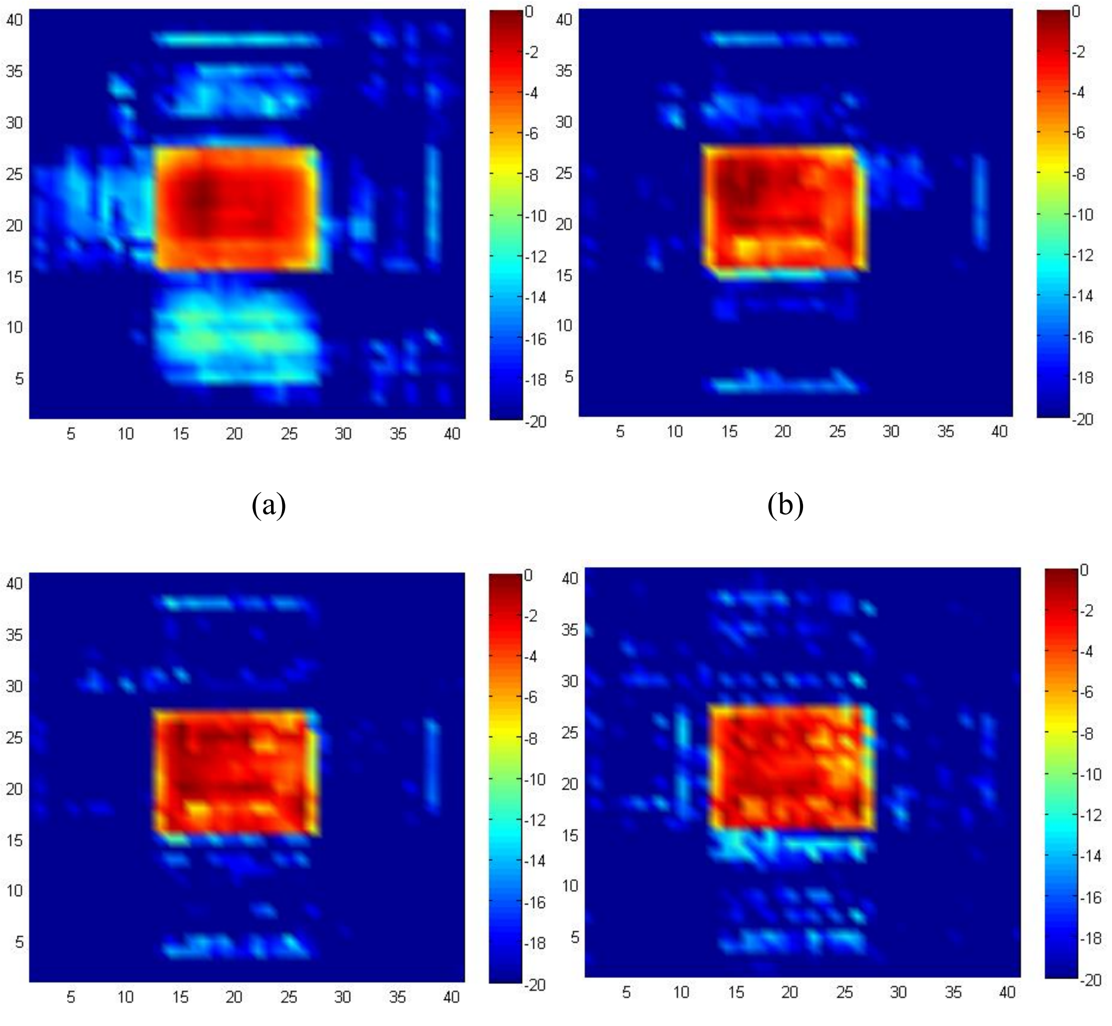

(a) (b)

(c) (d)

Figure 4-32 Reconstructed images with different PIC kernels: (a) 21-element, (b) 15-element, (c) 11-element and (d) 9-element (The legend indicates the normalised values in dB).

Normalized and oversized kernels perform worse compared to unnormalised ones. But in Figure 4-32 (c), (d) and Figure 4-33 (c) (d), normalized ones show the ghost image and background noise suppression performance. It has to be noted that the best

PIC kernel of 11 elements only applies to the experiment setting here which is correlated to the detection dynamic range, the screening distance, the beamwidth, and so on.

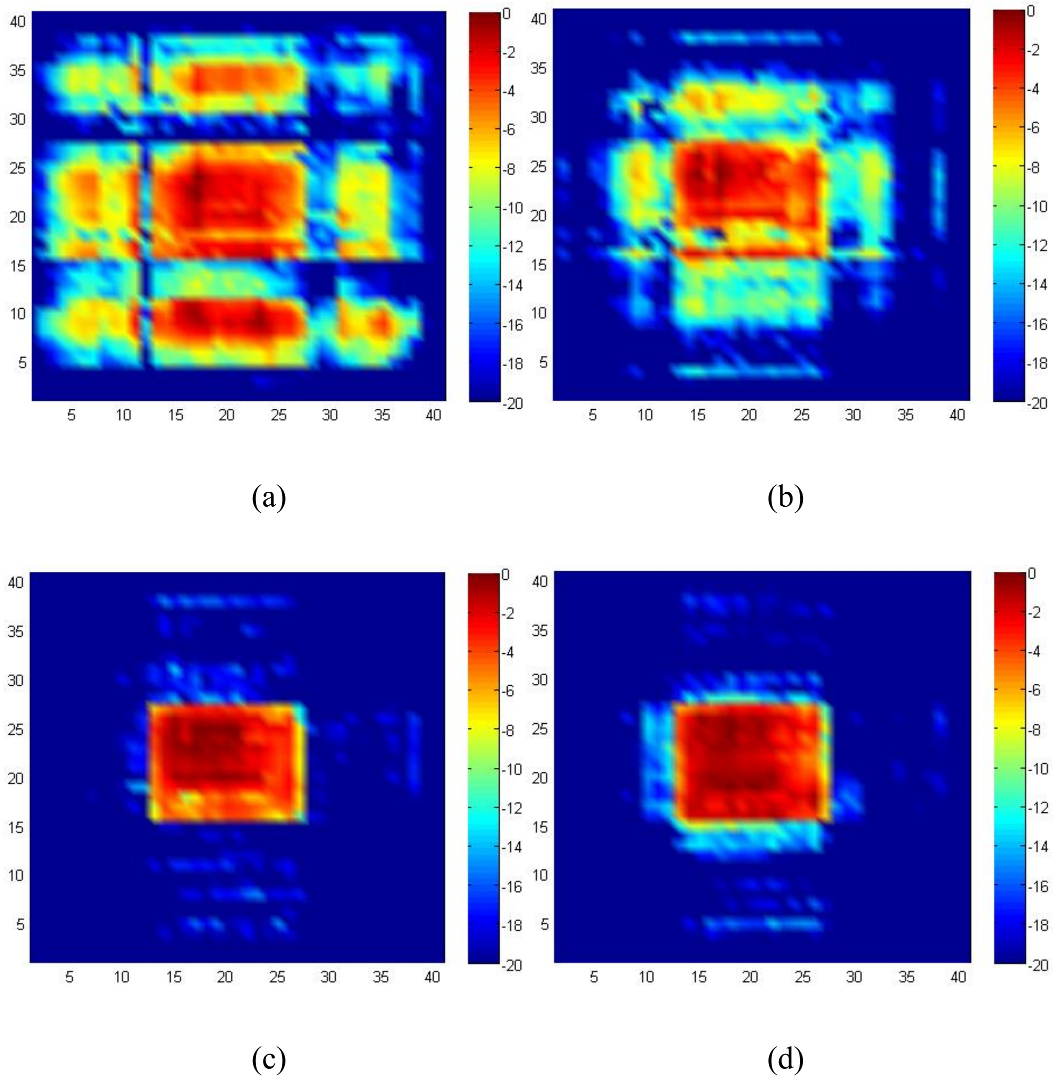

(a)

(b)

(c)

(d)

Figure 4-33 Reconstructed images with different normalized PIC kernels: (a) 21-element, (b) 15-element, (c) 11-element and (d) 9-element (The legend indicates the normalised values in dB).

In early studies, we found that reconstructed elements near target edges are not good compared to central elements. Only a part of the convolution kernel is applied in the calculation of PIC kernel, leading to the error near target edges. As shown in the left figure of Figure 4-34, the light red part was ignored in the calculation. To avoid this error, for elements near area edges, the kernel matrix is moved to the centre before the zero padding and PIC kernel calculation, as illustrated in Figure 4-34. Required PIC kernel size for different sampling points range from 21 to 101 are given in Table 4-3.

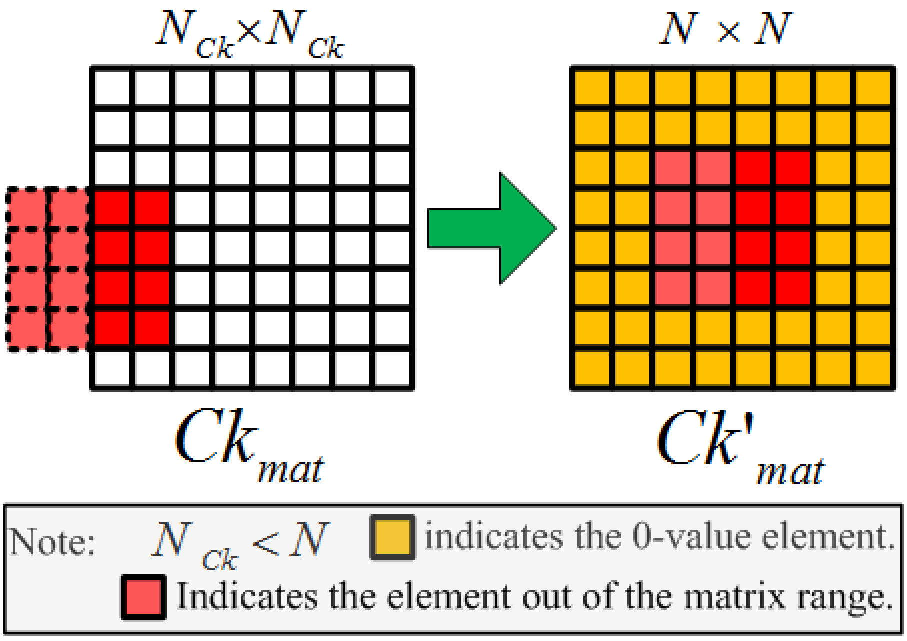
$N_{Ck} \times N_{Ck}$
$N \times N$
Ck_{mat}
Ck'_{mat}
Note: $N_{Ck} < N$
indicates the 0-value element.
Indicates the element out of the matrix range.

Figure 4-34 The zero padding for elements near area edges: from the small-sized Ck_{mat} to the large-sized Ck'_{mat}.

Table 4-3 Required PIC kernel size for different sampling points.

Points	21	31	41	51	61	81	101
kernel size	5	7	11	17	25	51	71

4.5 Summary

This chapter introduced the theory of Physical Optics and the application in the simulation of two scanning schemes. The performance of both raster-scanning and beam-scanning are studied using the PO simulation in Matlab with a rectangular target. It is demonstrated that the angular beam scanning can achieve a comparable image as the raster scanning with a negligible increase of processing time. Then in the second part, Transposed Convolution and Partial Inverse Convolution algorithms are proposed and compared with the conventional Back Propagation algorithm. By applying these two new algorithms, the reconstruction of the images can be speed up while remaining the image quality. Both of these algorithms have potential in following imaging system development.

4.6 References

[1] R. E. Collin and F. J. Zucker, Antenna theory, 1969.

[2] C. Scott, Modern methods of reflector antenna analysis and design. Artech House on Demand, 1990.

[3] TICRA, TICRA GRASP 9, GRASP9 Reference Manual, 2002.

[4] S. Hu, M. Zhou and X. Chen, Study on a Sparse Antenna Array for Terahertz Imaging, 10th UK-China Millimetre Waves and Terahertz Technology Workshop (UCMMT 2017), 2017.

[5] M. Zhou, S. Hu, Y. Alfadhl and X. Chen, Investigation of THz Image Reconstruction by Inverse Convolution Algorithm, 10th UK-China Millimetre Waves and Terahertz Technology Workshop (UCMMT 2017), 2017.

[6] http://deeplearning.net/software/theano/tutorial/conv_arithmetic.html.

[7] F. Gumbmann, L. Schmidt. Millimeter-wave imaging with optimized sparse periodic array for short-range applications. IEEE Transactions on Geoscience and Remote Sensing, vol. 49, no. 10, pp. 3629-3638, 2011.

[8] F. Gumbmann, P. Tran, A. Cenanovic, et al. Millimeter-wave imaging concepts: Synthetic aperture radar (SAR) and digital beam forming (DBF). Frequenz, vol. 63, pp. 106-110, 2009.

[9] F. Gumbmann, P. Tran, J. Weinzierl, et al. Multistatic short range Ka-band imaging

system, IEEE Microwave Conference, pp. 1-4, German, 2009.

[10] G. R. Lockwood, P. C. Li, M. O'Donnell, et al. Optimizing the radiation pattern of sparse periodic linear arrays. IEEE Transactions on Ultrasonics, Ferroelectrics, and frequency control, vol. 43, no. 1, pp. 7-14, 1996.

[11] M. Zhou, Y. Alfadhl and X. Chen, Study of Scanning Schemes for THz Holographic Imaging, 32nd International Union of Radio Science General Assembly and Scientific Symposium (URSI 2017 GASS), 2017.

[12] M. Zhou, Y. Alfadhl and X. Chen, Study on a THz beam-scanning system with offset Dragonian dual-reflector antenna, 9th UK-Europe-China Workshop on Millimetre Waves and Terahertz Technologies (UCMMT 2016), 2016.

[13] D. M. Sheen, D. L. McMakin, and T. E. Hall, Three-dimensional millimetre-wave imaging for concealed weapon detection, IEEE Transactions on Microwave Theory and Techniques, vol. 49, no. 9, pp. 1581–1592, 2001.

Chapter 5. Experimental evaluation of THz imaging systems

5.1 Introduction

In the previous chapters, the beam scanning THz imaging system is proposed and simulated compared with the raster scanning scheme. In the raster scanning scheme, Transmitter/Receiver (T/R) antenna is moved on the scanning (aperture) plane. The $\mathrm{z_f}$-axis of the T/R antenna is pointed to different points on the target area. Then in beam scanning scheme, T/R antenna is fixed at the origin. For the sake of comparison, the $\mathrm{z_f}$-axis of the T/R antenna is pointed to different points on the target when the whole coordinate rotates. In this chapter, some experimental works based on the raster scanning scheme and the beam scanning scheme will be presented for the purpose of comparison. More detailed analyses are also included to study scanning schemes from different perspectives.

5.2 Experimental configuration of the raster scanning system and imaging result analysis

The configuration of the raster scanning imaging system is shown in Figure 5-1. Two identical corrugated horns are used as the transmitter and receiver with the half-power beam width (HPBW) of about 14°. In this figure, the imaging distance Δz and, the dimension of target D_T are chosen to be 1600 mm and 400 mm, respectively. The main parameters need to be determined in this experiment are imaging array element spacing Δd and array dimension D_A. Several groups of different Δd and D_A are tested and reconstructed images are compared to achieve optimal values.

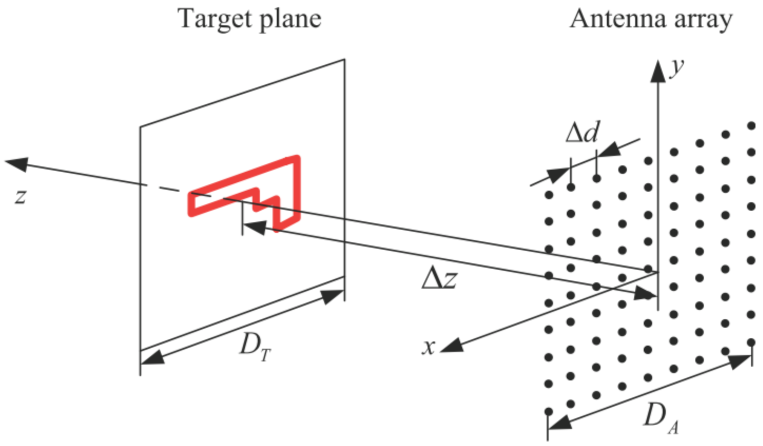

Figure 5-1 Raster scanning system configuration.

The schematic of this terahertz imaging system is shown in Figure 5-2. Transmitter and receiver antennas are connected to PNA-X through two N5256AW05 millimetre-wave modules. In the raster scanning procedure, a single antenna is moved in two dimensions controlled by motors with a specific step. Data are recorded with the antenna at each position. These data are summarized together then to construct an image of the target. With the antenna at the different position, a virtual antenna matrix can be formed. However, considering the rigid waveguide connection between antennas and other devices, the target is fixed on a scanner which can be moved in x-dimension and y-dimension with two motors controlled by NSI 2000 measurement system instead [1]. Considering the reciprocity, the movement of the target can also achieve the same performance of the raster scanning on the aperture plane. Then the signal from PNA-X and NSI 2000 are imported into PC to reconstruct the image of the target [2].

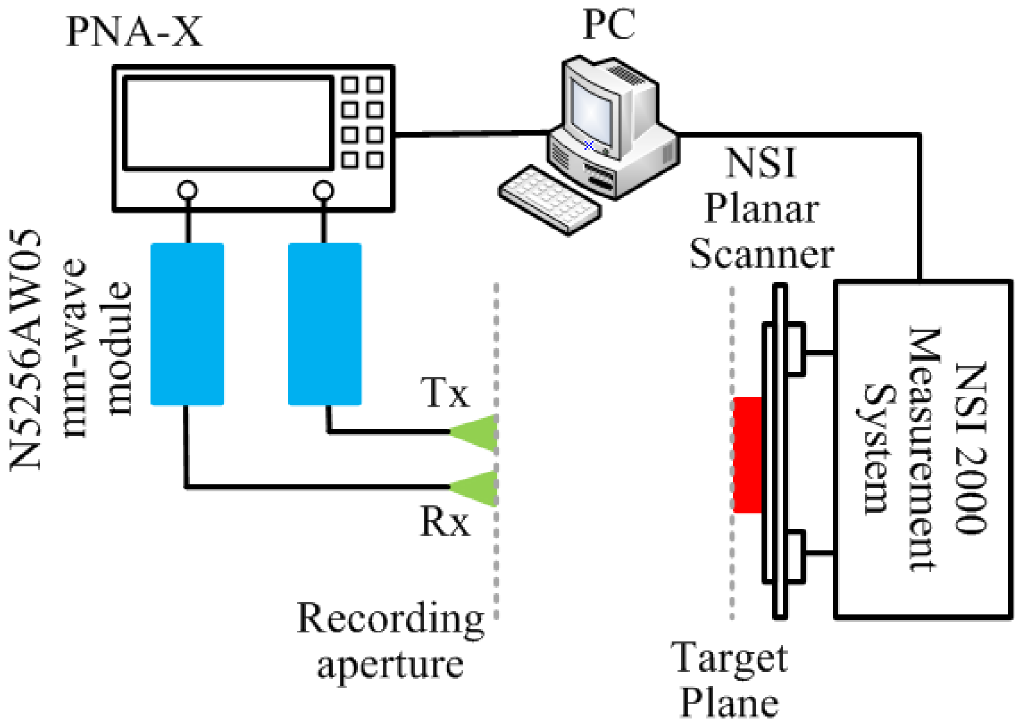
PNA-X
PC
NSI
Planar
Scanner
N5256AW05
mm-wave
module
Tx
Rx
Recording
aperture
NSI 2000
Measurement
System
Target
Plane

Figure 5-2 Schematic of terahertz imaging system.

A photograph of the experimental environment is shown in Figure 5-3.

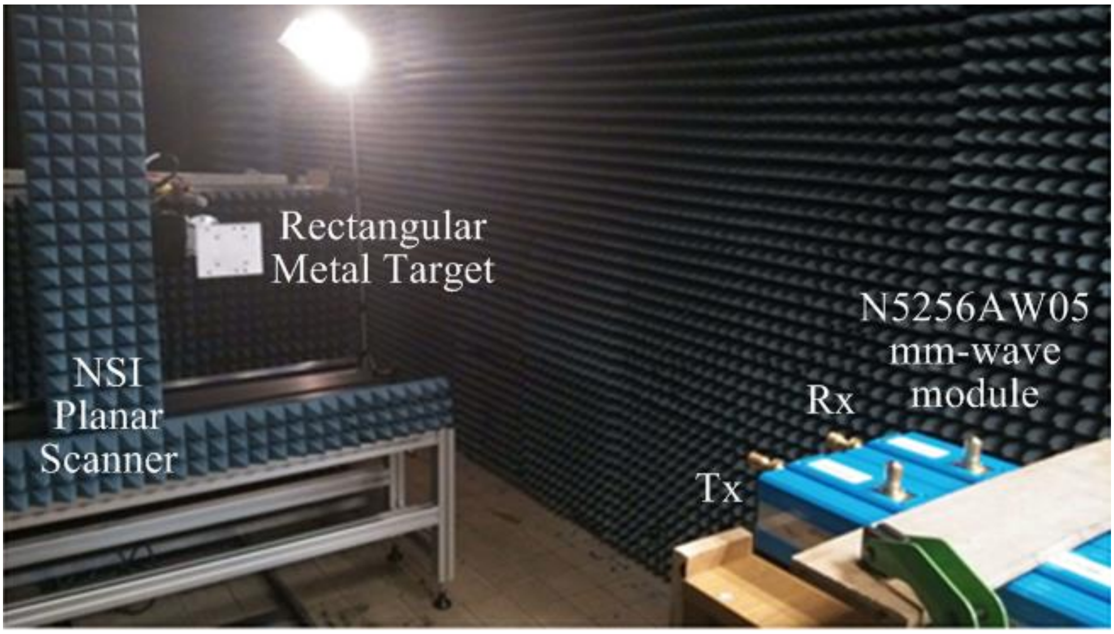
Rectangular
Metal Target
NSI
Planar
Scanner
N5256AW05
mm-wave
module
Rx
Tx

(a)

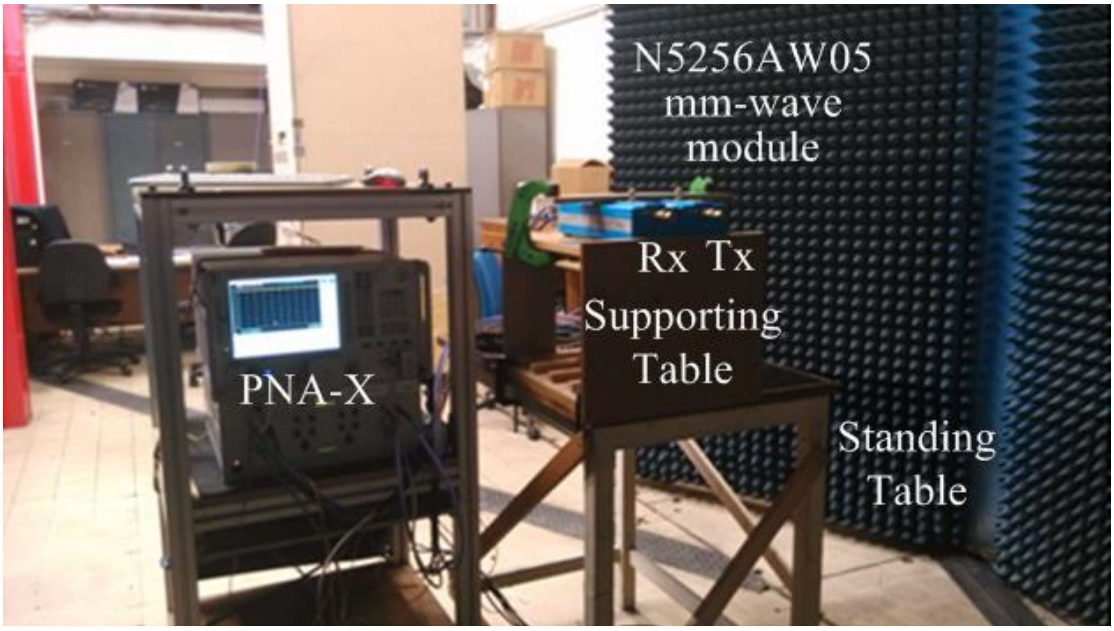

(b)

Figure 5-3 Photographs of the experimental environment (a) the NSI 2000 scanner and the target and (b) the PNA-X and horn antennas.

5.2.1 Holography transformations in the experimental system

By applying the algorithm derived earlier, the image at the target plane can be imaged as demonstrated in Figure 5.10. Compared with an ideal continuous situation, the data received is a discrete one. The antenna near-field problem in rectangular coordinates is particularly suitable for the DFT (Discrete Fourier Transformation) technique because their near field and PWS (Plane Wave Spectrum) are both of finite extent; that is, they are 'almost space-limited' and 'almost band-limited' [3]. The first step is to decompose the electric field into the superposition of a series of plane waves

$$F_A(k_x, k_y) = \sum\sum E(x, y) e^{-j(xk_x + yk_y)} \tag{5-1}$$

Where x, y is the position of the sampling points on target plane, k_x and k_y are the azimuth and elevation spatial frequency, respectively, $E(x, y)$ is the two dimensional field distribution measured (include the amplitude and the phase), and $F_A(k_x, k_y)$ is the two dimensional angular spectrum [1]. Then the plane wave components is phase shifted back to the depth of the target

$$F_T(k_x, k_y) = F_A(k_x, k_y)e^{k_z\Delta z} = \sum\sum E(x, y) \cdot e^{-j(xk_x+yk_y)}e^{k_z\Delta z} \qquad (5\text{-}2)$$

Where k_z is the spatial frequency along z-axis and Δz is the distance between antenna aperture and the target. Inverse 2-D FFT is then applied to transform the angular spectrum on the target plane, $F_T(k_x, k_y)$, back to the spatial domain

$$f_T(x, y) = \sum\sum F_T(k_x, k_y)\, e^{j(xk_x+yk_y)} \qquad (5\text{-}3)$$

Where $f_T(x, y)$ is the two dimensional field distribution at the target plane. At last, the target image can be achieved with the amplitude of the IFFT yields. The equations below are the definition of k and the relationship between k_x, k_y, k_z and k, respectively.

$$k_z = \sqrt{(2k)^2 - k_x^2 - k_y^2} \qquad (5\text{-}4)$$

$$k = 2\pi/\lambda \qquad (5\text{-}5)$$

It has to be noticed that $k_{xm} \neq k$ and $k_{ym} \neq k$. k_{xm} and k_{ym} are only determined by Δx and Δy while k_z is still affected by k. It means that the wave length λ or the frequency f only plays a role in k_z. In Equation (5-4), k in normally known $k_z = \sqrt{k^2 - k_x^2 - k_y^2}$ is replaced by *2k* because the situation is a round-trip one.

5.2.2 Spatial sampling interval

An adequate selection of sampling interval plays a key role in a successful imaging system. Normally, many researchers have used the Nyquist sampling criterion in the worst case scenario for the selection of the sampling spacing.

However, the worst case Nyquist sampling interval will result in a long scanning time, which is not desirable for the security related applications. Considering a compromise between the imaging speed and the image quality, an optimal sampling scheme needs to be studied. Actually, the sampling scheme is related to many factors, including the wavelength (λ), size of the aperture (D_A), size of the target (D_T), the distance between the target and the aperture ($\varDelta z$) and the transceiver antenna beam width.

In the quasi-monostatic experimental imaging system, the transmitting and receiving horn antennas are separated but in approximately the same location, and it appears to be a round-trip problem. Consider the frame displayed in Figure 5-4, the maximum size of the target is d and the target is located at the centre of the scanning area. The weak signal received beyond the target area can be ignored because it doesn't affect the holographic imaging quality. So the maximum phase shift occurs between two sampling points near one edge of the target when receiving the signals reflected from the other edge will be $2k_0(L_1 - L_2)$. The difference in distance is

$$\begin{aligned} L_1 - L_2 &= \sqrt{d^2 + (\Delta z)^2} - \sqrt{(d - \Delta d)^2 + (\Delta z)^2} \\ &= \frac{2d\Delta d - (\Delta d)^2}{\sqrt{d^2 + (\Delta z)^2} + \sqrt{(d - \Delta d)^2 + (\Delta z)^2}} \\ &\approx \frac{2d\Delta d}{2\sqrt{d^2 + (\Delta z)^2}} = \frac{d}{\sqrt{d^2 + (\Delta z)^2}}\Delta d \\ &= \Delta d sin\theta_T = \Delta L \end{aligned} \tag{5-6}$$

where $\varDelta d$ is the distance between two sampling points, i.e. sampling interval. Then the Nyquist sampling criterion must be satisfied as

$$2k_0(L_1 - L_2) < \pi \tag{5-7}$$

Considering Equation (5-6), we have

$$2k_0 sin\theta_T \Delta d < \pi \tag{5-8}$$

$$\Delta d < \frac{\pi}{2k_0 sin\theta_T} \tag{5-9}$$

For the worst case scenario that the target being very near to the aperture, we have $\theta_T \approx 90^{\circ}$. According to Equation (5-9), the sampling interval (Δd) should satisfy

$$\Delta d < \frac{\lambda}{4} \tag{5-10}$$

where $\lambda = 2\pi/k_0$. This sampling interval is in agreement with the theoretical one in Ref. 4.

In addition, we need to consider the beam width of the highly directional transmitting and detecting antennas. The received signal would be below the detection threshold if it arrives beyond a certain beam width angle of the antenna. We define this angle as Threshold Power Beam Width (TPBW) angle, which is system dependent. If θ_T is larger than the TPBW angle, then the distance difference should be calculated as

$$L_1 - L_2 \approx \Delta d sin\theta_{TPBW} \tag{5-11}$$

where θ_{TPBW} is the angle of the TPBW. The following sampling interval limit must be satisfied:

$$\Delta d < \frac{\pi}{2k_0 sin\theta_{TPBW}} \tag{5-12}$$

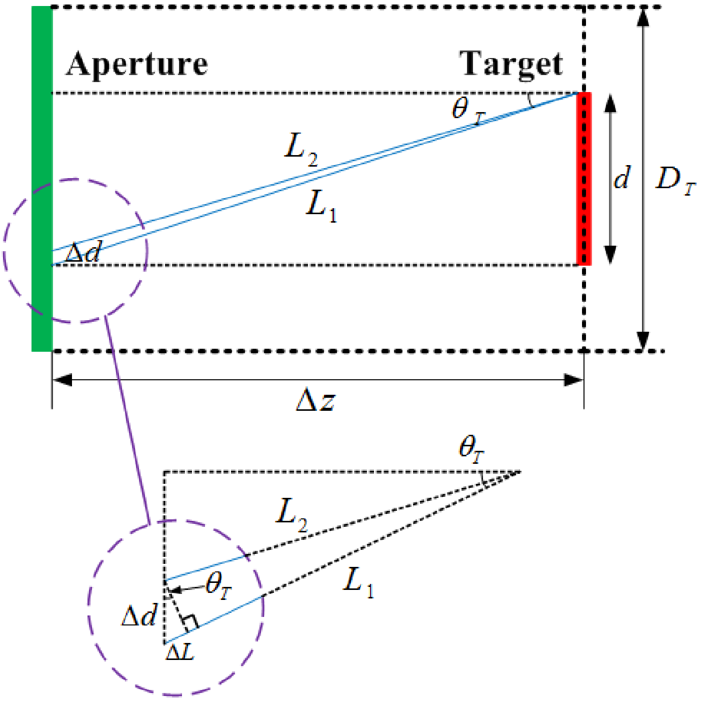

Figure 5-4 The schematic for sampling interval calculation. The maximum phase shift between two sampling points is approximatively $2k_0\Delta L$.

We can conclude that in order to satisfy Nyquist sampling criterion, the sampling interval should be

$$\Delta d < \frac{\pi}{2k_0 sin\theta} \;,\; \theta = min\{\theta_T, \theta_{TPBW}\} \tag{5-13}$$

5.2.3 Line spread function (LSF)

Here we have followed the same approach adopted in Ref. 1 to assess the Point Spread Function (PSF) and Line Spread Function (LSF) of the imaging system. A target with knife-edge as shown in Figure 5-5 is imaged horizontally and vertically. The knife-edge is tilted 1.75° from vertical or horizontal. As the rectangular-aperture imaging system is assumed to have a PSF of Sinc function, the Min-Max normalized Sinc Integral-function is fitted to brightness curves across horizontal and vertical knife-edge (Edge Spread Function -ESF) [4]:

$$Si\left(\theta_{pix}(x)\right) = \frac{2}{x}\left(\int sinc\frac{k_0 L\theta_{pix}}{2} d\theta_{pix} + \frac{\pi}{2}\right) \tag{5-14}$$

where L is the length of the image area and $\theta_{pix} = \tan^{-1}(x_{sub}/\Delta z)$ is the angular direction from the aperture to the sub-pixel location on the edge, x_{sub} is the sub-pixel x value which is determined by $\Delta x_{sub} = \Delta d tan(1.75^{\circ})$ (shown in Figure 5-6) [4].

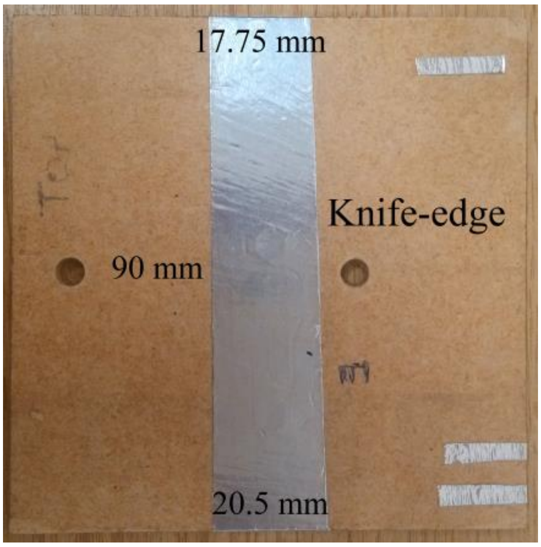

Figure 5-5 Photograph of the knife-edge target.

The LSF is an estimate of PSF and can be calculated as [4]

$$LSF = \frac{d}{dx} ESF = sinc(\frac{k_0 L \theta_{pix}}{2}) \tag{5-15}$$

With the measurements of the brightness distribution on the scanning area with the knife-edge target placed in the vertical and horizontal directions, the brightness distribution from the non-metal part to the metal part across the knife edge builds the brightness curves. Appling Equation (5-14) to fit the experimental brightness curves (least squares fit) results in the equivalent image length: $L_H = 370\, mm$ and $L_V = 380\, mm$ for horizontal and vertical knife-edge, respectively. Therefore, the experimental LSF with horizontal and vertical knife edge can be calculated respectively [4].

The theoretical PSF can be calculated by simply taking L = 400mm (image aperture size). Figure 5-7 shows the LSF with horizontal and vertical knife-edge compared to the theoretical PSF. Comparing the LSF curves in two directions, we can see any that images spread slightly more in the vertical direction than in the horizontal direction, which is due to the imperfection in the scanning set-up [1]. The half power width of theoretical PSF is 2.06 mm while the half power width of experimental LSF are 2.18 mm and 2.24 mm, respectively. Therefore, the realised resolution of this scanning system is about 2.24 mm [4].

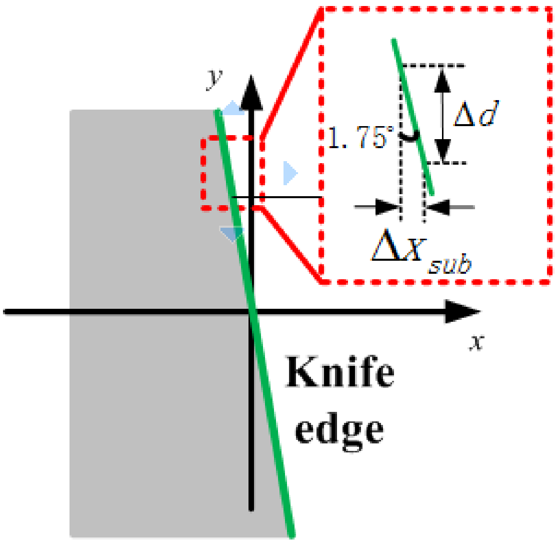

Figure 5-6 The schematic of parameters of the knife edge.

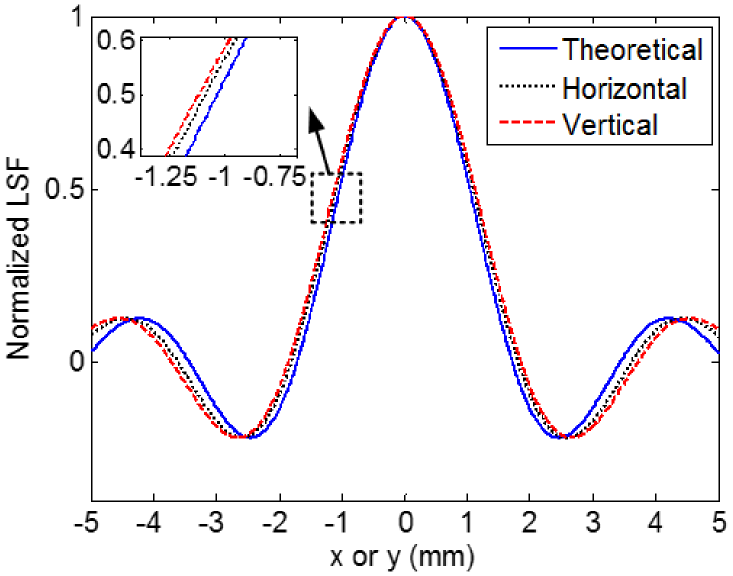

Figure 5-7 Experimental LSF results (horizontal-dotted line, vertical-dashed line) compared to the theoretical PSF (solid line).

5.2.4 Calibration of the imaging system

A rectangular metal target with the dimension of 140mm × 110mm as shown in Figure 5-8 is fixed on the scanner. The gradienter is used to ensure that transceivers are placed horizontal and the metal plate is perpendicular to transceivers.

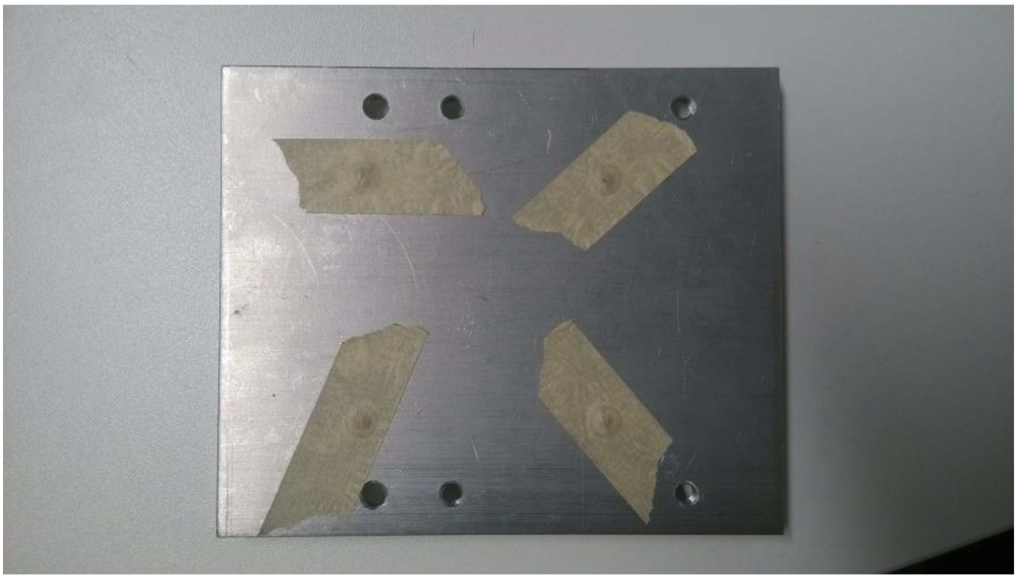

Figure 5-8 Photograph of the rectangular metal target used in the raster scanning experiment.

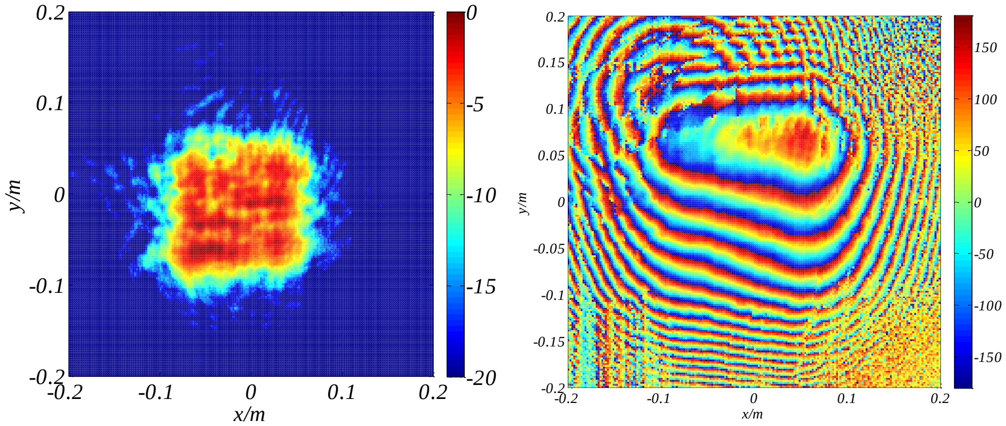

(a) (b)

Figure 5-9 Uncalibrated (a) amplitude and (b) phase images constructed by signals received at the aperture plane. (The legend indicates the normalised values in dB and degrees)

However, a small tilted angle will lead to uneven distribution of the amplitude and phase. Figure 5-9 illustrates uncalibrated amplitude and phase images at the aperture plane. Compared with the amplitude image, the uneven distribution can be more obviously observed in the phase image. The peak value can be found at the upper right corner of the phase image which means that the upper corner of the metal plate is closed to transceivers. Scraps of paper are carefully attached behind lower fixing holes to change the distance between transceivers and the lower part of the metal plate.

Figure 5-10 illustrates calibrated amplitude and phase images at the aperture plane. Uniform distribution can be observed in the phase image (Figure 5-10 (b)) compared with Figure 5-9 (b). Then this calibrated system can be deployed to conduct more experiments.

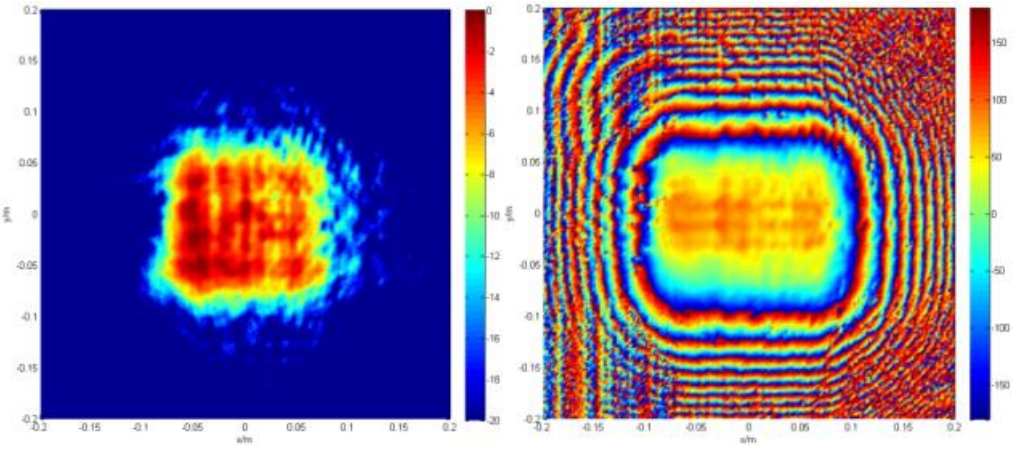

(a) (b)

Figure 5-10 Calibrated (a) amplitude and (b) phase images constructed by signals received at the aperture plane. (The legend indicates the normalised values in dB and degrees)

5.2.5 Imaging results and analyses

From the data received by the receiver horn, we can get the amplitude and phase distribution of electric field on the aperture plane. The target image at the aperture plane from the original data is shown in Figure 5-11.

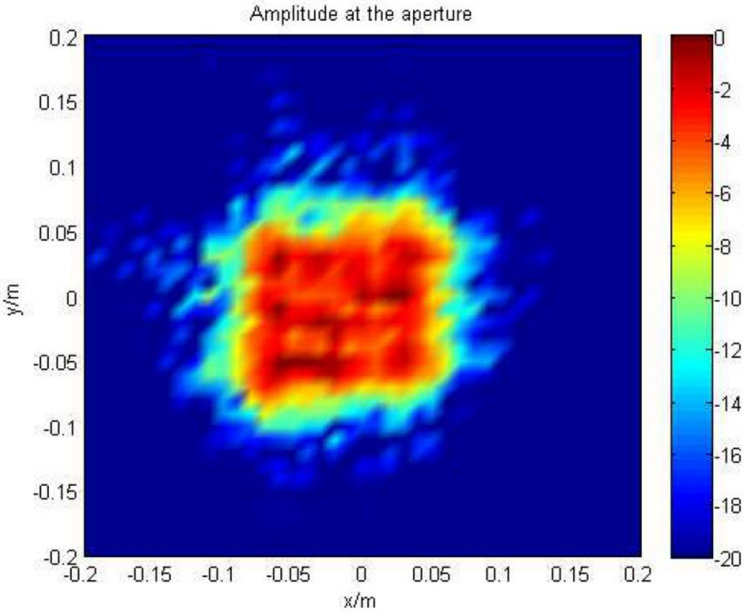

Figure 5-11 The image of the rectangular target recorded at the aperture plane. (The legend indicates the normalised values in dB)

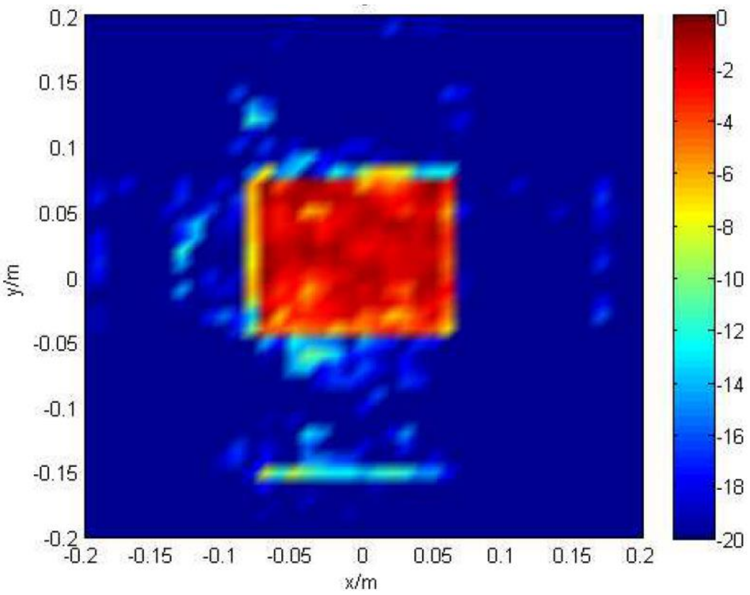

Figure 5-12 The reconstructed image of the rectangular target. (The legend indicates the normalised values in dB)

From the reconstructed image shown in Figure 5-12, the shape and the dimensions can be discriminated clearly but the resolution has been limited by N_x and $\mathrm{N_y}$ we chose. Considering the relations between the space domain and the space frequency domain, the range of k_x and k_y need to be extended. Then the resolution will be enhanced with the reduction of Δx and Δy. The range changing which is also called interpolation of k domain can be achieved by add zeros in the F_T array. Then a solution enhanced image of the target is achieved in Figure 5-13. However, this method of enhancing image quality will act much better when the number of sampling points is small (there are 41 points in one dimension in this experiment). When there are enough sampling points (such as 201 points), the quality of the image at the target plane without any processing is still good enough (Figure 5-14 and Figure 5-15). But considering the time or money consumed when there are many sampling points, the resolution enhancement method discussed above has its advantages in applications [2].

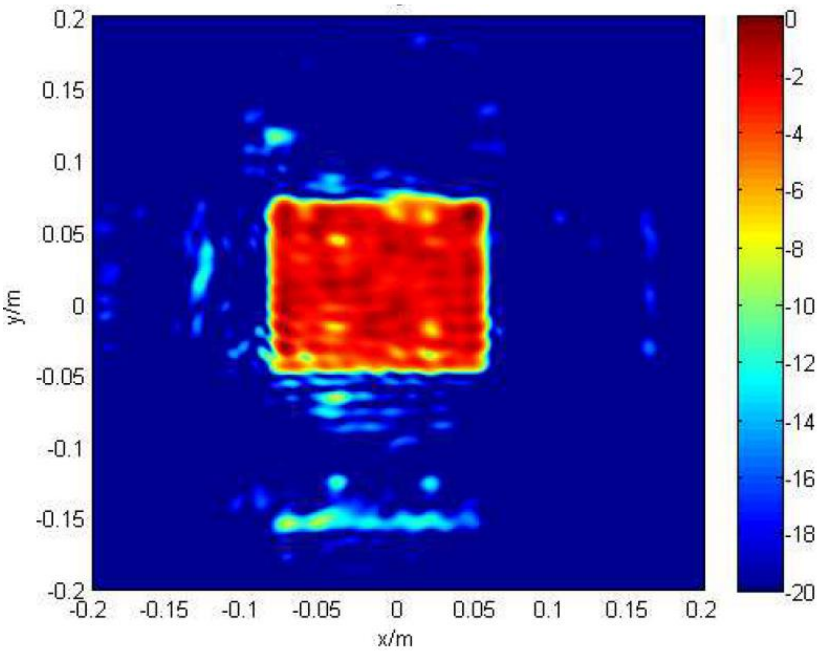

Figure 5-13 The image of the rectangular target with resolution enhanced. (The legend indicates the normalised values in dB)

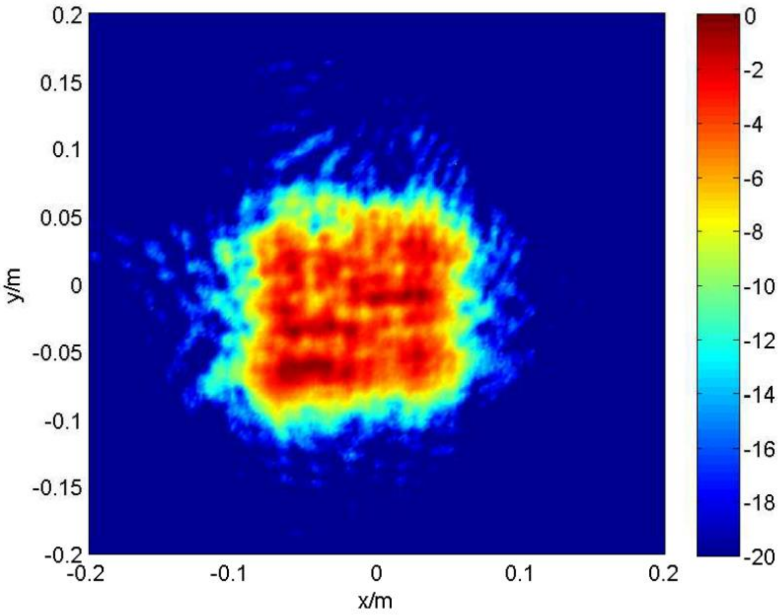

Figure 5-14 The image of the rectangular target at the aperture plane with 201 sampling points in each dimension. (The legend indicates the normalised values in dB)

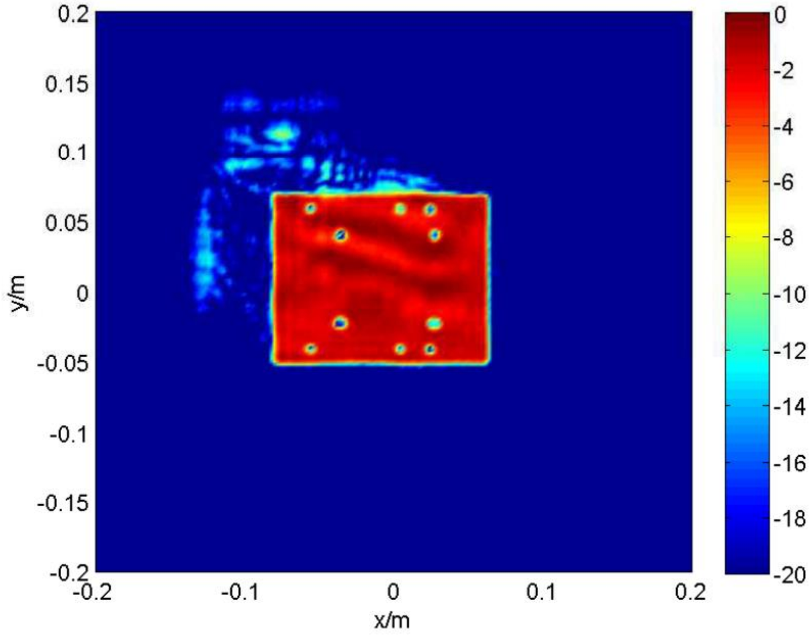

Figure 5-15 The image of the rectangular target on the original data with 201 sampling points in each dimension. (The legend indicates the normalized values in dB)

The second experiment is based on a gun-shaped target with a size of about

$160\ \mathrm{mm} \times 130\ \mathrm{mm}$ shown in Figure 5-16. This target is made from a gun-shaped wood wrapped with metal foil. From the image at the aperture plane without any processing in Figure 5-16, it is difficult to discriminate what is the target really like. Applying the holography algorithm, the image at the target plane can be imaged as demonstrated in Figure 5-18. Then a solution enhanced image of the target is achieved in Figure 5-19. Compared with Figure 5-17, the quality has been improved largely. Most details of the gun-shaped target have been presented. One problem arisen in this experiment is that the image will be very bad when the foil has not been wrapped well on the surface of the gun-shaped wood. The holography algorithm is derived after the target plane paralleled with the aperture plane is assumed. It means that the surface of the target used has to be plat. When the foil has not been wrapped well, the incident signal will be reflected irregularly. Then no useful data can be received on the aperture plane.

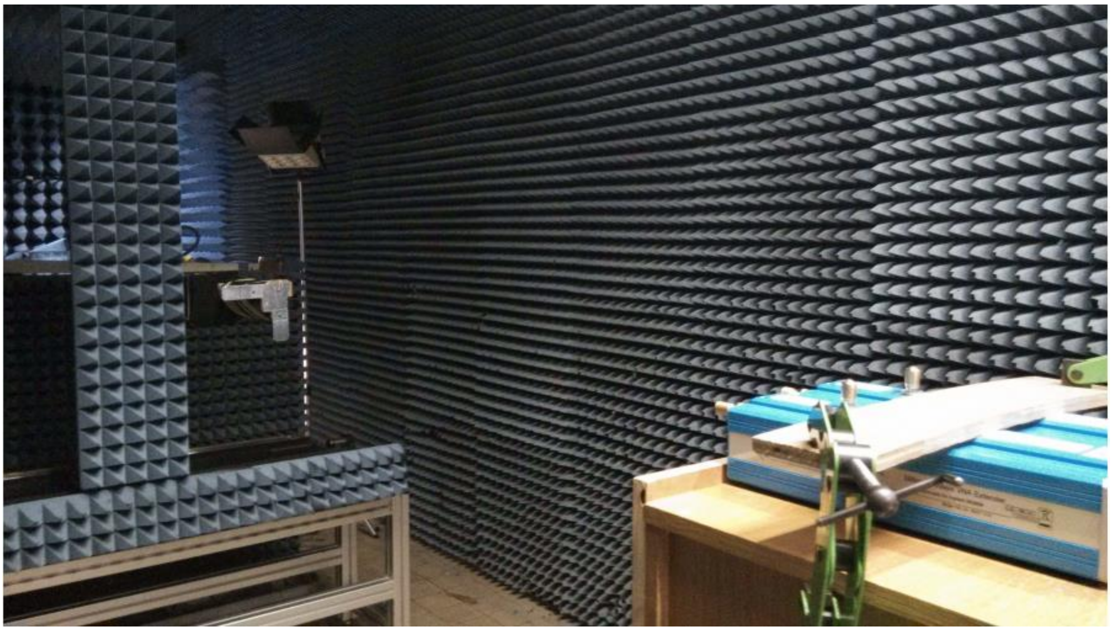

Figure 5-16 Photograph of the gun-shaped metal target.

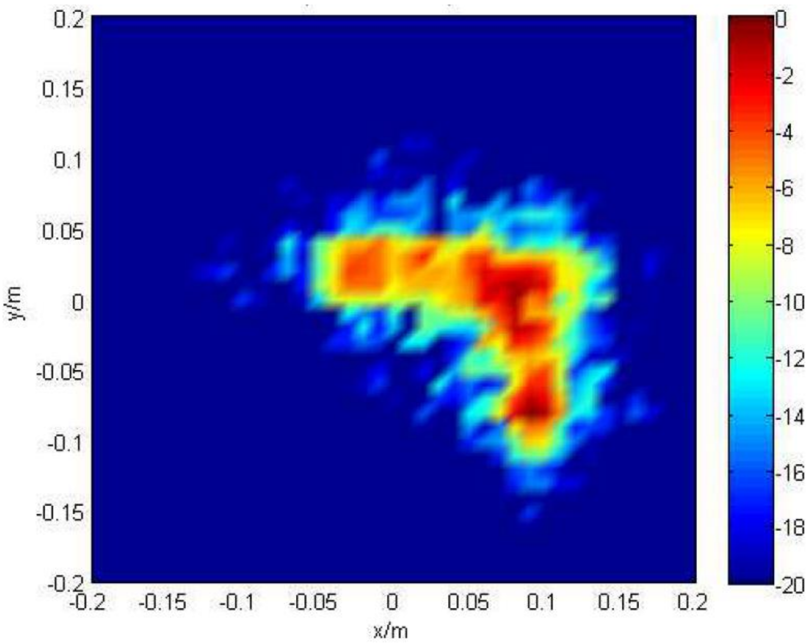

Figure 5-17 The image of the gun-shaped target at the aperture plane. (The legend indicates the normalised values in dB)

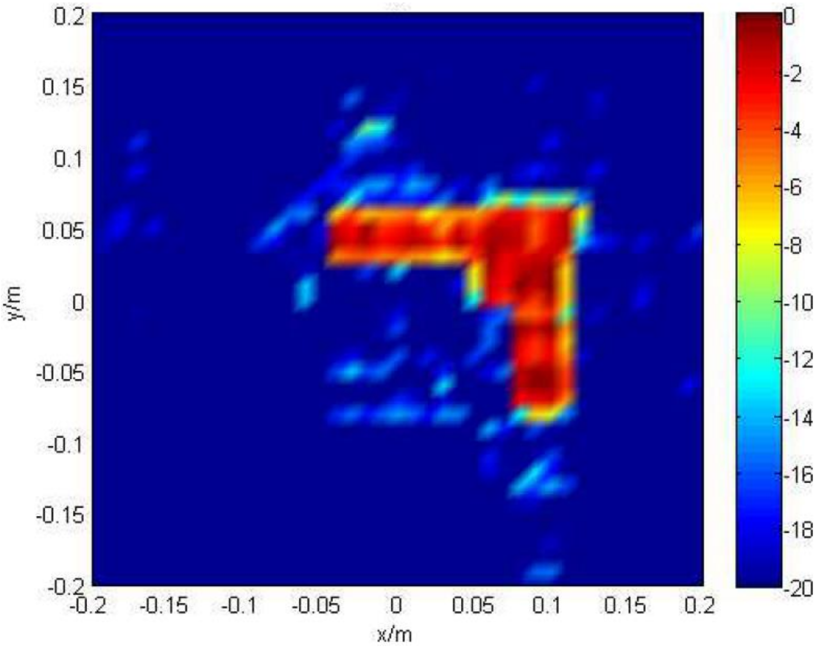

Figure 5-18 The image of the gun-shaped target on the original data. (The legend indicates the normalised values in dB)

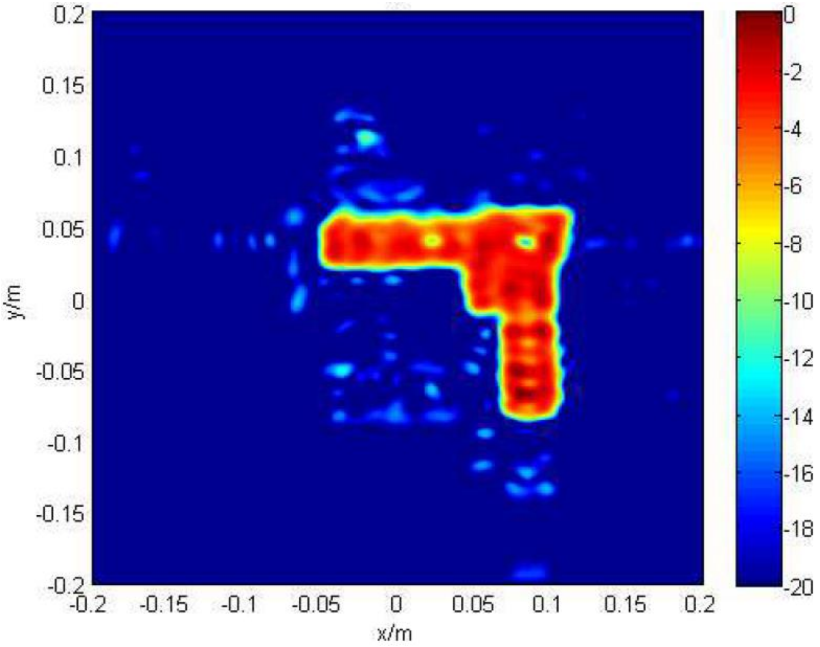

Figure 5-19 The image of the gun-shaped target with resolution enhanced. (The legend indicates the normalised values in dB)

The third experiment is still based on a gun-shaped target with the same size shown in Figure 5-20. The difference between this target and the previous one is that this one is only partially wrapped with metal foil. From the image at the aperture plane without any processing, metal parts can be easily discriminate but it is difficult to distinguish two adjacent ones. Applying the holography algorithm, the image at the target plane can be imaged as demonstrated in Figure 5-22. Then a solution enhanced image of the target is achieved in Figure 5-23. From Figure 5-22 and Figure 5-23, the differences between metal parts and wood parts are obvious. We can recognise the shape of the target regardless of which material. The amplitude of the electric field reflected by metal material and wood material are quite different. What is more important, THz signal applied in imaging offers a higher resolution to provide more details.

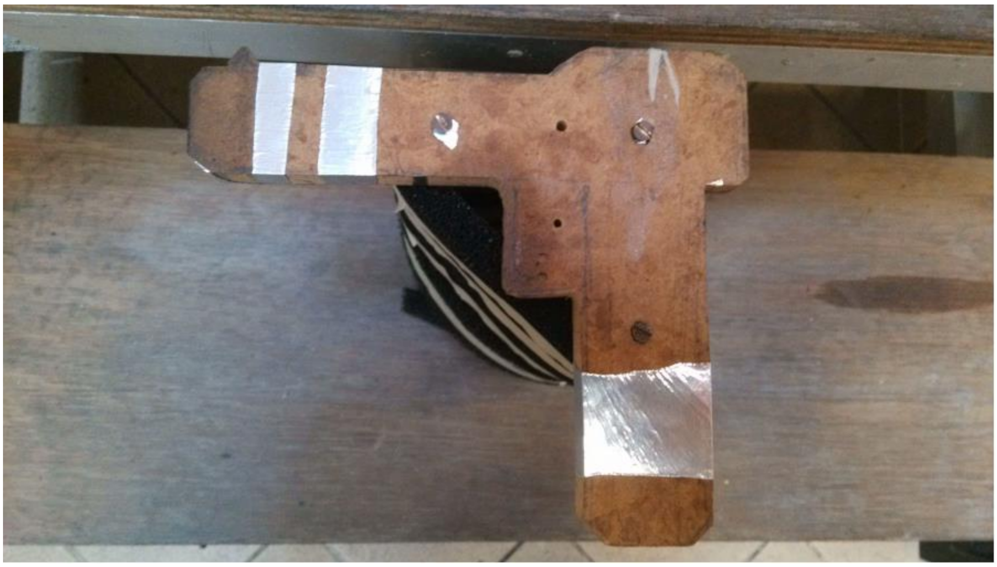

Figure 5-20 Photograph of the gun-shaped target with partially metal foil wrapped.

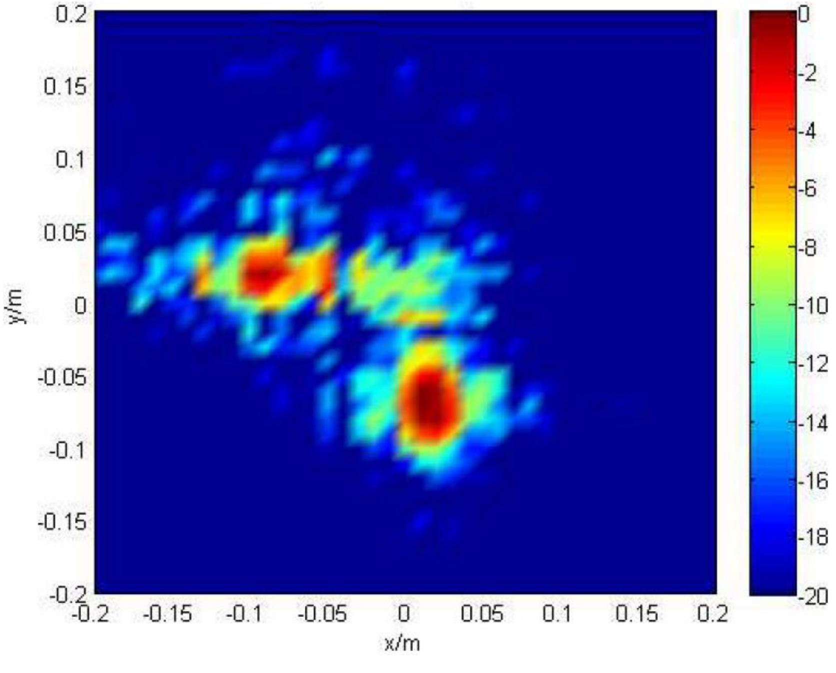

Figure 5-21 The image of the gun-shaped target partially metal foil wrapped at the aperture plane. (The legend indicates the normalised values in dB)

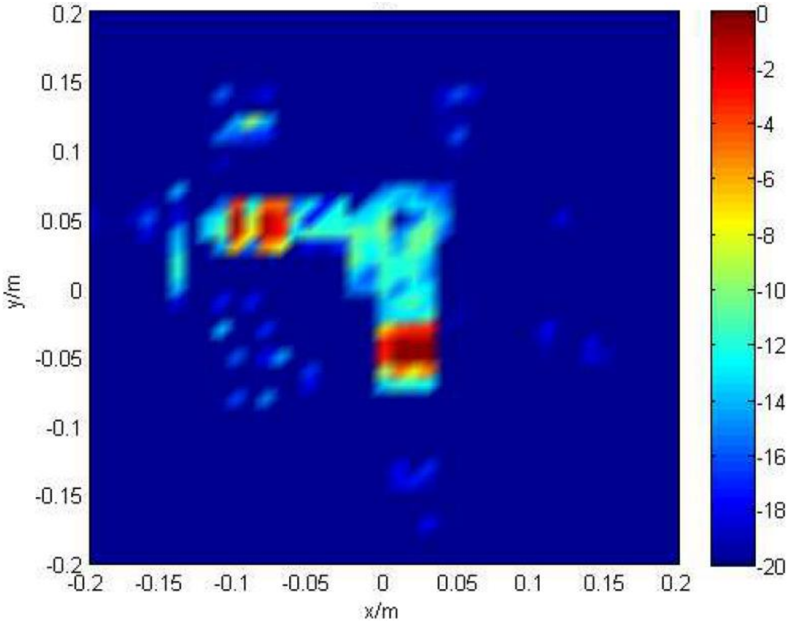

Figure 5-22 The image of the gun-shaped target partially metal foil wrapped on the original data. (The legend indicates the normalised values in dB)

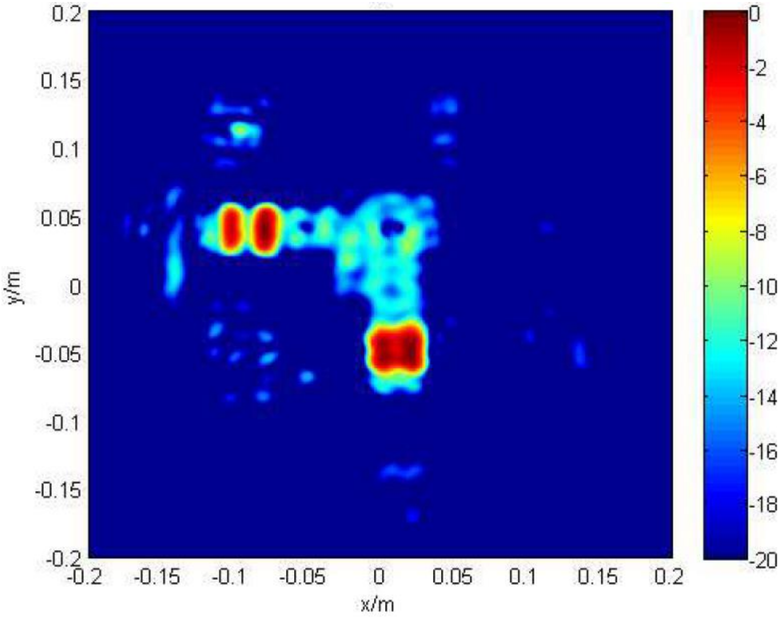

Figure 5-23 The image of the gun-shaped target partially metal foil wrapped with resolution enhanced. (The legend indicates the normalised values in dB)

5.2.6 Image SNR and NEΔR

Two concepts, SNR_I and $NE\Delta R$ of images with different conditions will be discussed to quantitatively assess the quality of the images. SNR of the image (SNR_I) is determined from the bright and dark areas on the image. SNR_I is defined as the ratio of brightness' difference and the standard deviation of the dark area brightness [4]

$$SNR_I = \frac{\overline{B_{bright}} - \overline{B_{dark}}}{\sigma(B_{dark})} \tag{5-16}$$

Where $\overline{B_{bright}}$ and $\overline{B_{dark}}$ are the mean brightness of the target area and non-target area. $\sigma(B_{dark})$ is the standard deviation of the dark area brightness (represented by the amplitudes of the image) [4].

Noise equivalent reflectivity difference in an image is defined in the equation below and can be calculated by setting $SNR_I = 1$ [4].

$$NE\Delta R = \frac{\overline{B_{R+\Delta(R)}} - \overline{B_R}}{\sigma(\overline{B_1})} = \frac{SNR_I \sigma(B_{dark})}{\overline{B_1}} \tag{5-17}$$

Where $\overline{B_{R+\Delta\,(R)}}$ and $\overline{B_R}$ are brightness' in areas with incremental reflectivity difference, and $\overline{B_1}$ is the brightness of the area with the reflectivity of R=1. In this case, the target area in the image is assumed to represent reflectivity of R=1, i.e., $\overline{B_1} = \overline{\mathrm{B}_{bright}}$. According to Rose's Criterion [5], the contrast difference in an image detected by an observer is about $5 \times NE\Delta R$. The edge between bright and dark is determined by the large areas of relatively constant maximum and minimum brightness [4].

In order to acquire more information, several comparsion experiments have been conducted. With one fixed D_A of 400 mm, the total sampling points vary which means different Δz is used in this part. 21, 31, 41, 51, 61, 81, 101 and 201 points in one dimension are adopted to achieve eight images of the same target. The images of the rectangular target are shown in Figure 5-24 [1].

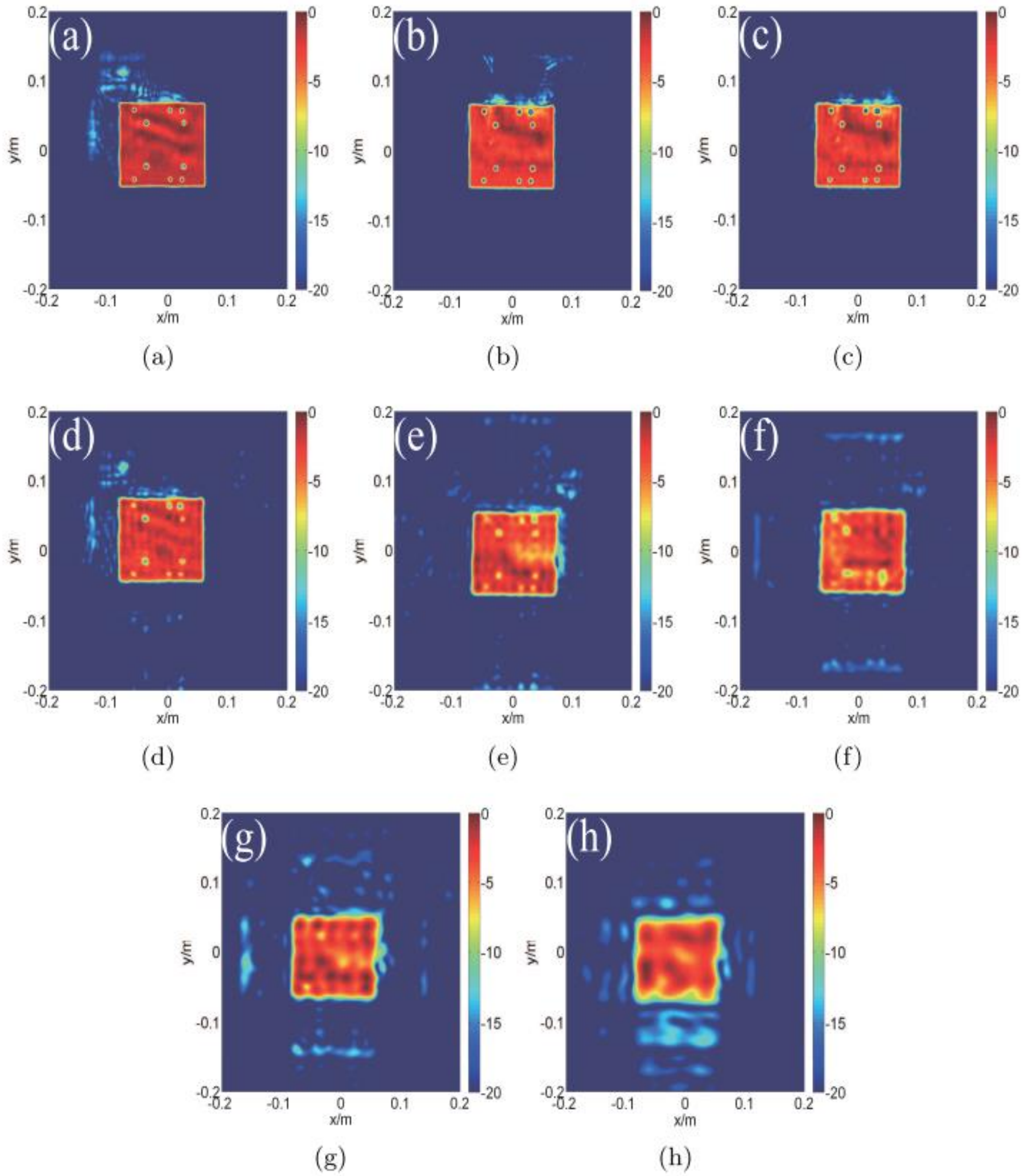

(a) (b) (c)

(d) (e) (f)

(g) (h)

Figure 5-24 Images of the rectangular target with different sampling points (a) 201×201 (b) 101×101 (c) 81×81 (d) 61×61 (e) 51×51 (f) 41×41 (g) 31×31 (h) 21×21. (The legend indicates the normalised values in dB)

The sampling density or the imaging array element spacing details and the corresponding SNR_I, $NE\Delta R$ of the rectangular target are calculated and listed in Table 5-1. From data in the table, we can know that when the number of points increases (which means the resolution will be enhanced) SNR_I will increase while NEΔR decreases, correspondingly. The reduction of total number of sampling points causes the decreasing of dynamic range [1]. Data in Table 5-1 is plotted in Figure 5-25.

Table 5-1 SNR_I and $NE\Delta R$ of images in Figure 5-24.

Figure	Total sampling points	$\mathrm{SNR_I}$	$\mathrm{NE\Delta R}$
Figure 5-24 (a)	201 × 201	35.27	0.027
Figure 5-24 (b)	101 × 101	31.94	0.031
Figure 5-24 (c)	81 × 81	30.86	0.034
Figure 5-24 (d)	61 × 61	29.01	0.037
Figure 5-24 (e)	51 × 51	26.28	0.044
Figure 5-24 (f)	41 × 41	24.18	0.052
Figure 5-24 (g)	31 × 31	20.36	0.056
Figure 5-24 (h)	21 × 21	14.99	0.071

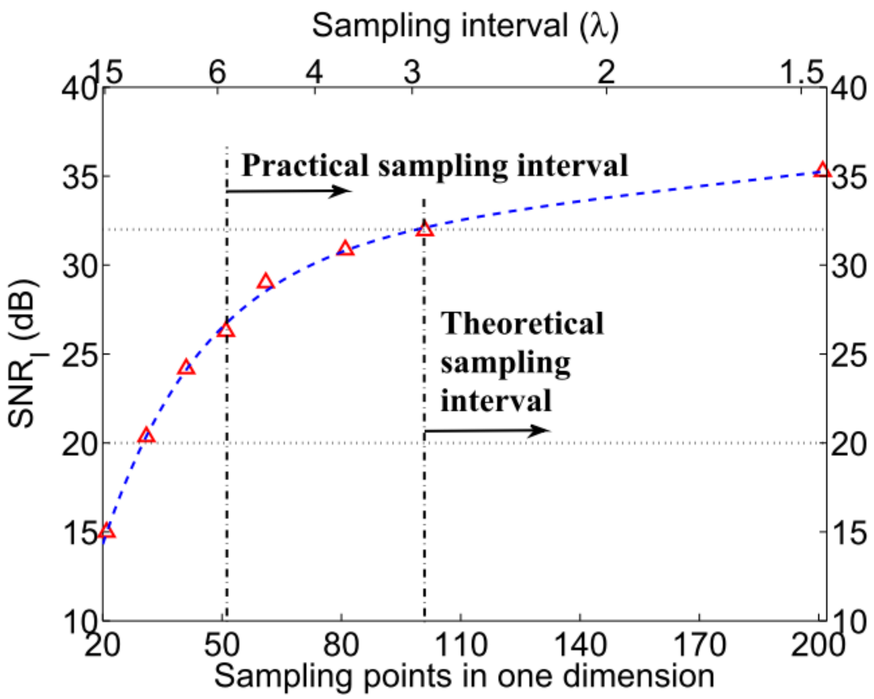

Figure 5-25 SNR_I versus sampling points and the sampling interval (The theoretical sampling interval being 2.87λ while the practical sampling interval being 5.74λ).

As shown in Figure 5-25, SNR_I starts to level off above 32 dB after the optimal sampling interval (2.87λ). At the acceptable sampling interval (5.74λ), the image in Figure 5-24 (e) is still recognisable with blurring fine features (holes) at a SNR_I value of 26.28 dB. In Figure 5-24 (b), we can see that when the sampling interval is increased beyond the acceptable sampling interval (5.74λ), the images deteriorate quickly in (f) to (h) cases. Though the edge of the target can still be discriminated in (f), the holes start to disappear. In the sparsely sampled cases of (g) and (h), the images can only show the shape of the target.

And considering a different analytical method, another experiment focusing on the size of the aperture is conducted. With one fixed Δz of 5 mm, the size of the aperture varies as 250 mm, 400 mm and 500 mm. The images of the rectangular target are shown in Figure 5-26. The sampling density or the imaging array element spacing details and the corresponding SNR_I, $NE\Delta R$ of the rectangular target with different sizes of the aperture are calculated and listed in Table 5-2. When the element spacing set to 5 mm,

SNR_I and $NE\Delta R$ is stable as shown in the table. 5 mm can be an appropriate spacing in the imaging at 220 GHz.

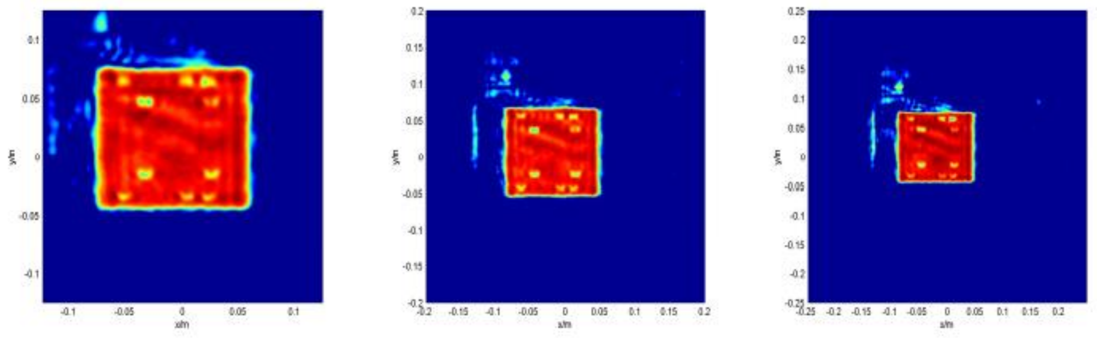

(a) (b) (c)

Figure 5-26 Images of the rectangular target with different sizes of the aperture (mm^2) (a) 250×250 (b) 400×400 (c) 500×500.

Table 5-2 SNR_I and $NE\Delta R$ of images in Figure 5-26.

Figure	Aperture size (mm^2)	$\mathrm{SNR_I}$	NEΔR
Figure 5-26 (a)	250×250	26.64	0.035
Figure 5-26 (b)	400×400	27.43	0.034
Figure 5-26 (c)	500×500	30.77	0.031

Another comparison is made on SNR_I and $NE\Delta R$ at different distances away from the aperture. Figure 5-27 and Figure 5-28 are SNR_I and $NE\Delta R$ at different distances away from the aperture of rectangular target and gun-shaped target, respectively. Extremums are obvious at the target plane. This characteristic can be utilised to determine the aperture-target distance which is unknown to achieve the best imaging resolution.

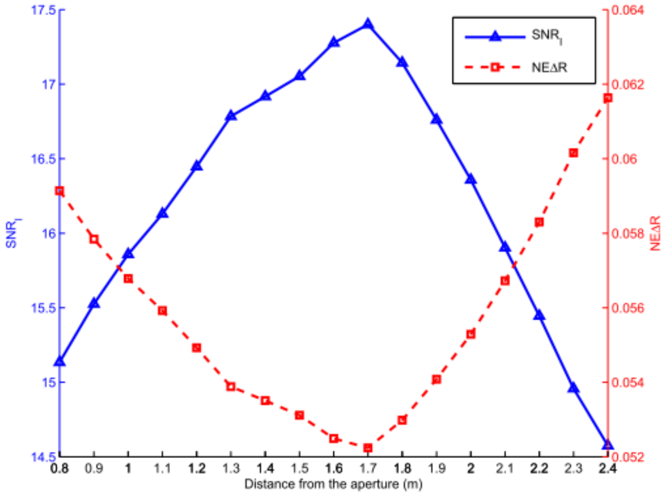

Figure 5-27 SNR_I and $NE\Delta R$ vs. distance from the aperture of the rectangular target.

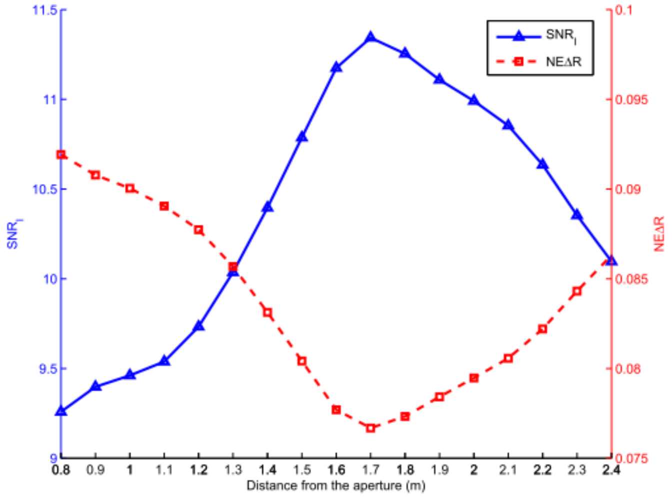

Figure 5-28 SNR_I and $NE\Delta R$ vs. distance from the aperture of the gun-shaped target.

5.2.7 Study on transceiver antenna positioning/alignment

In the previous schematic discussed and applied, two transmitter and receiver horns are placed parallel with the minimum gap between them, which means that the offset of the horn from the centre of the aperture plane is only limited by the size of millimetre-wave modules. In this following part, different distances between the centres of horn apertures have been applied and results are compared to verify the importance of small gap and target-pointed settings which can be seen in Table 5-3. Three different transceiver antenna alignments can be found in Figure 5-29 [6].

In three different situations, horn antennas will be moved along x, y and z dimension respectively. At the same time, the orientation of transceivers will vary to test the imaging system [6].

As shown in Table 5-3, the 1st situation is the result of the most compacted structure we can achieve when two horns are parallel. And the centres of result images are always corresponding to the centre of horn positions. From the 2nd and 3rd situations, we can know that there will be no obvious effect on the image quality [6]

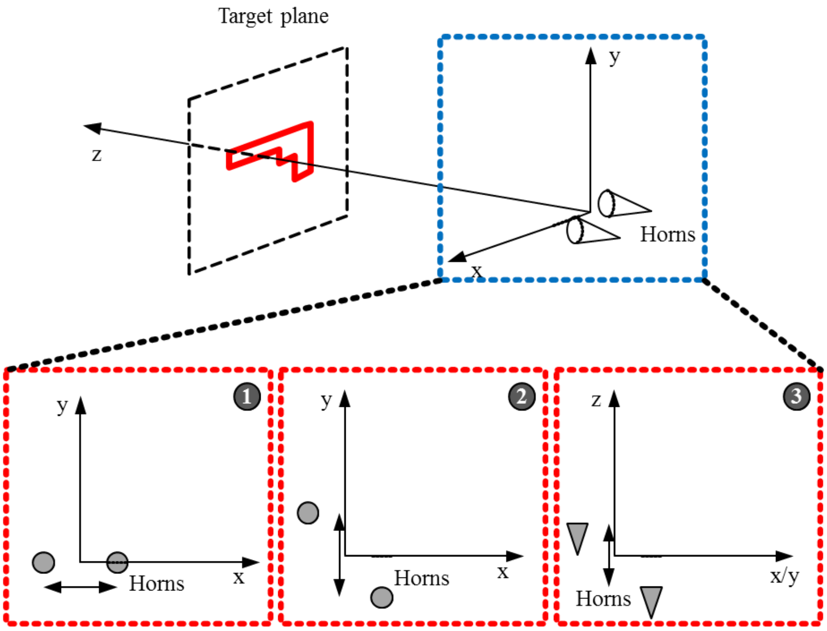

Figure 5-29 Different transceiver antenna alignments [6].

Table 5-3 SNR_I and $NE\Delta R$ of the rectangular target in different horns settings [6].

	x/cm	**y/cm**	**z/cm**	**Target pointed**	SNR_I	$NE\Delta R$
1	10.668	0	0	N	22.97	0.041
2	20.668	0	0	N	23.39	0.040

3	20.668	0	0	Y	21.87	0.043
4	36.668	31.5	0	Y	14.10	0.062
5	36.668	31.5	0	N	8.17	0.097
6	18.668	0	0	N	22.85	0.041
7	18.668	0	15	N	22.48	0.042

when the gap is not too large. Then with the gap continues being wider, a large deterioration will be observed from the 4th and 5th ones. And the one with target-points horns (the 4th) performs much better than another one (5th). In the situations with different distances between horns and the target (the 6th and 7th), no obvious deterioration can be observed. What needs to be noticed is that when the gap is large enough and horns are not pointed to the target, the image quality will not be determined by SNR_I and $NE\Delta R$ since that the reflected/scattered signal can't be distinguished from the noise but this situation can be easily recognised by the image physically or comparison of the signal extremums. The conclusion can be drawn that for small gap situations, the quality of images will not deteriorate largely whether horns point to the target and how much the gap changes since beams of horns can cover a large effective area with stand-off distance. When we come to large gap situations, directions of horns will be a vital problem [6].

5.2.8 Evaluation of TC and PIC algorithms

This plate has the size of 0.15 m * 0.1 m size. The scanning area coverage is still 0.4 m* 0.4 m. Figure 5-30 shows the unprocessed image of the amplitude and phase distribution which are built directly from the amplitude of the received signal. The reconstructed image using BP algorithm can be found in Figure 5-31 (a). As a comparison, the reconstructed image using the proposed TC algorithm is shown in Figure 5-31 (b). It is shown that the reconstructed images using the BP and TC algorithm have a comparable quality.

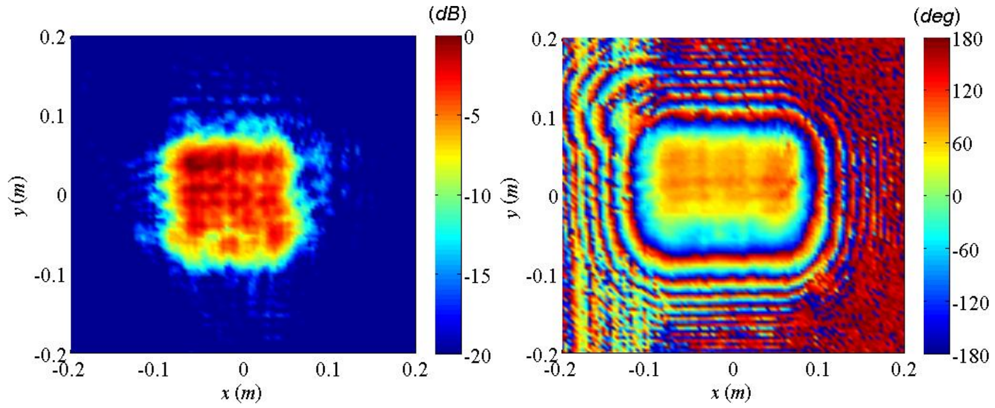

(a)amplitude (b) phase

Figure 5-30 Experimental E-field (a) amplitude and (b) phase distribution based on signals received by the raster scanned antenna (The legend indicates the normalised values in dB and degrees).

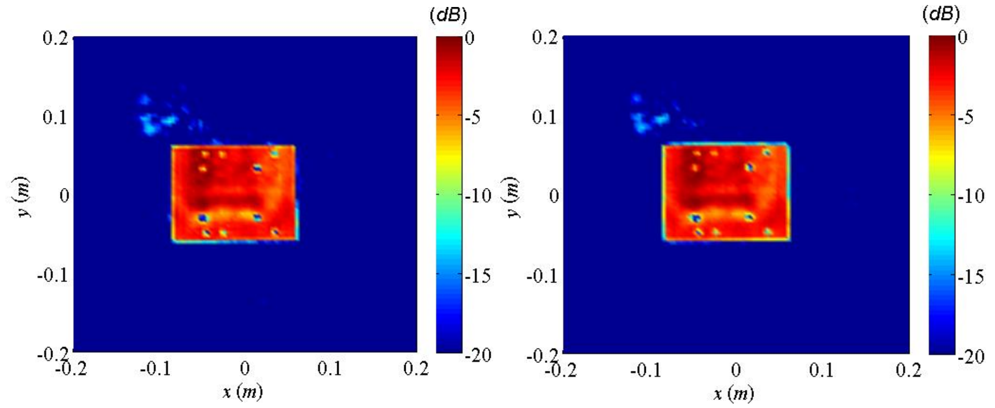

(a) BP (b) TC

Figure 5-31 Reconstructed images by applying (a) backpropagation algorithm; (b) proposed transposed algorithm for the experimental evaluation (The legend indicates the normalised values in dB).

Furthermore, to compare these two algorithms in more details, we select single row result to have a comparison. The reference row is located at the yellow line shown in Figure 5-32. Comparable results can be observed in it.

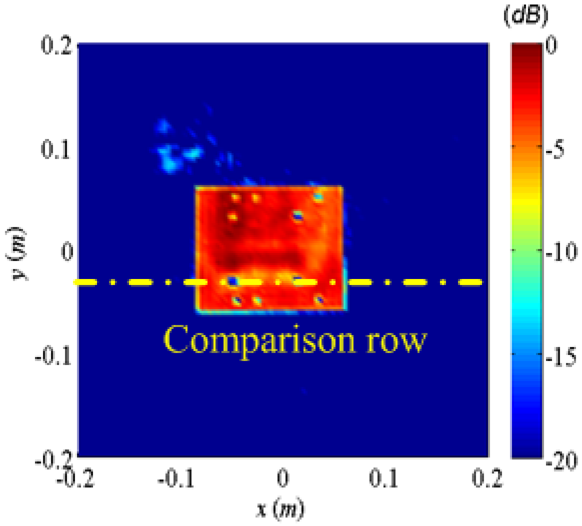

Figure 5-32 The reference row in the reconstructed image for more comparison (The legend indicates the normalised values in dB).

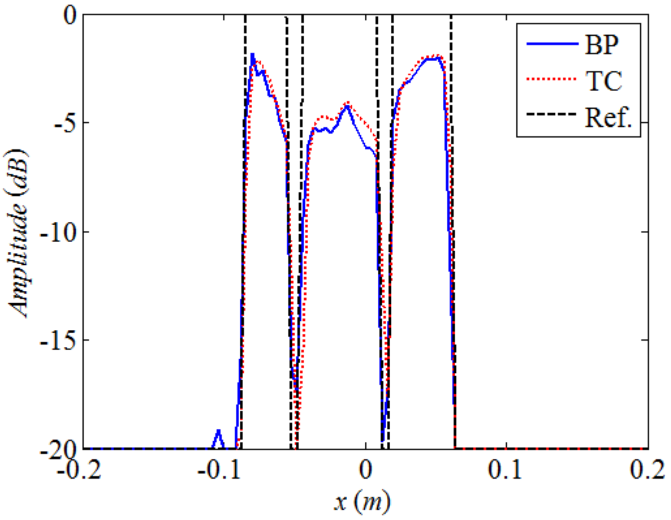

Figure 5-33 Comparison between the reconstructed single row result for BP and TC algorithms.

Figure 5-34 illustrates the reconstruction time comparison between BP and TC algorithms under different sampling point situations. Results show that averagely 0.2 s is less consumed by employing TC algorithm. The efficiency increase ($(t_{BP} - t_{TC})/t_{BP}$) value is also given in Figure 5-34 indicating that the reconstruction is about 20% faster on TC algorithm.

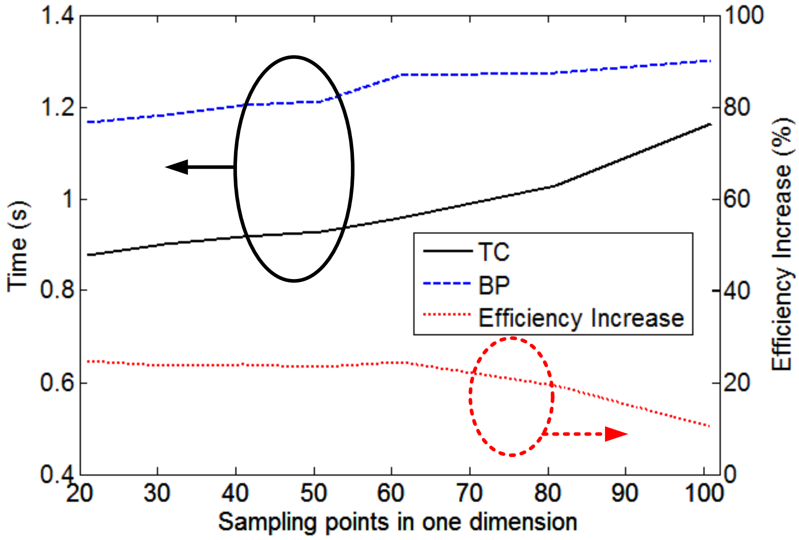

Figure 5-34 Comparison between BP and TC algorithms under different sampling point situations and the efficiency increase of TC algorithm.

Applying the proposed PIC algorithm to differently sampling points listed above, we can have different reconstructed images shown in Figure 5-35.

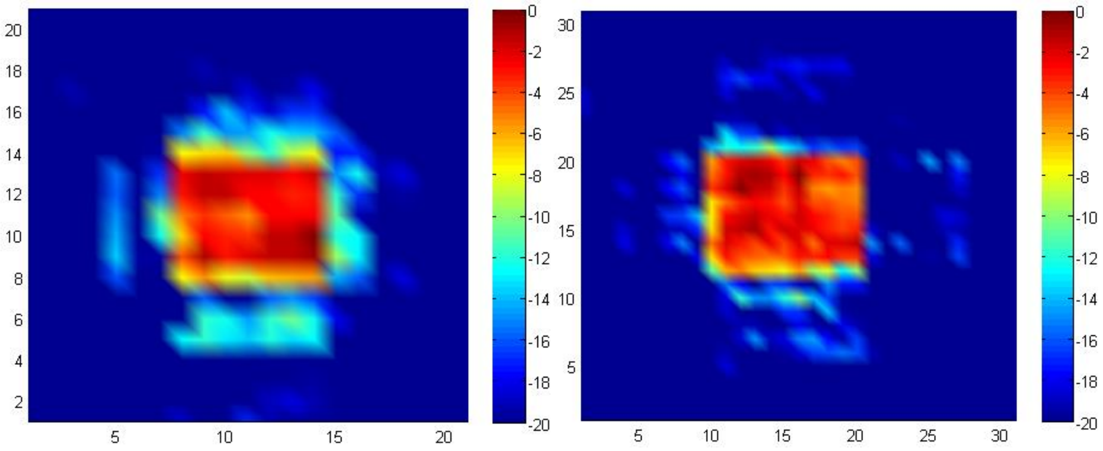

(a) (b)

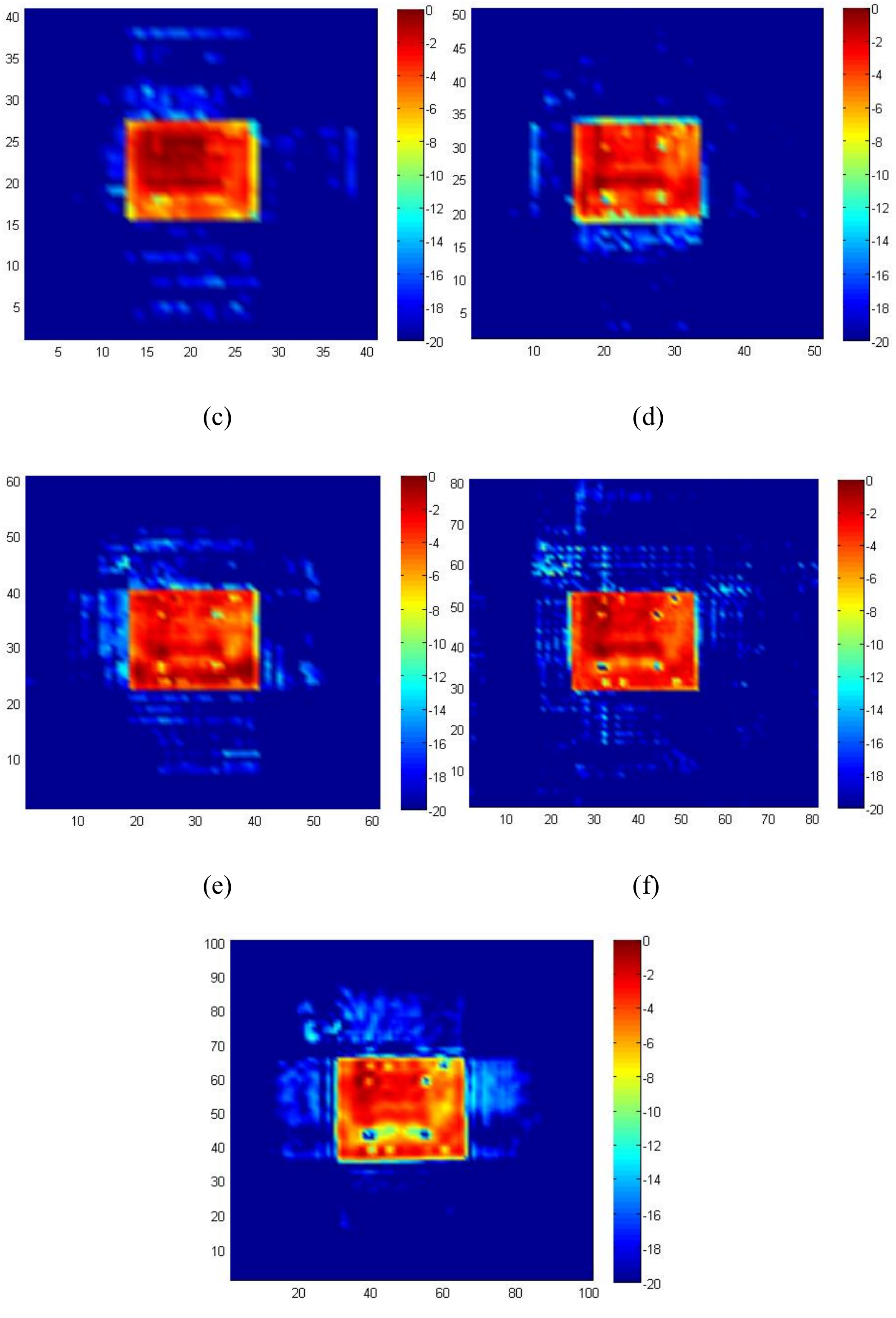

(c) (d)

(e) (f)

(g)

Figure 5-35 Reconstructed images with different sampling points using normalized PIC kernels: (a) 21 by 21, (b) 31 by 31, (c) 41 by 41, (d) 51 by 51,

(e) 61 by 61, (f) 81 by 81, (g) 101 by 101 (The legend indicates the normalised values in dB).

Reconstructed images are comparable with results of BP and TC algorithms except some background noise and possible ghost images. These problems will be studied in the future work. Reconstruction times for different sampling points applying these three different algorithms are listed in Table 5-4. This comparison is also plotted as Figure 5-36. The reconstruction similarity comparison is also given in Table 5-5. The reconstruction results from the BP algorithm are taken as the reference results since they meet the real target best. The percentage values indicate the percentage of similar points (less than 10 dB difference) in all reconstructed points compared to the BP results. It has to be noted that only reconstruction time is included here. For BP and TC, the input data is a matrix, while for PIC, the input data is a vector. Consider that for practical imaging systems, the unprocessed data can be either a matrix or a vector, the transformation time between the matrix and the vector is excluded here. TC and PIC act more efficient than the conventional BP, especially for sampling points less than 81. So for raster scanning method, TC or PIC can be an adequate alternative. However, PIC has its advantage in beam scanning method. Independent PIC kernels can perform well in the situation of varying kernel convolution which will be much complicated for BP and TC. At the same time, the time consumption of PIC is limited by the large-scaled matrix multiplication. If the large-scaled matrix multiplication can be improved to reach the efficiency of FFT in Matlab, PIC will be potential for more applications with variant convolution kernels which will be difficult for BP and TC algorithms to resolve.

Table 5-4 Reconstruction time comparison for different sampling points in an area of 0.4 m by 0.4 m.

Points	21	31	41	51	61	81	101
BP	0.358	0.364	0.359	0.366	0.369	0.375	0.384
TC	0.073	0.076	0.083	0.092	0.104	0.151	0.227

PIC	0.104	0.104	0.113	0.121	0.146	0.244	0.479

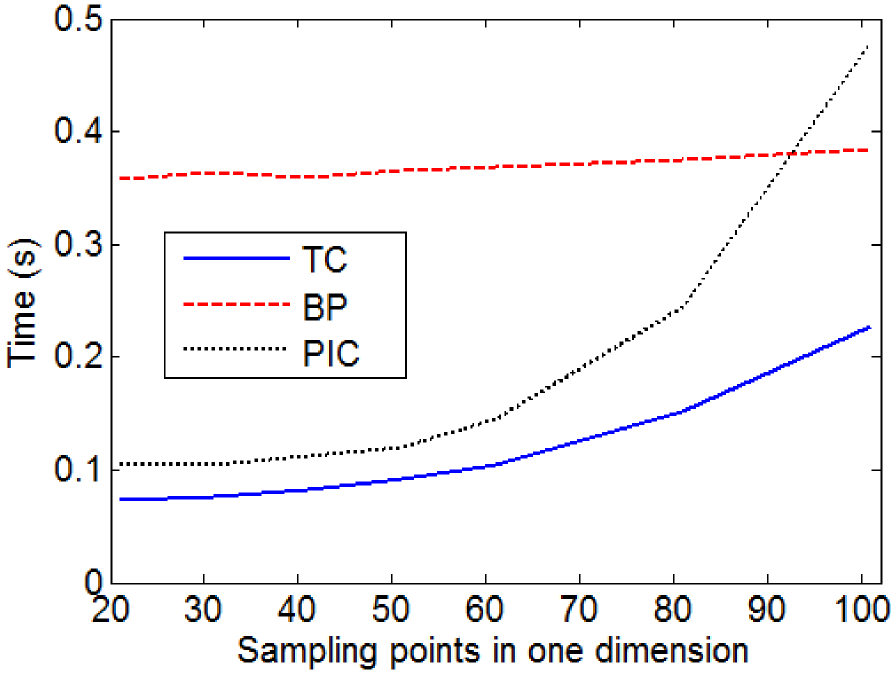

Figure 5-36 Comparison between BP, TC and PIC algorithms under different sampling point situations (only reconstruction time included).

Table 5-5 Reconstruction similarity between BP, TC and PIC for different sampling points in an area of 0.4 m by 0.4 m (BP results are taken as the reference).

Points	21	31	41	51	61	81	101
BP	100%	100%	100%	100%	100%	100%	100%
TC	86.85%	94.17%	91.91%	85.47%	84.92%	91.24%	94.80%
PIC	78.46%	88.66%	85.72%	86.85%	84.95%	85.08%	74.72%

5.3 Experimental configuration of the beam scanning system and imaging result analysis

The configuration of the beam scanning imaging system is shown in Figure 5-37. Two identical corrugated horns are used as the transmitter and receiver with the half-power beam width (HPBW) of about 14°. To evaluate the beam scanning approach, a rotation structure is employed to convert the raster movement of the NSI 2000 to an angular rotation. The principle of the conversion is demonstrated in Figure 5-38. The structure mainly consists of a supporting platform, two joints and a telescopic rod as shown in Figure 5-38 (a). When the joint 2 is moved in the planar scanner plane, the supporting platform will rotate around joint 1 following the movement of joint 1. The telescopic rod is added to compensate the distance change between the supporting platform. Then the beam can reach any point on the target plane as demonstrated in Figure 5-38 (b). Figure 5-38 shows the conversion for the 1D scenario. The 2D scenario can be realised simply by replacing joints to universal joints. There is a relationship among d_{jt} (the distance between the target plane and the joint 1), d_{jj} (the distance between two joints), x_s or y_s (the scanning point position) and x_t or y_t (the pointed position):

$$\frac{x_t(or\ y_t)}{x_s(or\ y_s)} = \frac{d_{jt}}{djj} \tag{5-18}$$

The imaging distance d_{jt} and, the dimension of target area D_t are chosen to be 1500 mm and 600 mm, respectively. d_{jj} is set as 500 mm, then the required scanning area will be the dimension of 200 mm (D_s). Compared to the raster scanning experiment conducted on the same NSI 2000 scanner, the beam scanning experiment here requires the smaller scanning step because the step on the target plane also satisfies the relationship in Equation (5-18).

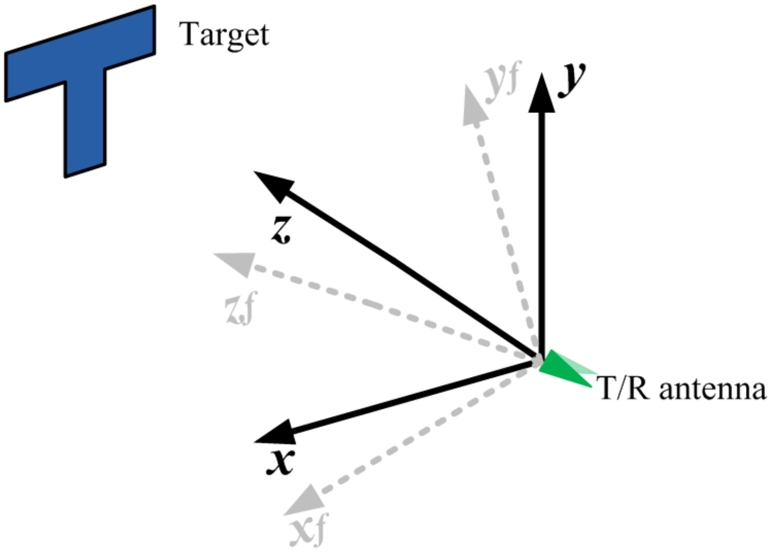
Target
yf
y
z
zf
T/R antenna
x
xf

Figure 5-37 Beam scanning system configuration.

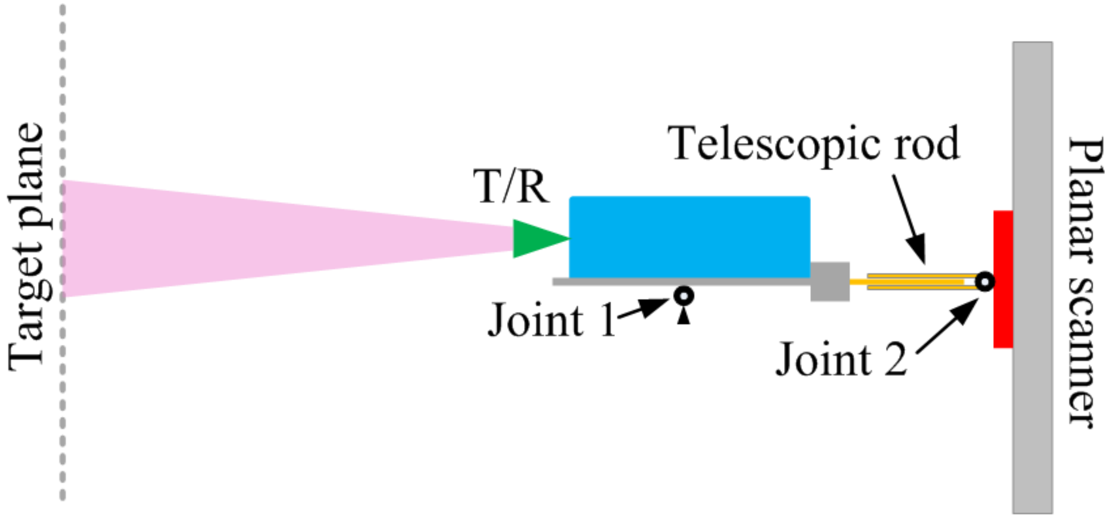
Target plane
T/R
Telescopic rod
Joint 1
Joint 2
Planar scanner

(a)

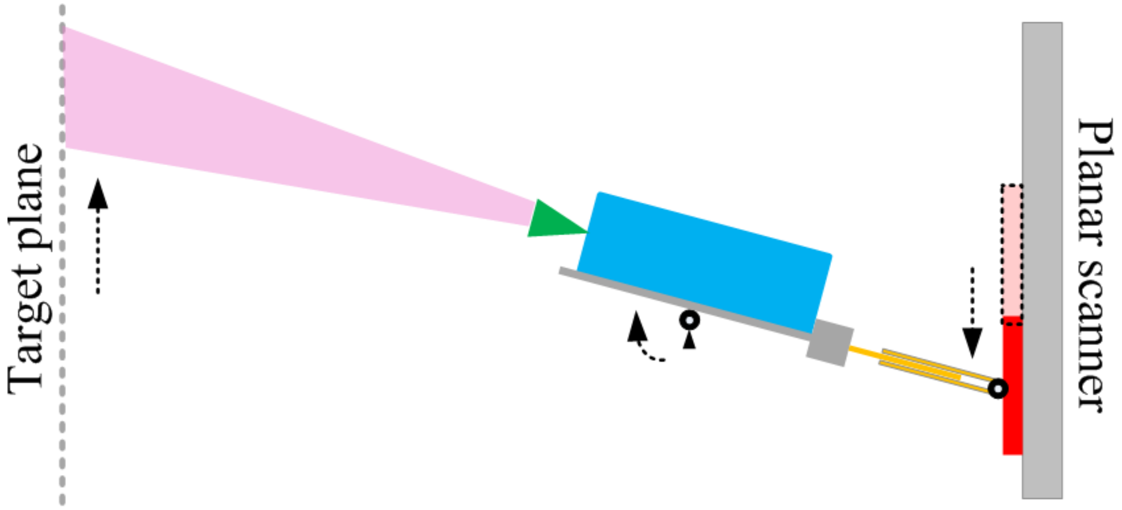

(b)

Figure 5-38 The conversion structure from the raster scanning to angular scanning: (a) The central part of the target plane is covered, (b) The edge part of the target plane is covered.

Figure 5-39 shows the conversion structure Solidworks model which convert the planar scanning of NSI 2000 scanner to the angular scanning. The millimetre wave modules will be placed on the supporting platform. Two horn will be pointed to the right area shown in the figure. Two additional springs which are not included in this figure are used in the real system to ensure the stability of the supporting platform. At the same time, a rotation foot is placed along with springs to make the rotation on the ground more smoothly.

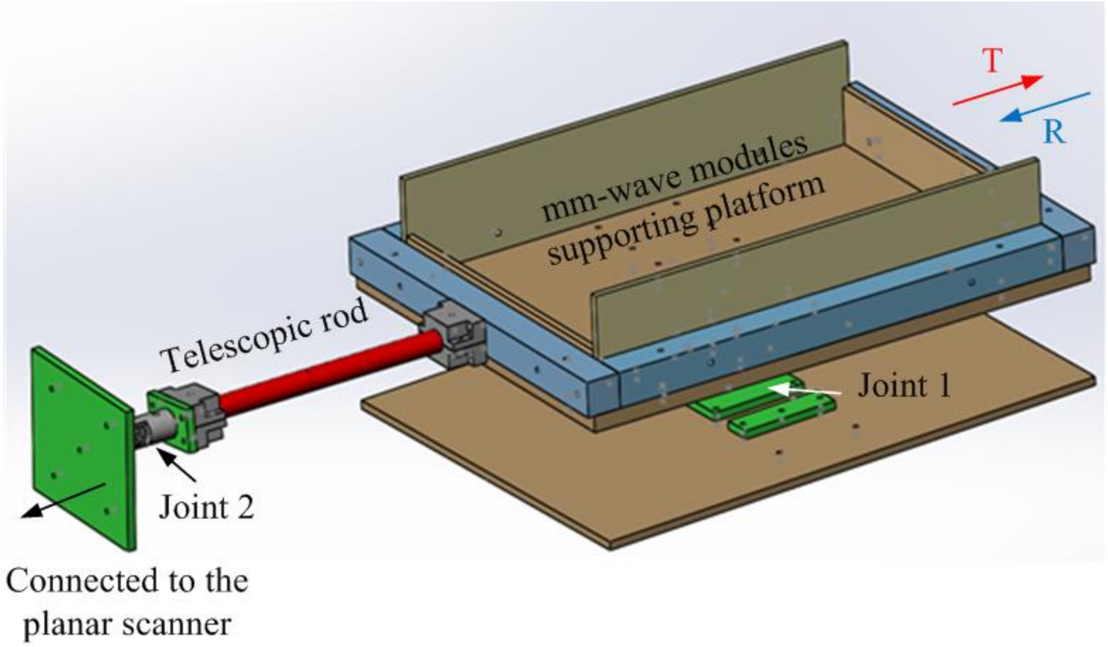
T
R
mm-wave modules supporting platform
Telescopic rod
Joint 1
Joint 2
Connected to the planar scanner

(a)

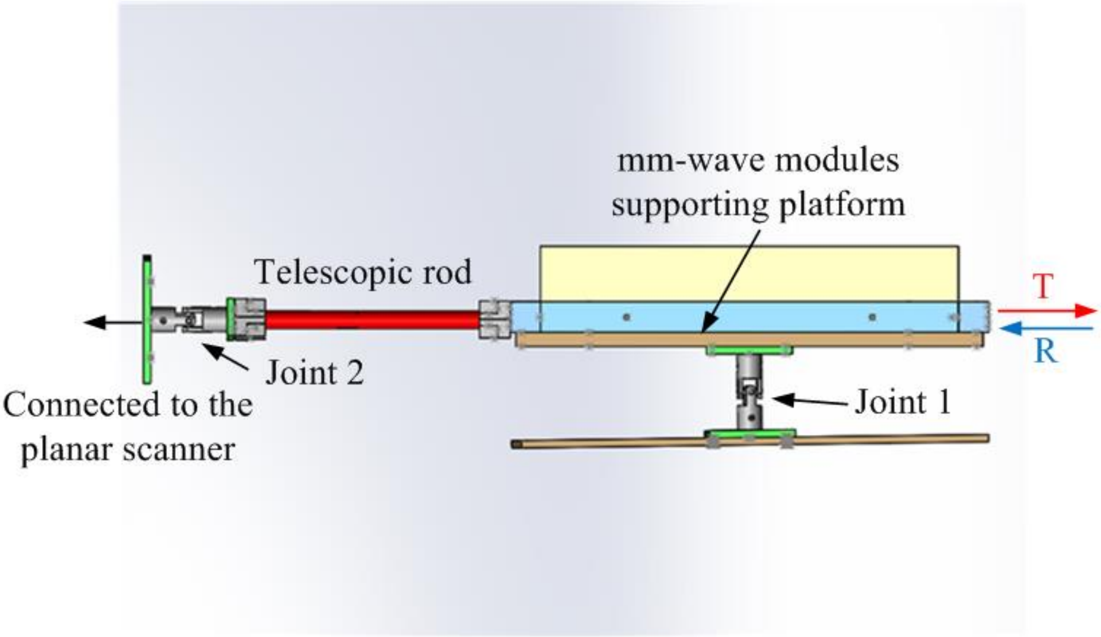
mm-wave modules supporting platform
Telescopic rod
T
R
Joint 2
Joint 1
Connected to the planar scanner

(b)

Figure 5-39 Solidworks model of the planar to angular scanner conversion structure.

The schematic of this beam scanned terahertz imaging system is shown in Figure 5-40. Transmitter and receiver antennas are connected to PNA-X through two

N5256AW05 millimetre-wave modules. Joint 2 is moved in two dimensions controlled by motors with a specific step. Data at each position are recorded. These data are summarized together then to construct an image of the target. With the antenna at the different position, a virtual antenna matrix can be formed. Then the signal from PNA-X and NSI 2000 are imported into PC to reconstruct the image of the target. The difference for the beam scanning system here is that the position on the aperture plane is not the same with the target plane. Before the reconstruction processing, the position needs to be transferred from the aperture plane coordinate to the target plane coordinate.

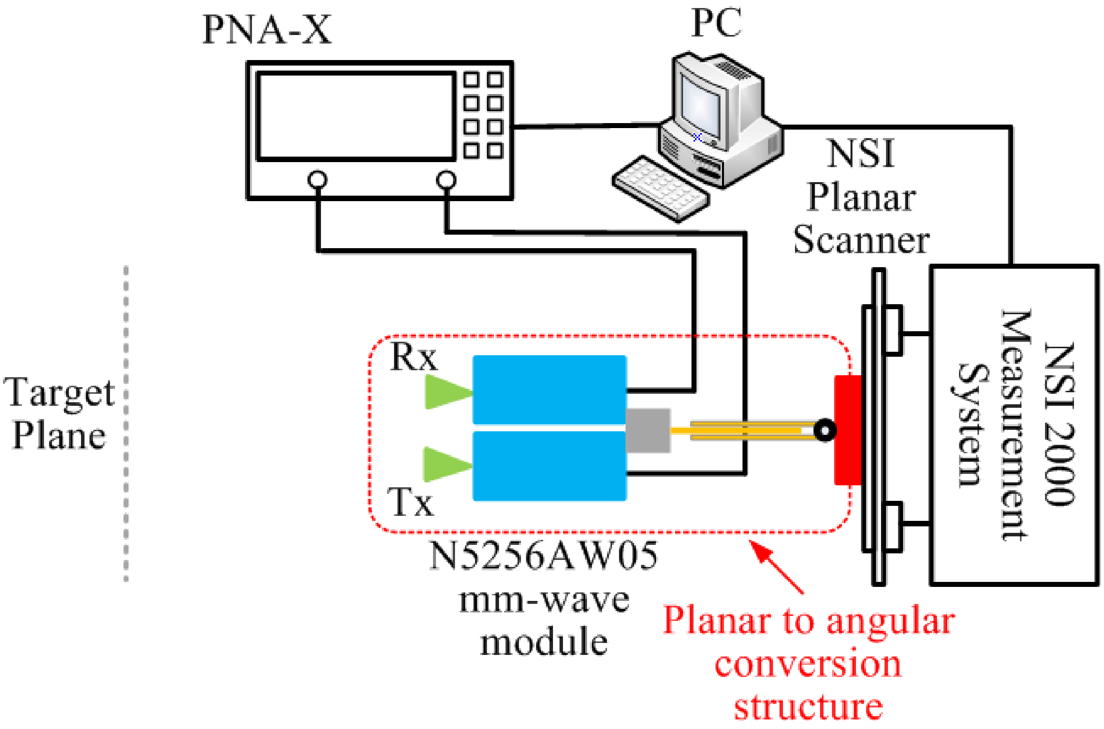
PNA-X
PC
NSI Planar Scanner
Target Plane
Rx
Tx
NSI 2000 Measurement System
N5256AW05 mm-wave module
Planar to angular conversion structure

Figure 5-40 Schematic of the experimental beam scanned imaging system.

Photographs of the experimental environment are shown in Figure 5-41. The conversion structure is fixed on the standing table with tapes.

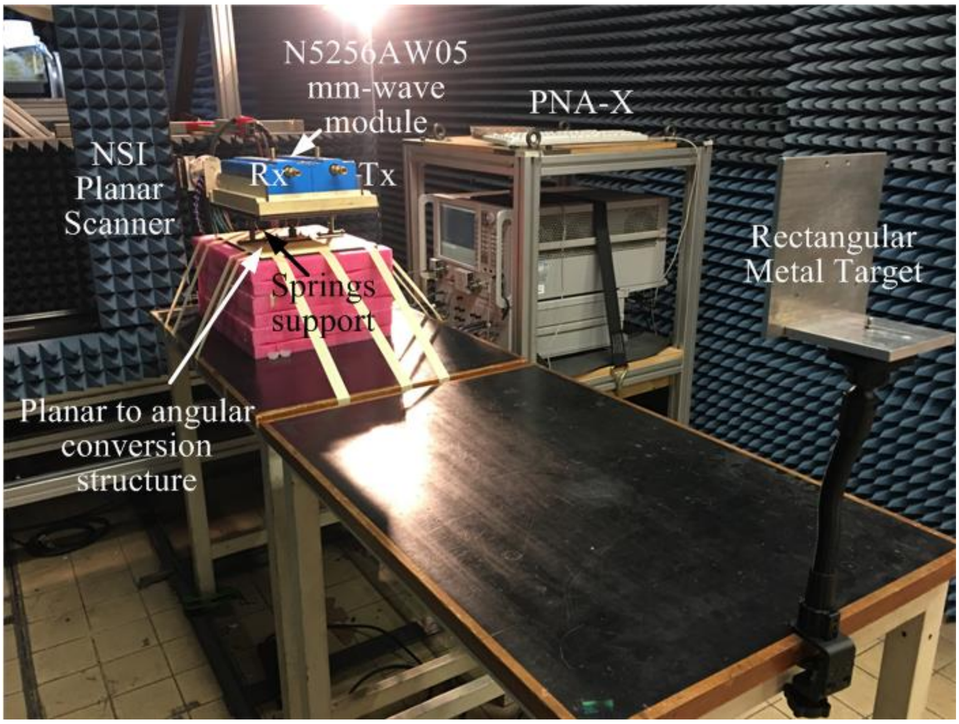
N5256AW05
mm-wave
module
PNA-X
NSI
Planar
Scanner
Rx
Tx
Rectangular
Metal Target
Springs
support
Planar to angular
conversion
structure

(a)

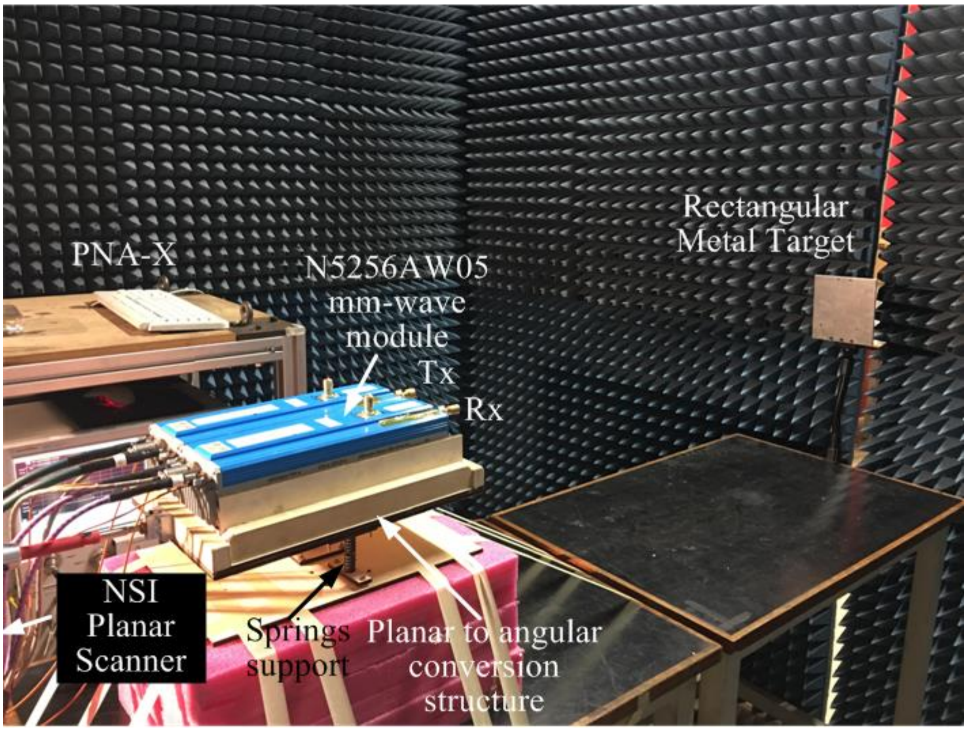
Rectangular
Metal Target
PNA-X
N5256AW05
mm-wave
module
Tx
Rx
NSI
Planar
Scanner
Springs
support
Planar to angular
conversion
structure

(b)

Figure 5-41 Photographs of the experimental environment (a) the front side (b) the back side.

A rectangular metal target with the dimension of $149\ \mathrm{mm} \times 159.5\ \mathrm{mm}$ as shown in Figure 5-42 is fixed on a lifting stick which ensures the centre of the target is in line with the scanning centre. Some small holes with the diameter of 4 mm are located at different positions on the target.

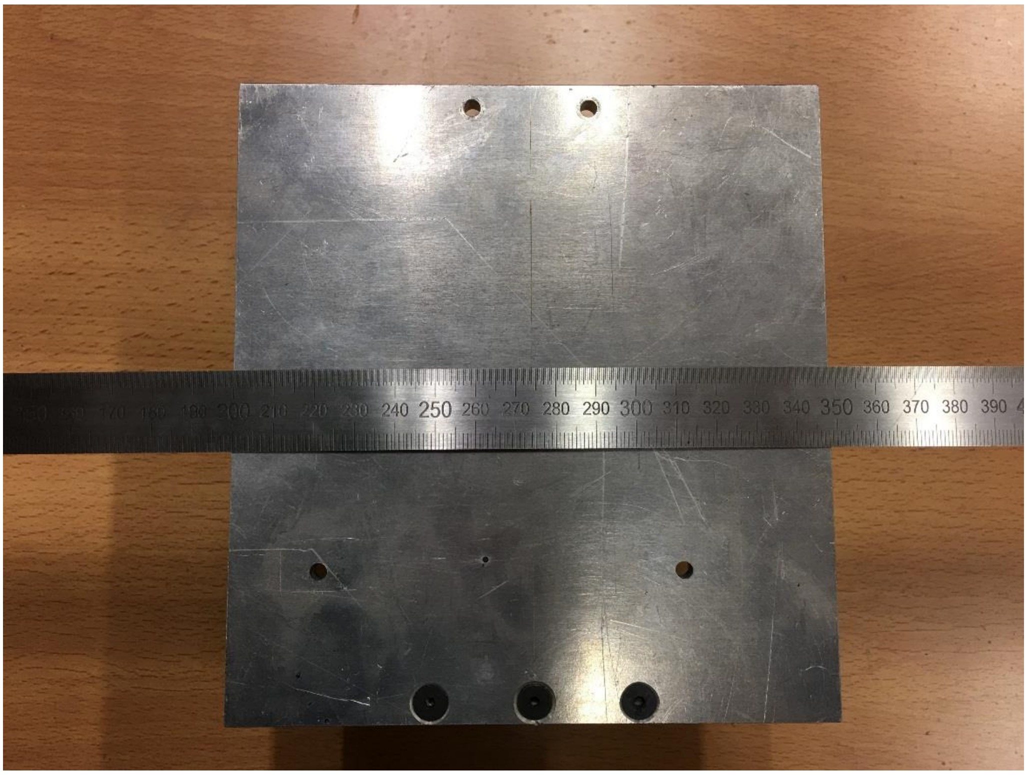

Figure 5-42 Photograph of the rectangular metal target used in the beam scanning experiment.

From the data received by the receiver horn, we can get the amplitude and phase distribution of electric field on the aperture plane (shown in Figure 5-43). As set in the experiment, the recording area has the size of 0.3 m. Since of the proportion of the distance from the target to joint 1 and the distance from joint 1 to the planar scanner, the real imaged area covers 0.6 m by 0.6 m. In this figure, the area size has been transferred. These two figures show the approximate position and size of the target.

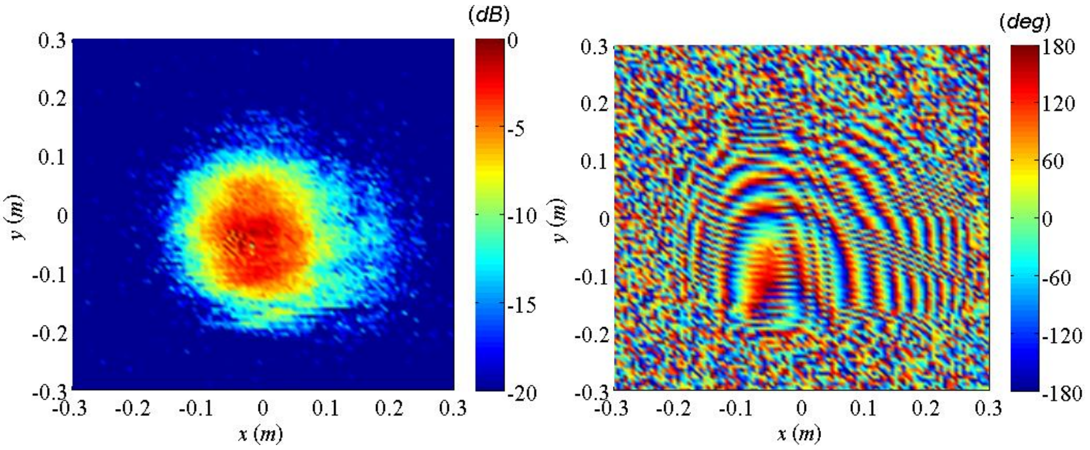

(a) (b)

Figure 5-43 (a) amplitude and (b) phase images constructed by signals received and the area size has been transferred from 0.3 m to 0.6 m. (The legend indicates the normalised values in dB and degrees)

The reconstruction is a little different from the reconstruction for the raster scanned imaging system. The compensation has been conducted to off-axis the amplitude and phase deviation due to different angles between the target plane and the beam central line and the distance changing between transceivers and the recorded target point. Detailed distance change from L1 to L2 is demonstrated in Figure 5-44. When the platform is rotated in an angle of θ, the distance change is

$$L_2 - L_1 = (d_2 tan\theta + L/cos\theta) - L \tag{5-19}$$

Where d_2 is the vertical distance from the horn centre to joint 1, L is the distance between the target plane and joint 1, d_1 is the horizontal distance from the horn centre to joint 1. The compensation here different from previous beam scanning scheme simulation lies on the vertical off-axis distance d_2.

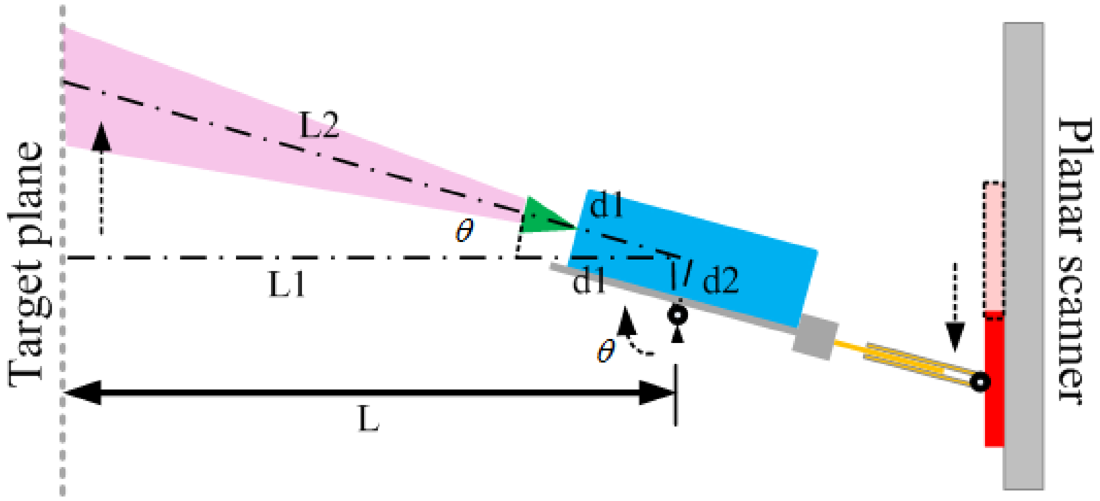

Figure 5-44 The detection distance change in the beam scanning experimental system.

Reconstructed images of the rectangular target with different sampling points on each dimension from 101 to 41 are demonstrated in Figure 5-45. From the reconstructed image shown in Figure 5-45 (a), the shape and the dimensions can be discriminated clearly but the resolution has been limited. Actually, the scenario with 201 sampling points here only has the similar performance of the scenario with about 134 sampling points in the raster scanning imaging system. Though the scanning step for the planar scanner here is 0.0015 m, the sampling step for the target area of 0.6 m by 0.6 m will be 0.003 m. Considering the target area of 0.4 m by 0.4 m in the raster scanning imaging system, the performance of this evaluation experimental beam scanning imaging system (*N* sampling points, the scanning step is Δd) shares the similar performance of the raster scanning imaging system (*2N/3* sampling points, the scanning step is $3\Delta d/2$). This means that the step has been enlarged by a factor of 1.5 in the experimental beam scanning system. The relation of the step set on the planar scanner and the real scanned step in the target area for the experimental beam scanning system is listed in Table 5-6. This means that for the 201 sampling points scenario in the beam scanning experiment, the imaging performance will be similar with the 134 sampling points scenario in the raster scanning experiment. Therefore, one needs to bear this in mind when comparing the imaging results between the beam scanning experiment and the raster scanning experiment. To realise the similar scanning step, the number of sampling points for two experimental systems are listed in Table 5-7. The relation only applies to these two experimental systems in this thesis. The maximum number of sampling points in this experiment is limited by the mechanical movement accuracy of NSI 2000 measurement system.

Table 5-6 The relation of the step set on the planar scanner and the real scanned step in the target area for the experimental beam scanning system.

Sampling point	**Step set on the planar scanner (mm)**	**Real step on the target plane (mm)**
201	1.5	3
101	3	6
81	3.75	7.5
61	5	10
41	7.5	15

Table 5-7 The number of sampling points for two experimental systems for the same scanning interval.

Scanning step on target plane (mm)	**Beam scanning sampling point**	**Raster scanning sampling point**
3	201	134
6	101	67
7.5	81	54
10	61	41

15	41	27

The size and boundaries of the reconstructed image in Figure 5-45 (a) match well with the real target. But the holes on the target (Figure 5-45 (b)-(e)) are not resolved. There are several possible reasons causing this problem. First of all, the loose spring support under the wooden platform (as shown in Figure 5-41) will introduce the positioning inaccuracy and instability during the scanning. The positioning inaccuracy of the planar scanner itself can also introduce some error in the result. For the raster scanning experiment, though some error exists, but it has been proved not affecting the final reconstruction result dramatically. However, for the beam scanning experiment, the error is enlarged to 2 times due to the ratio of lengths on the planar scanner side and the target side. Further improvements will be made on this experimental system. A spindle type of spring support under the platform can make the platform more stable. A smaller lever ratio can also reduce the scanning error caused by NSI scanner itself.

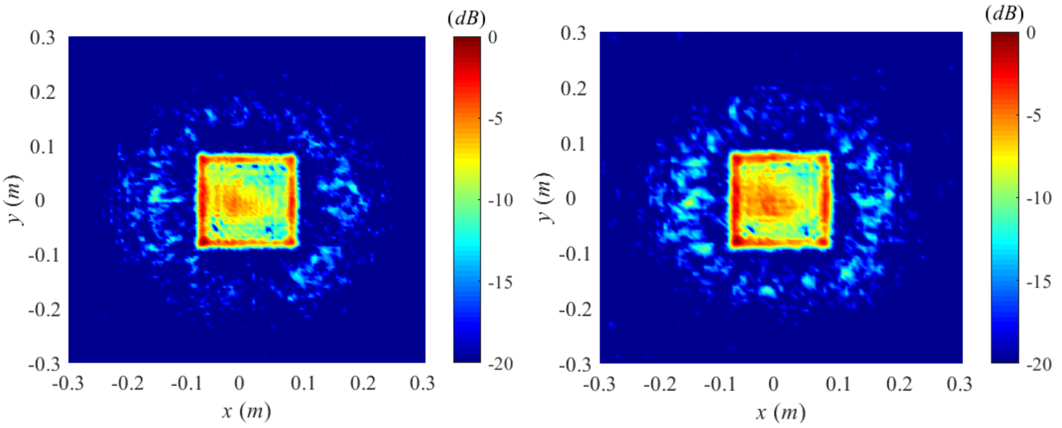

(a)

(b)

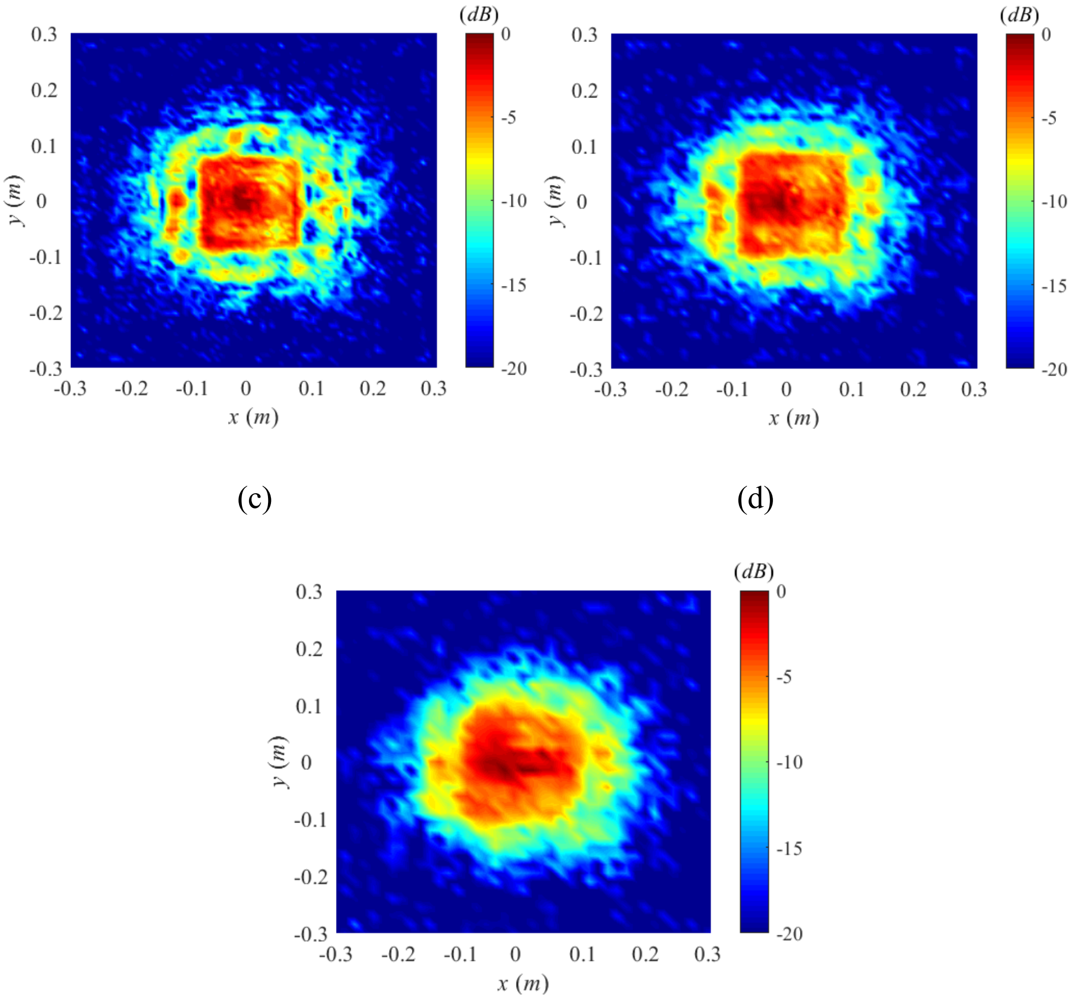

(c)

(d)

(e)

Figure 5-45 Reconstructed images of the rectangular target with different sampling points: (a) 201×201 (b) 101×101 (c) 81×81 (d) 61×61 (e) 41×41. (The legend indicates the normalised values in dB)

5.4 Summary

In this chapter, a simplified THz imaging system at 220 GHz based on the raster scanning scheme was assembled and investigated firstly. The results obtained from conducted experiments have verified the raster scanned scheme of the THz holographic imaging system. Then the proposed beam scanning scheme was also evaluated with a planar to angular scanning conversion structure and a planar scanner. Reconstructed images of the assembled beam scanning experimental system show the feasibility of the proposed beam scanned scheme. More improvements and studies need to be made in the future work.

5.5 References

[1] L. Zhang, Y. Hao, and C. Parini, Millimetre wave imaging system parameters at 95GHz, IET Microwaves, Antennas Propagation, vol. 5, no. 5, pp. 528–534, 2011.

[2] M. Zhou, Y. Alfadhl and X. Chen, Study of Scanning Schemes for THz Holographic Imaging, 32nd International Union of Radio Science General Assembly and Scientific Symposium (URSI 2017 GASS), 2017.

[3] J. J. H. Wang. An examination of the theory and practices of planar near-field measurement. IEEE Transactions on Antennas and Propagation, vol. 36, no. 6, pp. 746-753, 1988.

[4] A. Tamminen, J. Ala-Laurinaho, and A. R¨ais¨anen, Indirect holographic imaging: evaluation of image quality at 310 GHz, SPIE Defense, Security, and Sensing. International Society for Optics and Photonics, pp. 76 700A–76 700A, 2010.

[5] A. E. Burgess, The rose model, revisited, JOSA A, vol. 16, no. 3, pp. 633–646, 1999.

[6] M. Zhou, Y. Alfadhl ,X. Chen, H. Feng, H. Tu, D. Xiao and S. Wu, The Effects of Transceiver Antenna Alignments on THz Holographic Imaging System, 4th Asia-Pacific Conference on Antennas and Propagation (APCAP), 2015.

[7] D. Slater, Near-field antenna measurements. Artech House, 1991.

[8] ISO 12232: 1997 Photography – Electronic Still Picture Cameras.

[9] D. M. Sheen, D. McMakin, and T. Hall, Near-field three-dimensional radar imaging techniques and applications, Applied Optics, vol. 49, no. 19, pp. E83–E93, 2010.

[10] D. M. Sheen and T. E. Hall, Reconstruction techniques for sparse multistatic linear

array microwave imaging, SPIE Defense+ Security. International Society for Optics and Photonics, Conference Proceedings, pp. 90 780I, 2014.

Chapter 6. Summary and future works

6.1 Summary

This thesis mainly focuses on the development of THz holographic imaging systems for the security application. Many aspects have been investigated, including simulation of imaging schemes using Physical Optics (PO) algorithm in Matlab, design and simulation of Dragonian dual-reflector scanning system in GRASP, assessment of two image reconstruction methods: Transposed Convolution (TC) and Partial Inverse Convolution (PIC), and evaluation experiments based on the raster scanning scheme and the beam scanning scheme.

In Chapter 1, the recent development of Terahertz detection technology was reviewed. The THz wave has shown great potential in various applications. Active and passive detectors have been developed in research groups all over the world. The state-of-art THz imaging systems and products were surveyed and summarized. The requirement for high speed and high quality THz imaging systems has brought new technical challenges into the THz imaging field.

In Chapter 2, the introduction to the holography theory was given firstly. Optical holography and microwave holography were presented and compared. They share the same principle that both of the amplitude and the phase are employed to reconstruct the image. The equations for THz holographic image reconstruction were derived. Then, a new beam scanning scheme was proposed in comparison with the conventional raster scanning scheme. To realise the beam scanning, a Dragonian dual-reflector scanning system was designed. Required parameters of the mechanical part were calculated. Mechanical components were designed carefully to meet the scanning trajectory and assembling requirements.

In Chapter 3, the design of Dragonian dual-reflector scanning sub-system was presented. Firstly, the characteristics of various reflector antennas were reviewed. Then, a Dragonian reflector antenna in our proposed beam scanning scheme was simulated by using GRASP9. Path length error studies showed good performance over the whole scanned area of the scanning sub-system in comparison with a single ellipsoildal reflector antenna. Two different scanning schemes were also simulated and compared. The scheme where the main reflector rotates in y direction and the flat mirror rotates in x direction was proved to perform better. The scanning sub-system was proved to remain the beam consistent in the whole scanning area with the loss variation less than 1 dB.

In Chapter 4, the theory of Physical Optics and its application in the simulation of two scanning schemes were presented. PO algorithm was briefly presented at first. Then the PO algorithm in Matlab was validated with a single off-axis reflector antenna compared with simulated results by using GRASP 9. The performance of both raster-scanning and beam-scanning were studied using the PO simulation in MATLAB with a rectangular target. It was demonstrated that the angular beam scanning can achieve a comparable image as the raster scanning with a negligible increase of processing time. In the final part, the Transposed Convolution (TC) algorithm and the Partial Inverse Convolution (PIC) algorithm were compared and discussed with the conventional Back Propagation (BP) algorithm when reconstructing the same images. The application of TC and PIC algorithms were proved to reduce the reconstruction time while remaining the image quality.

In Chapter 5, the experimental evaluation of the THz holography imaging systems based on the raster scanning scheme and the beam scanning scheme were presented, respectively. Experiments of the raster scanned scheme are conducted on a simplified 2D holography system. Spatial sampling interval and Line Spread Function of the deployed system are analysed on the reconstructed images. A planar to angular scanning conversion platform is designed and assembled with the NSI 2000 planar scanner to conduct the experimental studies of the beam scanned scheme. Reconstructed images are investigated and discussed.

The detailed structure relationship of each chapters in this thesis is shown in Figure 6-1.

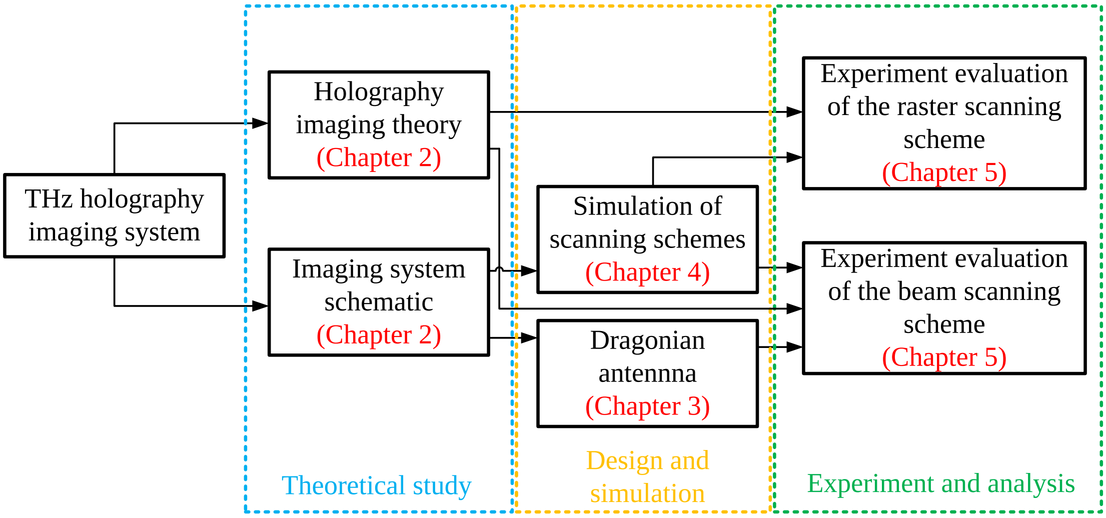
THz holography imaging system
Holography imaging theory
(Chapter 2)
Imaging system schematic
(Chapter 2)
Simulation of scanning schemes
(Chapter 4)
Dragonian antennna
(Chapter 3)
Experiment evaluation of the raster scanning scheme
(Chapter 5)
Experiment evaluation of the beam scanning scheme
(Chapter 5)
Theoretical study
Design and simulation
Experiment and analysis

Figure 6-1 The thesis structure of the THz holography imaging system.

6.2 Key contributions

1. A new beam scanning THz imaging system was proposed and analysed to demonstrate an improved performance in terms of size and imaging time.

A THz holographic imaging system operating at 220 GHz is investigated in simulation and experiments, comparing two scanning schemes: the raster scanning and the beam scanning, respectively.

The Dragonian multi-reflector antenna is introduced as the fundamental design of the mechanical scanning sub-system. By rotating the main reflector and an additional plate reflector in orthogonal dimensions, the scanning quasi-optical sub-system realises a balance of the transmitting beam consistent and the complexity of the system assembly.

2. The application of the Transposed Convolution and Partial Inverse Convolution in

THz image reconstruction algorithms.

In these newly proposed algorithms, only the convolution operation is conducted rather than FFT, multiplication and IFFT operations in the back-propagation algorithm. Compared the widely applied Back Propagation algorithm, the Transposed Convolution and Partial Inverse Convolution algorithm can reconstruct images in less time with comparable quality.

3. The development of Physical Optics (PO) models for the scanning systems in THz holographic imaging systems.

The performance of both raster-scanning and beam-scanning are studied using the PO simulation in MATLAB with a rectangular target. It is demonstrated that the angular beam scanning can achieve a comparable image as the raster scanning with a negligible increase of processing time.

4. The study of the optimal spatial sampling criterion in a 2D THz holographic imaging system.

Traditionally, the spatial sampling interval, which needs to satisfy the Nyquist sampling criterion, has mostly been selected based on the worst case scenario. We have derived in theory an optimal spatial sampling criterion based on the target size and the threshold power beam width angle of transmitter/receiver antenna. The optimal spatial sampling interval is much larger than the worst case Nyquist criterion and has been verified in the experiment, leading to a substantially reduced imaging time while maintaining the image quality.

5. The development of an experimental platform for assessing THz imaging system based on the beam scanning.

A simplified THz beam scanning holographic imaging system is established based on a planar scanner to evaluate the performance of the proposed imaging scheme experimentally.

6.3 Future work

Future work will mainly focus on the improvement of the experimental beam scanning imaging system, the build-up of the beam scanning imaging system utilising Dragonian dual-reflector sub-system and the application of proposed new image reconstruction algorithms.

1. A new design of the rotating component in the planar to angular conversion structure is needed. In the existing experimental system, the movement of the rotation part on the ground board is not smooth and stable enough. A spindle structure needs to be added to make this system more stable and accurate.

2. Further experiments of the beam scanning imaging prototype system are needed. More detailed parameters for the beam scanning scheme will be studied in experiments. Various practical scenarios are to be investigated.

3. The proposed beam scanning imaging system utilising Dragonian dual-reflector sub-system needs to be built in collaboration with other research group. After the feasibility study of the beam scan imaging prototype, the practical THz imaging system are to be developed.

4. The improvement of proposed new image reconstruction algorithms is to be carried out. Though two algorithms have been proved efficient in this thesis, some improvement still can be made especially the noise appeared in the reconstructed image using PIC algorithm. Meanwhile, the investigation on different mathematical principles in these algorithms will be continued to speed up the reconstruction efficiency even more.

List of publications

Journal papers:

[1] **Min Zhou**, Yasir Alfadhl, Xiaodong Chen, Hui Feng, Hao Tu, Dongping Xiao and Shuai Wu, Optimal Spatial Sampling Criterion in a 2D THz Holographic Imaging System, IEEE Access, accepted.

[2] **Min Zhou**, Shaoqing Hu, Yasir Alfadhl and Xiaodong Chen, Investigation on novel THz Image Reconstruction by Partial Inverse Convolution Algorithm, to be submitted.

Conference papers:

[1] **Min Zhou**, Shaoqing Hu, Yasir Alfadhl and Xiaodong Chen, Investigation of THz Image Reconstruction by Inverse Convolution Algorithm, 10th UK-China Millimetre Waves and Terahertz Technology Workshop (UCMMT 2017), 11-13 September, 2017, Liverpool, UK.

[2] Shaoqing Hu, **Min Zhou** and Xiaodong Chen, Study on a Sparse Antenna Array for Terahertz Imaging, 10th UK-China Millimetre Waves and Terahertz Technology Workshop (UCMMT 2017), 11-13 September, 2017, Liverpool, UK.

[3] **Min Zhou**, Yasir Alfadhl and Xiaodong Chen, Study of Scanning Schemes for THz Holographic Imaging, 32nd International Union of Radio Science General Assembly and Scientific Symposium (URSI 2017 GASS), 19-26 August, 2017, Montreal, Canada.

[4] **Min Zhou**, Yasir Alfadhl, and Xiaodong Chen, Study on a THz beam-scanning system with offset Dragonian dual-reflector antenna, 9th UK-Europe-China Workshop on Millimetre Waves and Terahertz Technologies (UCMMT 2016), 5-7 September, 2016, Qingdao, China.

[5] **Min Zhou**, Yasir Alfadhl and Xiaodong Chen, Study on a THz image scanning

system with ellipsoidal reflector, 8th UK-China Millimetre Waves and Terahertz Technology Workshop (UCMMT 2015), 14-16 September, 2015, Cardiff, UK.

[6] **Min Zhou**, Yasir Alfadhl ,Xiaodong Chen, Hui Feng, Hao Tu, Dongping Xiao and Shuai Wu, The Effects of Transceiver Antenna Alignments on THz Holographic Imaging System, 4th Asia-Pacific Conference on Antennas and Propagation (APCAP 2015), 30 June-3 July, 2015, Bali island, Indonesia.

[7] **Min Zhou**, Yasir Alfadhl and Xiaodong Chen, Study on terahertz holography system at 220 GHz, 7th Europe/UK-China Workshop on Millimetre Waves and Terahertz Technologies (UCMMT 2014), September 2-4, 2014, Chengdu, China.

Appendix I: Parameters calculation in Dragonian antenna design

(1) β (the tilt angle between the secondary reflector coordinate system z_s axis and the main reflector coordinate system z_m axis):

$$\beta = arctan\left(\frac{4Ftan\left(\frac{\theta_E}{2}\right)sin(\theta_P)}{D_m+4Ftan\left(\frac{\theta_E}{2}\right)cos(\theta_P)}\right) \tag{I-1}$$

(2) α (the tilt angle between the secondary reflector coordinate system z_s axis and the feed coordinate system z_f axis):

$$\alpha = \theta_P - \beta \tag{I-2}$$

(3) e (the eccentricity of the secondary reflector):

$$e = \frac{sin\left(\frac{\beta+\alpha}{2}\right)}{sin\left(\frac{\beta-\alpha}{2}\right)} \tag{I-3}$$

(4) θ_0 (the offset angle of the main reflector):

$$\theta_0 = 2arctan\left(\frac{tan\left(\frac{\beta}{2}\right)\left[\left(\frac{e+1}{e-1}\right)^2-1\right]}{tan^2\left(\frac{\beta}{2}\right)+\left(\frac{e+1}{e-1}\right)^2}\right) \tag{I-4}$$

(5) h (the offset distance of the main reflector):

$$h = 2Ftan\left(-\frac{\theta_0}{2}\right) \tag{I-5}$$

(6) θ_U (the offset angle of the top of the main reflector):

$$\theta_U = -2arctan\left(\frac{h+\frac{D_m}{2}}{2F}\right) \tag{I-6}$$

(7) θ_L (the offset angle of the bottom of the main reflector):

$$\theta_L = -2arctan\left(\frac{h-\frac{Dm}{2}}{2F}\right) \tag{I-7}$$

(8) d_{fs} (the distance between the centre point of the secondary reflector and the feed):

$$d_{fs} = \frac{sin(\beta-\theta_0)}{sin(\alpha)}\left[\frac{h}{sin(|\theta_0|)} - d_{sm}\right] \tag{I-8}$$

(9) a (the distance between vertices of two hyperboloid branches):

$$a = \frac{h}{2sin(|\theta_0|)} - \frac{d_{sm}+d_{fs}}{2} \tag{I-9}$$

(10) f (the half of the distance between two focal points):

$$f = ae \tag{I-10}$$

Appendix II: Physical optics derivation

In the theory of PO, the induced current on the surface of the illuminated scatter $\mathbf{J}(\mathbf{r}')$ can be calculated as:

$$\mathbf{J}(\mathbf{r}') = \begin{cases} 2\hat{n} \times \mathbf{H}^i(r') & \textit{illuminated region} \\ -j\left(k_x^2 + k_y^2 - k^2\right)^{1/2} & \textit{otherwise} \end{cases} \tag{II-1}$$

where $\mathbf{r}'$ is the position vector of a random point on the surface of the scatter, $\hat{n}$ is the unit surface normal which points outward on the illuminated side of the surface at the point with the position vector $\mathbf{r}'$. $\mathbf{H}^i(r')$ is the incident magnetic field at the point with the position vector $\mathbf{r}'$. $\mathbf{H}^i(r')$, $\mathbf{J}(\mathbf{r}')$ and $\hat{n}$ are shown in Figure II-1.

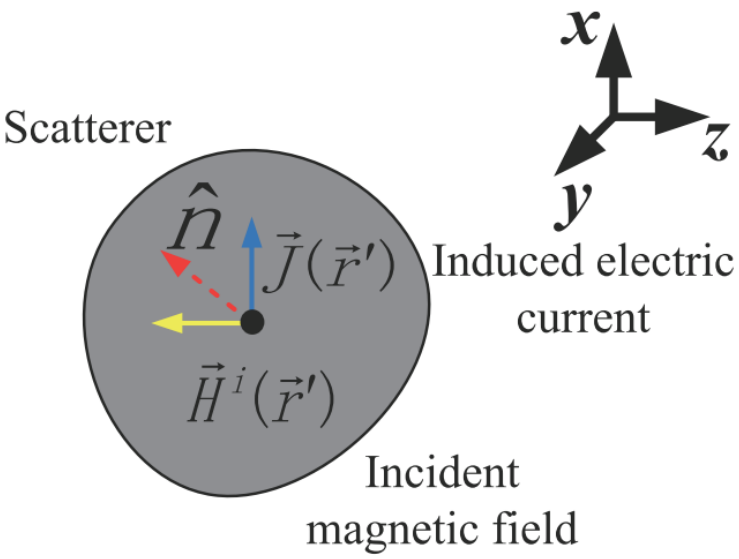

Figure II-1 Induced electric current on the illuminated scatterer.

The radiation field of the scatter can be derived from the surface induced current $\mathbf{J}(\mathbf{r}')$ as:

$$\mathbf{E}(\mathbf{r}) = j\omega\mu\mathbf{A}(\mathbf{r}) + \frac{1}{j\omega\varepsilon}\nabla[\nabla \cdot \mathbf{A}(\mathbf{r})] \tag{II-2}$$

$$\mathbf{H}(\mathbf{r}) = \nabla \times \mathbf{A}(\mathbf{r}) \tag{II-3}$$

where *r* is the vector of the observation point and the magnetic vector potential $\mathbf{A}(\mathbf{r})$ can be calculated as

$$\mathbf{A}(\mathbf{r}) = \iint_{s'} J(\mathbf{r}')G(\mathbf{r}|\mathbf{r}')ds' = \iint_{s'} J(\mathbf{r}')\frac{e^{-jk|\mathbf{r}-\mathbf{r}'|}}{4\pi|\mathbf{r}-\mathbf{r}'|}ds' \tag{II-4}$$

where the free space wave number $k = \omega\sqrt{\varepsilon\mu}$. Scalar Green function $G(\mathbf{r}|\mathbf{r}')$ satisfies

$$(\nabla^2 + k^2)G(\mathbf{r}|\mathbf{r}') = -\delta(\mathbf{r} - \mathbf{r}') \tag{II-5}$$

The radiation field of the illuminated scatter as:

$$\mathbf{E}(\mathbf{r}) = -jk\eta \iint_{s'} \left[g_1\mathbf{J}(\mathbf{r}') - g_2\big(\mathbf{J}(\mathbf{r}') \cdot \hat{R}\big)\hat{R}\right]\frac{e^{-jkR}}{4\pi R}ds' \tag{II-6}$$

$$\mathbf{H}(\mathbf{r}) = -jk \iint_{s'} \left[g_3\left(\hat{R} \times \mathbf{J}(\mathbf{r}')\right)\right]\frac{e^{-jkR}}{4\pi R}ds' \tag{II-7}$$

$$g_1 = 1 - \frac{j}{kR} - \frac{1}{(kR)^2} \tag{II-8}$$

$$g_2 = 1 - \frac{3j}{kR} - \frac{3}{(kR)^2} \tag{II-9}$$

$$g_3 = 1 - \frac{j}{kR} \tag{II-10}$$

$$\hat{R} = \frac{\mathbf{R}}{R} = \frac{\mathbf{r}-\mathbf{r}'}{|\mathbf{r}-\mathbf{r}'|} \tag{II-11}$$

where η is the free space impedance, $\eta = \sqrt{\mu/\varepsilon}$.

The scattered electromagnetic field from the scatterer can be found in Figure II-2.

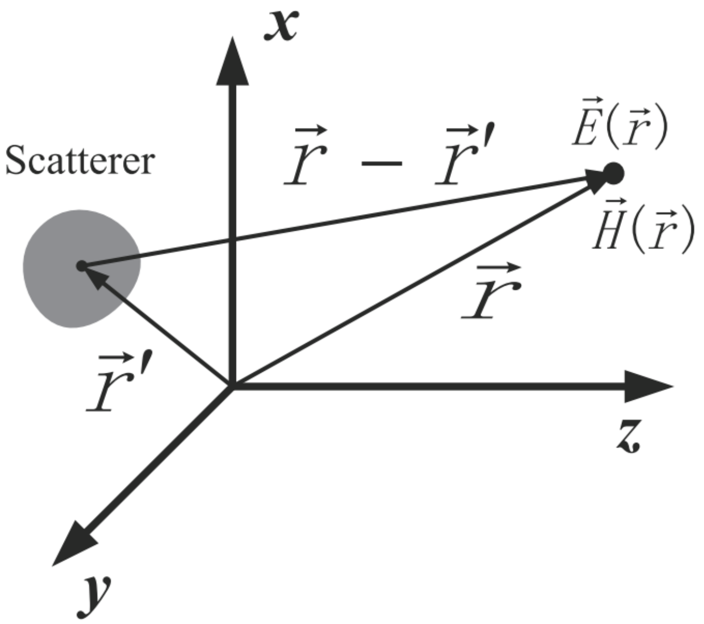

Figure II-2 The scattered electromagnetic field from the scatter.

Considering the far field, after the high order part of *1/R* ignored, the radiated far field can be realized as

$$\mathbf{E}^{far}(\theta,\phi) = -jk\eta\frac{e^{-jkr}}{4\pi r}(\bar{\mathbf{I}} - \hat{r}\hat{r})\iint_{s'}\mathbf{J}(\mathbf{r}')e^{jk\mathbf{r}'\cdot\hat{r}}\,ds' \tag{II-12}$$

$$\mathbf{H}^{far}(\theta,\phi) = -jk\frac{e^{-jkr}}{4\pi r}\hat{r}\iint_{s'}\mathbf{J}(\mathbf{r}')e^{jk\mathbf{r}'\cdot\hat{r}}\,ds' \tag{II-13}$$

where $\bar{\mathbf{I}}$ is unit dyad and $\hat{r}$ is the unit vector at the observation point:

$$\hat{r} = sin\theta cos\phi\hat{x} + sin\theta sin\phi\hat{y} + cos\theta\hat{z} \tag{II-14}$$

When calculating the radiation field of the reflector antenna, the integral on the curved surface can be transferred to the double integral on the projected plane. Assume that the surface satisfies:

$$z = f(x,y) \tag{II-15}$$

The unit normal of a point on the reflector surface is:

$$\hat{n} = \mathbf{N}/|\mathbf{N}| \tag{II-16}$$

where $\mathbf{N}$ and $|\mathbf{N}|$ can be expressed as:

$$\mathbf{N} = -\frac{\partial f}{\partial x}\hat{x} - \frac{\partial f}{\partial y}\hat{y} + \hat{z} \tag{II-17}$$

$$|\mathbf{N}| = \sqrt{\left(\frac{\partial f}{\partial x}\right)^2 + \left(\frac{\partial f}{\partial y}\right)^2 + 1} \tag{II-18}$$

Then field equations can be transferred to:

$$\mathbf{E}^{far}(\theta, \phi) = -jk\eta\frac{e^{-jkr}}{4\pi r}(\bar{\mathbf{I}} - \hat{r}\hat{r})\iint_D \mathbf{J}(\mathbf{r}')e^{jk\mathbf{r}'\cdot\hat{r}}\,|\mathbf{N}|dxdy \tag{II-19}$$

$$\mathbf{H}^{far}(\theta, \phi) = -jk\frac{e^{-jkr}}{4\pi r}\hat{r}\iint_D \mathbf{J}(\mathbf{r}')e^{jk\mathbf{r}'\cdot\hat{r}}|\mathbf{N}|\,dxdy \tag{II-20}$$

where *D* is the projected area of the reflector surface on the XOY plane.

Appendix III: Ideal gaussian feed

In the theoretical computation, the radiation pattern of the ideal feed is normally used to simulate the radiation characteristics of the real feed. Gaussian feed was chosen as the ideal feed deployed in our model. Gaussian feed has been proved to be a simple but very useful feed model. It can not only be used to approximately simulate the far field radiation pattern, but also give out the near field pattern of the corrugated horn which is crucial for the computation of the reflector located in the near field area of the feed. In recent years, this feed model has been widely applied in many commercial simulators such as, GRASP. The far field of the Gaussian feed has rotational symmetry.

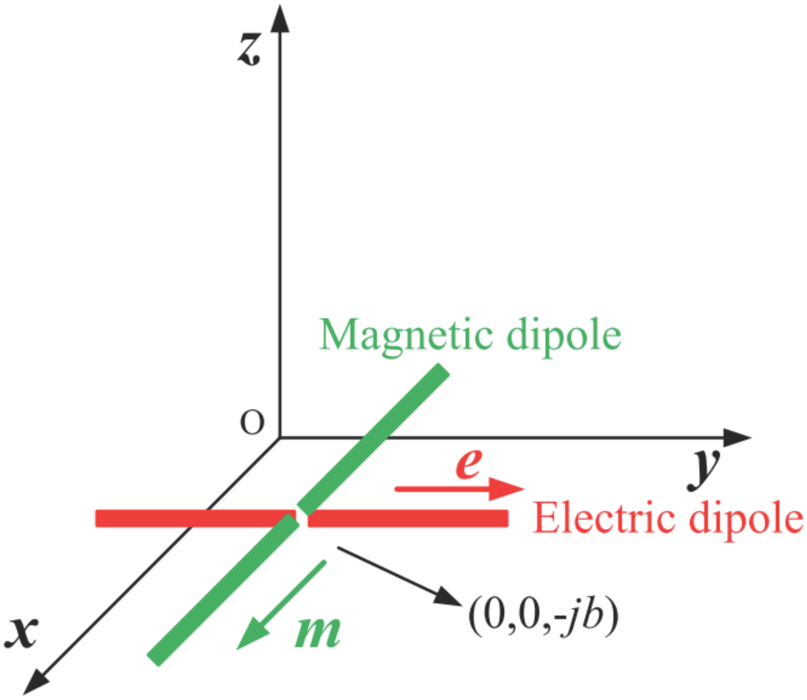

Figure III-1 Schematic of the linear x-polarized Gaussian beam.

The generation of linear x-polarized Gaussian beam is shown in Figure III-1. The Huygens source consisting of an electric and a magnetic dipole is put at the point (0,0,-*jb*) in the complex space. The electric dipole is placed in line with x-axis while the magnetic dipole is placed in line with y-axis. The parameter b controls the beam width of the Gaussian beam. In the complete expression of the Gaussian beam radiation, the distance between the complex point and the observation point need to be taken into field expressions of the electric and a magnetic dipole. To simplify the problem, the radiation of the Gaussian beam feed can be expressed as:

$$\mathbf{E}_{feed}(\theta,\phi) = \left[\hat{\theta}f(\theta)\left(a_1e^{j\varphi}cos\phi + a_2sin\phi\right) + \hat{\phi}f(\theta)(-a_1e^{j\varphi}sin\phi + a_2cos\phi)\right]\frac{e^{-jkr}}{r} \tag{III -1}$$

$$\mathbf{H}_{feed}(\theta,\phi) = \left[\hat{\theta}f(\theta)\left(a_1e^{j\varphi}sin\phi + a_2cos\phi\right) + \hat{\phi}f(\theta)(a_1e^{j\varphi}cos\phi + a_2sin\phi)\right]\frac{e^{-jkr}}{r} \tag{III -2}$$

where r is the distance between the observation point and the feed point. $f(\theta)$ is the directional function of the Gaussian beam which can be expressed as:

$$f(\theta) = e^{kbcos\theta}(1 + cos\theta) \tag{III -3}$$

The beam width of the Gaussian beam can be controlled by changing b and the relationship between b and the gain (A dB, A<0) at the angle of θ_q can be seen as:

$$b = \frac{20\,log_{10}\left((1+cos\theta_q)/2\right)-A}{20k\left(1-cos\theta_q\right)log_{10}\,e} \tag{III -4}$$

And A can also be expressed with b:

$$A = 20\,log_{10}\left((1 + cos\theta_q)/2\right) - 20bk\left(1 - cos\theta_q\right)log_{10}\,e \tag{III -5}$$

Different kinds of polarization can be realized by changing values of a_1, a_2 and φ. Table III -1 gives different values of a_1, a_2 and φ for linear polarization and circular polarization.

When designing the single feed single offset reflector antenna, appropriate values of half power band width angle must be chosen from the geometry, then calculate b from the illuminated taper.

Table III -1 The definition of different feed polarizations.

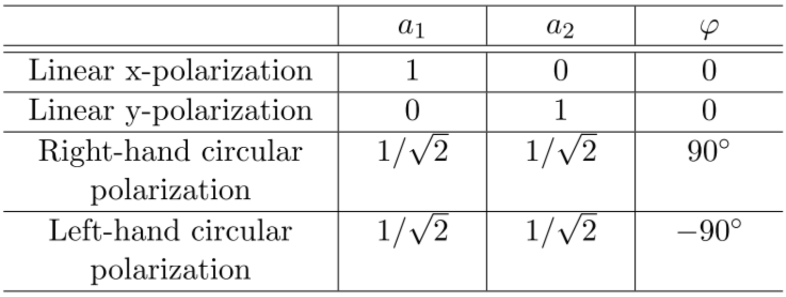

	a_1	a_2	φ
Linear x-polarization	1	0	0
Linear y-polarization	0	1	0
Right-hand circular polarization	$1/\sqrt{2}$	$1/\sqrt{2}$	$90°$
Left-hand circular polarization	$1/\sqrt{2}$	$1/\sqrt{2}$	$-90°$